Quantum Thermodynamics with Trapped Ions

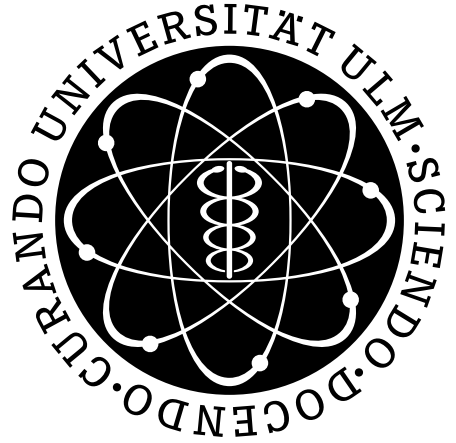

Dissertation

zur Erlangung des Doktorgrades Dr. rer. nat.
der Fakultät für Naturwissenschaften der Universität Ulm

Vorgelegt von

Gerhard Thomas Huber

aus München

2010

Amtierender Dekan:	Prof. Dr. Axel Groß
Erstgutachter:	Prof. Dr. Ferdinand Schmidt-Kaler
Zweitgutachter:	Prof. Dr. Tommaso Calarco

Die vorliegende Arbeit wurde angefertigt an der

Universität Ulm
Institut für Quanteninformationsverarbeitung
Albert-Einstein-Allee 11
89069 Ulm

Zusammenfassung

Die vorliegende Arbeit behandelt ein Gebiet, das experimentell bisher kaum erschlossen werden konnte: die Thermodynamik von kleinen Systemen im Quantenregime. In kleinen Systemen, das heißt in Systemen mit wenigen Freiheitsgraden, treten Phänomene auf, die von der makroskopischen Thermodynamik nicht bekannt oder sogar explizit verboten sind. Dazu zählen Nichtgleichgewichtsphänomene wie die statistische Fluktuation von sonst wohldefinierten Systemgrößen und die Verletzung des zweiten Hauptsatzes. Wie wichtig solche Phänomene sind, kann an biologischen Systemen gesehen werden, die sich genau diese Effekte zunutze machen, um im menschlichen Organismus lebensnotwendige Arbeit zu verrichten, um nur ein Beispiel zu nennen. Wenn kleine Systeme hinreichend ungestört sind, treten zusätzlich Quanteneffekte auf, die ihre Eigenschaften entscheidend beeinflussen, und ihrer Dynamik ein weiteres statistisches Element hinzufügen.

Während im Bereich der klassischen Physik auf diesem Forschungsgebiet bereits erste Experimente durchgeführt werden konnten, fehlt bisher noch der entscheidende experimentelle Schritt mit einem physikalischen System, das voll quantenmechanisch untersucht werden kann. Diese Arbeit diskutiert zunächst die Anforderungen, die ein physikalisches System überhaupt erfüllen muss, damit man entsprechende Experimente durchführen kann. Die Herausforderungen im Quantenregime sind ungleich höher als im klassischen Fall, weil Dekohärenz und Dissipation jegliche Quanteneffekte unbeobachtbar machen können. Dann zeigen wir, dass wir mit einem bestimmten System, nämlich einzelnen kalten Ionen, die in einer Paul-Falle gefangen sind, alle Anforderungen erfüllen können. Alle Punkte werden detailliert untersucht und die Lösungen experimentell belegt. Dabei ergeben sich viele Anwendungen und interessante Verbindungen zu anderen Gebieten der Physik wie der Quanteninformationstheorie. Es wird sich zeigen, dass das vorliegende System für die Erforschung thermodynamischer Nichtgleichgewichtsprozesse hervorragend geeignet ist. Einige konkrete Fragestellungen aus der aktuellen Forschung werden präsentiert, die mit den hier entwickelten Techniken erstmalig experimentell untersucht werden können.

Abstract

This thesis deals with a field of research, which is fairly new ground in experimental physics: the thermodynamics of small systems in the quantum regime. In small systems, which means systems with only few degrees of freedom, phenomena arise, that are unknown or even explicitly forbidden within the thermodynamics of macroscopic systems. Among these phenomena are non-equilibrium effects like the statistical fluctuation of otherwise well-defined system properties and violations of the second law. The importance of such phenomena can be seen from biological systems exploiting exactly these effects in order to perform vital work within the human organism, just to give one example. Additionally, quantum effects arise, when the systems are sufficiently isolated. These quantum features crucially alter the system's properties and introduce a further statistical element into their dynamics.

While first experiments could be performed on this field in the classical regime, one is still lacking the decisive step with a physical system, which allows for a full quantum mechanical investigation. This work first discusses general requirements put on a physical system in order to realize such experiments. The challenges in the quantum regime are distinctly higher than in the classical case, as decoherence and dissipation can render the observation of quantum effects impossible. Then we will demonstrate, that we can fulfill all requirements with a specific system, namely single cold ions confined in a Paul trap. All points will be discussed in detail and verified experimentally. In doing so, first applications arise unveiling close connections to other disciplines like quantum information theory. We will see, that the proposed system is in deed predestined for the investigation of non-equilibrium thermodynamic processes. Distinct questions raised by current research will be shown to become experimentally accessible for the first time by applying the developed techniques.

Contents

List of Figures

Chapter 1

Introduction

In the middle of the 19^{th} century, an epoch making technological progress inspired scientists to break new ground: the invention and successful application of steam engines gave rise to theoretical considerations about heat, work and energy in physical systems, which finally culminated in the development of classical thermodynamics and statistical mechanics. Since then, these theories have been extended and employed very successfully in many areas. They are, in some sense, *general-purpose* theories, pertaining to generality and the variety of physical systems they can be applied to: From biochemical processes within our cells over traffic behavior, financial markets to cosmological structures in the far universe, the applicability of thermodynamical concepts seems hardly limited.

All these systems have one feature in common: They are "large" with respect to the number of constituents (particles) they are composed of. Indeed, this is one of the reasons, why statistical predictions can be so precise. The sheer plenty of particles, together with the law of large numbers, ensures that a system's thermodynamic quantities have extremely well-defined values.

During the last decades, the technological progress has again given rise to reconsidering our description of nature. Advances in the possibility to observe and manipulate microscopic systems, both natural and artificially created ones, make us enter regimes, where the premise of a large system no longer holds. Such systems are ubiquitous in biology, chemistry or physics. For example, bio-molecules and their functioning as microscopic machines were investigated, and found to behave completely differently from large systems. In fact, thermodynamic quantities are no longer sharply defined in this regime, but are subject to fluctuations [Esp09]. A whole series of fluctuation theorems [Eva93, Eva94, Gal95, Jar97, Cro99] has been brought forth within the last two

decades, granting deeper insight into the properties of small systems. The term *thermodynamics of small systems* has been established for this area of research [Bus05], which revolves around the question, how the well-known laws of traditional thermodynamics can be applied to, or have to be modified to apply to, microscopic systems [Jar08].

In addition to the mere smallness of the systems, they mostly operate away from thermal equilibrium. This is, actually, a property of most non-trivial physical systems; but – from a stringent point of view – is not covered by classical thermodynamics, which deals with states of equilibrium and the transitions between them. While in traditional thermodynamics, for example, the second law strictly holds, it has to be revisited for the case of a small system's non-equilibrium process [Rit03].

Not by the investigation of steam engines, but by stretching single RNA[1]-molecules, first experiments were able to confirm some major results of this new research area [Lip02]. As a further example, the Kinesin biomolecule, which can be regarded as a subcellular motor, was found to harness thermal fluctuations in order to perform work on the human DNA[2] with impressive efficiency [Bus05].

Not only natural systems, but also artificially generated structures like nano-devices, micro-machines and "every-day" electronics, like highly integrated circuits, nowadays reach dimensions, that make traditional thermodynamics of large systems hit the wall sooner or later. Already today, down-scaled electronic circuits contain structures, which are only some nanometers in size, and contain only some thousands of electrons, for example, and an end in the progress of miniaturization is not within sight. It is obvious, that the upcoming, new phenomena connected with the non-equilibrium properties of small systems have to be accounted for; interestingly – as intriguing and complicated the new features might seem at first – nature showed us, that we might even profit from them.

In this thesis, we will make one decisive step forward, compared to all systems mentioned above: entering the *quantum regime*. Although small, the systems, that have been under experimental investigation so far, behave classically. Either, they are embedded in a thermal reservoir, which hampers the observation of genuine quantum features, or they are simply not small enough, having too many uncontrollable degrees of freedom. The system being introduced here, single trapped atoms, offers the full spectrum of features necessary for the observation of non-equilibrium phenomena in the quantum regime.

A single particle, which can be manipulated on the single quantum level, constitutes a

[1] Ribonucleic acid.
[2] Deoxyribonucleic acid.

text-book example for quantum mechanics. Similarly, it can be a rolemodel for quantum thermodynamic (qtd) systems, since it is a very well isolated system and can be easily prepared close to the zero point of temperature. Then, the energy separation between energy eigenstates is on the order of, or exceeds the mean thermal energy, and quantum effects become observable. Its conceptual simplicity, and its unique properties in terms of manipulation and detection capabilities make it a perfect workhorse for experiments elucidating the non-equilibrium thermodynamics of quantum systems.

There is a discipline in the field of quantum mechanics, for which these findings pertaining to non-equilibrium processes will be of fundamental interest: quantum information theory deals with quantum systems, that allow for information processing by controlled state transitions [Eke96, DiV95]. In analogy to classical information processing [Ben82], the transition process is called a *quantum gate* and the fundamental unit of information a *qubit*; it transforms the input state into a well-defined output state after the rules of quantum mechanics. Although the statements made here are absolutely general, the system we have in mind is, of course, the trapped-ion quantum computer [Cir95, Sch03].

For quantum information purposes, the focus lies on processes, that are unitary and reversible, in order not to loose information. The systems are ultimately cold and any upcoming of heat is suppressed as far as possible. A lot of effort is put on the goal to avoid dissipation, and the system is isolated almost perfectly from the environment. In this sense, such a system can be regarded as an extreme case of a thermodynamic system [Hen07]; this is the blank, smooth side of the coin. However, the rough side of the same coin is exactly what makes quantum information processing so demanding: The processes are not exactly adiabatic, since they must be performed in finite time. In fact, they are to be performed as fast as possible, so what is actually performed, is a non-equilibrium process! Additionally, as for the current status of research, the number of particles is really small, but has to be increased in order to advance the field. In fact, it is one of the greatest challenges in this field, to scale today's implementations up, so as to reach, say, a hundred qubits. Currently, it seems hardly feasible to control all degrees of freedom in a multidimensional Hilbert space. The most promising approach concerning this matter follows a "divide and conquer" philosophy, shuttling small numbers of qubit-carrying ions around between processor and memory regions [Kie02].

Residual coupling to the environment is one of the main sources of decoherence in the system, so we actually deal with weakly coupled, open systems, which constantly exchange energy with the environment. Figure 1.1 illustrates this circumstance.

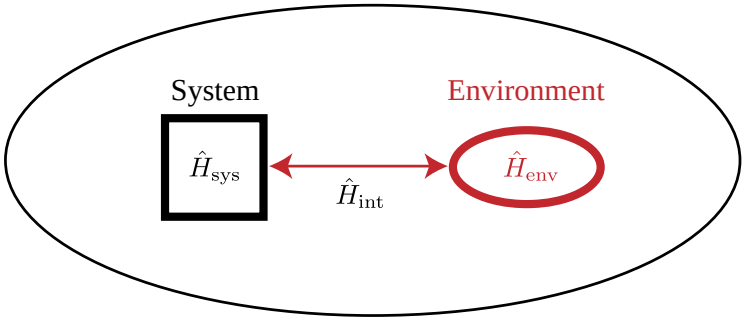

Figure 1.1: Interaction of a quantum system ($\hat{H}_{\mathrm{sys}}$) with an environment ($\hat{H}_{\mathrm{env}}$), represented by the interaction Hamiltonian $\hat{H}_{\mathrm{int}}$. The evolution of the total system, comprising both system and environment, is unitary; by the action of $\hat{H}_{\mathrm{int}}$, their respective degrees of freedom can be entangled with each other [Hil09]. Mostly, only the degrees of freedom of $\hat{H}_{\mathrm{sys}}$ are directly observable, so that tracing out the environment's degrees of freedom leads to decoherence. This scheme can be easily extended to the case of multiple subsystems [Paz08, Cor09] and multiple environments [Bee10].

To bring matters to a head, one could say, that quantum computation processes on the one hand, and quantum thermodynamic processes on the other hand, just differ by the perspective, from which the system is looked at. The controlled transport of an ion within the trap, for instance, can be seen as an implementation of the scaled quantum computer approach, where unwanted heating corrupts the process fidelity. Alternatively, the same process can be seen as a thermodynamic transformation of an external potential (like a gas being compressed), which is able to describe the system in a very natural way in terms of work and dissipation, for example. By these different perspectives, we are able to expand our horizons, and both research fields, quantum information and thermodynamics, profit. So far, this aspect has been investigated on a theoretical basis [Bra08], but this work will tackle arising issues also experimentally.

In addition to this physical relationship, utilizing trapped ions for qtd experiments can profit from the remarkable set of quantum optical techniques having been developed for quantum information [Nie00], quantum metrology [Ber98, Roo06] and quantum simulation [Fey82, Llo96, Joh09]. Indeed, the common motion of trapped ions, and the coupling between the information encoding, electronic structure of the ion to that motion, lies at the heart of the original and virtually all successive quantum gate proposals [Cir95]. This coupling is mediated by laser light and will prove to be the crucial ingredient for the success of the qtd approach with trapped ions, too.

The controlled interaction between light and matter is not only the basis for most ion manipulation and detection solutions, it also offers possibilities going far beyond what we are

used to from classical systems. Light reservoirs can be engineered so as to simulate a thermal bath, whose parameters are completely within the hands of the experimenter [Poy96]. This way, the influence of the environment on decoherence mechanisms has been investigated experimentally [Mya00] by application to a quantum superposition state. These reservoirs, however, can also be tailored to have no classical counterpart.

This thesis is structured as follows: This chapter gives a short introduction into quantum non-equilibrium phenomena on the basis of a couple of concrete issues of current research. A complete overview over the field of non-equilibrium thermodynamics would exceed this thesis's scope; rather, it will be demonstrated how interesting and rewarding the work on this field is. Then, we raise and address the question, what general features a real, physical system must exhibit, so that it can be used for quantum experimental experiments in order to investigate problems of the kind presented before. After that, chapter 2 introduces the trapped-ion system as a candidate. We shortly summarize the features and peculiarities known about the system. This will give a first idea about the experimental potential of the system with respect to qtd implementations. Key to the power of this approach is the coherent interaction between light and matter. Correspondingly, chapter 3 is dedicated to devising both the theoretical and the experimental essentials and notions of this concept. Then, chapters 4 to 7 consequently address *all* requirements having been formulated at the end of chapter 1 in detail, which were found to be necessary for the implementation of qtd. The results presented there will build the basis for the main conclusions of this work, which are summarized in chapter 8.

1.1 Non-Equilibrium Processes

During undergraduate lectures, every physics student learns, that the thermodynamic properties of a large, classical system like, pressure, temperature, heat and work, are amongst the most sharply defined quantities known in physics. This is due to the huge number of constituents involved in the corresponding thermodynamic processes, and the law of large numbers ensures that the uncertainties of the ensemble properties are negligible in all conscience.

The impressive progress having taken place over the last decades in the fields of miniaturization, micro-machining and nano-technology paved the way into a world, where a central assumption of standard thermodynamics – that the number of constituents can be considered to be infinitely large – does no longer meet the physical reality. Rather, these small systems feature two new aspects: First, *fluctuations* emerge in the ensemble properties;

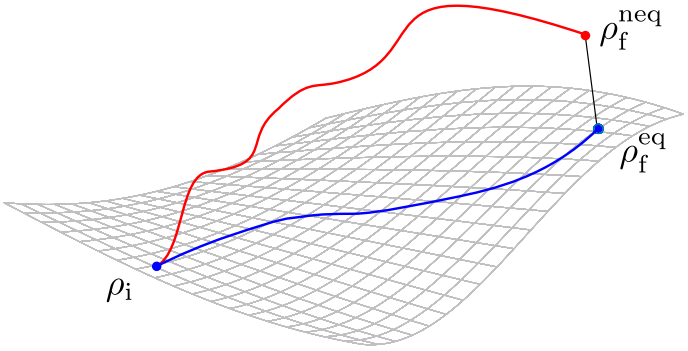

Figure 1.2: Visualization of the system's state change during the transformation processes. The system is supposed to start out from an equilibrium initial state ρ_{i}, which lies on a plane representing the subset of equilibrium states. If the process is performed in a quasi-static way, the system does not leave this plane and ends up in a final equilibrium state $\rho_{\mathrm{f}}^{\mathrm{eq}}$. If, however, the transformation process is conducted in finite time, the system is driven out of equilibrium and the final state of the system is a non-equilibrium state $\rho_{\mathrm{f}}^{\mathrm{neq}}$ [And84].

sometimes, they even dominate the system's behavior. Second, quantum effects enter the stage, giving rise to further unexpected, non-classical phenomena. In addition to the emergence of statistical fluctuations, another source of uncertainty enters the system through quantum mechanics. In the following, we point out some recently formulated aspects of quantum non-equilibrium processes, which seem most promising for investigation in the experiment.

1.1.1 The Jarzynski Equality

Consider a system initially in thermal equilibrium with inverse temperature $\beta := (k_{\mathrm{B}}T)^{-1}$ (here, k_{B} is the Boltzmann constant and T the temperature), but otherwise isolated. When one of the system's parameters is changed by an "external agent", its energy changes, in general. Due to the reasons mentioned above for small systems, the work performed on the system is not the same for every realization of the parameter change. In other words, the value W of the work may differ from one realization to the other. Formally, this can be accounted for by introducing the normalized work probability distribution $P(W)$, which gives the probability of the occurrence of the work W. The work performed on the system then is a statistical quantity with mean value $\langle W \rangle$, where by $\langle \ldots \rangle$, we denote average values over many realizations of the process.

During a quasi-static (infinitely slow) process, all work performed goes into the free energy

change of the system[3], ΔF, so that $\Delta F = \langle W \rangle$. The free energy of the system is the amount of energy, which can be used in a later process to perform work again[4] (*usable* work). When the process, however, is performed in finite time (which will be case for most real processes), the system is driven away from equilibrium and ends up in a non-equilibrium final state (see Fig. 1.2). Then, the work performed on the system not only increases the free energy of the system, but a certain part of it is "lost" for later application and absorbed in the irreversible work W_{irr}, so that we can write

$$\langle W \rangle = \Delta F + \langle W_{\mathrm{irr}} \rangle. \tag{1.1}$$

If the system was coupled to a reservoir at the end of the process, it would dissipate W_{irr} by energy exchange with the bath. The free energy change is different from the quasi-static case now. For arbitrary processes, $\langle W_{\mathrm{irr}} \rangle \geq 0$, where the equal sign holds for reversible, quasi-static processes. This leads us to one formulation of the second law of thermodynamics,

$$\Delta F \leq \langle W \rangle, \tag{1.2}$$

asserting that the free energy change is always smaller – or at best equal to – the work that has been performed on the system. From this form of the second law one can already guess, that – due to the fluctuating character of W – there may be single processes, which in this sense violate the second law, while on average it holds [Rit03].

Equation (1.2) is an inequality. Until recently, a general, exact expression for ΔF for arbitrary processes was not known, but in 1997, Jarzynski derived an exact equality for the free energy difference [Jar97]

$$\Delta F = -\frac{1}{\beta} \ln \langle e^{-\beta W} \rangle \quad \Leftrightarrow \quad e^{-\beta \Delta F} = \langle e^{-\beta W} \rangle \tag{1.3}$$

under *arbitrary* processes, i.e. even such ones driving the system far out of equilibrium. This equation, meanwhile known as the *Jarzynski equality*, is an absolutely remarkable result in non-equilibrium thermodynamics and its formal simplicity makes one almost forget about its generality. Covering both equilibrium and non-equilibrium processes, it interestingly allows for retrieving equilibrium information (ΔF) by performing only non-equilibrium processes. The latter ones are never strictly realizable and often only hard to reach in good approximation [Har07]. Instead, Eq. (1.3) makes it possible to map out free energy landscapes not accessible otherwise; since ΔF is process-independent, any

[3] F is an equilibrium property of the system and thus does not fluctuate.

[4] In classical physics, one may distinguish between the Helmholtz free energy (at constant temperature and volume) and the Gibbs free energy (constant temperature and pressure), respectively.

reproducible parameter transformation can be applied in principle. Although classical in its original form, Eq. (1.3) has been shown to be extendable to the quantum regime [Tas00, Muk03, DR04, Che04, Tal07a], although some classical concepts like the notion of work had to be revisited and refined [All05, Tal07b].

The Jarzynski equality gets in line with a series of fluctuation theorems [Eva93, Eva94, Gal95, Cro99] describing the mechanisms leading to fluctuations in small systems and making predictions about their probability of occurrence (for a review, see Ref. [Eva02]).

Experiments revealing the non-equilibrium features of small systems have only become possible by a tremendous progress in micro-manipulation techniques. In Ref. [Lip02], Liphardt et al. demonstrated the first verification of the Jarzynski equality in an RNA stretching experiment. Albeit small, the system under aspect is classical. A couple of subsequent experiments demonstrated the correctness of fluctuation theorems [Col05, Bli06] and the Jarzynski equality [Bli06, Har07] in small classical systems, and their usefulness in practical applications.

An experimental test of the Jarzynski equality in the quantum regime, however, is still lacking. It is one of the main motivations of this thesis to demonstrate, that and how such non-equilibrium experiments can be performed in the quantum regime. We will see, how a verification of the quantum Jarzynski equality can be accomplished, and how the fluctuations in work can be made visible by an experiment unveiling every single process's outcome; hereby, also those rare events violating the second law can be proven (see chapter 5.3).

1.1.2 The Clausius Inequality

As we have already seen, any real process is irreversible, since it has to be conducted in finite time. A natural question arising is, *how* good, or *how* close to equilibrium we can perform. Again, we imagine a system, which is in thermal equilibrium at the beginning. Its entropy change ΔS caused by a parameter transformation (cf. Fig. 1.2) can be divided into a reversible part ΔS_{rev}, and an irreversible contribution ΔS_{irr}, respectively:

$$\Delta S = \Delta S_{\mathrm{rev}} + \Delta S_{\mathrm{irr}}. \tag{1.4}$$

The reversible part $\Delta S_{\mathrm{rev}} = Q/T$ describes the heat (Q) exchange occurring during the process (in the case of open systems), where T is the temperature of the system. The so-called *Clausius inequality* states, that the irreversible entropy production is always positive

or – at best – zero, if the process is done reversibly,

$$\Delta S_{\mathrm{irr}} \geq 0. \tag{1.5}$$

Equation 1.5 is another formulation of the second law and gives a very general lower bound of the irreversible entropy production, which is closely related to the irreversible work $\langle W_{\mathrm{irr}} \rangle = \langle W \rangle - \Delta F$ defined above (see Eq. (1.1)), by $\Delta S_{\mathrm{irr}} = \beta \langle W_{\mathrm{irr}} \rangle$.

It has recently been shown [Def10b], that a full quantum treatment allows for deriving an exact expression for ΔS_{irr} by the help of the *Kullback-Leibler divergence* [Ume62] (which is also called *relative entropy*). For a closed equilibrium system being driven arbitrarily far out of equilibrium, and ending up in some final state represented by its density operator ρ_{f}, one can write

$$\Delta S_{\mathrm{irr}} = S(\ \rho_{\mathrm{f}} \,||\, \rho_{\mathrm{f}}^{\mathrm{eq}}\ ) := k_{\mathrm{B}} \mathrm{Tr}\ \left\{\ \rho_{\mathrm{f}} \ln \rho_{\mathrm{f}}\ -\ \rho_{\mathrm{f}} \ln \rho_{\mathrm{f}}^{\mathrm{eq}}\ \right\}. \tag{1.6}$$

Here, $\rho_{\mathrm{f}}^{\mathrm{eq}}$ represents an equilibrium state at the end of the process, which can, for example, result from weakly coupling the system to a reservoir. From this we see, that the entropy change can be obtained from final states only, and that it is – roughly speaking – determined by the "distance" of the final state from equilibrium[5].

This picture is supported by an estimate on ΔS_{irr}, which falls back on the well known fidelity $\mathcal{F}(\rho_1, \rho_2)$ between two quantum states ρ_1 and ρ_2,

$$\mathcal{F}(\rho_1, \rho_2) := \mathrm{Tr}\ \left\{ \sqrt{\sqrt{\rho_1}\, \rho_2\, \sqrt{\rho_1}} \right\}, \tag{1.7}$$

which is a very common measure for the "likeness" of two quantum states[6]. With this, the entropy production can be estimated to be [Def10b]

$$\Delta S_{\mathrm{irr}} \geq \frac{8 k_{\mathrm{B}}}{\pi^2}\ \left(\arccos \mathcal{F}(\rho_{\mathrm{f}}, \rho_{\mathrm{f}}^{\mathrm{eq}})\right)^2. \tag{1.8}$$

This is a very interesting generalization of the Clausius inequality $\Delta S_{\mathrm{irr}} \geq 0$ and gives an estimate, how well a process can be done with respect to energy dissipation, when one is "short of time", i.e. the process has to be performed in finite time.

From this example, we can already deduce a handful of demands posed on a quantum system in order to qualify for a real experiment. Apart from the preparation of a suitable quantum state, the possibility to perform exact non-adiabatic transformations of a system's parameter, it is necessary in some cases to control the coupling between system and

[5] As pointed out in Ref. [Def10b], the relative entropy does not have all properties of a true metric.

[6] Sometimes, the square of this expression is defined as fidelity. Following our definition, the fidelity reduces to the mutual overlap $\mathcal{F} = |\, \langle \Psi_1 | \Psi_1 \rangle\, |$ for pure states $|\Psi_1\rangle$ and $|\Psi_2\rangle$.

environment to allow for equilibration $\rho_\mathrm{f} \to \rho_\mathrm{f}^\mathrm{eq}$, for example. Additionally, the readout of the final state may require retrieving the full quantum state, or it may suffice to extract a more easily measurable quantity.

1.2 Experimental Requirements for Quantum Thermodynamics

Thermodynamic effects are ubiquitous. The experimental, quantitative access to these phenomena in the quantum regime, however, is not at all trivial. The reasons for this are divers; quantum effects tend to emerge at low temperatures only, i.e. in systems whose thermal energy is comparable to an energy quantum of that system. Therefore, their direct observation will be restricted to microscopic systems only. Additionally, coupling to the environment is often a source of decoherence, which prevents the observation of any quantum effects. On the other hand, exactly this interaction with an environment is a central concept in thermodynamics. Consider, for example, a system in thermodynamic equilibrium with a heat bath, to define the system's temperature. Therefore, the coupling between system and bath has to be controllable in some sense. Additionally, the observation of thermodynamic effects in quantum systems requires a high level of control over the degrees of freedom under aspect. Preparation, manipulation and detection of these degrees of freedom must happen with an accuracy and sensitivity on the single quantum level. In the following, we would like to raise and discuss the following question: What are the basic requirements posed on a physical system to realize quantum thermodynamic experiments?

Our approach to answer the stated question is motivated by the famous collection of David P. DiVincenzo's criteria about the implementation of quantum computation [DiV00]. This motivation might seem arbitrary at first sight, but it is motivated to a certain degree by the role information plays in thermodynamics. To start with, we repeat the five DiVincenzo requirements of quantum computing[7]:

1. A scalable physical system with well characterized qubits
2. The ability to initialize the state of the qubits to a simple fiducial state
3. A universal set of quantum gates
4. A qubit-specific measurement capability

[7] Shortened and reordered for convenience.

5. Decoherence times longer than gate operation time

Without going into detail about each point, we recognize that the first point requires the system to be "well characterized", i.e. both the internal parameters of the system and all interactions of the system with other systems or external fields should be known. For a thermodynamic system, we raise similar demands: the system requires a set of well-defined degrees of freedom, and the interaction between individual parts of the system with external fields must be well-known. One could, for example, imagine the spin of a quantum particle forming such a system. Then, the interaction between the spin particles and the interaction with an external magnetic field could fulfill this requirement. Another possibility is realized by the motion of an atomic particle in a potential well, interacting with light fields.

There is, however, a crucial difference between the quantum computing and the qtd case: while in the qubit case, only two-level systems (possibly plus ancillary levels) occur, no such restriction is put on the thermodynamic system. On the contrary, discrete as well as continuous variable systems with finite or infinitely many levels are conceivable. The first requirement we put on a physical system hence reads

(I) A physical system with a well characterized degree of freedom.

The second, third and fourth point in DiVincenzo's list address the possibility to initialize, manipulate and read out the system state. The ability to initialize the system into a fiducial state is certainly not only a reasonable but a necessary requirement for doing quantum thermodynamic experiments. While the above criteria certainly refer to the preparation to a *pure* state such as $|0\dots0\rangle$, this has to be revisited for our purposes. The most obvious and basic state conceivable for talking about thermodynamics is certainly a thermal state, i.e. a state, which can be assigned a certain temperature. Such a state, however, is not a pure but a maximally mixed state (its density matrix does not exhibit off-diagonal *coherences*).

This state, however, does not necessarily remain maximally mixed throughout its time evolution. An initially thermal state can experience arbitrary interactions and transformations leading far out of equilibrium. In the course of these processes, highly non-classical states can emerge. We demand, therefore, the system to be preparable in an initial thermal state ρ_{i} of the respective degrees of freedom:

(II) The possibility to prepare the system in a thermal state with respect to the degree of freedom defined in (I).

Once prepared, the system must be accessible to manipulation from outside. In the qubit case, unitary operations $\hat{U}$ (quantum gates) transform the initial state $|\psi_\mathrm{i}\rangle$ into the desired output state $|\psi_\mathrm{f}\rangle$: $|\psi_\mathrm{i}\rangle \xrightarrow{\hat{U}} |\psi_\mathrm{f}\rangle$. As for thermodynamics, one may be dealing with irreversible effects, like dissipation for instance, it is not possible to exclude non-unitary transformations from the discussion. Nevertheless, it will be sufficient and convenient in the most cases, to consider the transformation process itself unitary, and to treat non-unitary processes like cooling, thermal equilibration and so forth detached from the actual transformation – see point (VI).

The set of transformations performed on the system is described by a change of a general parameter λ of the system Hamiltonian[8] in time T. A classical analogy of this situation is the compression of a gas, for instance, where the system parameter represents the volume the gas is confined in. This parameter is changed in time along a certain *path* in parameter space, $\lambda(t)$, which completely describes the process transforming the initial state $\rho_\mathrm{i} := \rho(0)$ into the final state $\rho_\mathrm{f} := \rho(T)$:

$$\rho_\mathrm{i} \xrightarrow{\lambda(t)} \rho_\mathrm{f}. \tag{1.9}$$

This is a very general description of the transformation process. It comprises processes with sudden parameter changes as well as quasi-static ones with $T \to \infty$. A good control over the process execution $\lambda(t)$ is certainly one of the major experimental challenges. Therefore, the third requirement should be stated as

(III) The ability to perform transformations of the system Hamiltonian by a temporal change of one or several of its parameters.

After the transformation process, ρ_f has to be detected. That is, there has to be a measurement procedure yielding all relevant properties of the system. This does not necessarily have to be the whole information about the state ρ_f, but in some cases a subset of quantities may suffice. For instance, while sometimes the determination of (ensemble) average values may meet the requirements, there may also be cases where more sophisticated, specialized schemes have to be applied. This requirement is – from an experimental point of view – certainly among the most demanding ones, because it must rely on interactions controllable at the single quantum level; the detection techniques must exhibit quantum efficiencies so high that single-shot experiments can be performed. Thus, we formulate the fourth requirement as

(IV) A measurement process extracting all necessary information from the final state.

[8] Several parameters are conceivable, too. Then, λ can be written as a vector containing all individual parameters, $\lambda := (\lambda_1, \lambda_2, \ldots)^T$.

The next requirement posed on a physical system suitable for doing quantum thermodynamics experiments addresses the question, in how far the system is influenced by its environment. As for quantum computing, the case is quite clear: decoherence times have to be much longer than the timescales defined by the computing process, for example gate times. In our case, however, the situation is slightly more involved and we want to distinguish between pure decoherence and dissipative effects. Of course, the loss of decoherence on timescales shorter than typical times between preparation and detection of the state also corrupts the qtd process. Consequently, the requirement of long decoherence times also holds in our case:

(V) Decoherence times long enough to perform preparation, process and measurement.

Additionally, an (unavoidable) coupling to the environment leads to a corruption of relevant system properties by the stochastic nature of heat exchange. On the other hand, we do not want to restrict ourselves to isolated systems but also consider open ones. At some occasions, the interaction with external baths may even be desired, which could be in order to allow for system equilibration, for example. Indeed, the state preparation defined in requirement number two can be performed by coupling the system to a thermal bath for a certain amount of time. Isolated systems, i.e. systems not interacting with the environment, however, must exhibit interaction rates much smaller than the inverse duration time of a single experiment. We see from these examples that the control over the interaction with the environment should not be restricted to "well isolated" for our purposes. Rather, a controlled interaction is desirable, that's why we demand

(VI) Control over the system-environment coupling.

The strength and type of interaction can range from completely isolated to a strong coupling regime, in which the energy exchange with the environment dominates the system dynamics. This also includes time-dependent couplings, such that switching between an isolated and an open system is possible.

The above criteria are meant to yield a guide to possible physical implementations of qtd experiments. As could be seen, the analogy with the DiVincenzo criteria is revoked at distinct, crucial points. The diversity of processes and systems conceivable in qtd physical systems is huge. Accordingly, the six requirements were formulated as universal as possible; nevertheless, they will prove very helpful as a checklist, filling the "toolbox" for experimental quantum thermodynamics with concrete solutions.

Chapter 2

Trapped Ions for Quantum Thermodynamic Experiments

In the preceding chapter, we have analyzed what general requirements a physical system must meet to be suitable for quantum thermodynamic experiments. These requirements are diverse and put high demands on both the system properties and our experimental abilities to manipulate and control them. Now, we substantiate the discussion introducing a specific physical system, whose applicability in the context of quantum thermodynamics is going to be under close scrutiny by this work. Cold trapped ions have proven as systems offering unrivaled properties in the field of quantum optics, quantum information and quantum metrology [Ste97, Win98, Bla08]. In a long series of groundbraking experiments performed over the last decades they have been a paramount example for precision and control. This development has been substantially supported by the great advances in laser techniques and by the knowledge gathered about the interaction of light with atomic particles.

There are mainly two trapping techniques for single atomic ions: Paul traps based on the confining action of static and time-dependent electric fields on the one hand, and Penning traps utilizing static electric and magnetic fields, on the other hand. They can be regarded as the longest and best established single particle trapping techniques offering the longest storage times known ($\sim$ months [Die98]). One of the advantages of the Paul trap approach is that it is possible to cool the confined atomic ion by laser light – provided that the ion offers a suitable cooling transition. Although laser cooling has also been achieved in Penning traps [Tho09], the Paul trap has the great advantage of inherently confining the

particles "at rest" at a well-defined point in space[1]. This is especially of advantage when the ion is illuminated by laser light, where both intensity and duration of the exposure are critical.

2.1 Traps and Potentials

We utilize a segmented, linear Paul trap for qtd experiments. In contrast to conventional Paul traps offering fairly isotropic confinement in all three dimensions, the linear trap is designed to create anisotropic trapping potentials. When in one – the *axial* – direction, the ion is much weaker confined than in the other two *radial* directions, then the trap can be considered to be in effect one-dimensional, see Fig. 2.1. Single ions kept in such a potential configuration will arrange in a linear string, whereas their alignment follows the trap axis; they are, of course, kept at distance by their mutual Coulomb repulsion. All experiments presented within this thesis were performed in such a linear trap.

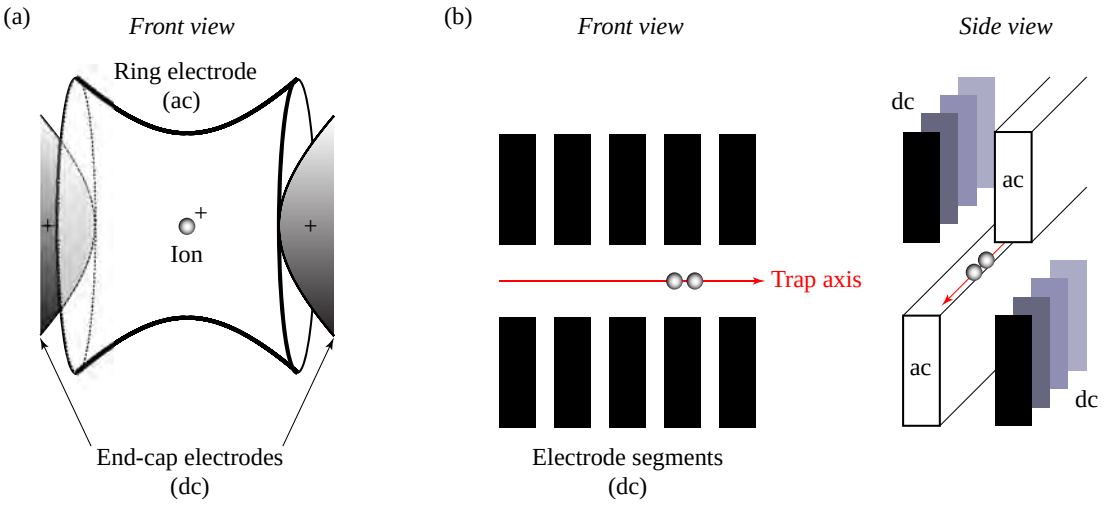

Figure 2.1: Paul trap designs. (a) Conventional Paul trap with hyperbolic electrodes. The end cap electrodes give rise to static confinement in one direction, and a pseudo potential resulting from ac voltages applied to the ring electrode provides confinement in the orthogonal directions. (b) Schematic front and side view of a linear, segmented Paul trap. Again, the confinement in the *radial* directions stems from a pseudo potential generated by ac voltages. The ac electrodes are elongated along the trap axis. A whole set of dc electrodes/segments replace the end caps and can be used to generate local axial potentials. Two or more ions in the same axial potential arrange in a string aligned along the trap axis (red), when the axial confinement is weak compared to the radial one.

[1] In Penning traps, the magneton motion generally prevents this feature. There are, however, techniques to tackle this drawback [Pow02].

The alternating current (ac) trapping fields of the Paul trap give not only rise to the so-called *pseudo potential* in the radial directions, but also causes micromotion. This small amplitude oscillation is the immediate action of the ac field and is oscillatory with the ac drive frequency (typically in the radio frequency (rf) regime, i.e. some tens of megahertz; the ac fields are therefore most often called the rf fields.). This micromotion can be effectively canceled out, because its amplitude disappears at the minimum of the pseudo potential (rf node) [Sch08]. When, due to imperfect trap construction or stray fields, the ion is not trapped in the rf node, static compensation fields can be applied to push the ion into the right position.

Axial Confinement

The axial confinement is generated by static electric fields. While two end cap electrodes biased to a positive voltage (for positive ions) were used in the traditional Paul trap, the linear trap design makes it possible to partition the axial electrode into several segments. Each of these segments contributes to the axial trapping field; this contribution is given by its individual voltage. By this segmentation trick it becomes feasible to generate almost arbitrary electric (axial) potentials for the ions. Originally proposed to scale up quantum computation operations by shuttling ions between different processing and memory regions [Kie02], this procedure is much more versatile as will become clear in the course of this work.

Figure 2.2 shows two special field configurations of our segmented trap (see chapter 9.1.1), illustrating its capabilities to actually realize multiple traps for confining several ions or small sets of ions independently. These kinds of potential configurations have applications not only in quantum information [Kie02], quantum simulation [Wun09] and quantum metrology [Hub10], but give also rise to quantum thermodynamic investigations [Hub08b].

Altogether, single ions in a linear, segmented trap form a system, where it is possible to hold single quantum systems in arbitrary, external potentials. Multiple particles confined in the same potential, i.e. in close vicinity to each other, interact via the Coulomb force. Single subsystems, each consisting of single or several particles can be realized independently. They can be split, merged and their constituents can even be redistributed. Thus, both single particles and small ensembles of particles and even whole sets of subsystems can be generated, analyzed and made interact by a proper choice of the potentials. Last but not least, it is even possible to trap different ion species with different particle masses within the same potential.

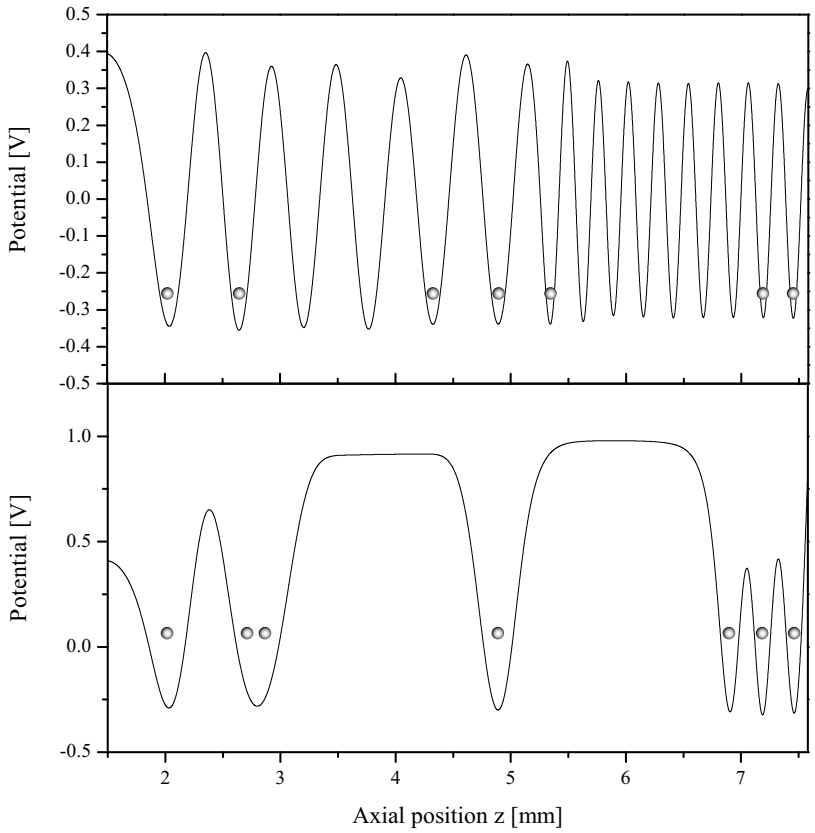

Figure 2.2: Demonstration of the capabilities to generate a variety of multi-trap potentials within the utilized segmented Paul trap (cf. 9.1.1). In the first case, a set of 15 individual traps was realized by exploiting the high segmentation of the trap. Each trapping well can store one or more ions, depicted by the circles. Below, a 2-1-3 configuration of adjacent traps is generated. The individual wells can have different or equal frequencies, arbitrary separations and they can be merged and split by applying suitable time-dependent voltages.

Time-Dependent Potentials

The physics of trapped ions becomes even more interesting when not only static but also time-dependent potentials are considered. Then, the ion experiences time-dependent forces that will change its state of motion. As an analog, imagine a classical gas confined within a certain volume (see Fig. 2.3(a)). When a plunger is pushed in, i.e. the confining potential is changed, forces act on the particles, giving rise to a change of their state of motion. The final state of the gas then depends on the way the potential is "transformed". There will be, for instance, a qualitative difference if this transformation is performed very slow or fast. We can translate this simple thermodynamic system into our single ion approach, when the confining "box" is replaced by the electric axial potential, cf. Fig. 2.3(b). In

perfect analogy, the state of the ion – represented by its spatial or motional wave function – changes under potential transformations. Pushing the plunger is then equivalent to making the potential stiffer, i.e. increasing the trap frequency in the case of a harmonic potential. This can happen, too, in various ways. In the single particle case, however, it is the ion's quantum state of motion, which is influenced by the potential transformation. Consequently, quantum features of the system emerge and give rise to a behavior different from a classical gas. In the pushing case, for example, some amount of force must be exerted to compress the gas. This means, that work is performed during the process and the system's energy changes accordingly. However, there is no 1:1 quantum analog of classical work performed on a system, since there is neither a path nor a force which could be multiplied or integrated, respectively. Other quantities (pressure, entropy, ...) familiar from classical systems must be revisited in the quantum case. In quantum mechanical systems, another interesting feature arises in contrast to classical ones: uncertainty exists for two reasons: apart from the probabilistic distribution of system properties due to a finite temperature, uncertainty arises due to the inherent statistical character of quantum processes. That implies, that even at zero temperature, a measurement outcome is not predictable in general. This feature is inherent to quantum measurements.

2.2 Quantum States of Motion

The potential engineering possibilities presented above pave the way to introduce the specific degree of freedom best suited for qtd experiments: the motion of a single ion represents a well-defined degree of freedom with respect to requirement (I) postulated in chapter 1.2. It is a very well isolated quantity and its interaction with other ions within its vicinity is well understood. The electric potentials couple to the ion charge and hence influence its state of motion. The motion of a particle in a confining potential is quantized, i.e. the energy eigenstates of the system are in general infinite but discrete.

The Harmonic Oscillator Potential

There is one kind of potential predestined for investigation in ion traps: the harmonic potential. This is due to the fact that the lowest order term of most confining potentials around their minimum is quadratic. Because of its microscopic extent, a cold ion experiences only a very small vicinity around the potential minimum, i.e. the harmonic part of the potential. That means, the implementation of an outstanding textbook example is provided almost for free. In this case, the harmonic oscillator $H = \frac{p^2}{2m} + \frac{m}{2}\omega_z^2 z^2$ and its

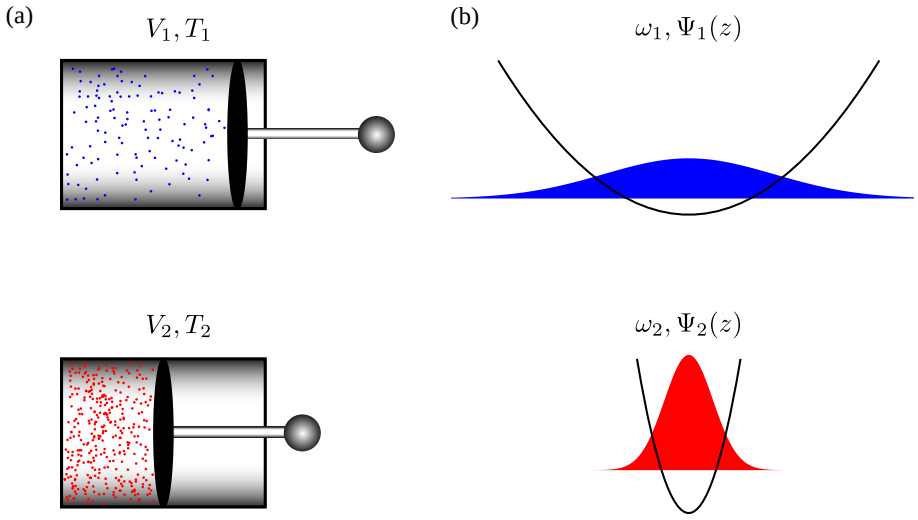

Figure 2.3: Time-dependent potentials change the system's state. (a) shows a classical gas confined in a certain volume V_1. Its temperature is given by T_1. By "transforming" the confining potential, here pushing a plunge into the gas vessel, the state of the system is changed. Depending on the temporal realization of the process, the state looks differently afterwards. For example, the temperature can change to T_2 for a non quasi-static process. Similarly, the quantum state of an ion confined in a potential could be "squeezed" by a temporal change of the potential. Here, the frequency of the harmonic potential is changed from ω_1 to ω_2, the spatial wave function of the ion changes accordingly from Ψ_1 to Ψ_2. Again, the final state critically depends on the process realization.

eigenstates $|n\rangle$, $n = 0, 1, \ldots$ with eigenenergies $E_n = \hbar\omega_z(n + \frac{1}{2})$ define the framework of the quantum thermodynamical system. Here, p and m are the momentum and mass of the particle, respectively, and ω_z is the angular frequency of the potential along the z-axis. The energy quantum of this system is often called a *phonon* following the terminology for vibrational quanta in solid state physics. The harmonic oscillator belongs to the best investigated physical concepts. For its formal simplicity, it is best-suited for a comparison between experiment and analytical calculations. Nevertheless, trapping potentials for ions are by no means restricted to be harmonic, but can go beyond this limitation.

The motion of a trapped ion can take on strongly non-classical quantum states, including highly entangled, intriguing ones like the Schrödinger cat states, which have been realized in various systems [Mee96, Bru96a, Mon96, Our06]. Figure 2.4 illustrates the vast variety of states by their Wigner function representations (cf. chapters 6.4 and 9.4). These examples can only grant a short glance at the experimental and theoretical diversity of the system we are dealing with [Ben03, Häf05a, Lei05]. The following chapters will show how such states can be generated and manipulated experimentally.

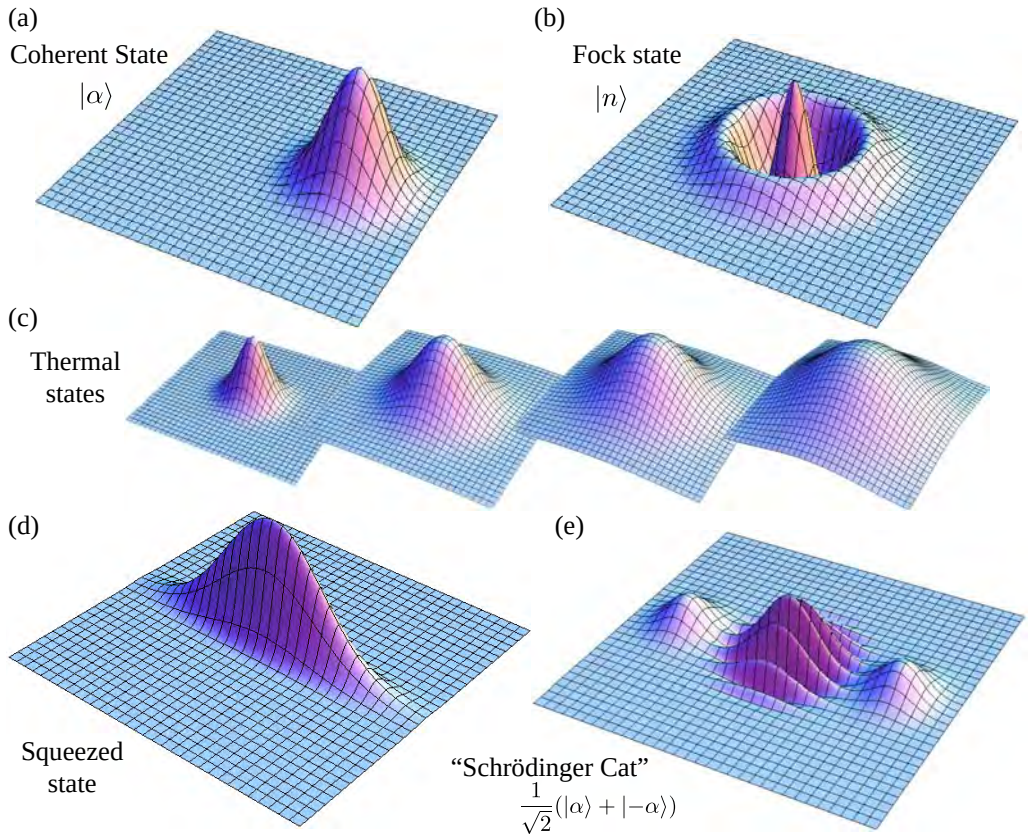

Figure 2.4: Illustration of quantum states. The states are represented by their Wigner function $W(x + iy)$ in complex phase space. (a) A coherent (Glauber) state $|\alpha\rangle$. Its representation is Gaussian. (b) A Fock state $|n\rangle$ with $n = 2$, i.e. the second energy eigenstate of a quantum harmonic oscillator. (c) Different thermal states; temperature increases from left (almost ground state) to right. (d) A squeezed vacuum state: uncertainty in position is reduced at the expense of uncertainty in momentum. (e) A "Schrödinger Cat" state, a superposition between two coherent states $\frac{1}{\sqrt{2}}|\alpha\rangle + |-\alpha\rangle$. Note the interference fringes in between the Gaussian amplitudes.

2.3 Electronic Structure, Motion and Light

As we have seen, the motion of a trapped ion is the degree of freedom most usable for qtd experiments. Accordingly, up to now we treated the ion as a point-like, charged particle moving in an external electric potential. The ion is, however, not point-like but exhibits a rich internal, electronic structure, too. While this electronic structure seems completely dispensable from a fundamental point of view, it shows that it offers exactly those features making the trapped-ion approach so promising: coupling the electronic and the motional degree of freedom by virtue of coherent laser light.

Light is able to influence the ion's motion because of the momentum transfer between

the ion and a photon that occurs during an emission or absorption process. Controlling the ion-light interaction thus means controlling the ion motion. The ability to control the interaction between light and matter was subject to a tremendous development in the last decades that paved the way for the emergence of modern quantum optics. The extremely high accuracy of the interaction between light and the electronic structure of the ion can thus be transferred to the state of motion. As we will see in chapter 3, it is then possible to manipulate the ion's motion deterministically and with high fidelity by adding or subtracting single quanta of motion, for example.

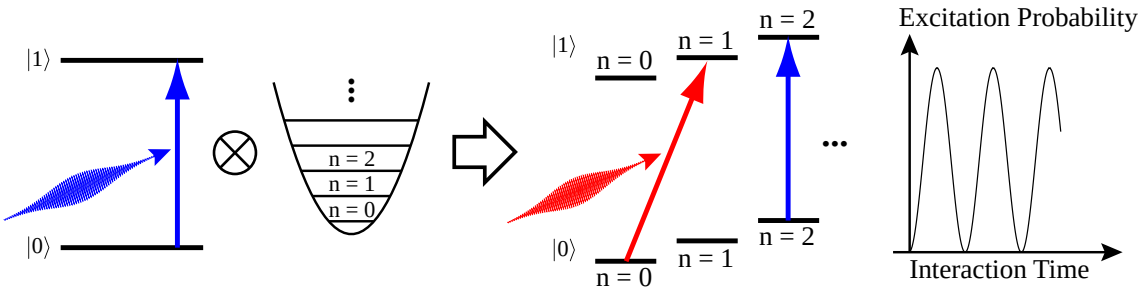

Figure 2.5: The internal, electronic structure (depicted by a two-level system) forms a composite system together with the ion motion (here, the harmonic oscillator). By virtue of coherent light (blue and red arrows), these two degrees of freedom can be coupled and coherent dynamics between them become feasible (see text for further details).

Figure 2.5 illustrates the coupling of the internal energy levels – represented by a simple two-level subsystem – to the motional degree of freedom, the well-known harmonic oscillator energy ladder in this case. The composite system consists of a double ladder of energy levels, each of which can be associated with the respective internal state $|0\rangle_i$ or $|1\rangle_i$ (the splitting between the electronic states is mostly much larger than the spacing of the oscillator states, so this picture of a double ladder is justified). Laser light of the correct energy (frequency) and momentum can change the internal state alone or go along with a change in the phonon state. This way it becomes possible to influence the ion motion on a single quantum level in a very controlled and deterministic manner.

We will first profit from these abilities when it comes to the preparation and the readout of the motional state. The well-established techniques of laser cooling (see chapter 4) allow for preparing the system in a very low-temperature initial state. Also, only by the described coupling to the internal dynamics, it becomes possible to determine the full quantum state of motion. Otherwise it would be very hard (impossible in the most cases) to measure low-excited states of motion.

The foundations of these techniques were mostly developed in the context of quantum

information experiments with single atoms or ions. In the case of the Paul trap, the internal state of the ion thereby stores the quantum information. The motion of two or more ions in the same potential is then utilized as a "bus" to exchange information between the ions. Especially, an ion's internal state evolution can thus be made conditional on the other ion's state. This is the prerequisite for performing entangling two-ion quantum gates and thus for performing quantum computation tasks. Due to the close relationship between quantum information and quantum thermodynamic topics, this work will use notions and concepts coming from the area of quantum information, like the *qubit*, describing a simple quantum two-level system, in our case embedded in the electronic structure of the ion.

Artificial Baths and Reservoirs

The interaction with light offers another interesting possibility, namely to "engineer" the coupling between the ion and an artificial environment [Die08]. The interaction with a large reservoir normally leads to decoherence, connected with a loss of the quantum features. It is therefore of great interest to understand the mechanisms and attendant circumstances under which the decoherence takes place.

As has been shown theoretically [Poy96] and experimentally [Mya00], tailored laser light fields can mimic the interaction with a reservoir, but in contrast to the "natural" case, the reservoir's properties and its interaction with the system now are perfectly controllable by the experimentalist. In a thermodynamic context, the possibility to have exact control over the system-bath interaction is a very fascinating idea, pertaining to the realization of open, closed (i.e. completely isolated), and mixed-form systems.

Altogether, our quantum thermodynamic system presents itself like it is illustrated in Fig. 2.6. Single ions carrying the internal structure of (at least) a qubit system are confined in several individual traps. The potentials making these traps can be static or time-dependent, harmonic or of arbitrary shape. The ions interact via the Coulomb force and form "crystals", i.e. regular spatial arrangements within each trap. Each ion can be individually excited and coherently controlled, and its motional state can be manipulated and measured by laser light.

The influence of the system's surroundings – the environment – can be kept small to guarantee an isolated system or an open system can be implemented by allowing for coupling to thermal baths. Also artificial baths like external, electric noise sources or light induced "baths" are feasible.

Because – as aforementioned – the coherent interaction between light and the ion forms

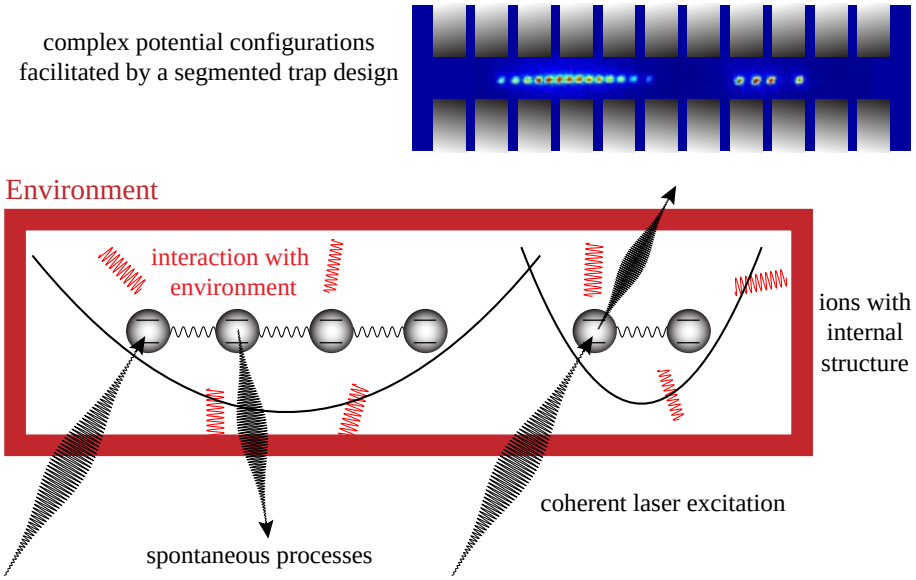

Figure 2.6: Illustration of a trapped ion box for quantum thermodynamics. Single ions and strings of ions confined in arbitrary potentials can be made interacting with each other or evolve independently. The ions of each string are coupled via the Coulomb force. Both their internal and external quantum states can be manipulated and read out by interaction with light. Both isolated and open systems are realizable; the coupling to a bath can be additionally mimicked by electromagnetic fields and even be switched on and off.

the basis for virtually all measurements in this context, the next chapter will introduce the corresponding theoretical framework, and then present experimental implementations of the needed quantum two-level system within the internal level structure of $^{40}Ca^{+}$.

Chapter 3

Coherent Ion-Light Interaction

In this chapter, a theoretical model is presented describing the coherent interaction of the ion with a light field. This kind of interaction lies at the heart of almost all experiments presented later and hence constitutes an essential part in our quantum thermodynamics toolbox. The model comprises both the electronic and the motional degrees of freedom. After that, two physical implementations are presented. It is shown, how the theoretical framework developed beforehand applies to each of them, and specific assets and drawbacks are discussed.

3.1 Theoretical Framework

In the following sections, a theoretical model will be introduced that describes our physical system very accurately: an atom, experiencing a harmonic potential and interacting with a light field. The internal structure of the atom is described as a simple two-level system, a *qubit*. This simplification is justified very well in most cases, since mostly only two electronic levels are coupled by a light field. The ion experiences a potential, which we assume to be harmonic. This is where the ion's external, motional degrees of freedom come into play[1]. Finally, the interaction between the ion and a light field must be accounted for. This interaction gives rise to coherent dynamics of the internal, atomic degrees of freedom but also to a coherent coupling between the internal and the external degrees of freedom. From a quantum information point of view, the internal dynamics correspond to single qubit rotations. By the coupling to the ionic motion, mutual qubit coupling (quantum

[1] Indeed, in the case of cold ions and static potentials, the assumption of a harmonic potential is excellent, since then, the ion is well located in the minimum of the potential.

gates) can be accomplished.

3.1.1 Atomic Hamiltonian

The full Hamiltonian $\hat{H}_{\mathrm{tot}}$ of an atom in an external potential that interacts with a light field can be logically separated into two parts: the atomic part (both electronic and motional) on the one hand, and that of the atom-field interaction, on the other hand:

$$\hat{H}_{\mathrm{tot}} = \hat{H}_{\mathrm{atom}} + \hat{H}_{\mathrm{atom-light}} = \hat{H}_{\mathrm{elec}} + \hat{H}_{\mathrm{mot}} + \hat{H}_{\mathrm{atom-light}}. \tag{3.1}$$

The light field itself shall not be perturbed by the interaction, so its contribution to $\hat{H}_{\mathrm{tot}}$ is omitted. As for the electronic contribution, we restrict ourselves to that of the qubit levels, which we denote by $|\downarrow\rangle \equiv |0\rangle_{\mathrm{i}}$ and $|\uparrow\rangle \equiv |1\rangle_{\mathrm{i}}$ to avoid confusion with motional eigenstates. The associated eigenenergies are $E_\downarrow$ and $E_\uparrow$, where $\hbar\omega_0 = E_\uparrow - E_\downarrow$ is the energy level separation. Then,

$$\hat{H}_{\mathrm{elec}} = \hat{H}_{\mathrm{qubit}} = E_\downarrow |\downarrow\rangle\langle\downarrow| + E_\uparrow |\uparrow\rangle\langle\uparrow| . \tag{3.2}$$

The energy zero point can be shifted right in between the two levels, so that $E_\uparrow = -E_\downarrow = \frac{1}{2}\hbar\omega_0$. This results in

$$\hat{H}_{\mathrm{elec}} = \frac{1}{2}\hbar\omega_0 \left(|\uparrow\rangle\langle\uparrow| - |\downarrow\rangle\langle\downarrow|\right) = \frac{1}{2}\hbar\omega_0\hat{\sigma}_z, \tag{3.3}$$

where the spin operator $\hat{\sigma}_z := |\uparrow\rangle\langle\uparrow| - |\downarrow\rangle\langle\downarrow|$ was introduced[2].

The part describing the motion of the ion within the harmonic potential is a simple harmonic oscillator Hamiltonian with frequency ω_z,

$$\hat{H}_{\mathrm{mot}} = \frac{\hat{p}^2}{2m} + \frac{m}{2}\omega_z^2\ \hat{z}^2 = \hbar\omega_z \left(\hat{a}^\dagger\hat{a} + \frac{1}{2}\right), \tag{3.4}$$

where $\hat{z}$ and $\hat{p}$ are the position and momentum operators, respectively, and m is the particle mass. $\hat{a}^\dagger$ and $\hat{a}$ are the creation and annihilation operators of the oscillator quanta (phonons):

$$\hat{a}^\dagger |n\rangle_{\mathrm{m}} = \sqrt{n+1}\,|n+1\rangle_{\mathrm{m}}, \quad \hat{a}\,|n\rangle_{\mathrm{m}} = \sqrt{n}\,|n-1\rangle_{\mathrm{m}} \tag{3.5}$$

for all $n \geq 0$, but $\hat{a}\,|0\rangle_{\mathrm{m}} = |0\rangle_{\mathrm{m}}$, where the oscillator eigenstates are denoted $|n\rangle_{\mathrm{m}}$ for all integer $n \geq 0$. The full wave function of the ion $|\Psi\rangle = |\psi\rangle_{\mathrm{i}} \otimes |\varphi\rangle_{\mathrm{m}}$ comprising both the

[2] The index only symbolically indicates the direction of the quantization axis and must not be confused with the trap axis direction; indeed the magnetic field intersects the trap axis under 45°.

internal (subscript i) and the motional (subscript m) degrees of freedom can be written as a superposition of the basis states $\{|s\rangle_\mathrm{i}\}_{s=\downarrow,\uparrow}$ and $\{|n\rangle_\mathrm{m}\}_{n\geq 0}$,

$$|\Psi\rangle = \sum_{s=\downarrow,\uparrow}\sum_{n=0}^{\infty} c_{s,n}\,|s\rangle_\mathrm{i}\otimes|n\rangle_\mathrm{m} = \sum_{s=\downarrow,\uparrow}\sum_{n=0}^{\infty} c_{s,n}\,|s,n\rangle, \tag{3.6}$$

where we introduced the more concise notation $|s,n\rangle := |s\rangle_\mathrm{i}\otimes|n\rangle_\mathrm{m}$. The subscripts will be omitted when the meaning is obvious.

3.1.2 Atom-Light Hamiltonian

The Hamiltonian $\hat{H}_\mathrm{atom-light}$ models the interaction between the atom and the light. It would be convenient to find an expression describing all the various qubit-light interactions presented in this work (stimulated Raman, optical dipole/quadrupole interactions). Indeed it is possible to derive a concise, uniform formalism for all of these variations with all the diversity accounted for by only slight modifications.

At the beginning, we consider a single propagating light field[3]

$$\boldsymbol{E}(\hat{\boldsymbol{r}},t) = \boldsymbol{\epsilon}\,E_0\cos(\boldsymbol{k}\hat{\boldsymbol{r}}-\omega_\mathrm{L}t+\phi) = \frac{\boldsymbol{\epsilon}\,E_0}{2}\left(e^{i(\boldsymbol{k}\hat{\boldsymbol{r}}-\omega_\mathrm{L}t+\phi)}+e^{-i(\boldsymbol{k}\hat{\boldsymbol{r}}-\omega_\mathrm{L}t+\phi)}\right) \tag{3.7}$$

with electric field amplitude E_0, wavevector $\boldsymbol{k}$, normalized polarization vector $\boldsymbol{\epsilon}$ and frequency ω_L, that interacts with a single atom. If the atomic wave function extent is small compared to the wavelengths of the light fields in question (i.e. $\boldsymbol{kr}\ll 1$), it is justified to neglect higher orders in the multipole expansion of the electronic states,

$$e^{i\boldsymbol{kr}} \approx 1 + i\boldsymbol{kr} + \ldots \tag{3.8}$$

Using only the first term entails the common dipole approximation for electric dipole allowed transitions, while for dipole forbidden transitions, the quadrupole component (second term) has to be taken into account. In the following, we assume that the light field described by Eq. (3.7) couples to an electrical dipole moment $\hat{\boldsymbol{d}}$, giving rise to the Hamiltonian [Lei03]

$$\hat{H}_\mathrm{atom-light} = -\hat{\boldsymbol{d}}\cdot\hat{\boldsymbol{E}} = \frac{1}{2}\hbar\Omega\,\left(\hat{\sigma}^+ + \hat{\sigma}^-\right)\left(e^{i(\boldsymbol{k}\hat{\boldsymbol{r}}-\omega_\mathrm{L}t+\phi)}+e^{-i(\boldsymbol{k}\hat{\boldsymbol{r}}-\omega_\mathrm{L}t+\phi)}\right), \tag{3.9}$$

where $\hat{\sigma}^+ := |\uparrow\rangle\langle\downarrow|$ and $\hat{\sigma}^- := |\downarrow\rangle\langle\uparrow|$ are the spin flip operators and

$$\hbar\Omega = E_0\,\langle\uparrow|\,\boldsymbol{\epsilon}\cdot\hat{\boldsymbol{d}}\,|\downarrow\rangle \tag{3.10}$$

[3] A standing wave configuration could be assumed here, too.

defines the Rabi frequency Ω. It is a measure for the coupling strength between light field and atom.

As the ion is confined in a one-dimensional potential along the z-axis, the position-dependent expression $\boldsymbol{k}\hat{\boldsymbol{r}}$ can be written as $\boldsymbol{k}\hat{\boldsymbol{r}} = k\hat{z}\cdot\cos\theta$, where θ is the angle under which the light beam intersects the trap axis and $k = |\boldsymbol{k}| = 2\pi/\lambda$, with λ being the wavelength of the monochromatic light field. Furthermore, we can express the position operator $\hat{z}$ in terms of the creation and annihilation operators of the harmonic oscillator, $\hat{z} = z_0(\hat{a}+\hat{a}^\dagger)$, where $z_0 = |\boldsymbol{z}_0| = \sqrt{\hbar/(2m\omega_z)}$ is the extent of the ground state wave function[4] for a particle of mass m in the harmonic well with frequency ω_z, yielding $\boldsymbol{k}\hat{\boldsymbol{r}} = kz_0\cos\theta(\hat{a}+\hat{a}^\dagger)$. $\boldsymbol{z}_0$ points along the trap axis, which determines the direction of the ion movement. Now we introduce the *Lamb-Dicke* parameter

$$\eta := \boldsymbol{k}\boldsymbol{z}_0 = kz_0\cos\theta = k\sqrt{\frac{\hbar}{2m\omega_z}}\cos\theta = \sqrt{\frac{E_{\text{recoil}}}{\hbar\omega_z}}, \tag{3.11}$$

which is proportional to the ratio between the extent of the wave function along the axial direction $\boldsymbol{z}$ and the wavelength of the light field. The expression after the second equal sign elucidates the physical meaning of η as the square root of the ratio between the recoil energy of the ion gained by a photon absorption/emission process ($E_{\text{recoil}} = (\hbar k\cos\theta)^2/(2m)$) and the phonon energy. Loosely speaking, the Lamb-Dicke parameter is a measure for the interaction strength between the light and the vibrational modes of the ion and is hence of great importance within the context of this work. This becomes obvious when Eq. (3.9) is rewritten in terms of η using $\boldsymbol{k}\hat{\boldsymbol{r}} = \eta(\hat{a}+\hat{a}^\dagger)$,

$$\hat{H}_{\text{atom-light}} = \frac{1}{2}\hbar\Omega\,\left(\hat{\sigma}^+ + \hat{\sigma}^-\right)\left(e^{i(\eta(\hat{a}+\hat{a}^\dagger)-\omega_{\text{L}}t+\phi)} + e^{-i(\eta(\hat{a}+\hat{a}^\dagger)-\omega_{\text{L}}t+\phi)}\right). \tag{3.12}$$

It is useful to transform this Hamiltonian into the interaction picture with respect to the atomic Hamiltonian $\hat{H}_{\text{atom}}$. The resulting Hamiltonian in the interaction picture is

$$\hat{H}^{\text{I}}_{\text{atom-light}} = U^\dagger(t)H_{\text{atom-light}}U(t), \tag{3.13}$$

where $U(t) = \exp\left(-\frac{iH_{\text{atom}}t}{\hbar}\right)$ achieves the unitary transformation. Doing this, we neglect terms $\exp(\pm i(\omega_{\text{L}}+\omega_0))$ oscillating at very high frequencies (rotating wave approximation) and end up with

$$\hat{H}^{\text{I}}_{\text{atom-light}} = \frac{1}{2}\hbar\Omega\,\hat{\sigma}^+\exp\left\{i\eta\left(\hat{a}e^{-i\omega_z t}+\hat{a}^\dagger e^{i\omega_z t}\right)\right\}e^{-i(\delta t-\phi)} + \text{h.c.} \tag{3.14}$$

Here, we introduced the detuning $\delta := \omega_{\text{L}} - \omega_0$ of the laser with respect to the atomic transition frequency.

[4] $z_0 = 9.5\,\text{nm}$ for $^{40}\text{Ca}^+$ in a trap with $\omega_z = 2\pi\times 1.4\,\text{MHz}$.

The Lamb-Dicke Regime

In a last step, we will write the first exponential in a series and truncate terms of order η^2 and higher. This is formally justified if $\eta\sqrt{\langle \hat{a} + \hat{a}^\dagger \rangle} \ll 1$, so if $\eta\sqrt{2n+1} \ll 1$ (this condition marks the borderlines of the so-called Lamb-Dicke regime). The physical interpretation of this formal condition is that the extent of the motional wave function of the harmonic oscillator in a Fock state $|n\rangle$, which is $z_0\sqrt{2n+1}$, must be smaller than the wavelength of the interacting light.

Under the assumption that the Lamb-Dicke condition is met, Eq. (3.14) simplifies to

$$\hat{H}^{\mathrm{I}}_{\mathrm{atom-light}} = \frac{1}{2}\hbar\Omega\,\hat{\sigma}^{+}\left\{1 + i\eta\left(\hat{a}e^{-i\omega_z t} + \hat{a}^\dagger e^{i\omega_z t}\right)\right\} e^{-i(\delta t - \phi)} \;+\; \mathrm{h.c.} \tag{3.15}$$

Eq. (3.15) is our final result modeling the interaction between the ion and the light field. It describes the dynamics of the atom's degrees of freedom (electronic plus motional) being subject to illumination by a light field. These dynamics crucially depend on the detuning δ of the light.

3.1.3 Carrier and Sideband Transitions

Carrier Transitions

It is possible to literally read the resonances of the atom-light interaction from the three terms of Eq. (3.15). First, neglecting terms proportional to η (which means that there is no interaction between the light and the vibrational modes), there is one resonance for $\delta = 0$. The corresponding part of the Hamiltonian $\hat{H}^{\mathrm{I}}_{\mathrm{atom-light}}$ is[5]

$$\hat{H}^{\mathrm{I}}_{\mathrm{car}} = \frac{1}{2}\hbar\Omega\;|\uparrow\rangle\langle\downarrow|\;e^{-i\delta t} \;+\; \mathrm{h.c.} \tag{3.16}$$

It describes pure qubit transitions not involving the motional degrees of freedom. These transitions $|\downarrow, n\rangle \leftrightarrow |\uparrow, n\rangle$ are not accompanied by a change in the phonon number distribution and are called *carrier* transitions.

The dynamics of an ion in a Fock state of motion $|n\rangle$, generated by the carrier Hamiltonian Eq. (3.16) are sinusoidal Rabi oscillations $|\downarrow, n\rangle \leftrightarrow |\uparrow, n\rangle$ with angular frequency Ω.

[5] In the following, we set $\phi = 0$ for convenience.

Red Sideband Transitions

The second term in Eq. (3.15) is proportional to η and reads (cf. Eq. (3.5))

$$\begin{aligned}\hat{H}^{\mathrm{I}}_{\mathrm{rsb}} &= \frac{1}{2}\hbar\Omega\ i\eta\ \sigma^{+}\hat{a}\ e^{-i(\delta+\omega_z)t}\ +\ \mathrm{h.c.}\\ &= \frac{1}{2}\hbar\Omega\ i\eta\sqrt{n}\ |{\uparrow}, n-1\rangle\langle{\downarrow}, n|\ e^{-i(\delta+\omega_z)t}\ +\ \mathrm{h.c.}\end{aligned} \tag{3.17}$$

It models the simultaneous absorption of a photon, changing the qubit state from $|{\downarrow}\rangle$ to $|{\uparrow}\rangle$, accompanied by the reduction of the phonon number by one (the analogous statement holds for the stimulated emission of a photon, which increases the phonon number). Such a transition, which has its resonance at $\delta+\omega_z = 0$, is called a *red sideband* (rsb) transition, as it is red detuned from the carrier transition.

The Hamiltonian Eq. (3.17) is well-known from the Jaynes-Cummings model [Jay63, Cum65], describing the interaction between a two-level atom and a single, quantized electromagnetic mode. It is a textbook model for quantum electrodynamics, and builds the basis for cavity quantum electrodynamics (QED) research. The creation (annihilation) of a phonon in our system can be identified with the emission (absorption) of a photon in the Jaynes-Cummings model.

Blue Sideband Transitions

In the very same way, the third term in Eq. (3.15) leads to so-called *blue sideband* (bsb) transitions, which are resonant for $\delta - \omega_z = 0$:

$$\begin{aligned}\hat{H}^{\mathrm{I}}_{\mathrm{bsb}} &= \frac{1}{2}\hbar\Omega\ i\eta\ \sigma^{+}\hat{a}^{\dagger}\ e^{-i(\delta-\omega_z)t}\ +\ \mathrm{h.c.}\\ &= \frac{1}{2}\hbar\Omega\ i\eta\sqrt{n+1}\ |{\uparrow}, n+1\rangle\langle{\downarrow}, n|\ e^{-i(\delta-\omega_z)t}\ +\ \mathrm{h.c.}\end{aligned} \tag{3.18}$$

Here, the absorption of a photon is accompanied by the excitation of one phonon. Apart from this, there is a crucial difference between red and blue sideband transitions: while light resonant with the blue sideband affects all phonon states $|n\rangle$, this holds only true for $|n>0\rangle$ on the rsb transition. The reason for this is the existence of the ground state of motion, $\hat{a}\,|0\rangle_{\mathrm{m}} = |0\rangle_{\mathrm{m}}$. This peculiarity of the rsb interaction can be exploited to generate (motional) state-dependent interactions.

Coupling Constants

The coherent dynamics on the carrier and sideband transitions can be described by Rabi oscillations between the respective levels

$$\begin{aligned} \text{car}: &\quad |\downarrow, n\rangle \leftrightarrow |\uparrow, n\rangle \\ \text{rsb}: &\quad |\downarrow, n\rangle \leftrightarrow |\uparrow, n-1\rangle \\ \text{bsb}: &\quad |\downarrow, n\rangle \leftrightarrow |\uparrow, n+1\rangle \end{aligned} \tag{3.19}$$

for all $n \geq 0$ except $n = 0$ on the rsb. As for state dynamics, the treatment of a qubit *plus* the external harmonic potential produces mainly two new features, that can be directly read from the Hamiltonians Eqs. (3.16)-(3.18). The first emerging feature are the sideband resonances at (positive and negative) integer multiples m of the trap frequency $\delta = m\omega_0$. The lowest order – for our interests the most important ones – are the first sideband transitions, $|m| = 1$. Second, the coupling constants, i.e. all Rabi frequencies, now depend on the motional quantum number n. In lowest order of η, these coupling constants have already been derived with the carrier and sideband Hamiltonians,

$$\begin{aligned} \Omega_{\text{car}} &\approx \Omega \\ \Omega_{\text{rsb}} &\approx \eta\sqrt{n}\Omega \\ \Omega_{\text{bsb}} &\approx \eta\sqrt{n+1}\ \Omega. \end{aligned} \tag{3.20}$$

A rigorous treatment of the coupling constants (without the truncation of higher order contributions in Eq. (3.14)) yields exact expressions for the resonant[6] Rabi frequencies $\Omega_{n,n+m}$ for a transition between $|\downarrow, n\rangle$ and $|\uparrow, n+m\rangle$, i.e. for an m-th red (blue) sideband transition for $m < 0$ ($m > 0$), and a carrier transition ($m = 0$), respectively. It can be seen from Eq. (3.14) that the coupling constant for a non-vanishing η is modified by the operator $e^{i\eta(\hat{a}+\hat{a}^\dagger)}$, resulting in a factor of [Win98]

$$\frac{\Omega_{n,n+m}}{\Omega} = \langle n+m|\, e^{i\eta(\hat{a}+\hat{a}^\dagger)}\, |n\rangle = e^{-\eta^2/2}\ (i\eta)^{|m|}\ \sqrt{\frac{n_<!}{n_>!}}\ L_{n_<}^{|m|}(\eta^2) \tag{3.21}$$

for a transition from n to $n+m$, where $n_< := \min(n, n+m)$ and $n_> := \max(n, n+m)$ and $L_{n_<}^{|m|}$ is the generalized Laguerre polynomial[7] of order $|m|$ (which reduce to the normal Laguerre polynomials for a carrier transition, since then $|m| = 0$, $n_< = n_> = n$ and $L_n^0(x) = L_n(x)$). It should be noted, that the expressions for the rsb transitions given here are valid for $n > 0$, and of course $\Omega_{n,n'} = 0$ for $n' < 0$ or $n < 0$.

---

[6] The generalized Rabi frequency reads $\sqrt{\Omega_{n,n+m}^2 + \epsilon^2}$, where $\epsilon = \delta - m\omega_z$ is the detuning from the m-th sideband resonance.

[7] An explicit expression is $L_n^\alpha(x) = \sum_{k=0}^{n}(-1)^k \binom{n+\alpha}{n-k}\ x^k/(k!)$.

We explicitly list the expressions for $|m| \leq 1$, as they will be of importance in subsequent sections,

$$\frac{\Omega_{n,n+m}}{\Omega} = \begin{cases} e^{-\eta^2/2}\, L_n^0(\eta^2) \;=\; 1 - \eta^2(n+\frac{1}{2}) + O(\eta^4) & \text{for } m = 0 \\ \eta e^{-\eta^2/2}\sqrt{\frac{1}{n}}\, L_{n-1}^1(\eta^2) \;=\; \eta\sqrt{n} + O(\eta^3) & \text{for } m = -1 \\ \eta e^{-\eta^2/2}\sqrt{\frac{1}{n+1}}\, L_n^1(\eta^2) \;=\; \eta\sqrt{n+1} + O(\eta^3) & \text{for } m = +1. \end{cases} \tag{3.22}$$

These expressions are in accordance with the results in Eq. (3.20) gained directly from the interaction Hamiltonians, where we neglected all terms of order η^2 or higher. For practical use it is more convenient to rewrite the Rabi frequencies in terms of a directly measurable quantity like the ground state carrier Rabi frequency $\Omega_{0,0} = \Omega e^{-\eta^2/2}$,

$$\frac{\Omega_{n,n+m}}{\Omega_{0,0}} = \begin{cases} L_n^0(\eta^2) \;=\; 1 \;-\; \eta^2 n \;+\; O(\eta^4) & \text{for } m = 0 \\ \eta\sqrt{\frac{1}{n}}\, L_{n-1}^1(\eta^2) \;=\; \eta\sqrt{n} \;+\; O(\eta^3) & \text{for } m = -1 \\ \eta\sqrt{\frac{1}{n+1}}\, L_n^1(\eta^2) \;=\; \eta\sqrt{n+1} \;+\; O(\eta^3) & \text{for } m = +1. \end{cases} \tag{3.23}$$

Figure 3.1 shows the coupling constants calculated from the exact expressions in Eq. (3.23)

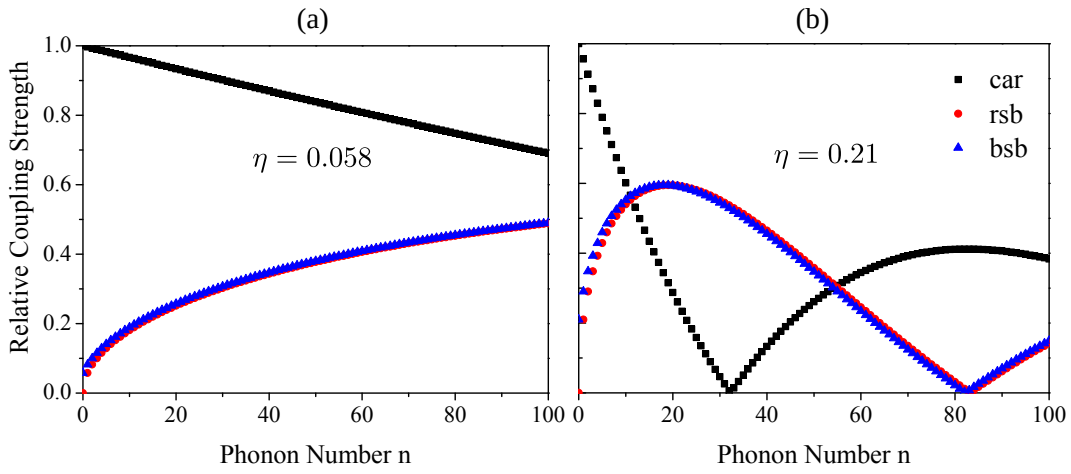

Figure 3.1: Relative coupling strength $|\Omega_{n,n+m}/\Omega_{0,0}|$ as a function of the phonon number n for carrier (car, $m = 0$), red sideband (rsb, $m = -1$) and blue sideband (bsb, $m = +1$) transitions. All values were calculated using the exact expressions from Eq. (3.23). (a) Coupling strength for a Lamb-Dicke parameter resulting from the interaction with the 729 nm laser coupling the levels in the optical qubit. (b) The same for the Lamb-Dicke parameter resulting from the Raman interaction with the spin qubit. For this higher η, one can clearly see the breakdown of the monotonic approximations, which are also given in Eq. (3.23).

as a function of n. While for small values of η, the validity of the Lamb-Dicke approximation manifests itself in the linear shape of the carrier couplings, the sideband couplings

are approximately proportional to $\sqrt{n}$ (in accordance with the lowest order expressions in Eq. (3.23). A fairly different behavior shows for higher η. In these cases, the Lamb-Dicke regime is limited to very small values of n only. It is noticeable that there exists a maximum in the sideband couplings, which comes along with a vanishing dependence on n.

As we are dealing with laser cooled ions, mostly very low mean phonon numbers occur in the experiment. For instance, with a typical trap frequency $\omega_z = 2\pi \times 1.4\,\mathrm{MHz}$, the theoretical (two-level) limit for Doppler cooling is about 9 phonons and after sideband cooling, we end up with $n < 1$, so that the Lamb-Dicke condition is very well met.

3.1.4 Motional State Dynamics of Phonon Distributions

The dynamics of a single qubit in a Fock state of motion undergoes a perfect Rabi oscillation in the excitation probability $P_\uparrow(t)$ as a function of the interaction time t (cf. Fig. 3.12 later). This means, there is only one frequency – the Rabi frequency Ω_0 in the resonant case – in the Fourier spectrum of the oscillations $P_\uparrow(t)$. Additionally, the amplitude of the oscillation is constant and maximal, implying a 100% population swapping between the two states.

From Eq. (3.21) we learned, that the Rabi frequency on a transition $|\downarrow, n\rangle \leftrightarrow |\uparrow, n+m\rangle$ depends on the phonon state $|n\rangle$ of the ion motion. If the ion is not in a Fock state of motion, but in a general superposition state, the oscillation will also be modified by the respective Rabi frequencies $\Omega_{n,n+m}$. This fact can then be utilized to deduce the phonon number distribution $P(n)$ from the Fourier components of the oscillation dynamics.

In general, the motional state of the ion can be written as a linear superposition of Fock states

$$|\varphi\rangle = \sum_{n=0}^{\infty} e^{i\vartheta_n} \sqrt{P(n)}\, |n\rangle\,, \tag{3.24}$$

with $P(n) \geq 0$ and $\sum_n P(n) = 1$, and phases ϑ_n. Consider an ion initially in state $|\uparrow, \varphi\rangle$. In accordance with the considerations made above, the excitation probability $P_\uparrow(t)$ as a function of the atom-light interaction time t then contains contributions from all states $|n\rangle$ weighted with their respective probability $P(n)$ [Win98]

$$P_\uparrow(t) = \frac{1}{2} \sum_{n=0}^{\infty} P(n) \left(\cos(\Omega_{n,n+m} t)\; e^{-t/\tau_\mathrm{c}} \;+\; 1 \right), \tag{3.25}$$

where we accounted for amplitude reduction by decoherence processes by introducing the

coherence time τ_c[8].

Equation (3.25) builds the basis for one of the most important motional state analysis tools. That's because the phonon distribution can be directly deduced from simple Rabi oscillations for a wide range of phonon distributions[9]. The exact procedure will be presented in detail in chapter 6.3.

3.2 Implementations

Two concepts to implement an effective two-level quantum system – a qubit – in the electronic level structure of a single $^{40}Ca^{+}$-ion will be presented and discussed in the following chapters: the so-called *optical qubit*[10] and the *spin qubit* (details can also be found in Ref. [Pos09]). Thereby, it will be shown that having both concepts – which partially build upon each other – at hand gives a very powerful set of possibilities to prepare, manipulate and readout the state of the ion. Many experimental issues concerning decoherence times and laser stability differ for the different realizations and will be discussed. The proper choice of the qubit system, or rather the choice of the specific set of levels involved and the way they are coupled, can help to minimize experimental problems significantly.

3.2.1 The Optical Qubit

The most obvious requirement for the experimental implementation of a qubit within the electronic level structure of an atom are long lifetimes of the two states it consists of. These lifetimes have to be much longer than experimental timescales to avoid errors introduced by relaxation via spontaneous emission. The optical qubit consists of the stable, non-decaying ground state $4\,S_{1/2}$ and the metastable excited state $3\,D_{5/2}$, see Fig. 3.2(a). This state decays back into the ground state via a quadrupole transition after a mean lifetime of 1.2 s [Bar00], so that sub-percent loss of population is guaranteed for experiments lasting as long as ~ 10 ms.

On the other hand, the upper state's long lifetime implies an extremely narrow linewidth

[8] In principle, the coherence time also depends on n. This can be exploited for state analysis under certain circumstances, too [Bud02]. As long as this dependence is small enough, it can be neglected and a constant τ_c can be assumed.

[9] The same phenomenon has been exploited in cavity-QED to show the light field's quantization [Bru96b].

[10] The name is inspired by the energy difference between the two qubit-levels, which allows for being covered by a laser in the optical wavelength range – 729 nm in our case.

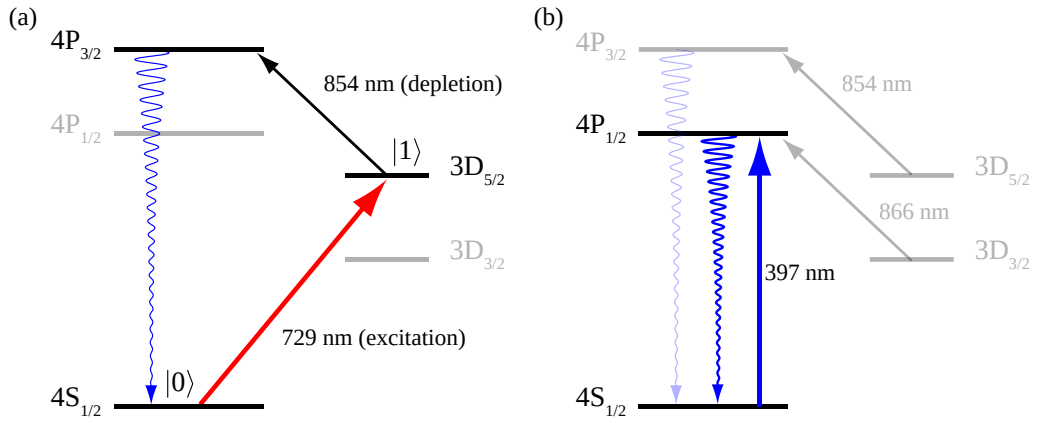

Figure 3.2: Relevant levels and transitions for the implementation of the optical qubit system. (a) Excitation of the qubit transition by a narrow bandwidth laser at 729 nm. The level $D_{5/2}$ has a lifetime of about 1.2 s; its population can be depleted on a dipole transition via $P_{3/2}$.
(b) The dipole transition $S_{1/2}$ $P_{1/2}$ is used for fluorescence detection and for Doppler cooling. Two repump lasers at 866 nm and 854 nm prevent population trapping in $D_{3/2}$ and $D_{5/2}$, respectively.

transition and requires a highly stable laser source at 729 nm to drive transitions between $|0\rangle \equiv |S_{1/2}\rangle$ and $|1\rangle \equiv |D_{5/2}\rangle$. For this purpose, an amplified diode laser locked to an ultra stable, high finesse cavity is used. The stabilized laser's spectral width is smaller than ≈ 5 kHz and provides up to 140 mW of light power to the ion. Focused down to a beam waist of $\approx 15\,\mu$m, this leads to typical Rabi frequencies $\Omega/(2\pi)$ of a few megahertz.

Figure 3.2 depicts all relevant transitions for the optical qubit. Due to the intrinsic long lifetime of $D_{5/2}$, it has to be possible to deplete (*quench*) the excited state, too. This is achieved by the help of additional levels: a short laser pulse at 854 nm of typically some microseconds duration couples the excited state to the rapidly ($\tau = 6.8$ ns [NIS10]) decaying level $P_{3/2}$, so that the ion ends up in ground state again, after emission of a photon at 393 nm.

Doppler Cooling

The ion is Doppler cooled on the $S_{1/2}$ $P_{1/2}$ transition, see Fig. 3.2(b). The excited level $P_{1/2}$ decays after $\tau = 7.1$ ns [NIS10], mostly back into $S_{1/2}$, but also with a small probability of about $\approx 1/16$ into $D_{3/2}$ [Lia95]. An additional laser at 866 nm repumps this population back to $P_{1/2}$. Similarly, the quench laser at 854 nm is used to repump population from $D_{5/2}$, which can be eventually populated by background gas collisions,

for instance[11]. Together with the repump lasers, a closed cooling cycle can be established.

Zeeman Splitting

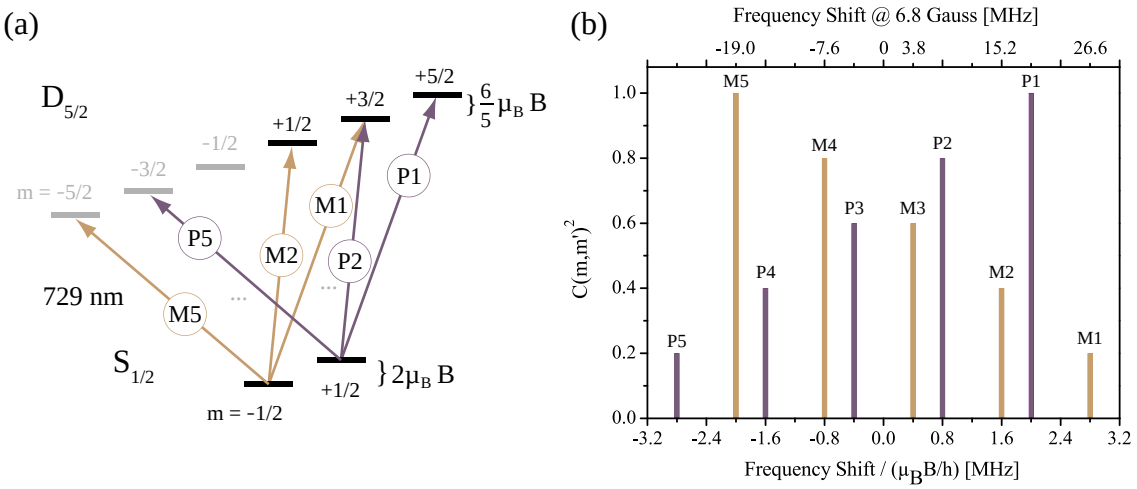

Figure 3.3: (a) Energy diagram showing the Zeeman splitting in the $S_{1/2}$ and $D_{5/2}$ fine structure by a static magnetic field $\boldsymbol{B}$. Ten transitions emerge, because transitions with $|\Delta m| \leq 2$ are allowed in the quadrupole interaction case. P1-P5 transitions start or end in $S_{1/2}, m = +\frac{1}{2}$, M1-M5 transitions start or end in $S_{1/2}, m = \ \frac{1}{2}$, respectively.
(b) All ten transitions in frequency space. The lower axis shows the frequency shift of the line in units of $\mu_B B/h$ relative to the case $B = 0$, where all lines are degenerate. The upper axis shows the shift in MHz for the actual magnetic field. The heights of the lines are given by the squared Clebsch-Gordan coefficients of the angular momenta involved. The transition strengths of the individual lines additionally depend on the light polarization (see also text).

When the ion experiences a magnetic field, then of course each fine structure level with angular momentum J is Zeeman-split into $2J + 1$ sublevels, labeled with their magnetic quantum number $m = \ J/2, ..., +J/2$. As such a Zeeman splitting is required for the implementation of the spin qubit, a constant non-zero magnetic field was applied at the ion's position throughout all experiments (see chapter 3.2.2).

This implies that out of one transition ten possible quadrupole transitions between $S_{1/2}$ and $D_{5/2}$ emerge; they are depicted and labeled in Fig. 3.3(a). Figure 3.3(b) shows all lines in frequency space, their height given by the squared Clebsch-Gordan coefficients $C(m, m')^2$ for transitions $|S_{1/2}, m\rangle \rightarrow |S_{1/2}, m'\rangle$. Additionally, some of the transitions can be suppressed by a proper choice of beam direction and polarization [Roo00]. In our

[11] All experiments were carried out under ultra high vacuum conditions. The residual gas pressure amounted to $\approx 3 \times 10^{-10}$ mbar.

experiments, the polarization vector of the 729 nm beam, the magnetic field vector and the beam direction were pairwise orthogonal, while the beam intersects the trap axis under an angle of 45°. This strongly suppresses all unwanted transitions but P1,M1,P5 and M5 [Roo00]. When other transitions are necessary, the polarization can be adapted.

Our qubit states should now correctly be labeled $|0\rangle \equiv |\mathrm{S}_{1/2}, m = +1/2\rangle$ and $|1\rangle \equiv |\mathrm{D}_{5/2}, m = +5/2\rangle$ (the choice of these specific magnetic sublevels will become obvious in chapter 3.2.2), i.e. the qubit transition is P1. As, however, the Zeeman-splitting makes no fundamental difference for the understanding of the optical qubit implementation, it will be neglected as far as possible until chapter 3.2.2 introduces the spin qubit.

State Preparation

The preparation of the optical qubit in state $|0\rangle$ is almost trivially achieved by exclusive application of the two repump lasers (854 nm and 866 nm, respectively), which deplete the D-levels, as all decay paths from the short living P-levels finally end up in the ground state. This process is a way of optical pumping (like any basic preparation procedure used) because all unwanted levels are either directly decaying (P-manifold) or coupled to (D-manifold) such decay paths ending up in $|0\rangle$, while the ground state itself remains untouched by the lasers.

If, as in our case, one has to cope with a Zeeman-split ground state, the simultaneous application of a σ^+-polarized beam parallel to the magnetic field makes sure that the ion ends up in the correct $m = +1/2$ level, because it only couples the $m = -1/2$ level to $\mathrm{P}_{1/2}$, while the $m = +1/2$ level cannot be excited to $\mathrm{P}_{1/2}$ under absorption of a σ^+-polarized photon.

Coherent Dynamics

As for the formal treatment of the coherent dynamics introduced in chapter 3.1, we considered a dipole qubit transition, interacting with a single light mode. In fact, the situation is slightly different in the present case. The $\mathrm{S}_{1/2} \leftrightarrow \mathrm{D}_{5/2}$ transition of the optical qubit is dipole forbidden. Nevertheless, the results are completely applicable. Only the expression describing the Rabi frequency has to be adapted. This is because the first term in Eq. (3.8) leads to a vanishing coupling for the dipole forbidden transition. Taking the next, leading order term, into account leads to the desired modified expression for the Rabi frequency, $\hbar\Omega = E_0 \langle\uparrow| (\boldsymbol{kr})(\boldsymbol{\epsilon d}) |\downarrow\rangle$. Besides this, the formalism can be applied without modification.

State Discrimination

The $S_{1/2} \rightarrow P_{1/2}$ transition at 397 nm is not only used for Doppler cooling, but due to its high fluorescence rate, it is also predestined for the discrimination of the qubit state. The technique applied for this purpose exploits the fact that an ion initially in the state $S_{1/2}$ exhibits resonance fluorescence on this transition on illumination by light at 397 nm, while an ion in state $D_{5/2}$ does not, because the laser does not couple this level to the S- or P-manifold. Of course, the repump laser at 866 nm has to prevent population trapping in $D_{3/2}$ during this procedure.

The fluorescence light at 397 nm is collected and imaged to both an electron-multiplying CCD-camera[12] and a photomultiplier tube[13] (PMT). While the camera is mainly used for monitoring purposes, the PMT yields quantitative fluorescence data used for state detection. Despite of losses of fluorescence light that are mainly due to the limited light collection solid angle ($\approx 2.5\,\%$ of 4π [Mai06]), the quantum efficiency of about 50 % in the detector and absorption losses in optical elements, we typically end up with 3×10^4 photons per second[14]. As for state discrimination, we have to distinguish between a bright, fluorescing ($|0\rangle$) and a dark ($|1\rangle$) ion, a very short time of the order of a millisecond suffices to collect some tens of photons for a bright ion in contrast to almost zero for a dark one (there is always a small amount of residual background light collected by the optics that does not originate from fluorescence; it can be efficiently suppressed by spectral and spatial filtering, however).

The number of photons obtained by either a dark or a bright ion during a certain detection time is Poissonian distributed. This means that the two cases can be distinguished if their probability distributions do not overlap. Figure 3.4 illustrates this situation.

At first sight, a longer detection time should always produce a clearer separation of the distributions and therewith a smaller discrimination error, which is obviously given by their mutual overlap. However, for longer detection times the finite lifetime of the $|1\rangle$-state leads to discrimination errors. This is because population in $|1\rangle$ can eventually decay during the measurement process into $S_{1/2}$ and is then mistakenly identified as state $|0\rangle$. An optimum detection time can be computed from fluorescence rates and the decay time (see, for instance [Roo00]). Usually, we choose the detection time as small as possible to profit from short experiment times, as long as the discrimination error is smaller than other pre-

[12] EMCCD Camera, iXon^{EM} DV860-BI (back-illuminated) by Andor Technology.

[13] P25PC by ET Enterprises.

[14] For simultaneous detection with camera and PMT, the fluorescence light is shrared by a beamsplitter; additionally, narrow spectral filters prevent detection of other light sources.

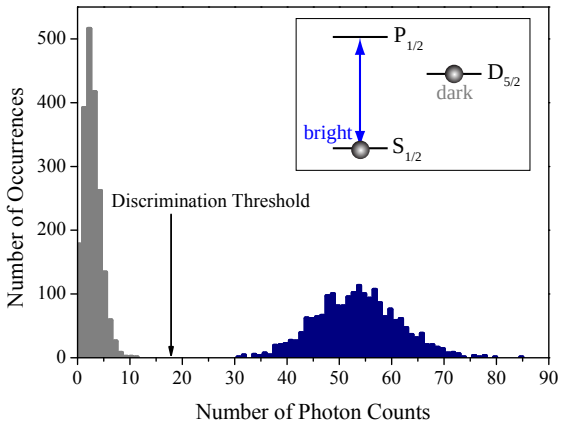

Figure 3.4: Histogram of the number of photons collected during a time span of 2 ms. The Poissonian distributions for a bright ion having scattered some tens of photons and that of a dark ion, where only background light was detected, are clearly separated. For the production of these data, the state preparation was repeatedly alternated between $|0\rangle$ and $|1\rangle$. Once a discrimination threshold (arrow) is obtained by such a gauge measurement, it can be applied to discriminate unknown qubit states in following experiments by comparing the measured fluorescence counts to the threshold.

dominant error contributions. Under typical experimental conditions, the discrimination error can be asserted to be smaller than 10^{-3}.

It is worth mentioning at this point that the described procedure fulfills the requirement of a projective quantum measurement. Any superposition state $a_0\,|0\rangle + a_1\,|1\rangle$, where a_0 and a_1 are complex amplitudes which satisfy $|a_0|^2 + |a_1|^2 = 1$, is *projected* onto $|0\rangle$ or $|1\rangle$, with probability $|a_0|^2$ and $|a_1|^2$, respectively. This means in particular, that successive measurements of the qubit state can be performed and yield the same result. We will make use of this fact in chapter 6.5 to measure single quanta of motion in a non-destructive way.

Stability Issues

The optical qubit presented here has a long but finite lifetime ($\tau \gg 1\,\mathrm{s}$), which leads to an exponential decay of the Rabi oscillation contrast with time constant τ. As typical Rabi oscillation periods achieved on this transition are of the order of microseconds, this is not a crucial problem for the observation of coherent dynamics.

A much more critical subject in terms of coherence loss is the non-monochromaticity of real laser sources. Fluctuations in the electric field phase corrupt the qubit's relative phase between $|0\rangle$ and $|1\rangle$. This leads to a loss of contrast on the timescale of the inverse laser

linewidth. On the other hand, the overlap between the transition's linewidth – which is extremely small – and the spectral laser profile determines the coupling strength between laser and atom. So, if the laser linewidth is too large, the coupling becomes small and the Rabi oscillation period can become too long to observe coherent oscillations.

Fluctuations in the laser's (center) frequency ω_{L} result in fluctuations in detuning and therewith in Rabi frequency. This, again, leads to a loss of contrast by dephasing. Similarly, fluctuations of the level separation ω_0, caused by magnetic field noise or drift, can cause decoherence on different timescales. These issues will also be subject to experimental investigation in chapter 7.1.

3.2.2 The Spin Qubit

The previous chapter introduced an implementation of a qubit system comprising the ground state and a metastable state of $^{40}\mathrm{Ca}^{+}$. As discussed, high laser stability requirements have to be met for driving coherent dynamics in this system. On the other hand, the qubit state discrimination can be accomplished fast and with high accuracy.

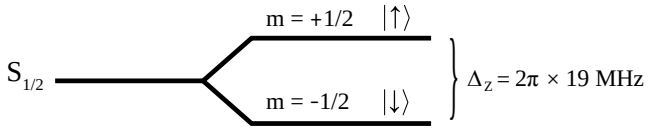

Figure 3.5: The spin qubit comprises the two Zeeman sublevels of the ground state $\mathrm{S}_{1/2}$. The splitting Δ_{Z} is caused by a homogeneous, static magnetic field.

Instead of two different fine structure levels, both levels of the so-called *spin qubit* emerge from the $\mathrm{S}_{1/2}$ ground state by application of a moderate magnetic field, which splits it into two magnetic sublevels

$$|\downarrow\rangle := |\mathrm{S}_{1/2}, m = -1/2\rangle \quad \text{and}$$
$$|\uparrow\rangle := |\mathrm{S}_{1/2}, m = +1/2\rangle\,,$$

respectively, as can be seen in Fig. 3.5. The Zeeman splitting $\Delta_{\mathrm{Z}} := (E_{\uparrow} - E_{\downarrow})/\hbar$ depends in first order linearly on the magnetic field and amounts to 19 MHz for a magnetic field[15] of 6.8 Gauss, which equals the value applied in our experiments. Of course, all other fine structure levels are subject to Zeeman splitting, too; this has already been discussed, cf. Fig. 3.3(a). The natural lifetime of the two different magnetic sublevels amounts to many years and has no practical influence on our experiments. Indeed, scattering events caused

[15] A short review of relevant quantities is given in section 9.5.

by residual light entail a much shorter, effective lifetime. In the following, the preparation and readout of the spin qubit system will be discussed before we address the controlled, coherent coupling of the qubit levels by laser light.

State Preparation

At the beginning of any experiment, the qubit has to be initialized in a specific state. This shall be $|\uparrow\rangle$ in the following, although all methods presented in this section analogously apply to the case in which the system is desired to start from $|\downarrow\rangle$. Two different ways to initialize the qubit by optical pumping were used, depending on accuracy requirements. Both methods employ laser pulses that are selective on the qubit state and thus achieve to deplete only one of the two states while the other remains untouched; into the latter, of course, all population is pumped into.

The methods differ in their respective ways to achieve state selectivity: One relies on laser polarization, the other one on the frequency separability of the levels [Ben08a]. In the first case, we exploit the fact that a σ^+ circularly polarized beam driving the $S_{1/2} - P_{1/2}$ transition will indeed couple $|\downarrow\rangle$, but not $|\uparrow\rangle$ to $P_{1/2}$, as there is no $P_{1/2}$-level with $m = +\frac{3}{2}$. Thus, all population ends up in $|\uparrow\rangle$ after some microseconds, as long as the repump lasers prevent population trapping in one of the D-states. This is exactly the way the optical qubit is prepared, too, when the degeneracy of the $S_{1/2}$-states is lifted by the magnetic field (see chapter 3.2.1). Figure 3.6(a) illustrates the polarization selective excitation into $P_{1/2}$ and the following spontaneous decay back into both qubit levels. This method suffers from the fact, that small fractions of π- or σ^- polarization in the exciting beam deplete the $|\uparrow\rangle$ level. Therefore, the polarization purity of the pumping beam is crucial for the pumping efficiency.

The second method (see Fig. 3.6(b)) makes use of the fact that all different lines on the quadrupole transition (P1, M1, ...) are well separated by frequencies of the order of megahertz, which can thus be individually addressed by the narrow linewidth laser at 729 nm[16].

The following pulsed scheme achieves the frequency selective optical pumping. (i) A π-pulse on the M1 transition transfers population from $|\downarrow\rangle$ into $D_{5/2}$ but leaves $|\uparrow\rangle$ untouched. (ii) A quenching pulse at 854 nm depletes $D_{5/2}$ into $P_{3/2}$. From here, it decays into either $D_{3/2}$ or, in most cases, back into $S_{1/2}$ (either $|\uparrow\rangle$ or $|\downarrow\rangle$). The number of pumping cycles can

[16] In contrast, this is not the case for the 397 nm transition, as the Zeeman splitting of both $S_{1/2}$ and $P_{1/2}$ is of the order of the transition linewidth.

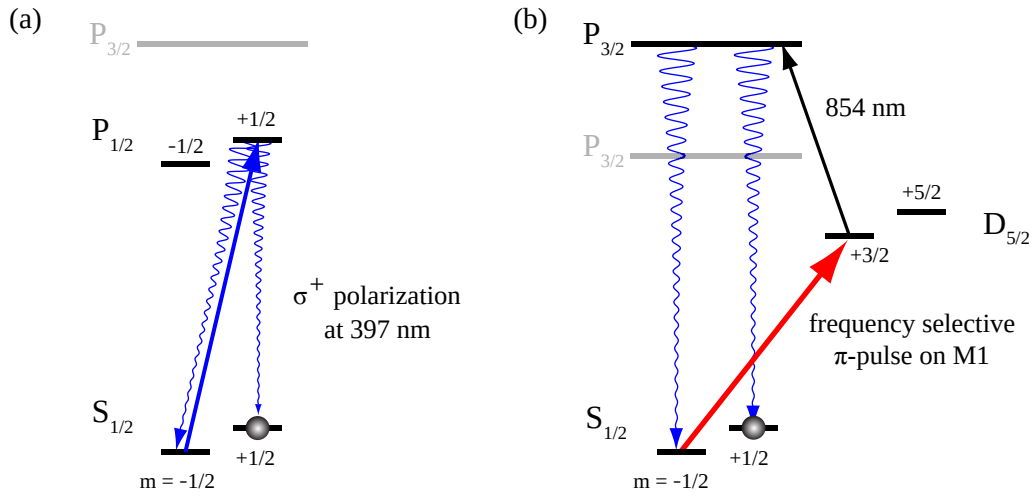

Figure 3.6: Two optical pumping schemes. (a) Polarization selective pumping. A beam at 397 nm continuously excites the $S_{1/2}$ $P_{1/2}$ transition. Its polarization ensures that only the state $|\downarrow\rangle$ is excited so all population is trapped in $|\uparrow\rangle$. (b) Frequency selective pumping. A narrow linewidth laser at 729 nm drives the transition M1, cleaning out all population in $|\downarrow\rangle$. The repumper at 854 nm ensures a closed cycle via $P_{3/2}$. After some cycles, all population resides in $|\uparrow\rangle$. For simplicity, only relevant levels and splittings are drawn.

be minimized by adjusting the quenching beam polarization to minimal σ components. This entails the highest probability to end up in $|\uparrow\rangle$ after each cycle, because the path via $(P_{3/2}, m = \frac{1}{2})$ into $|\downarrow\rangle$ is suppressed.

The repump laser at 866 nm prevents population trapping in $D_{3/2}$ and is constantly switched on. After a couple of iterations, the ion will have decayed into $|\uparrow\rangle$ and stay there as it is protected against laser excitation.

The efficiency of the polarization selective pumping is about 98 %. It is mainly limited by parasitic polarization components of the pumping beam. These can be caused by imperfect polarizers, birefringent windows in the beam path or by misalignment between the beam and the magnetic field axis.

Figure 3.7(a) shows the results of the pulsed, frequency selective optical pumping for different numbers of pumping cycles N. The pumping efficiency increases with N and saturates at a level as high as 99.6 %. Additionally, the pumped scheme proves to be very robust in terms of single pulse duration (at 729 nm) for higher N. This implies that intensity or alignment drifts in the pumping beam are not critical. Note that the results given here are not corrected for detection efficiency; in fact, they reflect the combined preparation and discrimination error.

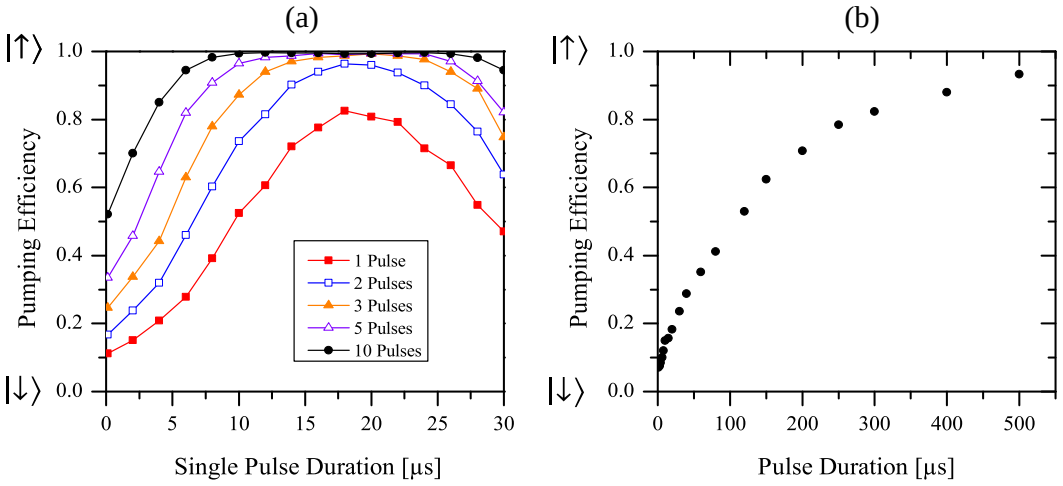

Figure 3.7: Frequency selective optical pumping results. For each measurement, the ion was prepared in $|\downarrow\rangle$ by application of circularly polarized light at 397 nm. The graphs show the probability to find the ion in $|\uparrow\rangle$ after the pumping. (a) The pulsed scheme ensures very high efficiency increasing with pumping cycle number N. It saturates at a combined readout and pumping efficiency of 99.6 %. The wide plateau for higher N indicates the scheme's robustness against pulse area errors, mostly caused by intensity drifts.
(b) For comparison, the results of continuous illumination by the same lasers is shown. While the overall duration is comparable to the pulsed scheme, the saturating level does not reach the same high level (see text for further details).

For comparison, Fig. 3.7(b) shows the results of a measurement where both the pumping and the quenching beam were continuously switched on: the efficiency saturates at a much lower level around 93.3 %. This is due to the fact, that the quenching beam couples the metastable state to the quickly decaying $P_{3/2}$ level and thereby interferes with the coherent population transfer during the pump pulse.

State Discrimination

As the Zeeman splitting of the spin levels is on the order of the linewidth of the $S_{1/2}-P_{1/2}$ transition, it is not possible to distinguish the two qubit states by simply tuning a narrow bandwidth laser to resonance with only one qubit level, because both Zeeman levels will fluoresce almost equally strong. Instead, to achieve state discrimination, we build upon the high detection efficiency of the optical qubit and establish a procedure that performs an unambiguous mapping between the spin qubit levels and the optical qubit levels $S_{1/2}$ and $D_{5/2}$.

The procedure relies on the fact that it is possible to transfer the population of exactly

one of the qubit states – in our case $|\uparrow\rangle$ – to the $D_{5/2}$ level without affecting the population in the other qubit state; if this is given, then the discrimination procedure described in chapter 3.2.1 can be utilized to read out the $D_{5/2}$ population and therewith indirectly the spin qubit's state. In other words, an ion in state $|\uparrow\rangle$ will be transferred into the level $D_{5/2}$, and a subsequent illumination on the $S_{1/2} - P_{1/2}$ dipole transition will yield no fluorescence, whereas an ion in state $|\downarrow\rangle$ will not be transferred but resides in the $S_{1/2}$ manifold, which strongly fluoresces on the dipole transition. This procedure is commonly named *ion shelving* [Nag86] because it prevents the qubit state from interacting with the fluorescence laser by putting it into a "safe place" – $D_{5/2}$.

Rapid Adiabatic Passage

The population transfer is accomplished by a method called *Rapid Adiabatic Passage* (RAP) [Wun07]. It makes a high transfer efficiency of over 99 % possible and is very robust against drifts of experimental parameters. The transfer efficiency of a simple π-pulse, for example, critically depends on the exact pulse area and on laser detuning. If either laser intensity, beam alignment, laser frequency or magnetic field are subject to temporal drift, the transfer efficiency and consequently, the detection efficiency would decline. The RAP method, however, has the advantage to be robust against both frequency and laser intensity drifts.

The basic idea behind the RAP can be most easily understood in a Bloch vector picture. Here, the south pole represents state $|0\rangle$, from where the population is to be transferred, and the north pole represents state $|1\rangle$, the destination of the population transfer. The ion state is represented by a vector[17] $\boldsymbol{\psi}$ pointing from the center to the surface of the sphere, see Fig. 3.8(a). At $t = 0$, all population is supposed to be in $|0\rangle$, so $\boldsymbol{\psi}$ is pointing straight downwards to the south pole.

When a laser field is applied to the two-level system, the dynamics of $\boldsymbol{\psi}$ obeys the differential equation $\dot{\boldsymbol{\psi}} = -\boldsymbol{\Omega} \times \boldsymbol{\psi}$, where $\boldsymbol{\Omega} = (\Omega_0, 0, \delta)^T$ describes the light field with Rabi frequency Ω_0 and detuning δ. From this, it is immediately obvious that the dynamics of the two-level system is simply described by a rotation of the state vector $\boldsymbol{\psi}$ around an axis which is given by $-\boldsymbol{\Omega}$, i.e. by the amplitude and detuning of the laser field[18].

For a resonant π-pulse, $\boldsymbol{\Omega}$ is aligned along the x-axis, and the state vector evolution is

[17] The formal definition of the vector is $\boldsymbol{\psi} = (u, v, w)^T = (2\mathrm{Re}\,\rho_{01}, 2\mathrm{Im}\,\rho_{01}, \rho_{11} - \rho_{00})$, where $\rho_{ij} = \langle i|\,\rho\,|j\rangle$ and ρ is the density operator of the two-level state.

[18] Here, we neglect all decoherence-inducing effects like spontaneous decay.

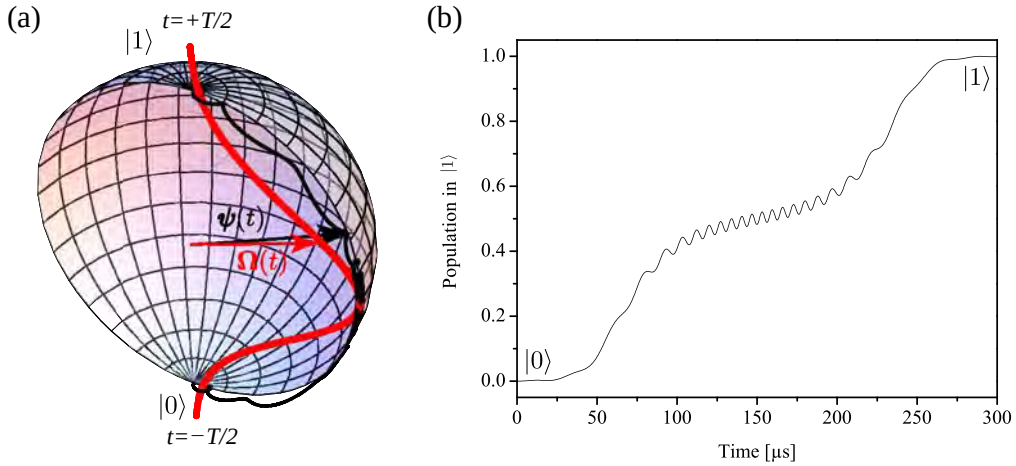

Figure 3.8: (a) Evolution of the state vector $\boldsymbol{\psi}(t)$ and the interaction vector $\boldsymbol{\Omega}(t)$ during a RAP-pulse. $\boldsymbol{\psi}(t)$ performs small precession movements around the time-dependent interaction vector but otherwise follows its trajectory from $|0\rangle$ to $|1\rangle$ adiabatically. The parameters for the RAP are $\Delta\delta = 2\pi \times 100\,\mathrm{kHz}, \widetilde{\Omega} = 1\,\mathrm{MHz}, \tau = T/3 = 100\,\mu\mathrm{s}$. (b) Probability to find the ion in the $|1\rangle$ state during the RAP pulse. The final transfer efficiency is around 99.9 %. The small oscillations are due to the precession movements of $\boldsymbol{\psi}$.

described by a straight trajectory on the sphere's surface from south to north pole, representing a complete population transfer from $|0\rangle$ to $|1\rangle$. $\boldsymbol{\psi}$ is orthogonal to $\boldsymbol{\Omega}$ throughout the whole interaction time T. That's why an orientation error of $\boldsymbol{\Omega}$ will directly imply an incomplete transfer. The same holds true for a deviation of the interaction time from the perfect $T = \pi/\Omega_0$ duration, because then, the state vector "overshoots" its destination.

The idea behind the RAP, however, is to introduce a *time-dependent* rotation axis $\boldsymbol{\Omega}$ and to design it that $\boldsymbol{\psi}$ remains almost parallel to it throughout the whole time evolution, see Fig. 3.8(a). Then, by moving $\boldsymbol{\Omega}$ slowly from south to north pole, the state vector is "dragged" along with $\boldsymbol{\Omega}$, from $|0\rangle$ to $|1\rangle$. The specific trajectory of the "dragging" has no major influence on the transfer efficiency as long as the initial and final orientation of $\boldsymbol{\Omega}$, respectively, is correctly aligned along the z-axis, and as long as the evolution is slow enough to allow the state vector to follow the trajectory of $\boldsymbol{\Omega}$. Formally (and in the limit of infinitely long interaction time), the two-level state remains in an eigenstate of the system Hamiltonian, which is adiabatically changed by altering the parameters Ω_0 and δ.

The following choices for the parameters amplitude $\Omega_0(t)$ and detuning $\delta(t) = \omega_\mathrm{L}(t) - \omega_0$ realize the described trajectory: the detuning is swept linearly over resonance from $\delta(-T/2) = -\Delta\delta$ to $\delta(+T/2) = +\Delta\delta$ in a total interaction time T (typical parameters used are $\Delta\delta = 2\pi \times 50\,\mathrm{kHz}$ and $\tau = T/3 = 50\,\mu\mathrm{s}$.) Simultaneously, the laser field amplitude and,

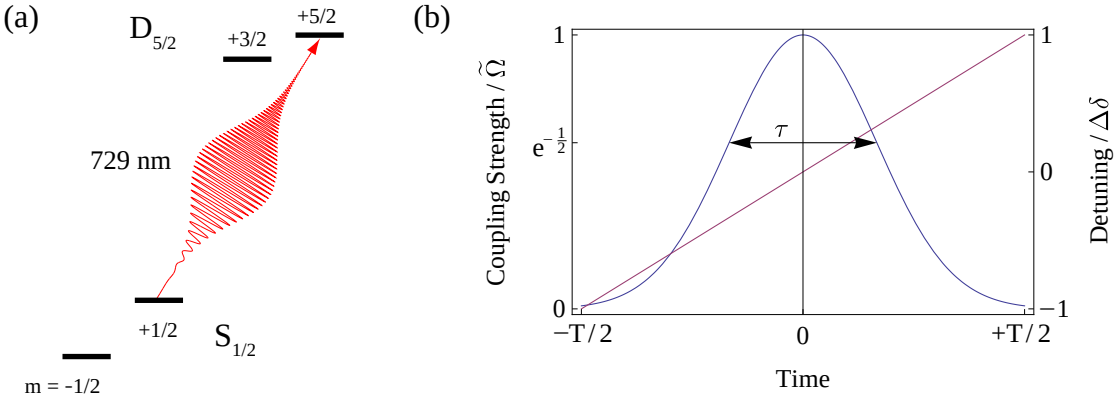

Figure 3.9: Population mapping between $|\uparrow\rangle \leftrightarrow \mathrm{D}_{5/2}$ and $|\downarrow\rangle \leftrightarrow \mathrm{S}_{1/2}$, respectively (*Electron Shelving*) by a Rapid Adiabatic Passage (RAP). (a) A chirped pulse on P1 transfers all population from $|\uparrow\rangle = |\mathrm{S}_{1/2}, m = +\frac{1}{2}\rangle$ into $|\mathrm{D}_{5/2}, m = +\frac{5}{2}\rangle$, while $|\downarrow\rangle$ remains untouched. Subsequently, the same detection scheme like for the optical qubit can be applied to distinguish the $\mathrm{S}_{1/2}$ from the $\mathrm{D}_{5/2}$ level (see chapter 3.2.1). (b) The RAP is achieved by a specially shaped laser pulse. Its frequency is chirped linearly across the resonance of the transition (P1), while at the same time its amplitude develops such that the result is a Gaussian envelope. The dynamics generated by such a pulse is robust against frequency and amplitude drifts and yields very high transfer efficiencies.

by implication, Ω_0 is altered in a Gaussian shape according to $\Omega_0(t) = \widetilde{\Omega} \exp\left(-\frac{t^2}{2(\tau/2)^2}\right)$, where $\widetilde{\Omega}$ is the peak amplitude of the pulse and τ is the full $e^{-\frac{1}{2}}$ width of the pulse, cf. Fig. 3.9. This parametrization ensures that the x-component $\Omega_0(t)$ of $\mathbf{\Omega}$ almost vanishes at the beginning and at the end, while the z-component $\delta(t)$ linearly evolves from south to north direction[19]. The adiabaticity of the process is given, if $|\dot{\mathbf{\Omega}}|/|\mathbf{\Omega}| \ll |\mathbf{\Omega}|$.

Figure 3.8 shows the trajectory of the state vector $\boldsymbol{\psi}$ and the interaction vector $\mathbf{\Omega}$ for a Rapid Adiabatic Passage. The only system-dependent parameter is $\widetilde{\Omega}$, the peak amplitude of the chirped pulse, which can be optimized for maximal efficiency experimentally. The frequency range $\Delta\delta$, however, underlies another restriction: it must be chosen small enough to avoid excitation of other transitions. In our case, the corresponding unwanted absorption lines[20] are at least some megahertz away from the $|\mathrm{S}_{1/2}, m = +1/2\rangle \rightarrow |\mathrm{D}_{5/2}, m = +5/2\rangle$ line, which is used for the RAP. Here, the Gaussian shape of the chirped pulse points out to be advantageous again, as its frequency spectrum is very well concentrated around resonance, whereas a simple, short square pulse has frequency components

[19] The truncation of the Gaussian can be chosen such that its effect is negligible.

[20] These come from transitions between different Zeeman sublevels in $\mathrm{S}_{1/2}$ and $\mathrm{D}_{5/2}$, respectively (cf. Fig. 3.3). Additionally, each transition exhibits motional sidebands (see chapter 3.1.3) whose excitations have to be avoided.

at its inverse duration, which can be several hundreds of kilohertz away for a short π-pulse, for example[21].

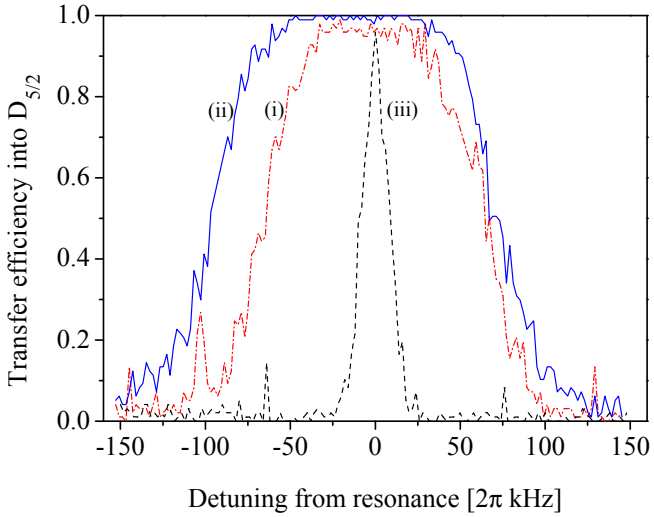

Figure 3.10: Population transfer efficiency for (i) one RAP pulse, and (ii) two subsequent RAP pulses on the transitions P1 and P2, respectively, as a function of the detuning from the atomic resonance. For the RAP pulses, this means that the chirp's center frequency is off from resonance by the given frequency. (iii) shows the efficiency of a π-pulse with a Gaussian amplitude envelope to suppress Fourier sidebands. One can clearly see the robustness of the RAP technique against frequency offsets, a very common error source in real experiments. The transfer efficiency is enhanced by the second pulse (ii) from 95 % to 99.6 %. For each experiment, the ion was first Doppler cooled and prepared in $|\uparrow\rangle$ by optical pumping. The results are not corrected for preparation errors.

A transfer probability of 95 % can be easily reached by a single passage. At this point, however, it is possible to exploit the fact that due to the Zeeman splitting, several transitions from $S_{1/2}$ to $D_{5/2}$ can be driven independently, see Fig. 3.3. Thus it is possible to perform a RAP on the P1 transition, that eventually leaves some residual population in the $|S_{1/2}, m = +1/2\rangle$ level. A second passage on the P2 transition will transfer the residual population into $|D_{5/2}, m = +3/2\rangle$ without affecting the previously shelved population (under state discrimination aspects it is irrelevant, how the population spreads over the Zeeman sublevels of $D_{5/2}$). By this combination of two passages, the transfer efficiency can be significantly increased. Finally, it should be noted that in perfect analogy, it is also possible to shelve the $|\downarrow\rangle$-population using the M1/M2 transitions.

[21] We also tested resonant, Gaussian shaped pulses. These, however, still suffer from frequency and amplitude drifts.

Laser Driven Transitions

In contrast to the optical qubit discussed in chapter 3.2.1, where the energy difference between the qubit states $\hbar\omega_0$ was in a frequency range easily accessible by an optical laser (729 nm), the energy gap of the spin qubit is of the order of some megahertz. Thus, it would in principle be possible to drive transitions between the Zeeman levels utilizing a highly stable radio frequency source, for example. A photon of such an electromagnetic field with the corresponding wavelength $2\pi c/\omega_0 \approx 100\,\mathrm{m}$, however, bears a negligible momentum compared to a photon with an optical wavelength. This implies that it is not possible to influence the motional state of the ion with a single radio frequency photon, which is, however, a key requirement for most of our experiments.

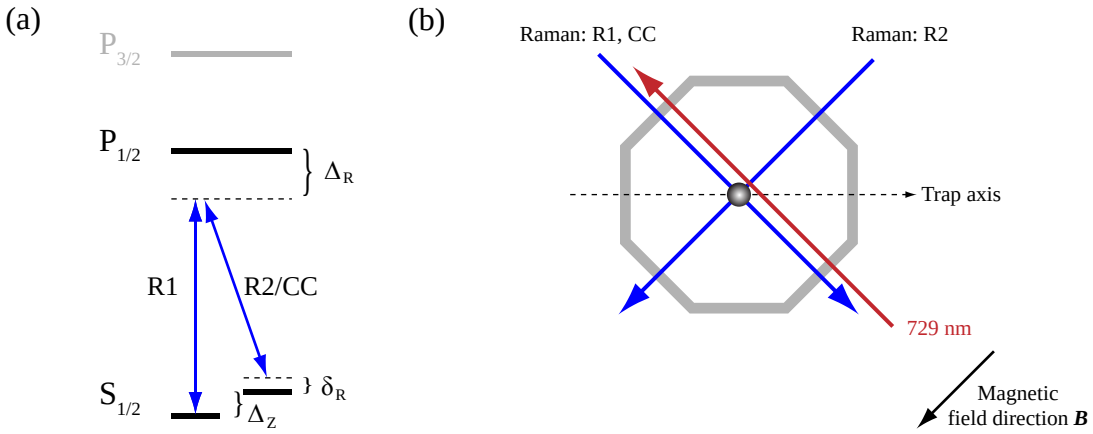

Figure 3.11: Relevant levels of the Raman transitions and beam directions. (a) Raman transitions driven by two beams; their frequency difference is δ_R, while their absolute detuning from $\mathrm{P}_{1/2}$ is $\Delta_\mathrm{R} \gg \delta_\mathrm{R}$. For $\delta_\mathrm{R} = \Delta_\mathrm{R}$, resonant transitions between $|\downarrow\rangle$ and $|\uparrow\rangle$ can be driven. The splitting of the P-levels is neglected as it is small compared to Δ_R.
(b) Sketch of the Raman and 729 nm beam directions and the magnetic field vector $\boldsymbol{B}$ (top view). R1 is horizontally polarized, parallel to $\boldsymbol{B}$. The co-propagating beam CC is vertically polarized, driving both σ^+ and σ^- transitions. R2, propagating orthogonally to R1/CC, has circular polarization.

Therefore, the spin qubit levels are not coupled by a single light field but by two optical fields driving Raman transitions between $|\uparrow\rangle$ and $|\downarrow\rangle$. The Raman process can be thought of a two photon process consisting of a combined stimulated absorption and a stimulated emission of a photon via an intermediate, virtual level (see Fig. 3.11(a)). The intermediate level must be far off the resonances of all (real) levels; otherwise, one of those could be populated in the course of the Raman process and its spontaneous decay would destroy the coherence of the process.

For resonant Raman transitions, the frequency difference of the two light fields (indicated by subscripts I and II, respectively) $\omega_{\mathrm{R}} := \omega_{\mathrm{I}} - \omega_{\mathrm{II}}$ must equal the qubit state level separation, $\omega_0 = \Delta_{\mathrm{Z}}$. In this case, the detuning $\delta_{\mathrm{R}} := \omega_{\mathrm{R}} - \omega_0$ is zero. The energy of the virtual level is counted relative to the $\mathrm{P}_{1/2}$-level and is denoted by $\hbar\Delta_{\mathrm{R}}$, where Δ_{R} is positive for blue detuning and negative for red detuning from the $\mathrm{S}_{1/2} - \mathrm{P}_{1/2}$ resonance. It is reasonable to speak of *one* Raman detuning Δ_{R} for both beams, since it is typically three orders of magnitude larger than the Zeeman splitting of the fine structure levels, $|\omega_{\mathrm{I}} - \omega_{\mathrm{II}}| \sim \Delta_{\mathrm{Z}} \ll \Delta_{\mathrm{R}}$.

Figure 3.12(a) shows coherent transitions (Rabi oscillations) between the states of the Raman qubit. These data are obtained by preparing the ion in $|\uparrow\rangle$; then, a resonant ($\delta_R = 0$), rectangular Raman pulse of duration t drives the ion into a superposition $a\,|\uparrow\rangle + b\,|\downarrow\rangle$ with complex amplitudes a and b, $|a|^2 + |b|^2 = 1$. The excitation probability $|b|^2 = P_{\downarrow}(t)$ can then be read out by the detection scheme presented above.

The results exhibit the expected periodic and coherent exchange of population between $|\uparrow\rangle$ and $|\downarrow\rangle$. The time period of the population exchange is $2\pi/\Omega_0 \approx 12\,\mu$s. The oscillations have an almost perfect contrast, which is maintained over many periods (Fig. 3.12(b)). This proves a low decoherence rate, which can be estimated to be larger than 1 ms. Another reason for the high visibility modulation is the special Raman beam configuration (CC, see below) used for the experiment, which effectively leads to $\eta = 0$. This means that there is only one Rabi frequency – that of the carrier transition – contributing to the dynamics, i.e. there is no dephasing of the signal.

Modifications to the Interaction Framework

After the preceding chapters showed how the spin qubit is initialized and read out, the following section addresses how to drive coherent transitions between the qubit states. The formalism developed in chapter 3.1 describes the interaction of a single light field with a two-level system. In the present Raman case, the situation looks at first more complicated. After all, the Raman scheme comprises two optical light fields and three energy levels (see Fig. 3.11(a)). If, however, the Raman detuning is large compared to the Rabi frequency, then the dynamics of the virtual level can be adiabatically eliminated [Mar94, Lei03] and the dynamics of the system reduces to that of an effective two-level system driven by a single light field. The reason for this is, that – due to the large detuning Δ_{R} of several gigahertz – the dynamics in the virtual level has an extremely small amplitude (small population) and is very fast compared to the time scales of the qubit state evolution. The

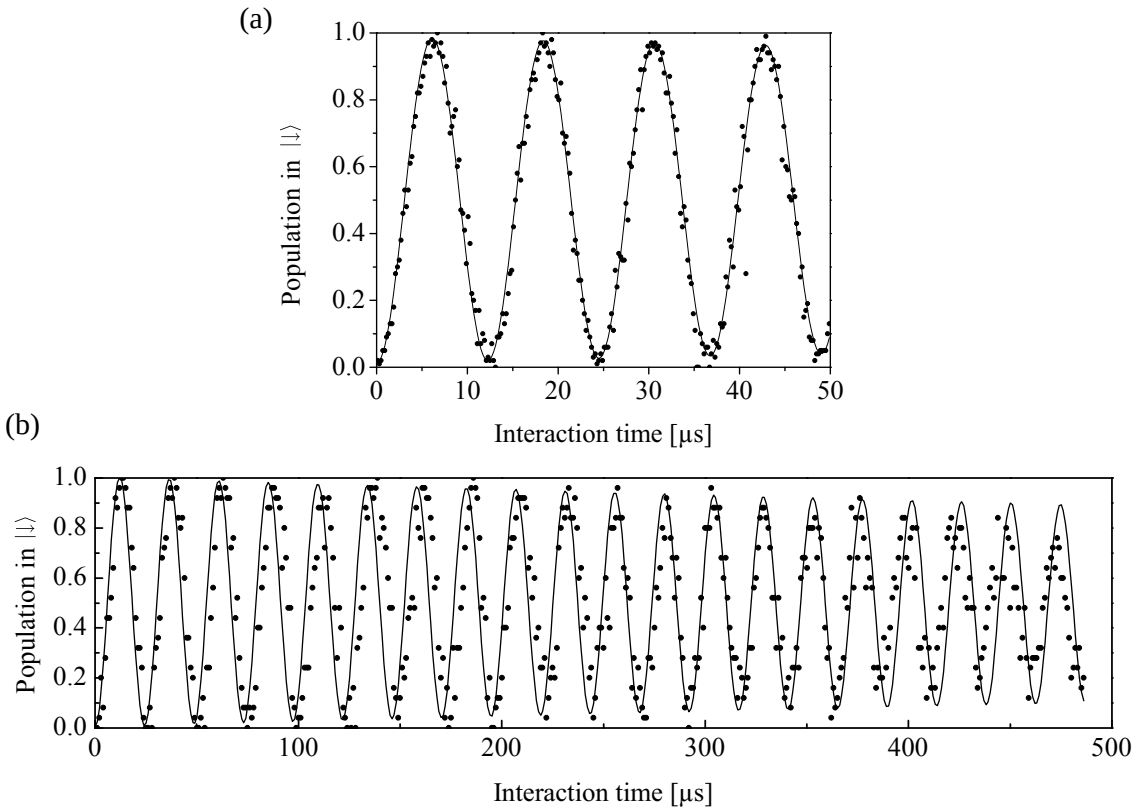

Figure 3.12: Rabi oscillations on the carrier transition in the spin qubit. Laser interaction leads to a periodic exchange in population between $|\uparrow\rangle$ and $|\downarrow\rangle$ for $\delta_{\mathrm{R}} = 0$; the quantity shown is the probability to find the ion in $|\downarrow\rangle$ as a function of the Raman pulse time, i.e. the interaction time between the light field and the ion. (a) was recorded with higher intensity and shorter time steps, while (b) shows the long-term behavior and thus the coherence of the interaction. The interaction was generated by the Raman R1/CC configuration, which has a Lamb-Dicke factor $\eta = 0$, so that motional dephasing does not occur.

"effective" field coupling the spin qubit levels can be obtained from the two Raman beams I and II following the replacement rules that are summarized in Table 3.1 and are shortly treated in the following.

The first replacement regarding the single field frequency by the frequency difference of the Raman beams represents the energy conservation law for the Raman process. The detuning from the atomic resonance is redefined accordingly.

The driving field's phase has to replaced by the phase difference of the two Raman beams. As these two beams are derived from one and the same laser source, their relative phase is fixed very well from the beginning on. Phases imprinted by modulators are electronically controllable with very high precision, so that the main contribution to relative phase

Quantity	Single beam	Raman configuration
Field frequency	ω_L	$(\omega_\mathrm{I} - \omega_\mathrm{II})$
Detuning from atomic resonance δ	$\omega_\mathrm{L} - \omega_0$	$(\omega_\mathrm{I} - \omega_\mathrm{II}) - \omega_0$
Field phase	ϕ	$(\phi_\mathrm{I} - \phi_\mathrm{II})$
wavevector $\boldsymbol{k}_\mathrm{eff}$	$\boldsymbol{k}$	$(\boldsymbol{k}_\mathrm{I} - \boldsymbol{k}_\mathrm{II})$
Lamb-Dicke parameter η	$kz_0 \cos\theta$	$2kz_0 \sin(\phi/2)$
Resonant Rabi Frequency	Ω_0	$\frac{\Omega_\mathrm{I}\Omega_\mathrm{II}}{2\Delta_\mathrm{R}}$

Table 3.1: Replacement rules for the Raman configuration. Indices I and II denote quantities of the respective Raman beam. ϕ is the angle between beam I and II and Δ_R is the Raman detuning with respect to the $\mathrm{P}_{1/2}$-level.

fluctuations originate from fluctuations in the index of refraction of the air the two beams pass on their different paths to the ion. These fluctuations can be caused by air convection, for example, and can be minimized by mechanical shielding. To avoid such influences, it is important to keep the path length that the two beams have to propagate separately as short as possible.

The two photon process can be figured as the combined absorption from beam I and a stimulated emission into beam II (or vice versa), so that the net momentum transfer to the ion is $\hbar(\boldsymbol{k}_\mathrm{I} - \boldsymbol{k}_\mathrm{II}) =: \hbar\Delta\boldsymbol{k}$ instead of $\hbar\boldsymbol{k}$ for a single beam configuration. The next replacement we have to perform therefore reads $\boldsymbol{k} \to \Delta\boldsymbol{k}$. Accordingly, the Lamb-Dicke factor $\eta = \boldsymbol{k}\boldsymbol{z}_0$ has to be replaced by

$$\eta = \boldsymbol{k}\boldsymbol{z}_0 \to \Delta\boldsymbol{k}\ \boldsymbol{z}_0 = |\Delta\boldsymbol{k}| z_0 \cos\theta. \tag{3.26}$$

When, as in our case, the beams are aligned such that $\Delta\boldsymbol{k}$ points along the trap axis, $\cos\theta = 1$. When ϕ denotes the angle between the two beams, we can write $|\Delta\boldsymbol{k}| = 2k\sin(\phi/2)$ and it follows

$$\eta = 2kx_0 \sin(\phi/2). \tag{3.27}$$

In these equations, $k = 2\pi/\lambda$ is the wavevector of a single Raman beam ($\lambda \approx 397\,\mathrm{nm}$).

The effective two-level Rabi frequency Ω for transitions between the qubit states depends both on the single beam (dipole) Rabi frequencies $\Omega_\mathrm{I}, \Omega_\mathrm{II}$ and the Raman detuning Δ_R [Win98],

$$\Omega = \frac{\Omega_\mathrm{I}\Omega_\mathrm{II}}{2\Delta_\mathrm{R}}. \tag{3.28}$$

Here, Ω_I and Ω_II describe the well-known resonant single beam Rabi frequencies on the respective dipole transitions. That is, the overall coupling between the qubit levels is

proportional to the inverse Raman detuning. This functional relationship between the coupling strength and the Raman detuning is of great importance: In spite of a large Raman detuning, high beam intensities can lead to population in $P_{1/2}$ and therefore to decoherence due to spontaneous emission. This excitation, however, scales like $1/\Delta_R^2$, in contrast to the coupling strength, which scales like $1/\Delta_R$ after Eq. (3.28). Thus, when Δ_R is increased, the probability for decoherence processes vanishes quadratically, while the coupling decreases only linearly; this, however, can be efficiently compensated for by higher laser intensities.

Raman Beam Geometry

In total, the two Raman beams have to perform a process with $|\Delta m| = 1$. Hence, both the polarization and the beam directions relative to the magnetic field are relevant for the interaction. Two different beam setups – with respect to direction and polarization – were realized in the experiment. The first beam pair (I/II)=(R1/R2) consists of orthogonal beams called R1 and R2, respectively, while for the second one (I/II)=(R1/CC), the beam called CC (*co-carrier*) co-propagates with R1. Figure 3.11(b) sketches all beam directions relative to the trap axis. R1 is aligned perpendicular to the magnetic field and has linear π-polarization (parallel to the magnetic field, so $\Delta m = 0$). R2 propagates parallel to the magnetic field and perpendicular to R1. It is circularly polarized (σ^+). CC has a linear polarization, which is orthogonal to $\boldsymbol{B}$. Due to its propagation direction perpendicular to $\boldsymbol{B}$, its polarization vector has both σ^+ and σ^- components.

The reason for the two different setups R1/R2 and R1/CC, respectively, is wellfounded by the fact that the R1/CC-configuration does not couple to the motion of the ion in contrast to R1/R2. Only by application of R1/R2, an interaction of the light with the external degrees of freedom becomes feasible. This is due to the Lamb-Dicke factor η, which vanishes for co-propagating beams, which can be read from Eq. (3.27) with $\phi = 0$. The following table summarizes values of η for the transitions of the optical qubit one the one hand and the spin qubit on the other hand. The Lamb-Dicke condition is formally fulfilled for $n \ll n_c$. For these values an axial trap frequency of $\omega_z = 2\pi \times 1.4\,\mathrm{MHz}$ was assumed.

Transition (λ)		η	n_c
Optical qubit (729 nm)		0.058	148
Spin qubit (397 nm)	R1/R2	0.21	11
	R1/CC	0	(∞)

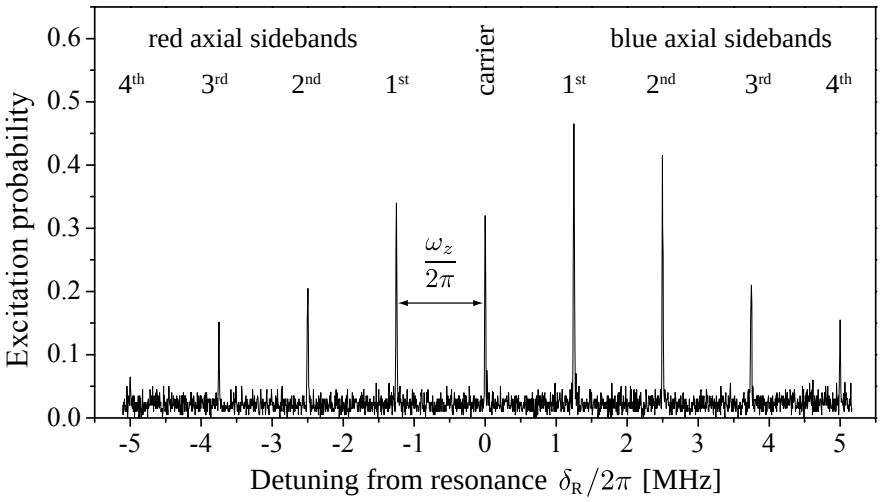

Figure 3.13: Excitation spectrum in the spin-qubit system, generated by the Raman beam configuration R1/R2. In addition to the carrier resonance ($\delta_R = 0$), which is the only one that would appear in the R1/CC case, there are sideband resonances of order m at detunings equal to integer multiples of the axial frequency, $\delta_R = m \cdot \omega_z$.

The Rabi oscillations shown in Fig. 3.12 were generated by the R1/CC beam combination. The visibility of the population transfer amounts to $\approx 99\,\%$, and there can be seen no dephasing caused by motional excitation. In contrast, the R1/R2 configuration does couple to the axial modes of the ion motion: Fig. 3.13 shows an excitation spectrum generated by R1/R2 beam combination; in addition to the carrier transition, multiple sideband resonances[22] appear at $\delta_R = m \cdot \omega_z$. The axial frequency ω_z can be measured very accurately by such an excitation spectrum.

Both R1, R2 and CC are derived from a single laser source[23], a frequency doubled and amplified diode laser system. The frequency of each of the three beams can be shifted over many megahertz by individual acousto-optic modulators (AOM). While the frequency of R1 is always kept constant, the Raman detuning δ_R of the respective beam combination is controlled through the AOM frequency of R2 or CC, respectively.

[22] Note that due to $\boldsymbol{k}_{\text{eff}} \,||\, \boldsymbol{z}$, no radial modes can be excited.

[23] TA-SHG Diode Laser by Toptica Photonics.

Chapter 4

Preparation of the System

As stated in requirement (II) in chapter 1.2, the motional state of the ion must be prepared in a thermal state. We characterize a thermal state by its mean phonon number $\overline{n}$ (see chapter 9.4.1). As our interest concentrates on states exhibiting quantum features, the preparation of low excitations $\overline{n} = O(1)$ is desired. The key to the preparation of these states is laser cooling; two techniques working in two different parameter regimes are distinguished: Doppler cooling and resolved sideband cooling.

Doppler cooling is also used for the actual "catching" of the ions out of a thermal ion beam ($\sim 300\,^{\circ}\mathrm{C}$). From this can be seen, that this cooling technique is optimal for a quick and effective reduction of the ion velocity at high energies. It is limited by the spontaneous emission of a photon from the excited state and reaches – for typical parameters – $\overline{n} \approx 10$ (which corresponds to a temperature of $\sim 1\,\mathrm{mK}$. In order to render the ion such that it is mostly found in the absolute ground state of motion ($\overline{n} < 1$), more sophisticated cooling techniques have to be applied.

The ground state of motion $|n = 0\rangle$ is not only a special case of the thermal states for $\overline{n} \to 0$; it is, of course, also the lowest Fock state of motion. Thus, it bridges, so to speak, between these two classes of states – especially from a practical, experimental point of view. Although the criterion mentioned beforehand does not require the preparation of non-thermal states, the possibility to do so is very convenient and sometimes facilitates experimental schemes. The generation of a variety of motional quantum states has been demonstrated in ion traps; see for example Refs. [Mee96, Mon96, Roo99, Lei05, Häf05a].

4.1 Doppler Cooling

Doppler cooling takes place on an atomic transition with short cycling times. In our case, the transition $S_{1/2} - P_{1/2}$ at 397 nm is used. The theoretical limit of the method given by $\beta^{-1} = \hbar\Gamma/2$ and corresponds to $\overline{n} \approx 7.5$ for $^{40}Ca^{+}$ in a trap with $\omega_z = 2\pi \times 1.4\,\mathrm{MHz}$[1]. Here, Γ is the spontaneous decay rate of the upper level ($\Gamma = 2\pi \times 22.4\,\mathrm{MHz}$ on the $S_{1/2} - P_{1/2}$ transition used).

As the trap frequency is much smaller than the scattering rate, $\omega_z \ll \Gamma$ (*weak binding*), motional sidebands are hidden within the absorption line and cannot be addressed individually. In this case, the lowest final temperature is reached for a red detuning of $\delta = -\Gamma/2$. For a different (red) detuning, the final temperature is higher [Win79]. This means, that hotter motional states can be easily accomplished by "imperfect" Doppler cooling generated by a different detuning. Such a preparation method will always rely on a suitable measurement of the ion's state of motion, which will be explained and demonstrated later in chapter 6.

Doppler cooling is one of the most time consuming steps in the experiment and usually takes $\sim 1\,\mathrm{ms}$; while this is not a problem in terms of coherence or isolation issues – since it takes place before the preparation is finished – it significantly contributes to the experimental repetition rate.

4.2 Resolved Sideband Cooling

This section describes a cooling technique [Neu78, Die89] that allows for cooling the ion almost into the ground state of motion (In Ref. [Roo99], 99.9 % ground state population has been demonstrated, for example). It is, however, based on the following requirements. First, the ion must initially be already cold enough, that the Lamb-Dicke criterion (see chapter 3.1.2) is fulfilled. That is, a preceding cooling step – e.g. Doppler cooling – has to be applied. Second, unlike the Doppler cooling, this method requires strong binding conditions, which are given when the cooling transition's linewidth Γ is small compared to ω_z. The $|S_{1/2}, m = +\frac{1}{2}\rangle \leftrightarrow |D_{5/2}, m = +\frac{5}{2}\rangle$ transition fulfills this condition very well as its natural linewidth of $\approx 1\,\mathrm{Hz}$ has to be compared with typical trap frequencies of $\approx 1\,\mathrm{MHz}$. The necessity of the strong binding requirement is obvious, since the method

[1] Strictly, this applies only to real two-level systems. Incidential decay into one of the D-levels has to be prevented by repump lasers, as has already been explained in chapter 3.2.1. These issues lead to the observation of a somewhat higher cooling limit ($\overline{n} \approx 10$).

relies on exciting the ion on motional sidebands by a narrow linewidth laser. Therefore, these sidebands must be spectrally resolvable, which is the case if $\ll \omega_z$, and if the laser linewidth is small enough ($\ll \omega_z$), too. In our case, the spectral width of the excitation is indeed dominated by the finite laser linewidth of $\approx 5\,\mathrm{kHz}$ for a weak beam.

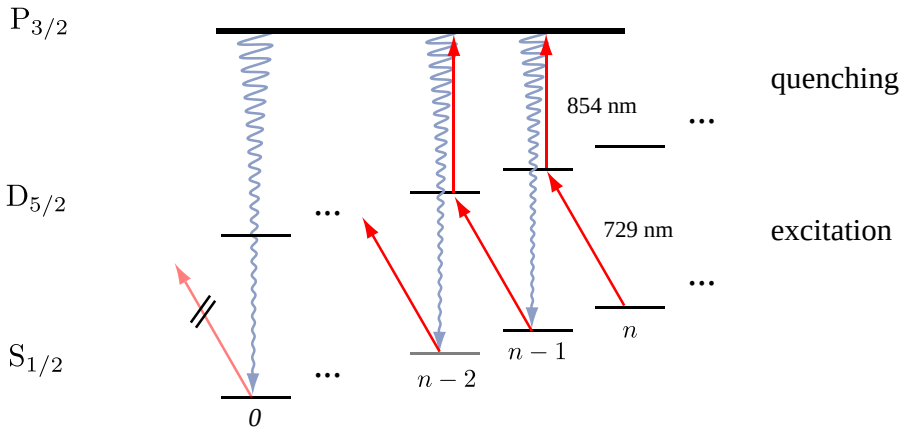

Figure 4.1: Schematic of the levels and transitions involved in the sideband cooling process. A red sideband π-pulse on the $S_{1/2} \rightarrow D_{5/2}$ transition decreases the phonon number by one. Due to the long lifetime of the D-levels, the population is quenched by a short, weak pulse at 854 nm into $P_{3/2}$, from where it quickly decays back into $S_{1/2}$. This decay happens preferably without a change in phonon number, as such processes are suppressed in the Lamb-Dicke regime.

When the above requirements are met, the laser can be tuned to the frequency of the first red sideband, $\delta = \omega_0 \quad \omega_z$. A π-pulse on this transition excites the ion from $|S, n\rangle \rightarrow |D, n \quad 1\rangle$, lowering the vibrational quantum number by one (cf. Fig. 4.1). In the Lamb-Dicke regime, the following decay back into $S_{1/2}$ happens with high probability on the carrier transition $|D, n \quad 1\rangle \rightarrow |S, n \quad 1\rangle$. The ion thus loses one phonon, while the initial internal state is restored. This means, that a cooling cycle is established. The procedure continues until all population is trapped in the "dark" state $|S, 0\rangle$, which is not affected by the laser light. This simple scheme is, however, not sufficient for a practical application, since the long lifetime of the $D_{5/2}$-state would lead to extremely long cycle periods. For this reason, the $D_{5/2}$-state is coupled to $P_{3/2}$ by irradiation with a short and weak beam at 854 nm. This effectively quenches the $D_{5/2}$-state population via $P_{3/2}$ and it ends up in $S_{1/2}$ again. As both the excitation and the quenching beam duration are on the order of a few microseconds, the whole cooling procedure consisting of 10 to 50 cooling cycles consumes about 100 to 500 μs.

Eventually, the decay from $P_{3/2} \rightarrow S_{1/2}$ may end up in the wrong Zeeman level $m = \quad \frac{1}{2}$. For that reason, a weak σ^+ polarized repump beam (397 nm) is applied from time to time

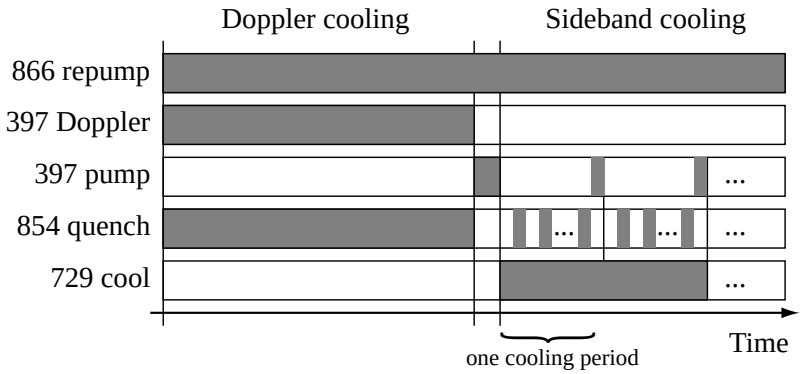

Figure 4.2: Timing schematic for performing pulsed sideband cooling. After Doppler pre-cooling and a short optical pumping pulse at 397 nm, preparing the ion in $|\mathrm{S}_{1/2}, m = +\frac{1}{2}\rangle$, the pulsed excitation and quenching of the $\mathrm{D}_{5/2}$-level population takes place. Instead of switching both excitation (729 nm) and quenching (854 nm) laser, only the latter is operated in a pulsed mode, while the former continuously irradiates the ion. This is legitimate, since the interaction with the quenching laser completely freezes the coherent dynamics caused by the cooling laser. This effectively implies a pulsed interaction with the excitation laser. After a certain number of cooling cycles, a weak pumping pulse (397 nm) is applied to avoid population trapping in $|\mathrm{S}_{1/2}, m = -\frac{1}{2}\rangle$. We typically apply five periods, each comprising ten excitation/quenching cycles.

to avoid population trapping. As this laser drives a dipole cycling transition, it must be strongly attenuated, short ($\approx 5\,\mu$s) and applied as scarcely as possible to avoid heating by fluorescence scattering. Figure 4.2 shows a schematic timetable[2].

As we have seen in chapter 3.1, the duration of a π-pulse depends on the phonon state n. This means, that the duration of the $|S, n\rangle \rightarrow |D, n-1\rangle$ pulses should be ideally adapted to the current mean phonon number during the cooling process. In the experiment, the duration of the π-pulses was increased stepwise to compensate for decreasing coupling strengths as the ion becomes cooler.

With this cooling method, it is possible to generate states that are found in the ground state of motion with a probability of far over 98 % [Die89]. As for our purposes, we are mainly interested in thermal states with $\overline{n} \sim 1$, it provides an optimal method to prepare the initial state. The lowest temperature reached in the micro-trap amounted to $\overline{n} \approx 0.2$, higher values can be easily achieved by interrupting the procedure after a certain number of excitation pulses.

[2] The described cooling mechanism is for obvious reasons called *pulsed* sideband cooling, in contrast to *continuous* cooling, where the ion is uninterruptedly irradiated by the same lasers.

4.3 System-Bath Coupling

This section is intended to shortly describe another approach to prepare a thermal state, that in some sense inverts the previous methods: while so far, we considered preparing the thermal state by cooling, it is also possible to reach the desired state by heating up a previously cold state. This cold, initial state can be, for example, a state with $\overline{n} \approx 0$ originating from sideband cooling. Any ion trap exhibits a natural heating rate that mainly stems from coupling between the charged ion and fluctuating electric fields on the electrode surfaces (see also chapter 7.2). This interaction leads to a motional heating of the confined ion. The mean phonon number $\overline{n}$ of the thermal state is thereby found to increase linearly with time. Typical heating rates are on the order of one phonon per millisecond, depending on trap characteristics. As the heating rate can be determined accurately in the experiment, and the heating time can be implemented very easy, this offers a perfect means to realize small changes in temperature. Additionally, the effect is well reproducible and involves minimal experimental effort.

Apart from the "natural" heating, it is possible to introduce artificial sources of noise contributing to the overall heating. Electric field noise generated by time-dependent voltages applied to a trap electrode can be adjusted roughly in amplitude by a proper choice of the distance between the electrode and the ion, and very accurately by electronic means. Even the noise spectrum can be easily controlled when the noise is generated by an electronic device, and multiple noise sources are feasible.

4.4 Multiple Ions and Mixed Strings

Several different cooling techniques exist that allow for preparation of a low thermal state of the ion [Ste86, Ita95, Mon95, Esc03]. Especially when it comes to the cooling of longer linear strings of ions, other schemes than the ones presented here may become advantageous. A method based on the phenomenon of electromagnetically induced transparency [Mor00, Sch01b], for example, allows for efficient cooling of ion strings in spite of their complicated mode spectrum (N ions in a linear trap exhibit N different axial oscillation modes. Each of these modes has to be cooled). Then, even long, mixed ion strings, i.e. those consisting of different ion species, can be cooled.

As for mixed ion strings, it is possible to make use of the sympathetic cooling effect [Bow99]. To this end, $^{40}Ca^{+}$-ions are directly cooled by conventional techniques, while those ions which are not directly affected by the laser light ("dark ions") are indirectly cooled via

the Coulomb interaction with the cold $^{40}Ca^{+}$-ions. This approach helps to overcome the necessity to provide many different laser wavelengths that would be necessary to cool the different species directly (some ion species cannot be directly laser cooled at all, due to the lack of suited transitions, or the needed laser wavelengths). A recent application of sympathetic cooling in the quantum information context is described in [Hom09] and [Jos09], for example, where mixed strings consisting of $^{9}Be^{+}$ and $^{24}Mg^{+}$ reach near-ground state population, while only the $^{24}Mg^{+}$-ions are directly (Doppler and sideband) laser cooled.

Chapter 5

Transformations of the Potential

The transformation of the external potential – as it was discussed in the context of the third quantum thermodynamics criterium (chapter 1.2) – is performed in a controlled way in order to act on the system's state. This chapter addresses the question how such transformations can be implemented in the trapped ion approach. In our case, time-dependent electric potentials interacting with the charged particles are used to realize these transformations. For a start, it is helpful to neglect all internal structure and to describe the ion as a pointless particle with charge e in a one-dimensional electric potential. The general motional Hamiltonian

$$H_{\mathrm{mot}} = \frac{p^2}{2m} + e\ \phi(z,t) \tag{5.1}$$

models this situation. Of course, the potential is a function of the axial position z. The time-dependence, however, is a novel feature within this work. Changes in the electric potential $\phi(z,t)$ affect the motional state of the ion. Such a change is normally performed by altering a system parameter $\lambda(t)$ in a controlled manner in time, $\phi(z,t) = \phi_{\lambda(t)}(z)$, while $t \in [0,T]$. For the realization of such potential transformations, it is necessary to be able to generate arbitrary electric potentials $\phi(z,t)$.

The following section explains how a desired potential can be realized by applying suitable voltages to the trap electrodes. It is a nontrivial task to find those voltages generating exactly the right potential configuration $\phi(z)$, because it postulates a detailed knowledge of the trap geometry and the electric fields generated by the electrodes.

In sections 5.2-5.4, a selection of applications of these techniques and the associated, resulting potential transformations will be presented.

5.1 Generation of Arbitrary Potentials

This chapter devises the theoretical basis for the calculation and simulation of arbitrary trapping potentials in a Paul trap. The presented methods are very general and their applicability in terms of trap geometry, for example, is not at all restricted to the demonstrated ones. Apart from the pcb-trap and the micro-trap design (see chapter 9.1), they have also been used to investigate two-dimensional trap structures, for example.

5.1.1 Simulation of Electrode Geometries

We consider an axial electric potential at a fixed time $\phi(z)$, i.e. here, we consider the static problem. This potential originates from electric charges on the trapping electrodes. Each electrode $i = 1, \ldots, N$ is thereby kept at a constant voltage V_i. The potential can therefore be written as a linear superposition of these voltages. If the z-axis is subdivided into M discrete points z_j $(j = 1, \ldots, M)$, we can write the potential at any of these points as

$$\begin{aligned} \phi_j := \phi(z_j) &= \sum_{i=1}^{N} A_{ij} \cdot V_i \\ \Leftrightarrow \qquad \boldsymbol{\phi} &= A\, \boldsymbol{v}. \end{aligned} \tag{5.2}$$

with $\boldsymbol{\phi} = (\phi_1, \ldots, \phi_M)^T$, $\boldsymbol{v} = (V_1, \ldots, V_N)^T$ and with the electrode potential matrix A with entries A_{ij}. This matrix describes the influence of the i-th electrode on the overall potential at position z_j. Each row i of A can be interpreted as a position-dependent function describing the potential generated by the i-th electrode (in units of V_i), when all other electrodes $i' \neq i$ are grounded ($V_{i'} = 0$). The matrix A is independent from a specific voltage configuration and is solely given by the trap geometry, i.e. the shape and size of the electrodes (the electrode material is treated to be perfectly conducting). This is a very good assumption for the used gold coating. It is, however, possible to take dielectric materials into account, too, see Ref. [Sin10]).

Then, the potential generation can be logically divided into two parts: First, the matrix A can be calculated independent from voltage constraints and independent from the desired potential. And second, for each desired potential $\boldsymbol{\phi}$, there has to be found a set of voltages $\boldsymbol{v}$ fulfilling the matrix equation (5.2).

As for the first problem, today's technological state of the art allows for segmented trap geometries in such a geometric complexity that conventional simulation techniques like the finite element method (FEM) fail. This is mainly due to the fact that precise discrete

models of complex geometrical structures require a fine spatial meshing. This, however, entails a strongly increasing number of geometric primitives, and most algorithms offer a too bad complexity scaling with this number.

We were able to overcome this obstacle by solving the boundary element problem of the segmented trap design. That is, all electrode surfaces (in contrast to the whole electrode volume, for example) are subdivided into small areas with a uniform surface charge [Poz02]; these surface charges can be calculated from the respective, given electrode voltages V_i, which are unity for segment i and zero for all others. This calculation scales like the third power of the number of surface elements, but can be significantly accelerated by the fast multipole method [Gre88, Nab94]. This method speeds up matrix inversion problems occurring during the calculation to iteratively obtain the solution. Details can be found in Refs. [Sin10, Car88, Gre97, Car99, Nab94, Gum05, She07], for example. Thus, the problem can be solved with an effort which increases only linearly with the number of surface elements, and allows for an efficient calculation of the matrix A.

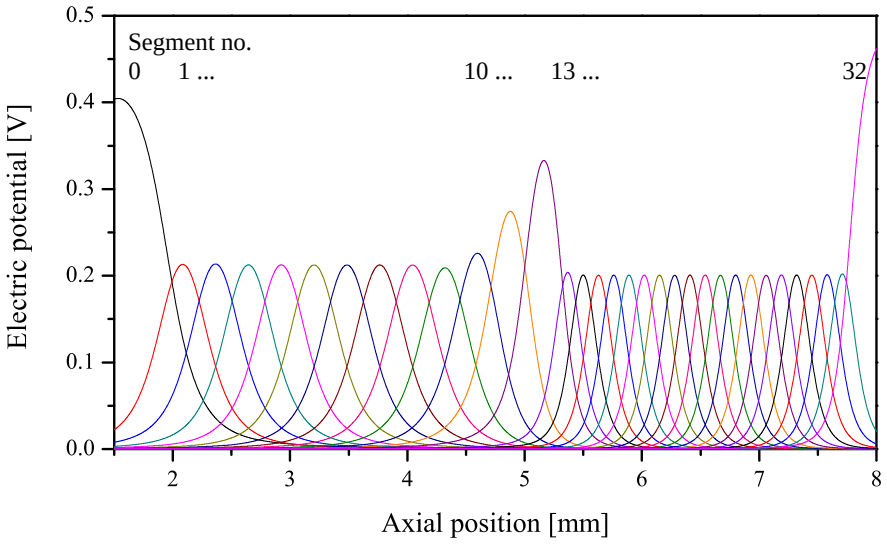

Figure 5.1: Potentials of the 33 opposing electrode pairs 0 to 32 calculated on the axis of the micro-trap (cf. chapter 9.1.1). While each of these pairs is biased to 1 V, the others are grounded. The different shapes of the graphs result from both the different widths of the respective electrodes, and their distances from the axis (see text for further details).

Figure 5.1 shows the results of the calculation for the micro-trap (see also section 9.1.1). Hereby, it was assumed that opposing electrode pairs are biased to the same voltage (1 V) and all others are grounded. Each of the graphs represents a row of the matrix A. Thus, the data depicted in Fig. 5.1 contain the full information about the influence of the trap geometry on the electric fields. One can clearly recognize the electrode widths by

the heights and spatial extents of their ranges of influence; the different trapping zones are also clearly visible: in the *processing zone* on the right hand side, the electrodes are narrower but have a smaller distance to the trap center than on the left hand side (*loading zone*). As a rule of thumb, the bell curve shaped region of influence of one electrode pair has a (half maximum) extent of about its width to each side of its maximum. Such results are very helpful for the development of new trap designs, see for example Ref. [Sch06].

5.1.2 Calculation of Electrode Voltages

When the matrix A, that contains all information pertaining to the trap geometry, is known, it is still an open question, which voltages $\boldsymbol{v} = \{V_i\}$ must be applied to obtain a specific potential $\phi(z)$. Any voltage vector $\boldsymbol{v}$ solving the matrix equation (5.2) is a solution to this problem, so in principle all that has to be done is inverting the matrix A. Several circumstances make this straight forward approach unfeasible: First, there is mostly no exact solution to the problem, because $\boldsymbol{\phi}$ is not an exactly realizable potential (note that in general $M \gg N$). In those cases, an approximate solution has to be found. Usually, the potential's exact shape is only interesting in a very local vicinity around the ion. The potential in trap regions far away from the ion may deviate from the exact shape. Secondly, when a specific electrode's contribution becomes insignificant, because it is far apart from the ion, its voltage is ill-determined. These cases have to be treated adequately by the algorithm.

The way the inversion problem was solved begins with a singular-value decomposition of the matrix A to identify its critical, singular values. Hereby, the real $N \times M$ matrix A is decomposed into the product

$$A = USW^T, \tag{5.3}$$

of the unitary matrices U $(N \times N)$ and W $(M \times M)$, and the diagonal $N \times M$ matrix S with non-negative entries $s_k, k = 1, \ldots, \min(M, N)$. This decomposition is part of many standard numerical libraries and can be performed for any input matrix A. The wanted inverse can then be written as

$$A^{-1} = WS^{-1}U^T. \tag{5.4}$$

This step is numerically trivial, because the inverse of the unitary matrices is simply given by their matrix transposes and the entries of S^{-1} are given by $1/s_k$. Now, the advantage of the decomposition becomes obvious, since small values of s_k indicate an (almost) singular, critical value. A simple way to overcome these singular values would be to introduce a cut-off for their diverging inverse values. Instead, the Tikhonov regularization [Tik77] method

implies a more clever, steady behavior by making the displacement $1/s_k \rightarrow s_k/(s_k^2 + \alpha^2)$. The latter expression behaves like the original $1/s_k$ for large values $s_k \gg \alpha$, has its maximum at $s_k = \alpha$ and tends to zero for small, critical values $s_k \ll \alpha$, cf. Fig. 5.2. From this we can see, that the choice of α is a compromise between exactness and boundedness of the results. For $\alpha = 0$, the exact solution (if existent) is obtained, whereas large values of α guarantee small inverse values and thus bounded voltage results.

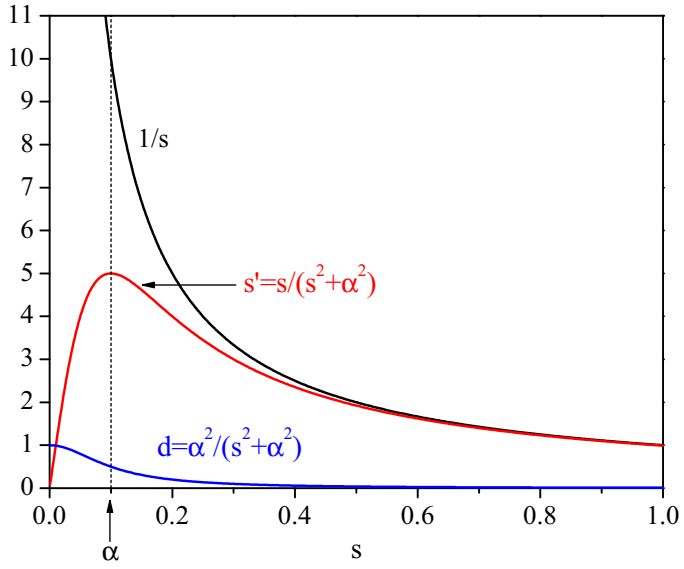

Figure 5.2: Graphs of the regularization terms for $\alpha = 0.1$ [Sin10]. The Tikhonov term (red) avoids divergence for $s \rightarrow 0$ in contrast to the exact $1/s$-term (black). The asymptotic behavior for $s \gg \alpha$, however, is identical. The second regularization term (blue) vanishes quadratically for $s \gg \alpha$, i.e. for uncritical values, but steadily approaches unity for the singular case $s \rightarrow 0$.

We label the regularized quantities with index α in order to avoid mistaking them for the exact expressions. Then, the approximate solution for $\boldsymbol{v}$ is

$$\boldsymbol{v}_\alpha = W S_\alpha^{-1} U^T \boldsymbol{\phi}, \tag{5.5}$$

with S_α^{-1} being the regularized matrix with entries $s_k/(s_k^2 + \alpha^2)$.

Before the problem of finding an optimal α is addressed, another constraint regarding time-dependent voltages, i.e. series of voltage configurations, has to be accounted for. In order to avoid voltage jumps between two consecutive time steps, we postulate that each voltage should be as close to its previous value as possible. This is achieved by modifying Eq. (5.5) by

$$\boldsymbol{v}_\alpha = W S_\alpha^{-1} U^T \boldsymbol{\phi} + W D_\alpha W^T \boldsymbol{v_0}, \tag{5.6}$$

where $\boldsymbol{v_0}$ represents the previous voltage set. The second term in Eq. (5.6) contains a diagonal matrix D_α with entries $d_k = \alpha^2/(s_k^2 + \alpha^2)$. d_k tends to zero for $s_k \gg \alpha$, so that

uncritical voltages are only affected little by the second term, cf. Fig. 5.2. For all critical voltages indicated by a value $s_k \ll \alpha$, however, the first term in Eq. (5.6) vanishes due to the regularization replacement, and what remains is the contribution from $\boldsymbol{v_0}$, since then, $d_k \approx 1$. Here, the choice of α determines how strong the algorithm tries to generate similar voltages in a (time) series of voltage sets.

The algorithm described above minimizes $||A\boldsymbol{v}_\alpha - \boldsymbol{\phi}||^2 + \alpha||\boldsymbol{v}_\alpha - \boldsymbol{v_0}||^2$ with respect to the Euclidian norm for given A, $\boldsymbol{\phi}$, $\boldsymbol{v_0}$ and α. That is, the potential $\boldsymbol{\phi}$ is reproduced as good as possible under the constraint that solutions similar to the previous one are preferred. What remains is to find the proper value of α. Doing so, one has to find a compromise between the boundedness of the voltages and their mentioned continuity. Under practical circumstances requiring $|V_i| \leq V_{\max}$ for some maximal voltage $V_{\max}$, α can be iteratively increased to fulfill this constraint on the one hand, and to obtain as continuous voltage sets as possible, on the other hand.

In chapter 9.2, the hardware-side demands of generating fast, synchronous and parallel trap voltage updates is discussed, and the utilized solution is described, too.

5.2 The Transport Transformation

As a first example of a controlled potential transformation we implemented the Hamiltonian

$$H_{\text{mot}} = \frac{p^2}{2m} + \frac{m}{2}\,\omega_z^2\,\left(z - z_0(t)\right)^2 . \tag{5.7}$$

It describes the familiar harmonic confinement of constant frequency ω_z, see for instance Eq. (3.4). The position of the potential well, however, is now no longer static but moves along the trap axis.

The system parameter $\lambda(t) \equiv z_0(t)$ gives the time-dependent position of the harmonic potential minimum. In the case of a slow, adiabatic change of $z_0(t)$ on timescales large compared to ω_z^{-1}, a cold ion will always reside in the minimum of the potential well throughout the transformation and its (center of mass) position will follow $z_0(t)$ (see Fig. 5.3). For that reason, this kind of transformation can be used to realize a transport of the ion along the trap axis, following $z_0(t)$, which is called *transport function*. When the transport function is linear in time,

$$z_0(t) = z_0(0) + \frac{t}{T}(z_0(T) - z_0(0)) \tag{5.8}$$

and the transport is adiabatic, i.e. $T \gg \omega_z^{-1}$, then the ion is shuttled with constant velocity from $z_0(0)$ to $z_0(T)$. Other transport functions are also possible, and can be advantageous

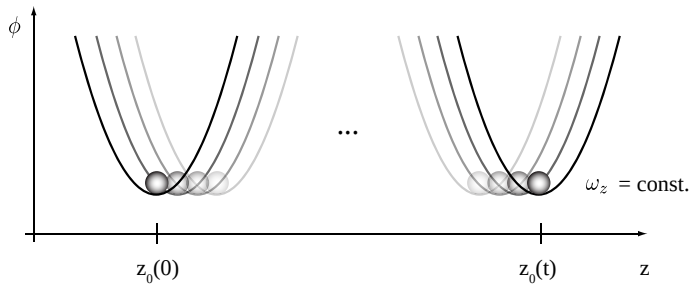

Figure 5.3: Illustration of the transport transformation. The electric potential experienced by the ion is parabolic at all times with constant curvature ω_z. The potential is shifted as a whole along the trap axis, with $z_0(t)$ describing the time-dependent position of the potential minimum. When the ion remains in the potential minimum throughout the process – which is the case for slow transformations – then $z_0(t)$ defines the classical trajectory of the ion.

over the linear transport pertaining to unwanted motional excitation by the transport. For slow transports, however, the differences are negligible.

Shuttling Ions

We denote by $\{V_i\}^{(z_0)}$ a set of electrode voltages that results in a harmonic potential with its minimum at position z_0. In the experiment, we pre-calculated such voltage sets for all values of z_0 ranging from the very left to the very right end of the trap. Figure 5.4(a) shows these voltages $\{V_i\}^{(z_0)}$ as functions of z_0. One can clearly see that the constraint $|V_i| \leq 10\,\mathrm{V}$ is obeyed and that each voltage varies fairly smoothly. This is important because very high frequencies, kinks or even unsteady jumps are not exactly realizable by the electronics. Figure 5.4(b) shows the simulated axial potential $\phi(z)$, resulting from voltage sets corresponding to two different positions z_0. A quadratic fit in the vicinity of the potential minimum yields the simulated trap frequency $\omega_{\mathrm{sim}}(z_0)$[1]. The two examples also demonstrate that the trap depth exceeds 1 eV for all positions z_0. This is sufficient to prevent ion loss even for fast transports.

To realize the Hamiltonian Eq. (5.7), it would suffice to produce potentials with static frequency ω_z only. To allow for a more general discussion[2], the frequency may also vary with the position, i.e. $\omega_z = \omega_z(z_0)$. Indeed, the trap frequency was kept *almost* constant.

[1] The fit also yields the simulated minimum position and the offset position $\phi(z_0)$.

[2] The reason for this will become clear in chapter 5.2.1.

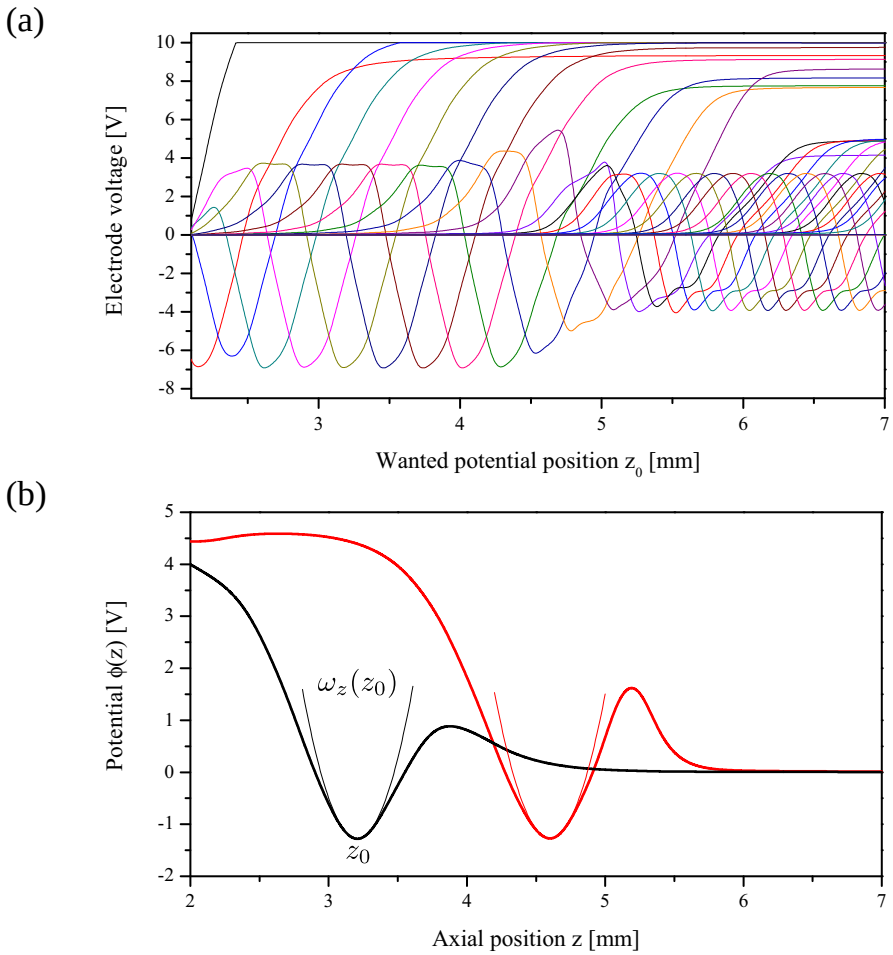

Figure 5.4: (a) Electrode voltages $\{V_i\}^{(z_0)}$ for all relevant values on the z-axis. For each parameter z_0, a harmonic well with its minimum at z_0 and a frequency of $\omega_z(z_0)$ results from applying the voltages to the trap electrodes. The trap frequency $\omega_z(z_0)$ is obtained from a quadratic fit (thin lines) to the simulated potential $\phi(z)$ (thick lines), as shown in (b) for two different values of z_0 (black and red color, respectively). The deduced parameters are $z_0 = 3.205\,\mathrm{mm}$ ($4.601\,\mathrm{mm}$), $\omega_z/(2\pi) = 1.49\,\mathrm{MHz}$ ($1.46\,\mathrm{MHz}$) and $\phi(z_0) = -1.27\,\mathrm{V}$ ($-1.27\,\mathrm{V}$) for the potential on the left (right) hand side.

With the calculations presented above, one finally ends up with the mapping[3]

$$(z_0, \omega_z(z_0)) \leftrightarrow \{V_i\}^{(z_0)}, \tag{5.9}$$

i.e. for each axial position given, exactly those voltages can be applied that result in a

[3] In fact, the real potential can have a non-zero offset voltage $\phi(z_0) \neq 0$, resulting in an additional term in Eq. (5.7), which means that it is dispensable as long as it is kept constant. In the experiment, such an offset voltage must be applied to keep the ion in the rf node (cf. chapter 2.1). It is, however, possible to generate the potentials with constant $\phi(z_0)$ and hence this parameter is omitted from the following discussion.

trap at z_0 with the right frequency $\omega_z(z_0)$. The voltage sets were calculated on a spatial $5\,\mu$m-grid. For arbitrary, in-between positions, the voltages were linearly interpolated.

In order to realize a transport of the ion between two positions $z_0(0)$ and $z_0(T)$, it is then possible to subsequently apply the voltage sets corresponding to $z_0(t)$, with $t = 0,\ \Delta t,\ 2\Delta t,\ \ldots,\ N \cdot \Delta t := T$ implying a transport in N steps.

5.2.1 Validation of the Potentials: Remote Spectroscopy

The task to realize potentials of the form $\phi(z,t) = \frac{m}{2e}\omega_z^2(z - z_0(t))^2$ giving rise to the Hamiltonian Eq. (5.7) is an optimal opportunity to test the voltage generation techniques described in chapter 5.1. This is for two simple reasons: First, the potentials have a convenient shape, i.e. their simple, parabolic form is completely defined by the two parameters $z_0(t)$ and ω_z and they can be easily calculated. The second and foremost benefit is, that these harmonic trap frequencies can be measured with high accuracy by spectroscopic means. The harmonic trap frequency experienced by the ion is, of course, directly given by the resonance frequencies of the carrier and the first red motional sideband. In the following section, it will be shown how transport potentials can be validated by a highly accurate and versatile method.

Remote Spectroscopy Scheme

In order to measure the trap frequency $\omega_z(z_P)$ at some probing position z_P on the trap axis spectroscopically, it is necessary to measure an excitation spectrum of a narrow linewidth transition there. In our case, this is most easily done by exciting the $S_{1/2} \rightarrow D_{5/2}$ transition by the 729 nm laser. As the probing positions can be several millimeters apart from the initial trapping position, all lasers necessary for cooling, pumping, excitation and readout of the ion's state plus all imaging optics would have to be moved and realigned for almost each new position. This would be a very tedious procedure. Instead, we developed a measurement scheme, that requires the relocation of the excitation (729 nm) laser only. All other components remain at the same position, where trapping, preparation and readout are well-established.

The application of the measurement scheme presented in the following is also a proof of principle of a much more general application of the ion as a local field probe. In our case, the electric field, which gives rise to the confinement of the ion, is probed. In general, it is possible to precisely investigate arbitrary fields following this scheme [Hub10].

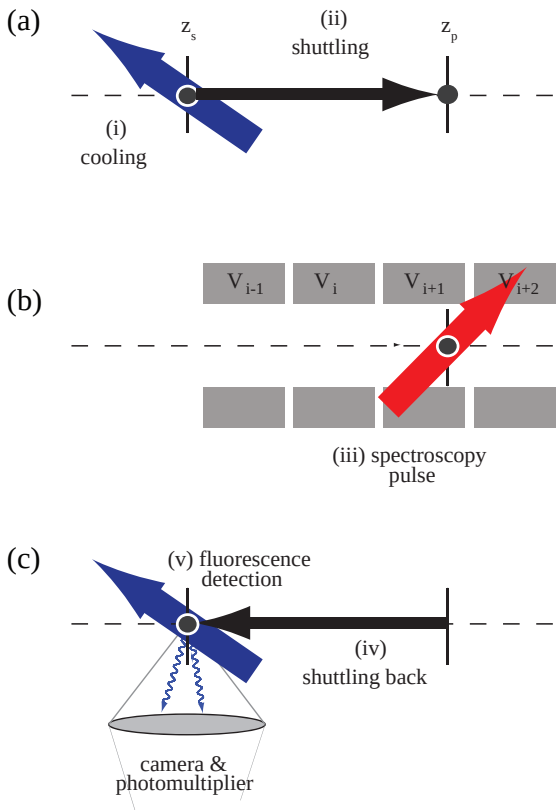

Figure 5.5: Illustration of the measurement procedure: (i) Cooling and preparation of the ion at starting position z_0 and (ii) transport of the ion to the probing position z_p. There, a spectroscopy pulse with a certain detuning excites the ion (iii). After shuttling the ion back (iv), the quantum state of the ion is read out (v). After many repetitions for different detunings, an excitation spectrum of the ion at z_p is obtained, from which the trap frequency $\omega(z_p)$ can be deduced.

The measurement scheme is illustrated in Fig. 5.5. It consists of the following steps:

(i) An initial voltage configuration is chosen to trap and cool the ion at the starting position $z_s := z_0(0)$. All lasers necessary for cooling, repumping, state preparation and detection are aligned to interact with the ion at this position. Additionally, z_s is the position where fluorescence emitted by the ion can be detected by a photomultiplier tube and a camera.

(ii) The ion is shuttled to the probing position $z_p := z_0(T)$. This happens in the way described above by subsequently applying the voltage sets $\{V_i\}^{(z_0(t))}$ with $t = 0$ to T.

(iii) A spectroscopy pulse is applied at the probing position z_p. Now, the voltages are exactly $\{V_i\}^{(z_p)}$. Resting at z_p, the ion is exposed to a spectroscopy pulse of fixed duration (100 μs) and frequency $f = \delta/(2\pi)$. This excites the ion into the upper state $|D_{5/2}\rangle$ with a probability $P(f)$.

(iv) The ion is shuttled back to z_s, inverting step (ii).

(v) Having arrived back at the starting position, the state of the ion is read out by illuminating it on the cooling transition. Whenever fluorescence at a level above a certain threshold is detected, the ion is found in the ground state $|S_{1/2}\rangle$, while a low fluorescence level indicates that the ion has been excited to the state $|D_{5/2}\rangle$.

The excitation probability for a specific detuning $P(f)$ at the remote position z_p is obtained by averaging over many repetitions of steps (i) to (v). By varying f, a spectrum of the quadrupole excitation at the remote position is obtained without moving any lasers or imaging optics but the spectroscopy laser used in step (iii).

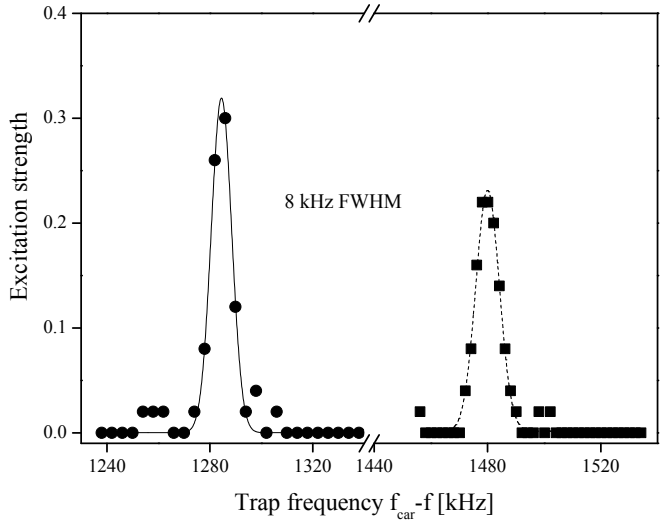

Figure 5.6: Resonances of the first red sideband excitation on the $S_{1/2} \rightarrow D_{5/2}$ transition. The two peaks are measured at different trap positions along the trap axis. The resonance frequencies are given with respect to the carrier resonance f_{car}, so that the trap frequency at the respective trap position can be read off. The full width at half maximum of the peaks equals 8 kHz and determines the measurement accuracy. The different peak heights stem from slightly different field intensities experienced by the ion.

The frequency difference between the red sideband and the carrier transition yields the angular trap frequency, $\omega_z = 2\pi(f_{\mathrm{car}} - f_{\mathrm{rsb}})$. Figure 5.6 shows two rsb resonance peaks obtained at different positions within the trap volume. The carrier frequency does not depend on the trapping potentials; it is therefore sufficient to measure it once. To exclude carrier frequency changes caused by magnetic field or cavity drifts, it was checked at different trap positions during the measurements. It turned out that f_{car} drifted on scales almost negligible for the measurement ($< 10\,\mathrm{kHz}$ per hour).

It is noticeable that each iteration cycle (i)-(v), including two ion transports of duration T, results – due to the binary nature of the projective readout – in exactly one bit information about the spectrum. Therefore, thousands of transports, each relying on the calculated potentials, are performed for the determination of one frequency $\omega(z_p)$. The transport, however, can be performed so fast ($\sim 100\ \mu$s) that its contribution to the overall experiment duration is secondary; this is still dominated by cooling and detection times ($\sim$ milliseconds).

Implementation and results

To implement the measurement scheme, we first calculated voltage sets $\{V_i\}^{(z)}$, where z covers the whole extent of the trap in steps of 5 μm. For arbitrary positions, the voltages can be interpolated. Each set results in a certain, wanted frequency $\omega_{\mathrm{sim}}(z)$. That means that for each arbitrary position z in the trap, there can be found a set of voltages resulting in a potential with its minimum at z and with trap frequency $\omega_{\mathrm{sim}}(z)$. Then, in order to shuttle the ion, we simply subsequently apply the voltage configurations for $z = z_0 \ldots z_p$.

The calculated voltages are tested with high axial resolution, i.e. in small steps of z_p, in two far distant regions of the trap. Doing this, both small local deviations are detectable and the stability over the whole trap structure can be tested for. To see a variation in $\omega(z_p)$ when increasing z_p, it is of advantage that small variations of the trap frequency around its means value occur. This is a reliable way to ensure that the ion in fact probes the remote position, and does not get "stuck" somewhere on its way.

Figure 5.7 shows the expected, simulated trap frequencies together with the measured ones. The data are in excellent agreement with the predicted frequencies. On both ends of the investigated trap structure, the predicted course of $\omega_{\mathrm{sim}}(z)$ is confirmed within the spectroscopic accuracy of 0.6%. The mean deviation of all measured data points is only 0.73%. Note that the solid line shown in Fig. 5.7 is based solely on geometric data from a technical drawing of the trap; there is no free parameter being used to match the simulations with the measurement.

These measurements render the whole potential generation process – including simulations, voltage calculations and voltage generation – as very reliable. They showed, that we can confide in numerical predictions on a percent level. The potential generation tools can hence be used in more complicated and involved applications.

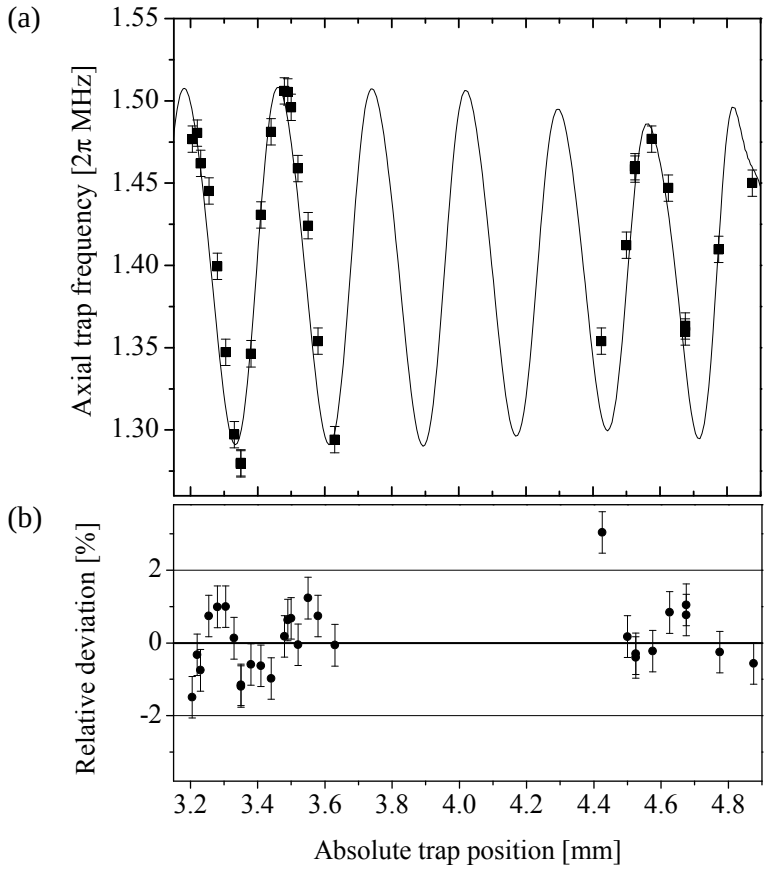

Figure 5.7: (a) Harmonic trap frequency as a function of the position along the trap axis. The electrode voltages were calculated and applied such that the trap frequency shows a small oscillatory variation around a mean value of about $2\pi \times 1.4\,\mathrm{MHz}$ to see the ion proceed along the axis. The solid line shows the frequency of the wanted harmonic potential $\omega_{\mathrm{sim}}(z)$. The data points are the spectroscopically measured, real trap frequencies $\omega_z(z)$. The error bars show the uncertainty due to the finite resonance linewidth. (b) Relative deviation of the measured from the simulated frequency $|\omega_z(z) - \omega_{\mathrm{sim}}(z)|/\omega_{\mathrm{sim}}(z)$.

5.2.2 Non-Adiabatic Transport Potentials

The transports implementing the remote spectroscopy scheme were realized with a linear transport function, and the transport time was much larger than an oscillation period of the ion within the local potential. This was advantageous, since the motional state of the ion is to be heated, or rather excited, as little as possible by the shuttling procedure; otherwise, a decline in laser excitation might occur.

In most cases, however, it is desirable to perform the transport as fast as possible. From a thermodynamic point of view, a fast transformation of the potentials is necessary to drive the system far out of equilibrium. For instance, a quick displacement of the potential will

transform a thermal state into a state with a non-equilibrium phonon distribution, while a slow, quasi-static transformation does not alter the state at all (within its moving frame).

For scaling up the linear ion trap quantum computer approach [Cir95], it is also necessary to be able to shuttle the carriers of information – the ions – around between different processor and memory regions [Kie02]. The time consumption of these shuttling processes, compared to the actual information processing tasks (quantum gates) is tremendous. Estimates hint that the ion is by far most of the time being shuttled around. Hence, it is clear that not only reliable, but also very fast transport processes have to be realized in this context.

As already mentioned, the timescale of the problem is determined by the "force" keeping the ion at rest, i.e. by the harmonic oscillator frequency. On timescales $T \gg \frac{2\pi}{\omega_z}$, the processes can be regarded quasi-static. Transports have been investigated experimentally in the context of scalable quantum computing [Hen06, Bla09], and can be realized with high fidelity; all these transformations, however, were performed in the adiabatic regime[4]. The following section investigates what happens, when the transformation time T is on the order of the oscillator's time period, $T = O(\frac{2\pi}{\omega_z})$. For this purpose, it is convenient to define the dimensionless quantity

$$\tau := T \cdot \frac{\omega_z}{2\pi} \tag{5.10}$$

giving the transport duration in units of one ion oscillation period. We will present theoretical investigations first, and then quantitative measurement results of non-adiabatic ion transports.

For this purpose, transports of the same kind as utilized for the remote spectroscopy scheme (see above) are considered: An initially cold ion resides in a harmonic potential, whose minimum position z_0 is moved along the trap axis according to some transport function $z_0(t)$. For experimental reasons, it is convenient to consider closed round trips starting from $z_0(0)$, reaching $z_0(T/2)$ after time $T/2$; then, the ion is shuttled back to its starting point again by exactly reverting the protocol in time. Thus, the ion resides at the same place for preparation and detection.

In contrast to the slow transports applied for remote spectroscopy, a linear transport function seems to be unsuitable for fast transports for the following reasons: Due to the unsteady behavior of $z_0(t)$ at the beginning and the end of the shuttling procedure, the ion sustains "kicks" at $t = 0$, $t = T/2$ and $t = T$, which are stronger the faster they are

[4] In Ref. [Cou08], non-adiabatic shuttling of ultracold neutral atom clouds is reported, albeit in a much slower parameter regime ($\omega_z \sim 2\pi \times 10^1$ Hz compared to $\omega_z \sim 2\pi \times 10^6$ Hz in our case).

performed. From this point of view, the transport function should be differentiable at least twice. For that reason, an error-function[5] shaped transport function

$$z_0(t) = \begin{cases} f_\sigma(t) & \text{for } 0 \le t \le T/2 \\ d - f_\sigma(T-t) & \text{for } T/2 < t \le T \end{cases}, \quad f_\sigma(t) = \frac{d}{2}\left(1 + \frac{\mathrm{Erf}\left[(4t/T-1)\,\sigma\right]}{\mathrm{Erf}[\sigma]}\right) \tag{5.11}$$

was implemented. Here, $d := z_0(T/2) - z_0(0)$ is the one-way transport distance. $f_\sigma(t)$ is infinitely differentiable, i.e. it starts and ends with vanishing accelerations, and offers a free parameter σ, by which the transport character can be continuously chosen between linear, sigmoid and step-like (see Fig. 5.8).

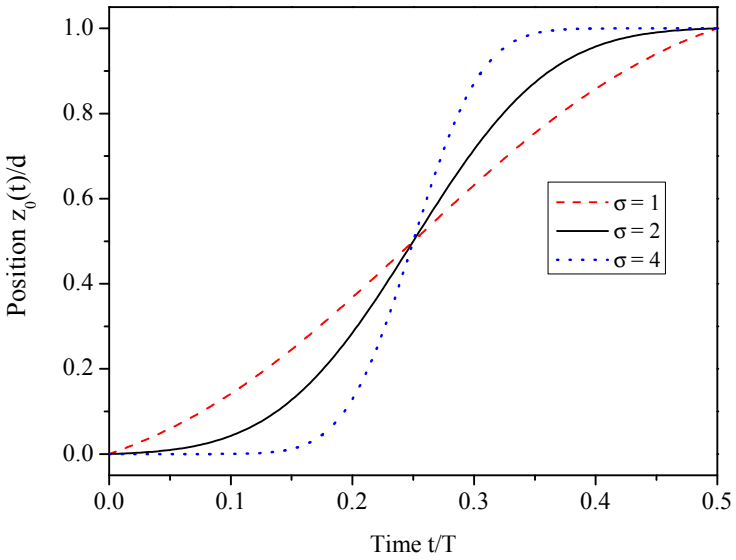

Figure 5.8: Parametrization of the utilized transport function (one way). In simulation and experiment, a smooth transport with $\sigma = 2$ was chosen. For $\sigma \to 0$, a linear transport results, while for $\sigma \to \infty$, the transport distance d is covered in a discontinuous step. These extreme choices for σ imply "kicks" to the ion, resulting in excess motion. The transport back ($T/2 < t \le T$) is realized exactly time-reversed.

Ion Trajectory Simulations

The dynamics of the ion motion in a perfect transport potential is governed by the differential equation

$$\ddot{z}(t) = -\frac{e}{m}\frac{\partial\phi(z,t)}{\partial z} = -\omega_z^2\,(z(t) - z_0(t)). \tag{5.12}$$

Accompanying the measurements, we performed calculations giving the classical trajectory $z(t)$ of the ion after Eq. (5.12), where the corresponding transport function $z_0(t)$ is to be

[5] $\mathrm{Erf}(x) := 2\,\pi^{-1/2}\int_0^x e^{-t^2}dt$.

set in. Here, a voltage update rate of 1 MHz was considered, so that $z_0(t)$ was indeed piecewise constant. This has a smaller effect on the dynamics, the slower the transport is realized. Another step towards a more realistic description and away from the idealized case was done by using the real electric potentials, deduced from field calculations, instead of using the theoretical, perfect harmonic potentials assumed in Eq. (5.12); the differences in the quantitative results are minimal, however, since the potentials seen by the ion have very small anharmonic contributions.

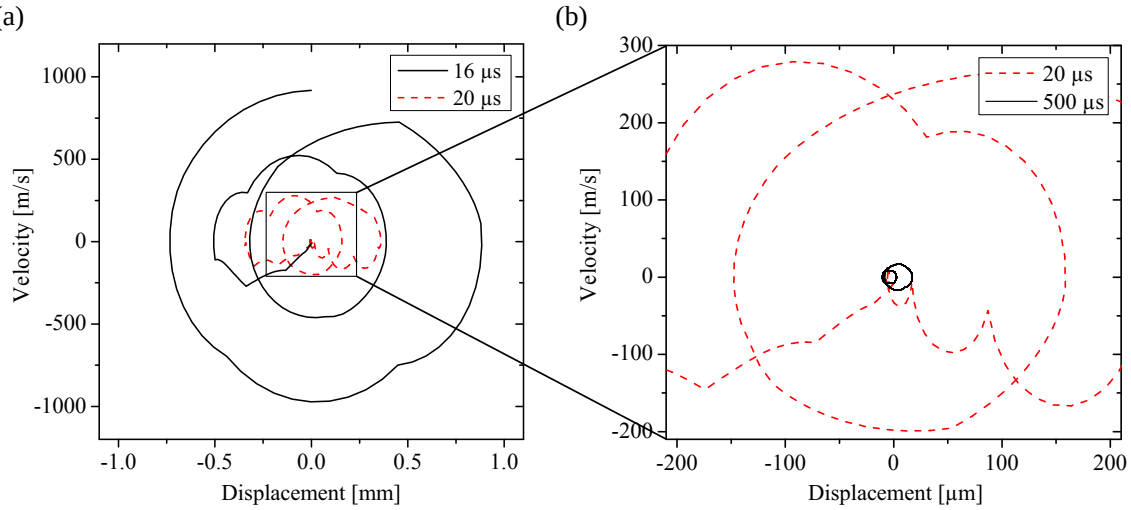

Figure 5.9: Phase space trajectories of an ion for two different transport durations. (a) The red dashed line shows a transport ($\tau = 20/5 = 4$) with low final motional energy, indicated by a closed trajectory. For $\tau = 16/5 = 3.2$ (black solid line), the ion does not reach its starting point again at $t = T$, but has a final energy of 171 meV. (b) In this closeup view, the trajectory of a slow transport with $\tau = 100$ can be seen (black solid line). Only small excursions and velocities occur during the transport, so that the exact duration has a minor impact on the final energy. Discontinuities in the trajectories result from a 1 μs time discretization to account for experimental constraints.

Figure 5.9(a) shows typical phase-space trajectories $(z(t), \dot{z}(t))$ of an ion subject to shuttling in a trap with transport duration τ. For $\tau = 4$, the ion returns to $z(0)$ at the end of the trip and has zero velocity. Whereas for $\tau = 3.2$, i.e. the transport time is not equal to $2k \times (2\pi/\omega_z)$ with integer $k \geq 2$, the ion does not return to $(0, 0)$, but has a large excess velocity (energy) at the end of the transport (equivalently, it can happen that the ion ends up with $\dot{z}(T) \approx 0$, but a large displacement from the potential minimum). The occurrence of these "resonances" in transport fidelity is typical for fixed-frequency transports (cf. Refs. [Rei06, Huc07]).

Thus we see, that for such fast transports the transport duration critically influences

the final energy. For adiabatic shuttles $T \gg 2\pi/\omega_z$, this dependency is much weaker, since the energies occurring during the transport are much smaller, anyway. This can be comprehended by the aid of Fig. 5.9(b), where for comparison, the trajectory for a shuttle with $\tau = 100$ is plotted. The excursion in phase space, i.e. the velocities and spatial displacements during the transport process, are much smaller than for the fast cases.

Those cases, where the ion returns to its initial state $(z(t), \dot{z}(t)) = (0, 0)$, are most desirable for transport processes, because they make a time-consuming and potentially internal-state destroying recooling of the ion superfluous. The question of how to implement such transports as quick and conservative as possible was subject to intensive studies. Different transport functions [Rei06, Sch06] and the possibility of utilizing optimal control techniques have been discussed [Mur09].

Measurement of the Transport Success Probability

The transports were realized in the pcb-trap and covered a transport distance of $2\times2.0\,\mathrm{mm}$, starting from electrode 10, the return point was close to electrode 13 (see Fig. 9.2). The potential transformations giving rise to the ion transports were generated in the same way described above: the voltages of all 15 electrode pairs were updated with an update time of $1\,\mu\mathrm{s}$. The voltages were derived from commercial analog-out cards[6] and were calculated such that $\omega_z \approx 2\pi \times 200\,\mathrm{kHz}$ stays constant throughout the transport process. The transport function was sigmoid with $\sigma = 2$, cf. Fig. 5.8.

The chosen voltage configuration $\{V_i\}^{z_0(0)}$ at the beginning and the end of the round-trip does not necessarily result in a potential ideally suited for laser-ion control. Especially in our case, a potential with different frequency and depth pointed out to be preferable for laser manipulation (trapping, cooling, etc.). For that reason, we decided to make the transport independent from other demands and inserted a potential morphing step at the beginning and the end of the transports; this is also included in the timing illustration shown in Fig. 5.10. The morphing procedure linearly transforms those voltages optimal for laser interaction into the "transport voltages" at $t = 0$. The same happens in time-reversed order after the transport at $t = T$. This morphing transformation was performed in $10\,\mu\mathrm{s}$.

After initial cooling of the ion and the morphing step, the ion is shuttled back and forth. Then, it is recooled for 1 s to make sure that each ion is recooled into the same initial state, no matter how high the energy was it returned with. Fluorescence detected during

[6] National Instruments NI PCI-6733 High-Speed Analog Output, 1 MS/s, 16-Bit.

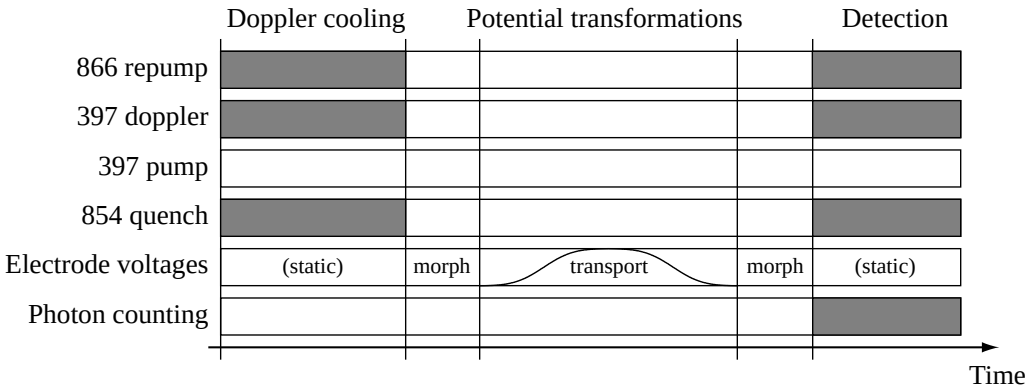

Figure 5.10: Schematic timing of an experiment determined to yield the probability of a successful round-trip shuttle of a single ion. At first, the ion resides in a static, harmonic laser-interaction potential (see text). After preparation by means of Doppler cooling, the potential is morphed into the first transport potential by varying the corresponding electrode voltages linearly. Then, the ion is shuttled back and forth symmetrically in time T. After another morphing step (symmetrical to the first one) restoring the interaction potential, the ion is detected and recooled on the 397 nm transition. Detection of fluorescence indicates a successful transport without ion loss.

recooling after the shuttling indicates a successful transport. Then, the procedure is started again. After n_i repetitions (i gives the number of the loaded ion), the ion is eventually lost due to excitation by the transformation process. Then, a new ion $(i+1)$ is loaded into the trap and is shuttled till it leaves the trap after n_{i+1} successful transports, and so on.

After N ions (i.e. $i = 1, \ldots, N$, N is about 10^2 to 10^3), the values n_i are binned such that their histogram gives the probability $P_\tau(n)$ that an ion survives at least n shuttle processes of duration τ. As the individual transports can be regarded independent from each other, this probability is equal to $\tilde{p}_\tau^n$, where $\tilde{p}_\tau$ is the single transport success probability and n is the number of successful transports carried out in a row. Thus, an exponential fit to $P_\tau(n)$ gives the single transport success probability $\tilde{p}_\tau$.

The results for different transport velocities can be seen in Fig. 5.11. For very slow shuttles ($\tau = 100$), the ions almost never get lost due to the transformation and the success probability is as high as 99.8(2) %. Reasons for an ion loss in this regime can be a still high inital temperature of the ion giving rise to unstable trajectories, or background gas collissions (indeed, the ion loss rate due to background gas collissions could not be neglected in the case of transports with high success probability. An ion loss measurement without executing the transport was performed to correct for this effect).

It is remarkable that from the adiabatic regime down to $\tau = 4$, the success probability

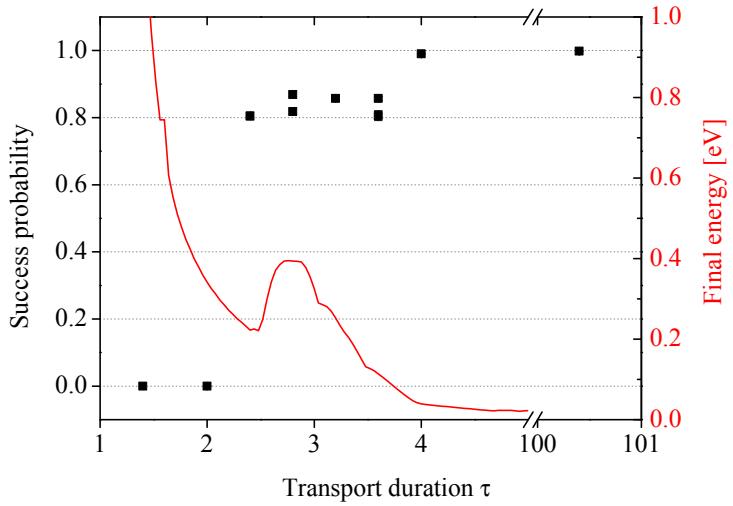

Figure 5.11: Transport success probability as a function of transport time τ (■, scale on the left). Slow, "quasi-static" transports with large τ show a success probability close to unity. Even for $\tau = 4$, the probability is still as high as 99.0(1) %. In an intermediate region $2 < \tau < 4$, the probability ranges between $80 - 90\%$, before it drops to virtually zero for $\tau \leq 2$. This behavior can be explained by the maximal energy occuring during the process, shown by the red line (scale on the right). If it becomes too high, the ion gets eventually lost, even if its final excitation would be low again.

is still as high as 99.0(1) %. In such a fast transformation, the ion undertakes only two oscillations until it is dragged back to the starting position again. Calculations show, that the displacement from the minimum of the instantaneous potential is as high as 300 μm for a transport with $\tau = 4$. The corresponding potential energy is 30 meV.

With decreasing τ, there can be distinguished a second regime with success probabilities of $80 - 90$ %, but remarkably lower than in the adiabatic case. This regime is delimited by transport times $2 < \tau < 4$; these are transports, during which the ion undertakes only a couple of oscillations on its way to the return point and back. For faster transports ($\tau \leq 2$), $\tilde{p}_\tau^n$ abruptly drops to zero within the error bars. Ion losses for $\tau < 4$ can be made plausible by calculating the maximum energy occurring during the whole transport process. This energy is also plotted in Fig. 5.11 (right scale) as a function of τ; it shows that in this regime, the maximum energy becomes as high as $100 - 1000$ meV – even if the final energy of a successful transport would be very small again. This energy corresponds to approximately one third of the theoretical potential depth and can be the reason for ion loss due to anharmonicities in the potential or a coupling between axial and radial modes.

The measurements presented here give a good insight into the motional dynamics of the

shuttling potential transformation. The results we gained from these experiments will be still refined in chapter 6.2.2, where we will introduce a technique to measure the final energy of the ion after the transformation process.

5.3 The Squeezing Transformation

In the previous chapter, the situation of an ion in a harmonic oscillator potential with constant frequency but time-dependent position was treated. From both a theoretical and practical point of view, this kind of transformation entails – because of its conceptual simplicity – an enormous potential. This chapter introduces a transformation of the quantum harmonic oscillator that is, under these aspects, in no way inferior to the shuttle process[7]. The transformation of interest is that of a harmonic oscillator whose frequency ω_z is parametrically changed, while the position of the potential minimum remains fixed. Hence, it complements in some sense the transport transformation. The corresponding Hamiltonian reads

$$H_{\mathrm{mot}} = \frac{p^2}{2m} + \frac{m}{2}\,\omega_z^2(t)\,z^2. \tag{5.13}$$

The transformation parameter of the system is $\lambda(t) \equiv \omega_z(t)$. By the illustration of Fig. 5.12, it becomes clear, why such a transformation is also-called *squeezing*: a particle confined in the time-dependent potential experiences something like a squeezing force when $\omega_z(t)$ is increased in time. In such a classical picture, one could also say that the "volume" the system is confined in, is decreased.

In this chapter, we are particularly interested in thermodynamic properties of this process. It is not only a nice analogue to the classical text book example of an ideal gas being confined in a volume, which is subject to compression or expansion (cf. Fig 2.3 in chapter 2.1), but has – under certain circumstances – analytical solutions. It is one of this chapter's core themes to derive and discuss exactly these solutions, and to show that the model can be experimentally realized by the help of trapped ions.

[7] In another context, this kind of transformation has recently been proposed for the simulation of cosmological particle creation [Sch07], for example.

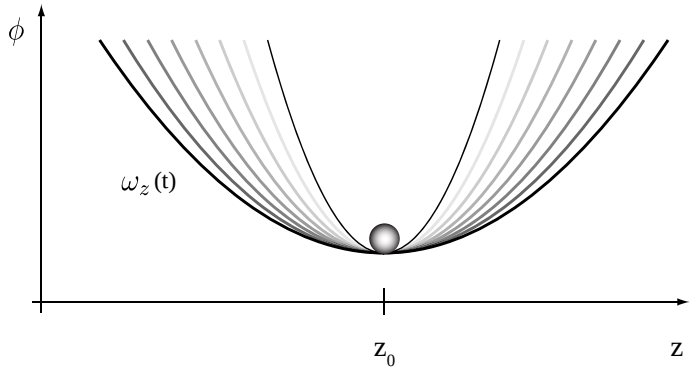

Figure 5.12: Illustration of the squeezing potential transformation. While the position of the potential minimum (with respect to space and voltage) remains unchanged, its harmonic frequency $\omega_z(t)$ is changed in time. Mostly, we consider increasing frequencies, but in general arbitrary transformation paths are possible.

5.3.1 The Transformation Model

We consider a one-dimensional quantum harmonic oscillator in z-direction with time-dependent frequency $\omega_z(t)$ defined by Eq. (5.13). The particles[8] confined in this potential are supposed to be in thermal equilibrium at $t = 0$ with inverse temperature β,

$$\rho(0) = \frac{1}{Z} \exp(\quad \beta H_{\mathrm{mot}}), \tag{5.14}$$

but the system is supposed to be isolated for $t > 0$. When the transformation $\omega_z(0) \rightarrow \omega_z(T)$ is conducted in time T, the state of the particle changes. We denote by $|n(t)\rangle$ and $\phi_n(x,t) := \langle x|n(t)\rangle$ the eigenstates of the instantaneous system Hamiltonian $H_{\mathrm{mot}}(t)$, and $E_n(t) = \hbar\omega_z(n(t) + \frac{1}{2})$ are the corresponding eigenenergies.

Solving the Schrödinger Equation

In order to solve the oscillator dynamics, we follow the work detailed in Refs. [Def08, Gal09, Def10a] and apply a Gaussian wave function ansatz by Husimi [Hus53]:

$$\psi(z,t) = \exp\left(\frac{i}{2\hbar}\left[a(t)\,z^2 + 2b(t)\,z + c(t)\right]\right). \tag{5.15}$$

[8] The model is realized with a single particle at a time. The notion of an ensemble of particles is to be understood as an ensemble of single particles which are prepared and manipulated one after the other. Each particle is weakly coupled to the same thermal bath and thus the density operator of the whole system is that of a thermal state. As all realizations of the system are completely independent of each other, it is justified to speak of a thermodynamic ensemble of non-interacting particles. Nevertheless, experiments with a small number of (interacting) particles are possible, too.

In combination with this ansatz, the Schrödinger equation yields a set of three coupled differential equations for the coefficients $a(t), b(t)$ and $c(t)$,

$$\dot{a}(t) = -\frac{1}{m}a^2(t) - m\omega_z^2(t) \tag{5.16}$$

$$\dot{b}(t) = -\frac{1}{m}\,a(t)\,b(t) \tag{5.17}$$

$$\dot{c}(t) = \frac{i\hbar}{m}a(t) - \frac{1}{m}b^2(t), \tag{5.18}$$

with m being the mass of the ion. We note that the solutions of Eqs. (5.16)-(5.18) are solely determined by the conduct of the process $\omega_z(t)$. The first of the three, Eq. (5.16), is of the Riccati type and can be mapped to the equation of motion of a classical harmonic oscillator with time-dependent frequency [Def08],

$$\ddot{X}(t) + \omega_z^2(t)X(t), \tag{5.19}$$

by setting $a(t) = m\dot{X}(t)/X(t)$. This equation is not analytically solvable for general transformations $\omega_z(t)$. For special realizations, however, there is an analytical expression for $X(t)$. One is given in Ref. [Def08] for a process, where $\omega_z^2(t)$ is linear in time.

From the solution of Eq. (5.16), the other two time-dependent coefficients can be calculated one after the other; hence, the wave function at any given time can then be obtained according to Eq. (5.15).

Work Performed on the System

As already discussed in chapter 1.1.1, the energy of the system under the squeezing transformation will change, when the transformation is performed. Depending on the exact shape of the transformation, i.e. $\omega_z(t)$ in our case, however, this energy change can be of very different quality. Even under the assumption that all processes begin and end in the same potential (fixed $\omega_z(0)$ and $\omega_z(T)$), the potential results of the transformation couldn't be more diverse: for a quasi-static realization, for instance, all work performed merely increases the free energy, $\Delta F = \langle W \rangle$. For arbitrary processes, however, some part of the imparted work is absorbed within the irreversible work $\Delta F = \langle W \rangle - \langle W_{\mathrm{irr}} \rangle$. Fortunately, the Jarzynski equality (1.3) makes it possible to calculate ΔF from the work probabilty distribution $P(W)$ for arbitrary processes and it is valid in both the classical and the quantum regime.

The distribution of the work performed on the system shows that its value is subject to fluctuations. While in macroscopic physics, work is a well-defined quantity, there are, in

fact, fluctuations around a mean value. These fluctuations can only be observed in small systems, as their magnitude falls off quickly with the system size [Cro99]. In the following, we will derive $P(W)$ for the case of the squeezing transformation and will show that it is possible to detect fluctuations and even those processes running against the second law of thermodynamics by using trapped ions in the micro-trap. A definite measurement scheme to verify the Jarzynski equation is proposed and investigated quantitatively.

In addition to fluctuations, which also occur in purely classical systems, the notion of work, howsoever familiar and well-defined in classical physics, has to be completely revisited in the quantum case. This already becomes obvious by its definition in classical mechanics as the integral of a force along a certain path; both doesn't exist in the quantum world. In particular, the idea of a system propagating along a path contradicts the uncertainty principle. Consequently, it has been pointed out recently, that work is not a quantum mechanical observable, but rather a time-ordered correlation function [Tal07b]. Nevertheless, the notion of work has by no means lost its justification in the quantum world. On the contrary, its extension into the quantum regime is fruitful and sheds light on processes on the border area between the classical and the quantum world.

While in a classical system work is a continuous variable, this cannot be the case in an energy-quantized system. When a system with instantaneous energy eigenvalues $E_n(t)$, $n = 0, 1, \ldots$ is subject to a transformation of the Hamiltonian, work W can be defined as the difference outcome of two energy measurements at $t = 0$ and $t = T$, respectively, and can hence be written as $W = E_m(T) - E_n(0)$.

The transformation changes the system state and thus – in general – the distribution of the energy eigenstates. This is modeled by the transition matrix[9] $P_{m,n}$, which gives the conditional probability to find the state in $|m(T)\rangle$ if it had initially been in $|n(0)\rangle$. The distribution of W is hence discrete and only has non-zero contributions for values $W = E_m(T) - E_n(0)$ for all combinations of n and m. Each of these combinations occurs with probability $P_{m,n} \cdot P_n$; the total probability distribution can hence be written as

$$P(W) = \sum_{m,n=0}^{\infty} \delta[W - (E_m(T) - E_n(0))]\ P_{m,n} P_n, \tag{5.20}$$

where δ is the Dirac δ-function. The discrete character of this distribution is due to the quantized energy spectrum; the transition from discrete to continuous distributions has been studied and found to be caused by either high temperatures or non-adiabatic processes [Def10a]. Both cases imply a higher mean energy in the system.

[9] Note that the off-diagonal elements in the density matrix of the input state have no influence on the work distribution [Tal08].

Equation (5.20) is not only interesting because it shows a way how to calculate and measure the work probability distribution; the origin of the work fluctuations can be seen from it, too: On the one hand, statistics enters through the thermal probability distribution P_n of the input states. On the other hand, the matrix $P_{m,n}$, describing the dynamics of the process and the outcome of the second measurement, introduces uncertainty due to the quantum process itself. While the density operator of the final state can – at least in principle – be calculated exactly for the final state, the result of the energy measurement cannot be predicted, i.e. the work performed on the system is subject to fluctuations.

The transition matrix element $n \to m$ can be calculated from the wave function overlap of the transformed state $U(T)\,|n(0)\rangle$ and the final state $|m(T)\rangle$, where $U(t)$ is the propagator corresponding to the system Hamiltonian,

$$\begin{aligned} P_{m,n} &= |\langle m(T)|\, U(T)\, |n(0)\rangle|^2 \\ &= \left| \int dz' \int dz\ \phi_m^*(z,T)\ U(z,z';T)\ \phi_n(z',0) \right|^2 . \end{aligned} \tag{5.21}$$

By noting that $\psi(z,T) = \int dz'\ U(z,z';T)\,\psi(z',0)$, the propagator can be read from the wave function in Eq. (5.15) and can be explicitly written as [Def08]

$$U(z,z';t) = \sqrt{\frac{m}{2\pi i\hbar X}}\ \exp\left(\frac{im}{2\hbar X} \left(\dot{X} z^2 - 2zz' + Y z'^2 \right) \right), \tag{5.22}$$

where both $X(t)$ and $Y(t)$ are solutions of Eq. (5.19) satisfying the boundary conditions

$$\begin{aligned} X(0) = 0, \quad \dot{X}(0) = 1 \\ Y(0) = 1, \quad \dot{Y}(0) = 0. \end{aligned} \tag{5.23}$$

In general, the transition probabilities $P_{m,n}$ can thus be calculated after Eqs. (5.15) and (5.21). As already mentioned, one of the main advantages of the squeezing transformation is, that it is analytically solvable under various conditions. Therefore, explicit analytical expressions for $P_{m,n}$ exist and can be found in the appendix of Ref. [Def10a].

Interestingly, these quantities merely depend on three process-dependent parameters: The initial and final values of $\omega_z(t)$, on the one hand, and a parameter $Q^* \geq 1$, which characterizes the process itself, on the other hand. Q^* was first introduced by Husimi and is a measure for the nonadiabaticity of the process, with $Q^* = 1$ for an adiabatic process. In the case of the squeezing transformation, it can be obtained from the solutions X and Y as

$$Q^* = \frac{1}{2\omega_0\omega_T} \left(\omega_0^2 \left(\omega_T^2 X^2(T) + \dot{X}^2(T) \right) + \left(\omega_T^2 Y^2(T) + \dot{Y}^2(T) \right) \right), \tag{5.24}$$

where $\omega_0 := \omega_z(0)$ and $\omega_T := \omega_z(T)$ are the initial and final potential parameters, respectively. It is remarkable that all details about the exact temporal protocol $\lambda(t) \equiv \omega_z(t)$ can be subsumed into this quantity. Its physical meaning becomes more obvious if the effect of the process is considered for an initial energy eigenstate $|n(0)\rangle$, whose wave function is "spread" over different final eigenstates $|m(T)\rangle$ by the transformation. It can be easily shown [Def08], that the distribution of the final quantum number then has an average value and variance of

$$\begin{aligned} \langle m \rangle &= \sum_m m P_{m,n} = \left(n + \frac{1}{2}\right) Q^* - \frac{1}{2} \quad \text{and} \\ \sigma^2 &= \sum_m (m - \langle m \rangle)^2 P_{m,n} = \frac{1}{2}\left(Q^{*2} - 1\right)(n^2 + n + 1), \end{aligned} \tag{5.25}$$

respectively. This tells us firstly, that the final mean energy is a linear function of Q^*. Secondly, the magnitude of Q^* directly gives the width of the distribution, i.e. tells us how strong the initial state's amplitude is spread. For $Q^* = 1$ follows $\langle m \rangle = n$ and $\sigma^2 = 0$, which confirms that no state transitions occur during adiabatic processes.

These properties of the transformation are of great importance when it comes to measuring the final states. From Q^*, we can estimate how far the system is driven out of equilibrium and which phonon states of the harmonic oscillator are populated. Starting from a state in thermal equilibrium, Q^* must be large enough to see non-equilibrium effects on the one hand, but must not be so large that the resulting phonon distribution exceeds measurable quantum numbers; too high excitations are difficult to detect. In the following section, a concrete transformation protocol will be investigated with a special emphasis on its realization with single ions in the micro-trap.

Verifying the Quantum Jarzynski Equality

When the initial temperature of the system and the frequencies ω_0, ω_T are well-known, then measuring the transition probabilities $P_{m,n}$ gives the complete work probability distribution $P(W)$ after Eq. (5.20). By the help of this, the free energy after the Jarzynski equality (1.3)

$$\begin{aligned} \Delta F &= -\frac{1}{\beta} \ln \langle e^{-\beta W} \rangle = -\frac{1}{\beta} \ln \int dW\, P(W)\, e^{-\beta W} \\ &= -\frac{1}{\beta} \ln \sum_{m,n=0}^{\infty} P_{m,n}\, P_n\, e^{-\beta\, \Delta E_{m,n}} \end{aligned} \tag{5.26}$$

can be calculated, where the short notation $\Delta E_{m,n} := E_m(T) - E_n(0) = \hbar\omega_T(m + \frac{1}{2}) - \hbar\omega_0(n + \frac{1}{2})$ for all occurring values of the work was used (β is the inverse temperature of

the system at $t = 0$). As the free energy change of the system does not depend on the protocol, but only on its endpoints ω_0 and ω_T, the Jarzynski equation can be verified by performing different protocols with the same endpoints; this includes, for instance, finite-time protocols along the same path λ, but with different durations T. In particular, a quasi-static realization of the process, $T \gg [\min_t \omega_z(t)]^{-1}$, must yield the same ΔF, too.

5.3.2 Proposed Realization in the Micro-Trap

We consider a squeezing transformation changing ω_z^2 linear from ω_0^2 to ω_T^2 during time T,

$$\omega_z^2(t) = \omega_0^2 + \frac{t}{T}\,(\omega_T^2 - \omega_0^2). \tag{5.27}$$

This special parametrization has two advantages: First, it allows for analytical solutions of Eq. (5.19) [Def08]. Second, as the axial trap frequency is a quadratic function of the applied voltages, the desired protocol can be implemented by linear voltage functions, which can be realized fast and in a very controlled way.

As a concrete example, realizable with a set of at most three electrode pairs, each supplied with voltages not exceeding 10 V in absolute values, we consider a change in trap frequency from $2\pi \times 1\,\mathrm{MHz}$ to $2\pi \times 3\,\mathrm{MHz}$ in $T = 50\,\mathrm{ns}$. Such a process is easily achievable with standard electronics. Since we are interested in the low-temperature, quantum features of the system, we consider a system, which is initially prepared into a thermal state with $\overline{n} = 1$ ($\Rightarrow \hbar\omega_0\beta \approx 1.0$). This can be accomplished by means of resolved sideband cooling, if necessary in combination with a controlled coupling to a heat reservoir (cf. chapter 4).

After the state has been prepared with fixed $\omega_z = \omega_0$, the time-dependent voltages perform the transformation of the potential. Hereby, the state of the ion is driven out of thermal equilibrium. The parameter Q^* describing the degree of nonadiabaticity of the process (see Eq. (5.24)) is 1.58 for $T = 50\,\mathrm{ns}$. This is not too far from the adiabatic value, $Q^* = 1$, but already suffices to observe the wanted fluctuation effects[10]. The free energy can be given in closed form for the squeezing operation as [Def08]

$$\Delta F = -\frac{1}{\beta}\ln\frac{\sinh(\beta\hbar\omega_0/2)}{\sinh(\beta\hbar\omega_1/2)}. \tag{5.28}$$

It amounts to $\Delta F/\hbar \approx 2\pi \times 1.807\,\mathrm{MHz}$ for the parameters given above.

[10] We will discuss later within this chapter, how Q^* can be efficiently increased.

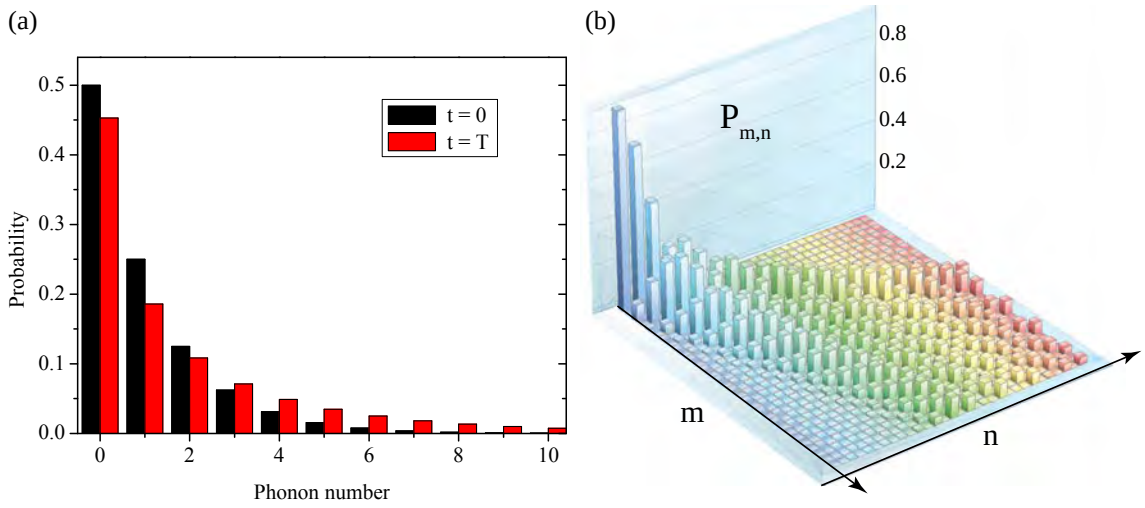

Figure 5.13: (a) Phonon number distributions of the initial equilibrium state with $\overline{n} = 1$ (black) and of the final state at $t = T$ (red). Due to the non-adiabatic process ($Q^* \approx 1.58$), the state is driven out of equilibrium. In contrast to the initial state, the final state's density matrix has in general off-diagonal elements, too. The process was parametrized after Eq. (5.27) with $\omega_0 = 2\pi \times 1\,\mathrm{MHz}$, $\omega_T = 2\pi \times 3\,\mathrm{MHz}$ and a transformation time $T = 50\,\mathrm{ns}$. (b) Transition probabilities $P_{m,n}$ $(n, m = 0, \ldots, 30)$ for the same process. This matrix generates the output from the input distribution.

Results of the Transformation

Figure 5.13(a) shows the calculated phonon number distributions of both the initial (P_n) and the final ($\sum_n P_{m,n} P_n$) state of the system. The final state's phonon distribution is no longer thermal. The transition probabilities $P_{m,n}$ after Eq. (5.21) associated with this transformation are illustrated in Fig. 5.13(b). Here, the non-adiabatic action of the process can be seen by the emergence of off-diagonal values. By virtue of $P_{m,n}$, which is a result of the quantum time evolution, the state is "spread" in Hilbert space. Note, that because the squeezing operator is quadratic in the creation and annihilation operators, only even transitions can occur, $n \to n + 2k$ with integer k.

Another important point can be learned from Figure 5.13(a): as it is not possible to discriminate arbitrarily high phonon numbers, it is necessary that the states have only negligible populations in higher Fock states. This is mostly given for a sufficiently cold initial state whose population decreases exponentially with n. When the system is driven far out of equilibrium, however, the energy spread is large and phonon numbers too high for detection are significantly populated. This qualitative consideration is also what we learn from Eq. (5.25). For our parameter choices, phonon states $n \geq 5$ are populated with 5 % or less.

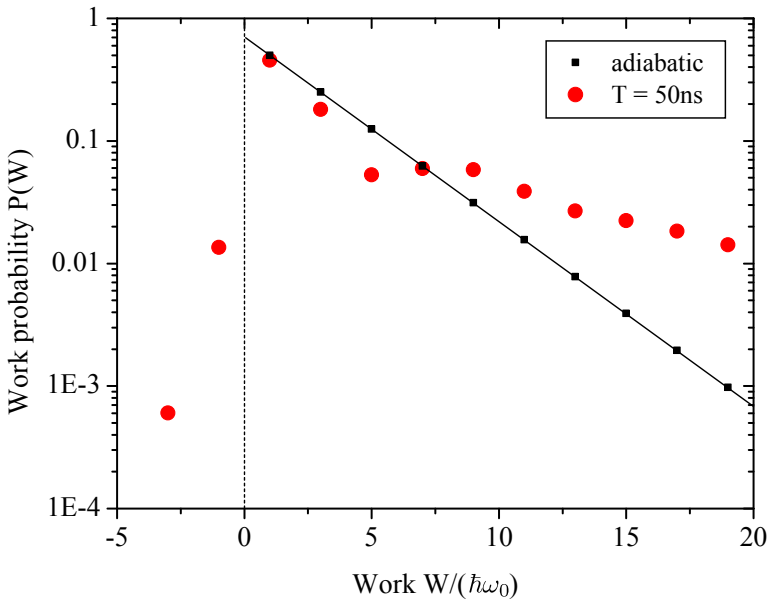

Figure 5.14: Work probability distribution $P(W)$ for an adiabatically slow (black squares and line) and finite-time (red circles) realization of the process, whose other parameters are the same as given in the caption of Fig. 5.13. In the adiabatic case, the work probability distribution is determined by the initial thermal (exponential) distribution of the states, because then $P_{m,n} = \delta_{m,n}$. In the finite-time case, the system is driven out of equilibrium, and negative work processes ($W < 0$) can occur.

Work Probability and Negative Work

The work probability distribution $P(W)$ after Eq. (5.20) is shown in Fig. 5.14. One can clearly see the deviations from the adiabatic case $T \to \infty$. Interestingly, now the work can take on negative values, too. This can happen with non-zero probability, when a transition $n \to m < n$ into a *lower* phonon state[11] takes place, and if $(n + \frac{1}{2})/(m + \frac{1}{2}) > \omega_T/\omega_0$.

This can be most clearly seen in the transition probabilities for specific starting values n (this corresponds to individual columns in Fig. 5.13(b)). Figure 5.15 shows $P_{m,n}$ for the four lowest values of $n = 0$ to 3, i.e. the probabilities that the population of $|n(0)\rangle$ goes into $|m(T)\rangle$. While for $n = 0$ and $n = 1$, transitions into lower phonon number states are impossible or forbidden, respectively, one such event can be found for $n = 2$ and $n = 3$ each: negative work occurs for $2 \to 0$ ($P_{0,2} \approx 10\,\%$) and $3 \to 1$ ($P_{1,3} \approx 23\,\%$)[12]. The prerequisite for the occurrence of negative work is a non-zero temperature and nonadiabaticity of the

[11] We assume $\omega_T > \omega_0$ ("compression") here.

[12] The absolute probability of these processes must still be multiplied with the probability of the respective initial phonon number, P_n.

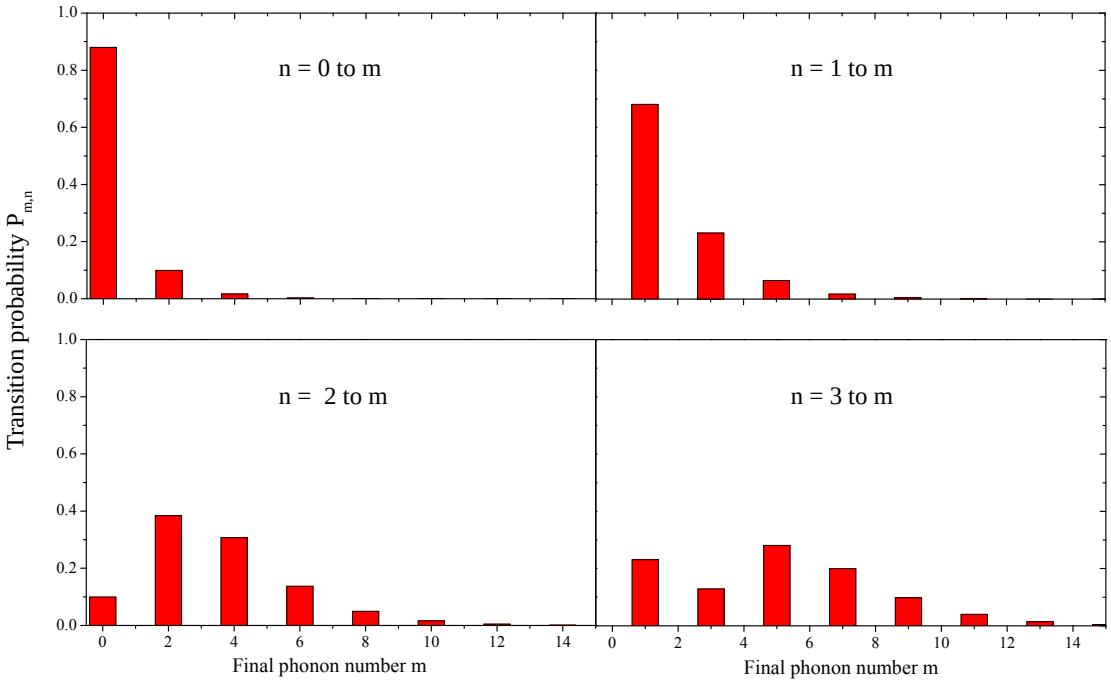

Figure 5.15: Conditional transition probabilities $P_{m,n}$ for initial eigenstates $n = 0, 1, 2$ and 3. The process was parametrized like in Fig. 5.13. Due to the quadratic squeezing operator, only even phonon changes $|m - n|$ occur. In the lower two graphs, one can clearly recognize processes, where the phonon number is decreased, $n \to m < n$. They are transitions of negative work.

transformation: at zero temperature, all population is in the ground state at the beginning, and transitions into lower phonon states are not possible; for adiabatic processes, the phonon numbers do not change at all so negative work cannot result, either.

The existence of negative work processes is most remarkable, since it describes processes, where energy is extracted from the system, while its frequency is increased – or in classical words, it is compressed. Since in these rare processes, the system is cooled and not heated, as one would expect, they can be said to violate the second law of thermodynamics [Wan02], which postulates that the heat increases in such a non-adiabatic process. On average, of course, the second law holds; but it's exactly these cases, these fluctuations around the thermodynamic average behavior, which become observable in the trapped ion system. In order to be able to see exactly these events, it is necessary to make every single event $n \to m$ visible by a proper measurement process and not to average over many realizations. Otherwise, the fluctuations would get lost in the mass of events. The measurement scheme presented in detail below fulfills this requirement.

Measurement Protocol to Verify the Jarzynski Equation

The experimental scheme for verifying the quantum Jarzynski equation relies on the phonon filter presented in chapter 6.5 [Hub08b]. In effect, it allows for testing the motional state of an ion for being in a certain energy eigenstate $|n = m_{\text{test}}\rangle$ or not. If the test is positive, then the state is projected into $|m_{\text{test}}\rangle$ and we know that the test was successful. If the test is negative, then the state is corrupted and we know that the test was not successful. Let's first introduce the scheme and analyze its action afterwards:

(1) Set the electrode voltages such that $\omega_z(0) = \omega_0$.

(2) Prepare the ion in a thermal state ρ_β with inverse temperature β.

(3) Choose an initial phonon number n and apply the phonon filter for n to ρ_β. If negative, restart from 2. If positive, the state has been projected into $\rho(0) = |n\rangle\langle n|$.

(4) Transform the potential from ω_0 to ω_T by altering the electrode voltages according to $\omega_z(t)$. The ion's motional state is transformed, $\rho(0) \to \rho(T)$.

(5) Choose a final phonon number m to test for, and apply the phonon filter to $\rho(T)$. If the test is positive, the process $n \to m$ was observed. If negative, start from 1.

Step (2) prepares the initial equilibrium state and thus the initial phonon distribution P_n. Note that the preparation of the initial state is based on a measurement of its temperature, that is, β is a measured quantity.

The succeeding test of this thermal state for being in the state $|n\rangle$ by the phonon filter yields a positive result with probability P_n. The great advantage of the filter is that the state is not destructed in the case of a positive result, but the experiment can go on with exactly the same state and ion. In this case, a non-destructive, projective quantum measurement was accomplished. If it was negative, what happens with probability $1 - P_n$, the state must be discarded and ρ_β is prepared again. As P_n decays exponentially with n, tests for higher n will fail most of the time. In order to save time, it could be an alternative to *prepare* the ion in $|n\rangle$ instead[13].

After the transformation, the filter is applied again. When its result is negative, we know that the process $n \to m$ did not occur and restart again. When it is positive, the process

[13] Note that in this case, one actually starts out with a microcanonical ensemble rather than with a canonical one. The final probability of a detected process $n \to m$ has to be weighted with its thermal probability P_n, then. The methodologically unassailable procedure is the one starting out from ρ_β.

$n \to m$ occurred. This way, the transition probabilities $P_{m,n}$ can be reconstructed from positive and negative phonon filter tests. In practice, two nested loops iterating through $n = 0, 1, \ldots$ and $m = 0, 1, \ldots$ can sample all possible transitions.

The frequencies at the beginning and at the end of the transformation can be measured very accurately by means of sideband spectroscopy in static potentials. Hence, the exponentiated work $e^{-\beta \Delta E_{m,n}}$ with the performed work $W = \Delta E_{m,n}/\hbar = \omega_T(m+\frac{1}{2}) - \omega_0(n+\frac{1}{2})$, corresponding to each transition $n \to m$, can be calculated and the sum in Eq. (5.26) can be evaluated to give the free energy difference ΔF.

Additionally, the presented non-destructive measurement scheme makes it possible to observe the rare and interesting transitions implying negative work. For example, both the processes $2 \to 0$ and $3 \to 1$ can be easily detected by virtue of the phonon filter scheme.

Different Protocol Times and Nonlinear Transformations

The verification of the Jarzynski equation is only complete, if the same value ΔF is obtained for various processes with the same endpoints. To this end, it seems natural to implement the linear parametrization Eq. (5.27) with different durations T. In Fig. 5.16, the parameter Q^* is plotted as a function of the process duration T, when all other parameters remain unchanged. For $T \gg \omega_z^{-1}(t)$, the transformation becomes quasi-static, indicated by $Q^* \to 1$. Interestingly, Q^* shows an asymptotic behavior for $T \to 0$ and does not exceed ≈ 1.67. In order to reach states even more distant to equilibrium, i.e. to realize processes with higher Q^*, it is necessary to extend Eq. (5.27) to nonlinear parametrizations. Luckily enough, the Jarzynski equation is valid for *any* transformation path, so the exact experimental realization is actually secondary, as long as it is reproducible, and allows for reconstructing the transition probabilities in the way described above.

One special form of $\omega_z(t)$ shall be mentioned here, which has originally been optimized to generate highly squeezed states out of the ground state [Jan92] and which has been investigated under non-equilibrium thermodynamical aspects [Gal09]. In this protocol, $\omega_z(t)$ consists of discrete jumps between two frequencies ω_1 and ω_2, whereas in between two jumps, the frequency is kept constant for a certain time. When this time between two consecutive jumps corresponds to a quarter oscillation period $\pi/(2\omega_z(t))$ of the instantaneous frequency, the squeezing is maximal. It can be shown, that the squeezing parameter r of the quantum state (see chapter 9.4.3) grows exponentially with the number of frequency jumps [Gal09][14]. The corresponding thermodynamic nonadiabaticity parameter

[14] Herein, a system initially in the motional ground state is considered.

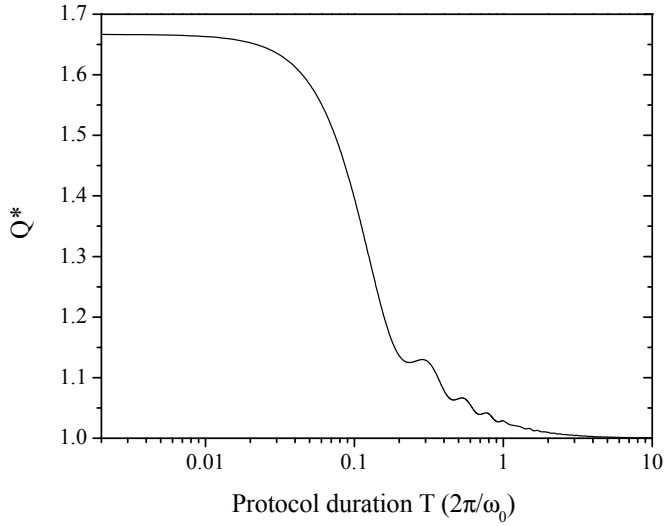

Figure 5.16: Measure of nonadiabaticity, Q^*, as a function of the protocol duration T (all other parameters as in Fig. 5.13). For large T, the quasi-static character of the process is indicated by $Q^* \to 1$. The faster the system is transformed, the more the system is driven out of equilibrium, until a maximal value for the special parametrization is reached. The oscillations around $T\frac{2\pi}{\omega_0} = O(1)$ are most probably due to resonance effects at the instantaneous frequency $\omega_z(t)$ during the transformation.

can be related to the squeezing parameter by

$$Q^* = \cosh 2r, \tag{5.29}$$

so the optimized squeezing protocol can also be used to increase Q^* efficiently.

Additionally, in this squeezed vacuum system, there is a simple and instructive relationship between Q^* and the mean energy $\langle H \rangle$ of the system, and the mean irreversible work $\langle W_{\mathrm{irr}} \rangle$ performed on the system:

$$\langle H \rangle = \frac{\hbar\omega_z(T)}{2} Q^*, \quad \langle W_{\mathrm{irr}} \rangle = \frac{\hbar\omega_z(T)}{2}(Q^* - 1). \tag{5.30}$$

Hence, the squeezed vacuum state is a system, where both the squeezing parameter and Q^* can be directly obtained by measuring the mean energy of the system through its phonon distribution.

5.4 The Driven Harmonic Oscillator

A very interesting time-dependent potential implements a driven harmonic oscillator. Again, we consider the one-dimensional case. Following the notation of the potential

transformations, the corresponding electric potential consists of two contributions: the static, harmonic trapping potential on the one hand, and a purely time-dependent term proportional to z on the other hand:

$$\phi(z,t) = \frac{m}{2}\,\omega_z\, z^2 + F(t)\cdot z. \tag{5.31}$$

In the case of the harmonically driven oscillator, $F(t)$ is a spatially uniform, classical ac field along the z-axis, which exerts a periodic force on the ion. It can be written as

$$F(t) = eE_z \sin(\omega_\mathrm{d} t + \varphi). \tag{5.32}$$

Here, φ is the phase offset of the field oscillating at frequency ω_d, and E_z is the field amplitude in z-direction. The force gives rise to the interaction Hamiltonian

$$\hat{H}_\mathrm{d}^\mathrm{I} = -eE_z z_0 \left(\hat{a}e^{-i\omega_z t} + \hat{a}^\dagger e^{i\omega_z t}\right)\, \sin(\omega_\mathrm{d} t + \varphi) \tag{5.33}$$

with respect to the motional frame $\left(z_0 = \sqrt{\frac{\hbar}{2m\omega_z}}\right)$ [Win98, Lei03]. The interaction modeled by this Hamiltonian is resonant for $\omega_\mathrm{d} = \omega_z$, i.e. when the ion "pendulum" is driven at its oscillation frequency given by the external, harmonic potential. Non-stationary terms rotating at $2\omega_z$ are neglected in a rotating wave approximation. Then, the evolution of the system is described by the operator

$$U(t) = \exp\left(\Omega_\mathrm{d}\, t\, \hat{a}^\dagger + \Omega_\mathrm{d}^*\, t\, \hat{a}\right) = D(\Omega_\mathrm{d}\, t), \tag{5.34}$$

i.e. it is equivalent to a displacement operator (see chapter 9.4.2), which displaces the state in phase space by[15]

$$\alpha = \Omega_\mathrm{d}\, t, \quad \text{where} \quad \Omega_\mathrm{d} = -\frac{eE_0 z_0}{2\hbar}\, e^{i\varphi}. \tag{5.35}$$

Equation 5.35 is interesting for two reasons. First, it tells us that the phase of the displacement can be chosen through the phase φ of the classical electric field. Second, the amplitude $|\alpha|$ of the excitation is proportional to both the duration and the amplitude of the electric field, i.e. the ac voltage amplitude applied to the electrode. Mostly, the duration of the pulse is kept constant and the amplitude is varied to realize a certain $|\alpha|$.

Two independent electronic synthesizers[16] are used to generate the displacement pulses. Each of them allows for applying highly accurately timed pulses at arbitrary frequencies,

[15] Here, we neglect the influence of the radial pseudo potential, which modifies the expression for Ω_d by a constant factor close to unity. It is not of interest in the present context because we are not interested in quantitative a priori predictions of Ω_d. Details can be found in [Lei03].

[16] WW1074, 100MS/s Four-Channel Arbitrary Waveform Generator by Tabor Electronics and 33250A Function/Arbitrary Waveform Generator, 80 MHz by Agilent.

amplitudes and phases[17]. Both devices are phase locked and their output can be synchronized with a jitter of less than 1 ns. All parameters can be dynamically programmed via the experimental control software, so that it is possible to perform parameter sweeps during a measurement. The generated pulses are applied to a pair of electrodes far away from the ion (electrodes EC1 in Fig. 9.1) to obtain an electric field only exerting forces in the axial direction.

The ability to implement coherent displacements will be very important in the following measurements. It should be noted that there are other possibilities to generate such displacements (see Ref. [Lei03] and references therein), even by virtue of light forces. These offer, for example, the advantage that they can be implemented internal state-dependent.

[17] Amplitudes can be chosen up to $\pm 10\,\mathrm{V}$ with a resolution of 16 bit; the phase has a resolution of 0.1°.

Chapter 6

Detection of the Motional State

In this chapter, different methods to detect and characterize the ion's motional state will be presented. The methods cover a wide spectrum of input states and different regimes of excitation. Some of the methods are tailored to work with special types of motional states, others are more general. For instance, temperature measurements assume a thermal energy distribution, which can then be easily characterized by a single quantity. In the most general case of an arbitrary mixed state, however, the full quantum state has to be measured, which entails a much more elaborate experimental effort.

6.1 Temperature Analysis by Sideband Excitation

The measurement technique presented in the following is used to obtain the temperature – or the mean phonon number – of an ion that can be assumed to be in a thermal state of motion[1]. It relies on the fact that the coupling strengths on the sideband transitions differ for the red and blue sidebands, respectively. This implies, that the strengths of the respective absorption lines depend on the phonon distribution of the state, so that the temperature of the distribution can be inferred from the ratio of these line strengths. In general, the mean phonon number of a thermally distributed state is given by

$$\overline{n} = \frac{R^{\frac{1}{m}}}{1 - R^{\frac{1}{m}}}, \tag{6.1}$$

where $R = P_{\uparrow}(-m\omega_z)/P_{\uparrow}(+m\omega_z)$ is the ratio of the excitation probabilities into the upper qubit state, when the ion is driven on the m-th red or blue sideband, respectively [Tur00]. Equation (6.1) is independent of the driving time and can still be applied if the coherence

[1] See section 9.4 for an overview of the most important states and their phonon distributions.

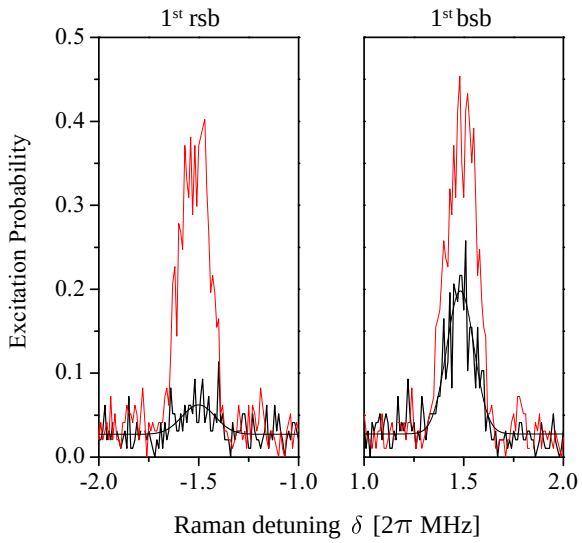

Figure 6.1: Spectrum of the ion excitation around the first motional sidebands $\delta = \pm\omega_z$. One can clearly see the asymmetry in excitation between the first red and the first blue sideband for a sideband-cooled ion (black, fitted data). In particular, the red sideband line vanishes for $\overline{n} \to 0$. From the excitation ratio, a temperature of $\overline{n} = 0.26(2)$ can be deduced after Eq. (6.1). For comparison, the same data for a hot ($\overline{n} > 10$) ion is shown (red), where no significant excitation asymmetry can be observed. The spectra were generated using the R1/R2 Raman beam configuration (see chapter 3.2.2).

times are very short. Another advantage over other techniques is, that it does not require knowledge of the Lamb-Dicke parameter.

Figure 6.1 shows the excitation spectrum of the spin qubit on the Raman transition (driven by R1/R2) around the first red and blue sideband resonance frequency (i.e. $m = \pm 1$). From the first red and blue sideband strengths, a mean phonon number of $\overline{n} = 0.26(2)$ can be deduced. This procedure works very well with very low temperatures, $\overline{n} \leq 2$. For higher $\overline{n}$, it can be advantageous to excite higher sidebands to increase the method's sensitivity (see Eq. (6.1)).

6.2 The Doppler Recooling Method

The method described in the preceding chapter enables us to determine the ion's temperature in a range of low excitations, i.e. for mean energies of some $\hbar\omega_z$. Virtually all measurement schemes throughout this chapter work in this regime, which is, of course, for a good reason: after all, the low energy regime is where interesting quantum effects come into play. However, sometimes it is necessary to be able to measure higher ener-

gies, too. This section presents such a kind of measurement, which points out to be very versatile and applicable to different kinds of states. Originally developed for temperature measurements of single ions [Wes07], we were able to extend it in order to obtain energy information about coherent excitations [Hub08a]. Energies of up to $\sim 5\,\mathrm{meV}$, corresponding to $\sim 6 \times 10^6\,\hbar\omega_z$ could be reliably determined.

6.2.1 Theoretical Model of the Scattering Process

The measurement takes place during the well-known Doppler cooling of a motionally excited ion on a fast dipole transition (in our case, this is the $S_{1/2} \leftrightarrow P_{1/2}$ transition), and is therefore called *recooling* method. It has been first proposed and applied in [Wes07, Eps07] to thermal states of the ion. As for the electronic structure, we assume a simple two-level system, where the spontaneous decay rate of the upper level be Γ. The ion itself is trapped in a harmonic well of frequency $\omega_z \ll \Gamma$, i.e. we consider the one-dimensional, weakly bound case, with the ion moving along the z-axis. As stated above, the method is to be applied in a regime, where the ion's mean motional energy is much greater than $\hbar\omega_z$, so it is justified to treat the ion motion in a classical way. Then, we can attribute the ion a certain energy E and velocity v_z, respectively.

A single laser with wavevector k_z, red detuned by $\Delta < 0$ from the atomic resonance, continuously drives the electronic transition to cool the ion. The Doppler shift $\Delta_\mathrm{D} = -k_z v_z$ leads to an effective detuning $\Delta + \Delta_\mathrm{D}$. The upper state population is then given by

$$\rho_{\mathrm{PP}}(\Delta_\mathrm{D}) = \frac{s/2}{1 + s + (2(\Delta + \Delta_\mathrm{D})/\Gamma)^2}. \tag{6.2}$$

Here, we define the saturation parameter $s := 2|\Omega|^2/\Gamma^2$ following [Wes07][2]. It is proportional to the beam intensity and is – next to the detuning – the second parameter, which can be adapted in the experiment. The spontaneous scattering rate is given by the product of the upper state population and the decay rate,

$$\frac{dN}{dt} = \Gamma \rho_{\mathrm{PP}}. \tag{6.3}$$

If we neglect heating caused by spontaneous photon emission, which only plays a role at the Doppler cooling limit, i.e. for low energies, then we can write the energy change per scattering event due to absorption of a Doppler shifted photon as

$$\frac{dE}{dN} = \hbar k_z v_z = -\hbar \Delta_\mathrm{D}. \tag{6.4}$$

[2] The definition $s := |\Omega|^2/\Gamma^2$ is common in literature, too. Then, a factor of two simply enters the formulas.

Before we proceed, we change into a dimensionless system of units by writing energies and detunings in terms of the half, saturation broadened line width E_0,

$$\varepsilon := E \,/\, E_0, \quad \delta := \hbar\Delta \,/\, E_0, \quad r := \frac{\hbar k_z^2}{2m} \Big/ E_0, \quad \text{with } E_0 := \frac{\hbar\Gamma}{2}\sqrt{1+s}, \tag{6.5}$$

while all times are rescaled according to

$$\tau := t \,/\, t_0, \quad \text{with } \; t_0 := \frac{1+s}{\Gamma s/2}. \tag{6.6}$$

In particular, $\delta_\mathrm{D} := \hbar\Delta_\mathrm{D}/E_0$ is the rescaled instantaneous Doppler shift. Now, we first rewrite Eqs. (6.3) and (6.4) in scaled units,

$$\frac{dN}{d\tau} = t_0 \frac{dN}{dt} = \frac{1}{1+(\delta+\delta_\mathrm{D})^2} \tag{6.7}$$

and

$$\frac{d\varepsilon}{dN} = \frac{1}{E_0}\frac{dE}{dN} = \frac{-\hbar\delta_\mathrm{D}}{E0} = -\delta_\mathrm{D}, \tag{6.8}$$

respectively. Combining Eqs (6.7) and (6.8) gives the energy change per time for an ion with instantaneous Doppler shift δ_D, which is determined by the ion's instantaneous velocity v_z,

$$\frac{d\varepsilon}{d\tau} = \frac{d\varepsilon}{dN}\frac{dN}{d\tau} = \frac{-\delta_\mathrm{D}}{1+(\delta+\delta_\mathrm{D})^2}. \tag{6.9}$$

As the ion undertakes harmonic oscillations due to the external potential, its velocity is sinusoidally modulated and its instantaneous Doppler shift is distributed according to the probability density [Wes07]

$$P_\mathrm{D}(\delta_\mathrm{D},\delta_\mathrm{M}) = \frac{1}{2\pi}\int_0^{2\pi} \delta_\mathrm{Dirac}(\delta_\mathrm{D} - \delta_\mathrm{M}\sin(\phi))\; d\phi = \begin{cases} \frac{1}{\pi\sqrt{\delta_\mathrm{M}^2-\delta_\mathrm{D}^2}}, & \text{if } |\delta_\mathrm{D}| < \delta_\mathrm{D} \\ 0, & \text{else} \end{cases} \tag{6.10}$$

with $\delta_\mathrm{M} := 2\sqrt{\varepsilon r}$ being the maximal Doppler shift occurring for a particle with energy ε, and δ_Dirac is the Dirac delta function. Now we can use this distribution to obtain the energy change averaged over all Doppler shifts occurring during one oscillation period,

$$\frac{d\varepsilon}{d\tau} = \int_{-\delta_\mathrm{M}}^{\delta_\mathrm{M}} P_\mathrm{D}(\delta_\mathrm{D},\delta_\mathrm{M})\; \frac{-\delta_\mathrm{D}}{1+(\delta+\delta_\mathrm{D})^2}\; d\delta_\mathrm{D}. \tag{6.11}$$

This integral can be analytically evaluated and yields a differential equation for $\varepsilon(\tau)$,

$$\frac{d\varepsilon}{d\tau} = \frac{1}{2\sqrt{\varepsilon r}}\left(\mathrm{Re}\, Z(\varepsilon) + \delta\; \mathrm{Im}\, Z(\varepsilon)\right), \tag{6.12}$$

with $Z(\varepsilon) := i\cdot[1-(\delta+i)^2/(4\varepsilon r)]^{-1/2}$. Equation (6.12) can be numerically solved to give the motional energy of the ion at any point in time during the cooling process. As long as

the parameters δ and s are fixed, the energy trajectory $\varepsilon(\tau)$ is completely determined by the ion's initial energy $\varepsilon(0)$. Similarly, the scattering rate, averaged over the oscillatory motion is

$$R(\tau) := \frac{dN}{d\tau} = \int_{-\delta_\mathrm{M}}^{\delta_\mathrm{M}} P_\mathrm{D}(\delta_\mathrm{D}, \delta_\mathrm{M}) \, \frac{1}{1 + (\delta + \delta_\mathrm{D})^2} \, d\delta_\mathrm{D}. \tag{6.13}$$

Solving this integral gives R as a function of the time-dependent energy $\varepsilon(\tau)$ [Wes07],

$$R(\tau) = R(\varepsilon(\tau)) = \frac{1}{2\sqrt{\varepsilon r}} \, \mathrm{Im}\, Z(\varepsilon) \tag{6.14}$$

i.e. $R(\tau)$ can be directly derived from the numerical result for $\varepsilon(\tau)$ (r and δ are time-independent parameters).

Equations (6.12) and (6.14) have approximate analytical solutions in the limit of high energies ($\varepsilon \gg (1 + \delta^2)/r$). These are

$$\varepsilon(\tau) \approx \left(\varepsilon_0^{3/2} + \frac{3\,\delta\,\tau}{4\sqrt{r}} \right)^{2/3} \tag{6.15}$$

and

$$R(\varepsilon) \approx \frac{1}{2\sqrt{\varepsilon r}}, \tag{6.16}$$

respectively. They are instructive to get an idea of the qualitative behavior of these functions. For quantitative analysis, the exact, numerical solutions were applied.

$R(\tau)$ is a quantity, which is directly accessible in the experiment. It is proportional to the fluorescence rate detected during the recooling process. Just like $\varepsilon(\tau)$, its temporal behavior is determined solely by the initial energy once the laser parameters are fixed. Figure 6.2 shows numerical results for $\varepsilon(\tau)$ and $R(\tau)$. The quantities are plotted for three different detunings $\delta = -\sqrt{3} \approx -1.73$, $\delta = -1$ and $\delta = -1/\sqrt{3} \approx -0.58$. In Fig. 6.2(a), the monotonic decrease of the ion's motional energy in the course of the cooling process can be seen. Figure 6.2(b) depicts the fluorescence rate of the ion during cooling.

Interestingly, the scattering rate is not necessarily a monotonic function of time but has a maximum when $\delta < -1/\sqrt{3}$. This maximum occurs at an energy, where the maximum of the Doppler shifted absorption line (Eq. (6.7)) coincides with one of the two peaks of the Doppler distribution (Eq. (6.10)). Then, the two terms in the integral of Eq. (6.13) contribute maximally. For $\tau \to \infty$, a constant scattering rate ensues, when the energy has reached its steady state.

Extensions and Numerics

So far, we assumed ions with definite initial energy. Now, we want to generalize this picture to such cases where the energy follows a certain probability distribution $P_{\bar{\varepsilon}}(\varepsilon')$.

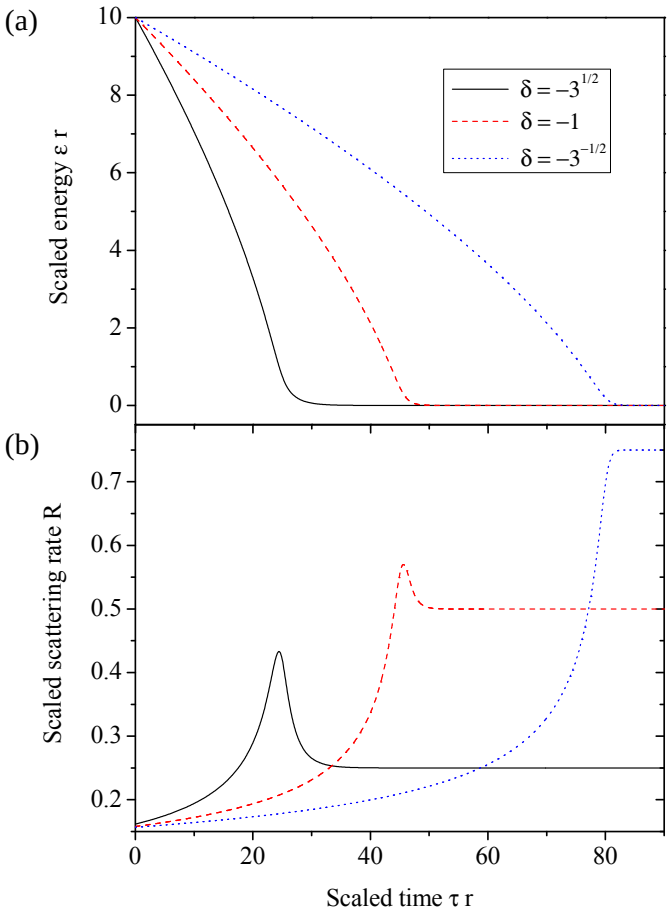

Figure 6.2: (a) Motional energy of the ion as a function of time during the cooling process for different laser detunings after Eq. (6.12). Starting from $\epsilon = 10/r$, the energy decreases monotonically and reaches a steady state-value, which is small compared to the starting value.
(b) Photon scattering rates R during cooling after Eq. (6.14), corresponding to the three situations in (a). For $\delta < -3^{-1/2}$, $R(\tau)$ has a maximum before the steady state is reached (see text). As expected, the smaller δ is chosen, the higher is the final scattering rate.

For example, in order to measure thermally distributed initial states, a thermal distribution of the initial energies can be assumed. In these cases, the scattering traces $R(\tau)$ must be averaged over all initial energies ε', weighted according to the probability density $P_{\bar{\varepsilon}}(\varepsilon')$,

$$R_{\bar{\varepsilon}}(\tau) = \int_0^\infty P_{\bar{\varepsilon}}(\varepsilon')\ R[\varepsilon = \Xi(\varepsilon', \tau)]\ d\varepsilon', \tag{6.17}$$

where the index $\bar{\varepsilon}$ indicates that a distribution with mean value $\bar{\varepsilon}$ is considered. $R[\varepsilon]$ is the scattering rate of an ion with energy ε. An ion with initial energy ε', which was cooled for a time span τ, has the energy $\Xi(\varepsilon', \tau)$ afterwards. Note, that the trajectory of $\epsilon(\tau)$ (Fig. 6.2(a)) is fixed for given laser parameters, i.e. ions with different initial energies simply start from different points on the curve. Having this in mind, the action of the propagator

$\Xi(\varepsilon', \tau)$ becomes obvious, since it simply makes the ion proceed on the trajectory: starting from $\varepsilon = \varepsilon'$ it moves on for time τ, and thus reaches the energy $\Xi(\varepsilon', \tau)$.

In a first step, we will subdivide the evolution into discrete time steps of size $\Delta\tau$; the corresponding energies start at $\varepsilon_0 := \varepsilon(\tau = 0)$ and all succeeding energies can be written in terms of the propagator, $\varepsilon_n := \Xi(\varepsilon_0, n\Delta\tau)$ for $n = 0, 1, \ldots, \infty$. That means, that the propagator simply proceeds n "steps" on a discretized version of $\varepsilon(\tau)$. Thus, it becomes obvious that $\Xi(\varepsilon_m, n\Delta\tau) = \Xi(\varepsilon_0, (m+n)\Delta\tau) = \varepsilon_{m+n}$.

The integral in Eq. (6.17) covers values from 0 to ∞. In good approximation, we can replace the lower limit by the ion's ("cold") steady-state energy $\varepsilon_\infty \ll \bar{\varepsilon}$ and the upper limit by some finite, large value $\varepsilon_0 \gg \bar{\varepsilon}$. Then, the integral can be split into parts according to

$$\int_0^\infty \approx \int_{\varepsilon_\infty}^{\varepsilon_0} = \sum_{m=0}^{\infty} \int_{\varepsilon_{m+1}}^{\varepsilon_m}. \tag{6.18}$$

and we get

$$R_{\bar{\varepsilon}}(\tau) \approx \sum_{m=0}^{\infty} \int_{\varepsilon_{m+1}}^{\varepsilon_m} P_{\bar{\varepsilon}}(\varepsilon')\ R[\varepsilon = \Xi(\varepsilon', \tau)]\ d\varepsilon'. \tag{6.19}$$

Secondly, the scattering rate $R(\tau)$ is assumed to be constant within each time interval of size $\Delta\tau$. The average rate $R_n \approx R[\Xi(\varepsilon_0, \tau)]$ for $\tau \in [n\Delta\tau, (n+1)\Delta\tau[$ corresponds to the energy occurring after the n-th propagation step. It can be calculated independently from the specific distribution $P_{\bar{\varepsilon}}(\varepsilon)$ after Eq. (6.14). Then, with $\tau \approx n\Delta\tau$ we can approximate the propagator $\Xi(\varepsilon', \tau)$ within each interval $\varepsilon' \in [\varepsilon_m, \varepsilon_{m+1}[$ by

$$\Xi(\varepsilon', n\Delta\tau) \approx \Xi(\varepsilon_m, n\Delta\tau) = \Xi(\varepsilon_0, (m+n)\Delta\tau) = \varepsilon_{m+n}, \tag{6.20}$$

so that the scattering rate occurring in the integral can be replaced by $R[\varepsilon = \Xi(\varepsilon', \tau)] \approx R_{m+n}$, giving the scattering rate in the n-th time step as

$$R_{\bar{\varepsilon}}(n\Delta\tau) \approx \sum_{m=0}^{\infty} R_{m+n} \int_{\varepsilon_{m+1}}^{\varepsilon_m} P_{\bar{\varepsilon}}(\varepsilon')\ d\varepsilon'. \tag{6.21}$$

This equation enables us to determine the time-dependent scattering rate for arbitrary initial state distributions. For a given distribution, the integral in Eq. (6.21) can be evaluated analytically or numerically. In the case of a (classical, $\hbar\omega_z \ll k_\mathrm{B}T$) thermal distribution

$$P_{\bar{\varepsilon}}(\varepsilon) = \frac{1}{\bar{\varepsilon}}\, e^{-\varepsilon/\bar{\varepsilon}}, \tag{6.22}$$

there is an analytical solution given in [Wes07].

Large Ion Excursions

So far, we assumed the ion to be uniformly illuminated by the cooling laser. This is a fairly good assumption if the motional wave function of the state is small compared to the beam diameter, as it is the case for "trapped" thermal states. When, however, we consider states implying classical oscillations of the particle within the harmonic potential, then the finite beam waist has to be taken into account. For example, the oscillation amplitude of a $^{40}Ca^{+}$-ion with energy 1 meV is as big as 55 μm in a trap with $\omega_z = 2\pi \times 200\,\mathrm{kHz}$. Even worse, as the laser beam points to the potential minimum, the velocity of the ion is maximal in the beam center, i.e. its dwell time is minimal here, while it is found most of the time in the lower intensity periphery of the beam (the cooling beam has a Gaussian intensity profile with $1/e^2$ waist w_z). Accordingly, the scattering and cooling processes can be strongly reduced, so that the model above has to be modified.

The inhomogeneity of the cooling laser intensity is accounted for by a modification of the saturation parameter [Deu07] according to

$$s = s(\delta_\mathrm{D}, \delta_\mathrm{M}) = \frac{I_0}{I_\mathrm{sat}} \exp\left[-\frac{2\lambda}{r}\left(\frac{z_0}{w}\right)^2\left(\delta_\mathrm{M}^2 - \delta_\mathrm{D}^2\right)\right], \tag{6.23}$$

where λ is the laser wavelength, $z_0 = \sqrt{\hbar/(m\omega_z)}$ and $I_\mathrm{sat} = 2\pi^2\hbar c\Gamma/(3\lambda^3)$. I_0 is the peak intensity at the beam center. As the saturation parameter is now no longer static, it is removed from the system of units and all quantities are rescaled by replacing E_0 in Eq. (6.5) by

$$E_0 \to E_0' := \hbar\Gamma/2, \tag{6.24}$$

and times are expressed in units of $t_0 \to t_0' := 1/\Gamma$. Then, s appears explicitly in Eq. (6.11), which becomes

$$\frac{d\varepsilon}{d\tau} = \int_{-\delta_\mathrm{M}}^{\delta_\mathrm{M}} P_\mathrm{D}(\delta_\mathrm{D}, \delta_\mathrm{M}) \, \frac{-\delta_\mathrm{D} \cdot s/2}{1 + s + (\delta + \delta_\mathrm{D})^2} \, d\delta_\mathrm{D}. \tag{6.25}$$

Accordingly, the modified version of Eq. (6.13) reads

$$R(\tau) := \frac{dN}{d\tau} = \int_{-\delta_\mathrm{M}}^{\delta_\mathrm{M}} P_\mathrm{D}(\delta_\mathrm{D}, \delta_\mathrm{M}) \, \frac{s/2}{1 + s + (\delta + \delta_\mathrm{D})^2} \, d\delta_\mathrm{D}. \tag{6.26}$$

The solution of these equations can be found in the same way as has been described above, i.e. by stepwise integration along an energy trajectory. The following section will show results from measurements on coherently excited ions. When the coherent excitation is large enough, the energy uncertainty of the ion becomes negligible and the distribution simplifies again to $P_{\bar{\varepsilon}}(\varepsilon') = \delta_\mathrm{Dirac}(\varepsilon' - \bar{\varepsilon})$. This is the case in the following, where the mean energies are on the order of 1 meV.

6.2.2 Recooling Measurement of Shuttled Ions

In the previous chapter, a procedure was introduced that allows for measuring the (mean) energy of ions, which overcharges those techniques sensitive for single quanta. It is now applied to characterize the quality of ion transports in the segmented trap. The transport scheme has already been extensively discussed in chapter 5.2, so that only a short summary will be given here. We already discussed the need of *fast* transports, i.e. transports which are not so slow to be regarded quasi-static any more, but rather happen on timescales given by the inverse trap frequency $2\pi/\omega_z$. In chapter 5.2.2, we saw that the probability for a successful ion transport depends on the transport duration. This could be explained by the aid of the maximum energy imparted to the ion during the transport. If this energy gain becomes too high, the ion gets lost, i.e. falls out of the trap. Next, a more quantitative study is presented to understand the dynamics in the system. For this purpose, transports like the ones in chapter 5.2.2 are performed and the final energy of the shuttled ions is measured by the recooling scheme. This, carried out for different types of transports, yields very helpful insight into the transport mechanism and helps to improve its realization.

The experiments were conducted in the pcb-trap (see 9.1.2). The transports were, again, performed as closed round trips with a one-way distance of 2 mm; they were realized by moving an electric, harmonic potential along the z-axis according to a transport function $z_0(t)$, where $z_0(t)$ is the momentary position of the potential minimum at time t (illustrated in Fig. 5.3). We decided for a sigmoid, smooth transport function after Eq. (5.11); by a proper choice of its "steepness"-parameter σ, the transport character can be implemented almost linear ($z_0 \propto t$), sigmoid, or – as an extreme – in a single step. Apart from σ, the transport duration T is the second parameter whose influence on the shuttle quality is to be tested for now. Again, we denote by T the time needed for a complete round trip, i.e. $z_0(0) = z_0(T)$, and $\tau = T\omega_z/(2\pi)$ gives the total duration measured in oscillation periods. The trap frequency was chosen fairly low, $\omega_z = 2\pi \times 200\,\mathrm{kHz}$, in order to be able to reach a non-adiabatic regime with the electronics available; the update time of the trap voltages was $1\,\mu$s.

The experimental protocol is close to that of the transport success probability measurements, cf. chapter 5.2.2. Here, however, the fluorescence of the ion during the laser cooling process after each ion shuttle was recorded time-resolved, see Fig. 6.3. This means, that the ion is prepared by Doppler cooling on the 397 nm $S_{1/2} \rightarrow P_{1/2}$ -transition at the starting position $z_0(0)$, is then shuttled to $z_0(T/2)$ and back to $z_0(0)$ again by applying the corresponding transport voltages [Hub08a]. Finally, the same cooling laser typically

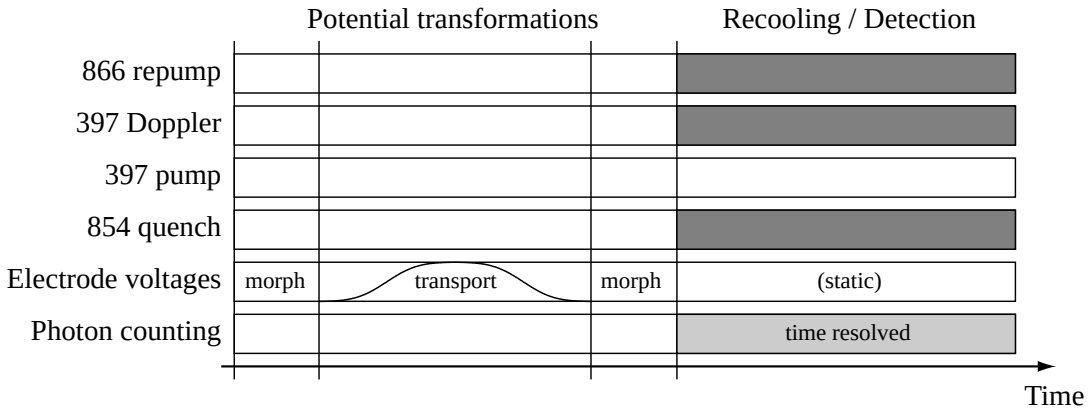

Figure 6.3: Illustration of the temporal sequence of a recooling experiment. After morphing the potential from laser-interaction potential into the initial transport potential, the ion is shuttled back and forth. Then, the potential is morphed back and the fluorescence emitted by the ion during the recooling is recorded in a time-resolved manner. The recooling finally prepares the ion into a cold state for the next experiment round.

illuminates the ion for several milliseconds, red detuned by approximately half the natural linewidth of the transition. This was ensured by setting the detuning such that half the level of the peak fluorescence at resonance was observed. This recooling beam was attenuated to end up with a low saturation parameter s, but enough intensity to let the scattering rate drop not too low.

The fluorescence photons emitted by the ion from the point of time on when the recooling laser is switched on are detected by a photomultiplier, whereas each photon's arrival time is recorded with $1\,\mu$s resolution. The applied trick to accomplish this with the standard counter hardware is detailed in chapter 9.3. The recooling time must be chosen long enough to ensure that the ion is in a well-defined, reproducible state before the next transport starts. Thus, the transports can be regarded independent from each other, and the recooling process of the current transport can be used to prepare the ion for the succeeding cycle. Typically, these transports are repeated some hundred to some thousand times for one specific transport type. From the measured fluorescence traces, the energy of the transported ions can be deduced as it was described above.

Figure 6.4 shows raw recooling data after a transport with $T = 2 \times 14\,\mu$s. It was realized with a fairly smooth transport function ($\sigma = 2$) to avoid momentum kicks at the corner points. In Fig. 6.4(a), the arrival time of the first 150 photons during the recooling process is plotted against the photon number. The first photon arrived $7\,\mu$s after the laser was switched on, and the last photon plotted arrived $\approx 13\,$ms later. The graph in Fig. 6.4(b) shows the same data, whereas here, the total number of detected photons is plotted as a

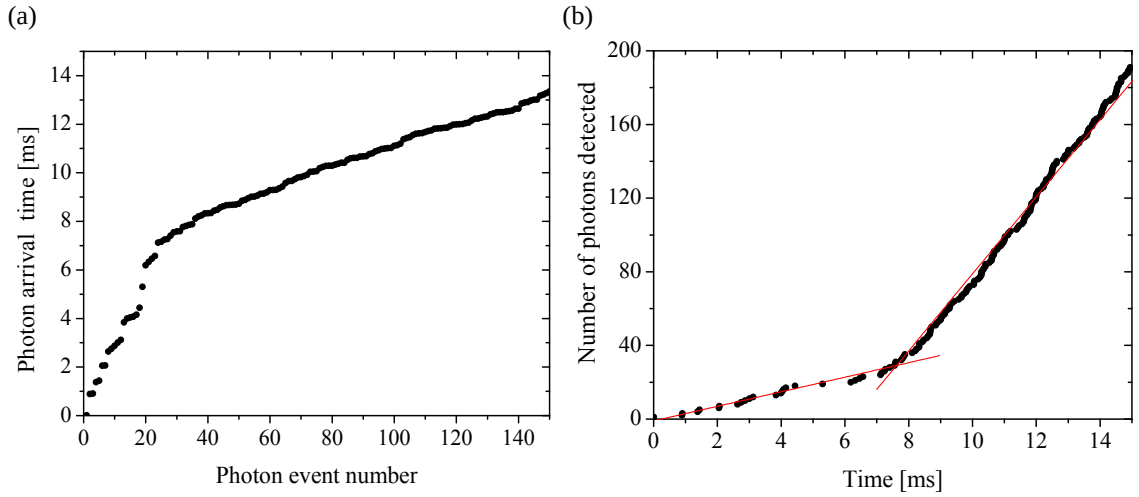

Figure 6.4: Data obtained by the recooling method. Each data point corresponds to one photon detected during laser cooling of a single ion. Time starts when the cooling laser is switched on. (a) shows raw data, i.e. the time of arrival of each photon event plotted against the event number. The "kink" at $\approx 8\,\mathrm{ms}$ indicates a rapid increase in fluorescence scattering rate due to efficient cooling setting in. (b) The same data in a more intuitive representation. Here, the accumulated number of photons is plotted as a function of time. The red lines are guides to the eye corresponding to fluorescence rates of 4 kHz and 21 kHz, respectively.

function of time. From both graphs, two different scattering behaviors can be discerned: a very low fluorescence rate until $t \approx 8\,\mathrm{ms}$, when the rate abruptly increases and quickly saturates at a high level.

This behavior becomes even more evident in a histogram of the photon detection events (see Fig. 6.5(a)). Such a histogram contains the number of photons detected during time intervals of equal duration (here, one time bin covers 1 ms), which is equivalent to the photon count rate. In this depiction, the rapid increase in scattering rate can be clearly seen.

For the evaluation of these traces, the ion was assumed to be in a coherent state with such an amplitude that its movement can be treated classically, i.e. the ion effectively oscillates back and forth within the final harmonic potential, and doing so, it traverses the cooling beam; this beam has a waist of only $60\,\mu\mathrm{m}$, so at the beginning, when the oscillation amplitude of the ion still exceeds the beam diameter, the ion spends most of the time outside the beam and is decelerated only inefficiently. The smaller the amplitude of the oscillation becomes, the more efficient is the cooling process, however; when it has become so small, that the ion stays within the beam diameter, the energy decrease takes place abruptly and the fluorescence rate quickly saturates. Thus, the main contribution

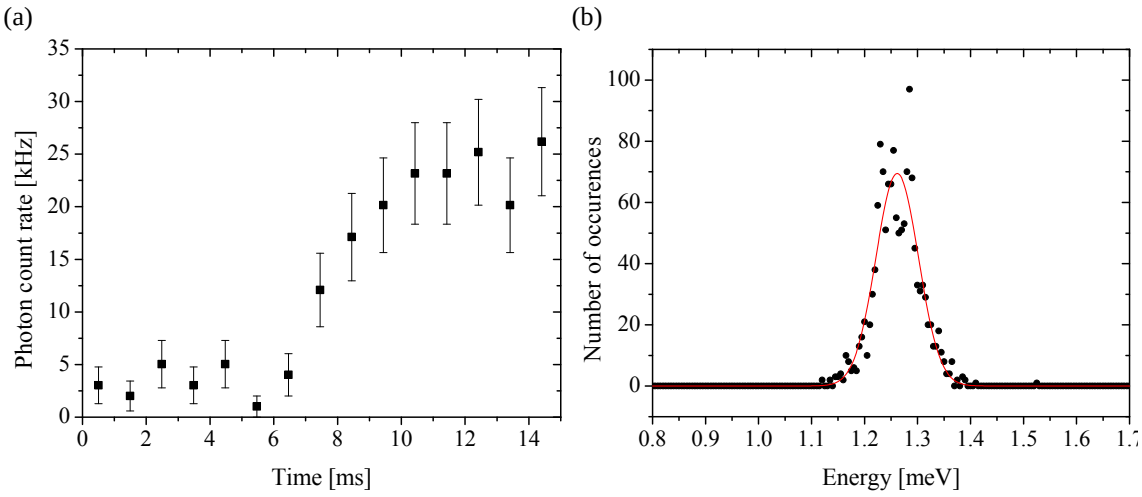

Figure 6.5: (a) A histogram of the arrival times taken from a single recooling trace gives the fluorescence rate as a function of time (the error bars indicate the statistical uncertainty (standard deviation) of the fluorescence rate). Again, a rapid increase in the scattering rate at $t \approx 8\,\mathrm{ms}$ indicates efficient cooling setting in. From this time, the initial energy ε_0 of the ion can be deduced (see text). (b) shows a histogram of the initial ion energies obtained from 1412 identical transports. The red line is a Gaussian fit giving a mean energy of 1.262 meV with a standard deviation of 0.040 meV.

of cooling happens within 1 to 4 ms, which is in accordance with common cooling times of trapped ions. The time it takes the ion to reach 50 % of the final fluorescence level is indeed characteristic for the ion's initial energy and thus can be used as a qualitative measure for this quantity.

As explained in chapter 6.2.1, a trace of the scattering rate like the one depicted in Fig. 6.5(a) is determined by its energy at the beginning of the recooling process, i.e. immediately after all potential transformations. We evaluated several thousand of such traces, each performed with a certain transport duration T. It is worth mentioning that each of these traces is the result of a single recooling process after a single ion transport. This means that the energy of each ion could be measured, in contrast to an averaging measurement summing up the signals generated by many transport executions. This makes it possible to investigate the single ion energy distribution. Such a distribution for the same shuttles like in Fig. 6.5(a) is shown in Fig. 6.5(b). Here, an energy histogram of 1412 identical, independent transports proves that the energy distribution of the ions after the transport has a width of only 3%. This speaks for a high degree of reproducibility in terms of preparation, voltage generation and detection.

Variation of the Transport Duration

Now, the effect of the transport duration on the final ion energy is to be investigated by performing measurements with different durations τ. Shuttles close to the adiabatic case resulted from $\tau = 50$; the voltage generation electronics allowed for lowering this value down to $\tau = 4.4$ without significant increase of ion loss (this behavior was already discussed, cf. Fig. 5.11). This value is still remarkable, since it means that – due to the limiting update rate of 1 MHz – the one-way transport over 2 mm was indeed carried out in only 11 discrete steps; each discrete step involves a small momentum kick for the ion. Simulations confirm that the discrete character of the trap voltages plays a role for τ approaching unity, but its influence remains acceptable for $\tau \gtrsim 5$. All transports were conducted with a sigmoid transport function after Eq. (5.11) with $\sigma = 2.0$.

Figure. 6.6(a) shows averaged recooling traces for a range of values of τ. In general, one can recognize that the recooling effect, indicated by a strong increase in fluorescence, sets in later, the faster the transport is realized. This, again, indicates a higher motional excitation as explained above.

The derived ion energies after the transport as a function of τ are depicted in Fig. 6.6(b). As can be seen, the theoretically predicted final ion energy (red dotted line) based on classical trajectory simulations is not confirmed by the experimental data. Indeed, the measured energies are systematically larger than the expected ones. The simple, idealized model of the transport does not, however, include the morphing steps immediately before and after each transport round.

From measurements replacing the ion shuttling by simple waiting times of duration T, but with constant electrode voltages in between the two morphs, the motional excitation energy due to the morphing could be deduced; it amounts to 427(73) μeV. Adding this offset energy to the theoretical contribution of the shuttle process (solid red line in Fig. 6.6(b)) yields a model fitting well to the data.

The results retrieved here match the expectations arising from the success probability measurements in chapter 5.2.2. For slow transports, the excitation caused by the shuttle process is small and the ion mainly resides in the potential minimum throughout the transport. The faster the process is carried out, the higher the excitation becomes. The sharp resonances (see chapter 5.2.2) at $\tau = 4, 6, 8, ...$ could unfortunately not be resolved with the control electronics at hand; nevertheless, these results pave the way for the realization of accurate, reliable and non-adiabatically fast ion shuttles.

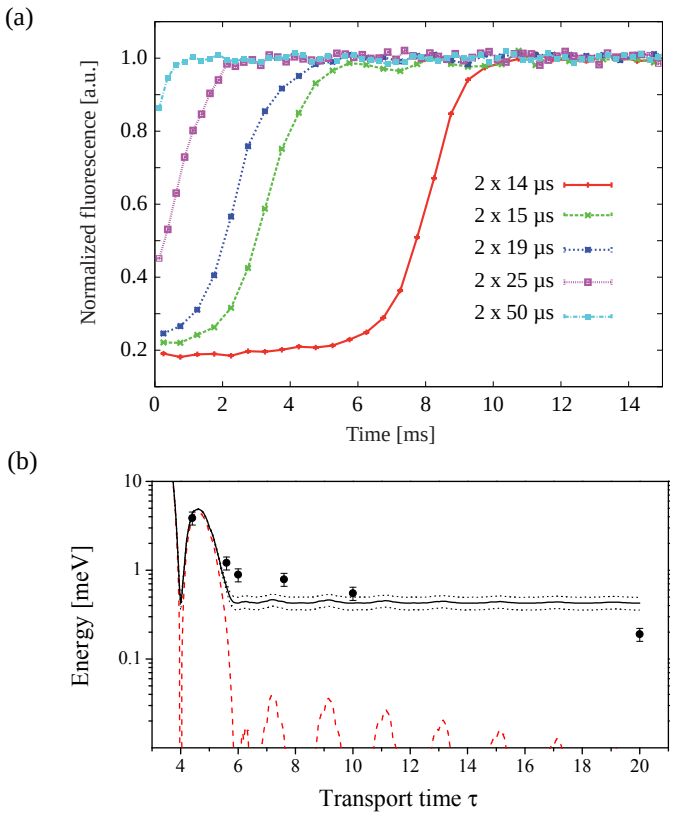

Figure 6.6: a) Fluorescence rate after the transport and during Doppler recooling, averaged over many realizations. The faster the transport, the later the ion can be recooled into its steady state, indicating a higher vibrational excitation. b) Energy after the transport with $\tau = 4.4 - 20$, deduced from the recooling scattering traces. Error bars indicate uncertainties in terms of laser beam waist $(30(5)\,\mu\mathrm{m})$, laser saturation and detuning $(2\pi \times 30\,\mathrm{MHz})$. The overall uncertainty results in 15 % errors. The red dashed line is a theoretical prediction of a simple model of the transport process alone, which must be extended by taking the morphing steps into account (see text); the black solid line shows the modified prediction together with its standard deviation (black dashed line).

Influence of the Heating Rate

The recooling method has also been applied to obtain the trap's heating rate. This heating occurs due to time-varying, unavoidable electric fields in the trap and affects the motional state of the ion such that it slowly thermalizes with its environment. This effect will be investigated in detail in chapter 7.2.

To find out, how fast the thermalization takes place in the pcb-trap, the ion was repeatedly prepared by Doppler cooling. In a static potential, i.e. without potential transformation, and after a waiting time T_h, during which all lasers are switched off, the motional state of the ion was measured; this happened by means of the recooling method assuming a

thermal phonon distribution. The obtained mean energies for $T_\mathrm{h} = 0.5\,\mathrm{s}$ and $T_\mathrm{h} = 2\,\mathrm{s}$, respectively, are in good approximation proportional to the heating time T_h and amounted to $3(1)\,\mathrm{meV/s}$. This means, that the energy increase during the transport due to this heating effect is about $1.5\,\mu\mathrm{eV}$ and thus negligible.

The obtained heating rate corresponds to $\approx 3.6 \times 10^3$ phonons per millisecond and therewith exceeds comparable heating rates by three to four orders of magnitude. This cannot be solely attributed to the low phonon energy of $h \times 200\,\mathrm{kHz}$. Rather, it is probably caused by patch charges on the relatively large insulating surfaces of this trap design. This finding was an important input for the design and development of a new generation of segmented traps: the segmented micro-trap (see chapter 9.1.1), in which most of the experiments presented in this thesis were performed in, could be made to perform much better in this respect.

Another reason is a noisy voltage supply for the trap electrodes, giving rise to random, fluctuating forces on the ion. Frequency components around ω_z can change the ion's motional state[3] in an unwanted and damaging way. One way to overcome this problem of most commercial supplies, could be low-pass filtering the electrode voltages. While this is an easy and effective means to get rid of the noise, it is not always applicable if time-dependent potentials are to be used. Especially fast transformations imply frequency components on the order of the trap frequency that must not be filtered away. So either, the wanted voltage changes can be amplified frequency-dependent in order to compensate for the filter transmission, or instead of filtering the voltages, one tries to get rid of the noise. This is even more demanding considering the long-term aim to scale up the electrode number, and – consequently – the number of voltages needed (the applied solution for fast, parallelized voltage generation for the micro-trap is described in chapter 9.2).

The Optimal Transport Function

The exact shape of the transport function $z_0(t)$ plays a crucial role in terms of energy excitation and different types (sinusoidal, sigmoid, ...) have been investigated theoretically [Rei06, Mur09]. Their differences become especially important if it comes to short times and very low excitations, i.e. single motional quanta. We investigated the influence of the transport function on the transport quality by performing the same transports ($T = 50\,\mu\mathrm{s}$) with different parameters σ in Eq. (5.11). The action of this parameter can best be seen in Fig. 5.8.

[3] Of course, the radial and micromotion-caused resonances have to be taken into account here, too.

The measurements show indeed that the optimal parameter (for a given T) is a compromise between a smooth behavior at the corner points, and not too high velocities on the way. The slower the ion starts and stops (i.e. the larger σ), the faster the ion has to go in the middle of the shuttle. This fast acceleration strongly excites the ion in the harmonic well. On the other hand, the more linear the transport becomes, the stronger the ion is excited by kicks[4] at $t = 0, T/2, T$.

Consequently, we found an optimal value of $\sigma \approx 2.3(2)$, indicated by a minimal motional excitation of the ion after the transport (see Ref. [Hub08a]). This value realizes a sigmoid transport function as it has been used for the non-adiabatic transports presented. Lower values $1 \leq \sigma < 2$, implying a more and more linear shuttle, result in a higher energy gain. When $z_0(t)$ becomes too steep ($\sigma \gtrsim 3.0$), the energy gain is so strong that it often led to ion loss. This must be attributed to the sudden "step" in $z_0(t)$, which is too fast for the ion to follow.

6.3 Motional State Analysis by Coherent Excitation

In contrast to the recooling method, the following measurement procedure works in a regime of single motional quanta and is a very versatile tool [Mee96]. It allows for measuring the phonon number distribution $P(n)$ of an arbitrary input state. $P(n)$ gives the probability of finding the ion in the n-th eigenstate of the harmonic oscillator, $|n\rangle$. In the most general case, these probabilities are given by the diagonal elements of the density matrix, $\rho_{nn} = \langle n| \rho |n\rangle$. As non-diagonal elements do not influence the measurement signal, these cannot be measured by this procedure. Nevertheless, it is an excellent and fast tool to characterize a wide variety of states, especially if a certain class of states can be presupposed. These classes, for example, comprise thermal states (which do not have off-diagonal elements), Fock states, coherent and squeezed states.

The technique is based on the dependence of the Rabi frequency $\Omega_{n,n+m}$ of the m-th sideband transition on the quantum number n. In the regime we are interested in ($n \leq 15$), this dependence is much stronger on the first sidebands than on the carrier transition (cf. Fig. 3.1). As the coupling on the first red sideband vanishes for $n = 0$, the first blue sideband transition is the best choice, $m = +1$. We exploit the dependence by measuring the evolution of the qubit state when the first bsb transition is resonantly

[4] The error function is, of course, always truncated at finite times, so that its derivatives do not vanish exactly. However, this truncation effect becomes smaller the larger σ is and can be neglected if it is of the same magnitude as the steps caused by the digital-to-analog converters.

driven. According to Eq. (3.25), the resulting function $P_\uparrow(t)$ can be written as a sum of cosine functions with amplitudes proportional to $P(n)$ at frequencies $\Omega_{n,n+1}$. As these frequencies are known, a Fourier transform of the measured trace yields the probabilities $P(n)$.

It is also possible to fit Eq. (3.25) with $m = +1$,

$$P_\uparrow(t) = \frac{1}{2} \sum_{n=0}^{\infty} P(n) \left(\cos(\Omega_{n,n+1} t)\ e^{-t/\tau_c} \ + \ 1 \right) \tag{6.27}$$

directly to the signal, whereby τ_c and all $P(n)$ are fit parameters. This mostly yields satisfactory results. The lowest Rabi frequency $\Omega_{0,1}$, and from that all others, can be obtained beforehand by a frequency analysis. A variation of the fit parameters and an analysis of their influence on the overall fit result makes it possible to estimate their error bars. While the phonon distribution is defined for an infinite number of $n \geq 0$, the sum in Eq. (3.25) has to be truncated in practice at some point $n_{\max}$, and only values $0 \leq n \leq n_{\max}$ are taken into account. As the choice of $n_{\max}$ is arbitrary to some extent, it is convenient to average the obtained results over different choices of $n_{\max}$. Typically, $n_{\max} = 4 - 12$ in our applications.

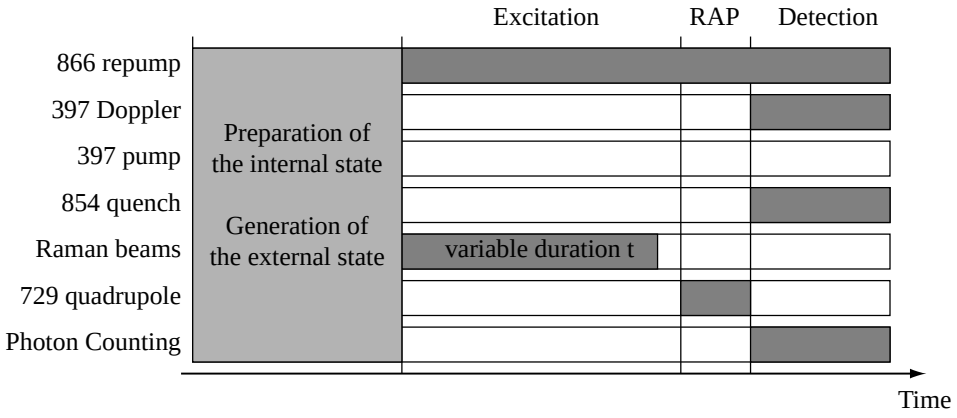

Figure 6.7: Schematic timing for state analysis by Rabi flopping. We assume that the ion has been prepared in the internal state $|\uparrow\rangle$ and in an unknown motional state. A Raman pulse of duration t excites the ion on the bsb transition and generates a superposition between $|\uparrow\rangle$ and $|\downarrow\rangle$. The amplitude of this superposition is detected by the common detection scheme of the spin qubit (see chapter 3.2.2). Repetitive application of this scheme yields $P_\uparrow(t)$.

A schematic timing table for measuring the evolution of $P_\uparrow(t)$ is depicted in Fig. 6.7. First, the ion is cooled, its internal state is prepared by optical pumping into $|\uparrow\rangle$, and then the motional state of the ion is generated, which could have happened, for example, by one of the techniques described in chapters 4 and 5. Then, the ion is illuminated by the Raman

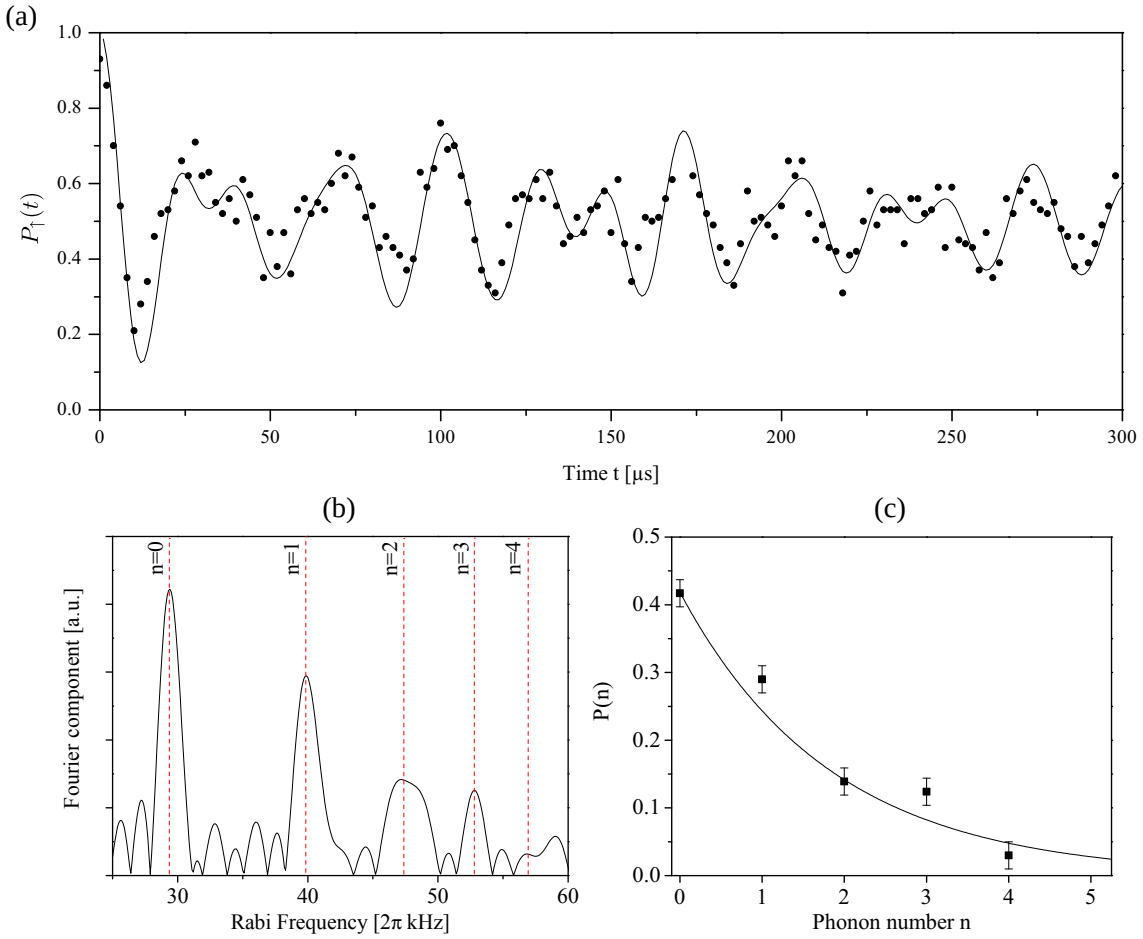

Figure 6.8: Illustration of the state analysis method by Rabi flopping. The ion was prepared in $|\uparrow\rangle$ and an unknown motional state. (a) Population in $|\uparrow\rangle$ after excitation of the first bsb transition for a time t. Solid line: Theoretical evolution of a state with the phonon distribution obtained in (c). (b) shows the result of a cosine Fourier transform of $P_\uparrow(t)$. One can clearly see that the signal exhibits discrete frequency components. The lowest frequency peak can be associated with $\Omega_{0,1} = 2\pi \times 29.4\,\mathrm{kHz}$. (c) Phonon number distribution deduced from the Fourier components shown in (a). The solid line is a fit of a thermal distribution with $\overline{n} = 1.39(17)$.

laser beams R1/R2 on the first bsb transition for a certain time t. This excites the ion into a superposition state between the spin qubit states, which is read out in the following detection procedure. Repeating this often (typically 100 to 200 times), yields the mean excitation $P_\uparrow(t)$ for time t.

Figure 6.8(a) shows a typical trace of an ion in a low thermal state. Here, t was varied between 0 and 300 μs. Due to the low decoherence rate, one can clearly see many oscillations and the non-harmonic evolution caused by the different frequency components.

To obtain the distribution $P(n)$, we performed a cosine Fourier transform of $P_\uparrow(t)$ yielding

frequency components $\Omega_{n,n+1}$, which are directly proportional to $P(n)$. Figure 6.8(b) shows the frequency spectrum of the signal in (a) obtained by such a signal transformation. One can clearly see that the signal has a discrete frequency spectrum. Each peak can be associated with a phonon state and its bsb Rabi frequency, respectively. The corresponding phonon number distribution can be seen in Fig. 6.8(c). It fits to a thermal state with $\overline{n} \approx 1.4$. The corresponding temperature in a trap with $\omega_z = 2\pi \times 1.4\,\mathrm{MHz}$ is $125\,\mu\mathrm{K}$.

Therewith, we have demonstrated a method for the quick and reliable measurement of general phonon distributions. This method also forms the basis of measuring the complete density matrix ρ of the motional state. This will be described in section 6.4.

It is worth mentioning, that this method is predestined for a fast determination of mean values. For instance, the mean energy, i.e. the expectation value of the Hamiltonian H of an arbitrary mixed state ρ, can be written as

$$\langle H \rangle = \mathrm{Tr}\,\{H\rho\} = \sum_{n=0}^{\infty} E_n \cdot \rho_{nn}, \tag{6.28}$$

where $E_n = \hbar\omega_z(n + \frac{1}{2})$ is the eigenvalue of H corresponding to the eigenstate $|n\rangle$. These eigenvalues, of course, are well-known in the case of the harmonic oscillator, where the trap frequency can be measured very accurately by spectroscopic means.

6.3.1 Analysis of Displacement Amplitudes

In the following, a couple of applications are described proving the presented detection scheme's power and versatility. It is used as an "all-round" tool in diverse situations. Here, a special focus of interest lies on testing our abilities to generate coherent displacements $D(\alpha)$ of an unknown state, a prerequisite for many future applications. In chapter 5.4, an experimental possibility was presented to generate coherent displacements of an arbitrary motional state. Now that we also have a method at hand to detect the motional state of the ion, we can apply and test the method. As described above, the displacement is caused by an oscillating force acting on the ion. This force is due to an electric ac potential. The according ac voltage has frequency ω_z and amplitude U. For quantitative measurements, it is necessary to know which amplitude U has to be applied in order to generate a certain displacement[5] $|\alpha|$. Figure 6.9 shows the results of such a gauge measurement. Here, a near-ground state cooled ion has been displaced by fields with $U = 10\,\mathrm{mV}$, $20\,\mathrm{mV}$ and $30\,\mathrm{mV}$ amplitude, before $|\alpha|$ has been determined by the Rabi oscillation method. Figure 6.9(a) depicts the corresponding coherent blue sideband dynamics excited by the

[5] The phase of the coherent state is not detected in this measurement.

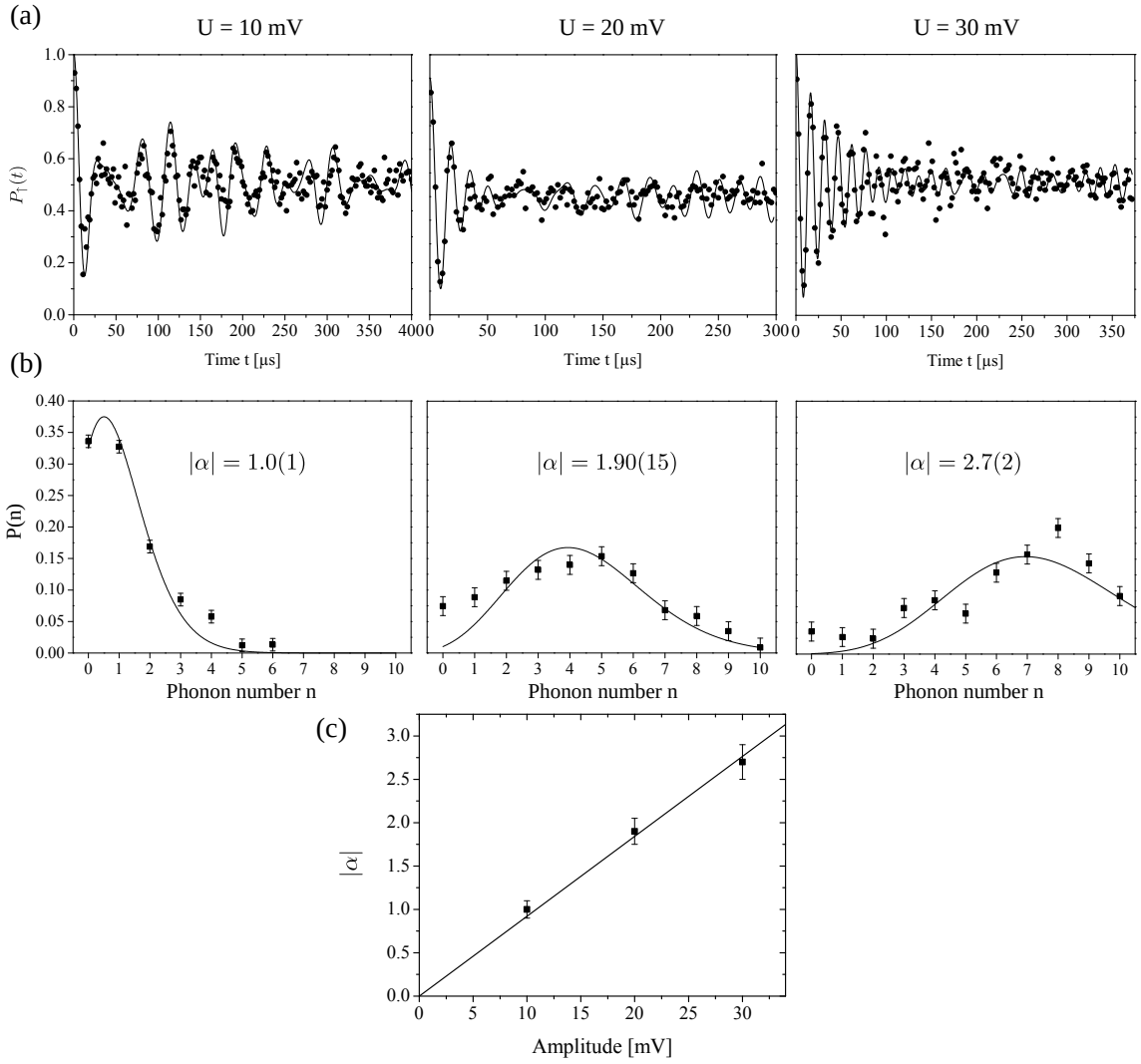

Figure 6.9: State analysis of coherent states generated by application of displacement pulses to the motional ground state. The voltage amplitude U of the displacement pulse increases from left to right in (a) and (b). (a) shows coherent sideband dynamics generated by excitation with the R1/R2 beams. Solid lines show fits to the data. These fits yield the phonon number distributions $P(n)$ for each U, which are shown in (b). Herein, the solid lines are fits assuming coherent state phonon distributions while the only fit parameter is the coherent state amplitude $|\alpha|$. (c) As expected, $|\alpha|$ scales linear with U and we find $|\alpha|/U = 92(2)\,\mathrm{V}^{-1}$.

Raman beams after application of the displacement force. From these traces, the phonon number distributions for the three different amplitudes can be deduced, which are shown in Fig. 6.9(b). To each of these measured distributions, the distribution $P_{\mathrm{coh}}(n)$ of a coherent state (see Eq. (9.11)) was fitted, whose only free parameter is $|\alpha|$. Thus, we obtained the coherent excitation amplitudes $|\alpha|$ arising from different amplitudes U. Here, the displacement pulses had a duration, which corresponds to 30 ion oscillation periods

at $\omega_z = 2\pi \times 1.43\,\mathrm{MHz}$. One can clearly see from Fig. 6.9(c), how the resulting coherent state's amplitude $|\alpha|$ increases linearly with U. Here, it becomes obvious, too, that the generation of higher excited states is possible, but their detection becomes more and more involved, because the bsb frequencies $\Omega_{n,n+1}$ become more and more indistinguishable for higher n.

The presented gauge measurement ensures that arbitrary, small displacement amplitudes $|\alpha|$ can be generated and reproduced reliably. For the generation of arbitrary displacements $D(\alpha)$, also the phase of the displacement force has to be controlled.

6.3.2 Phase Coherence: A "Motional Ramsey" Experiment

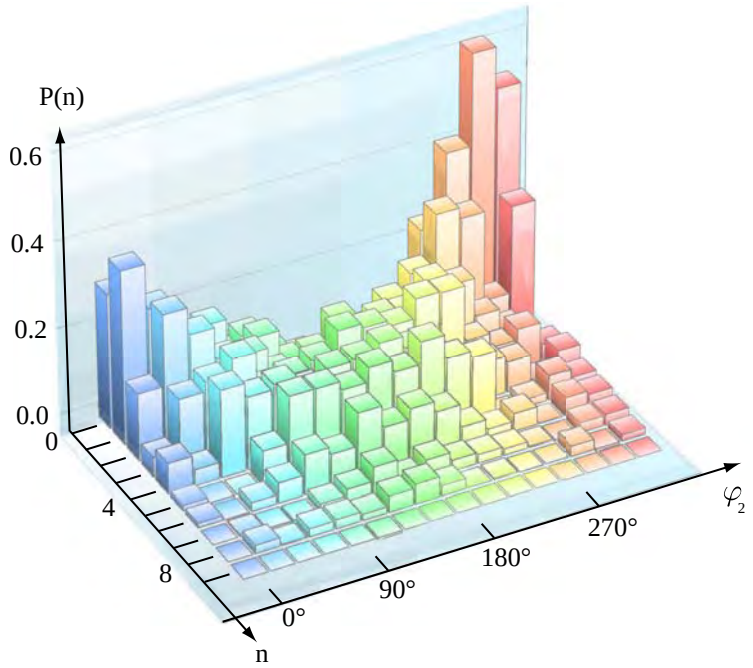

Figure 6.10: Phonon number distributions $P(n)$ for $n \leq 9$ obtained by the Rabi flopping method. Each column/color corresponds to a certain phase of the second displacement pulse φ_2, while the first one's φ_1 is fixed. For $\varphi_2 \approx 315°$, there is an almost perfect revival of the input state, i.e the first displacement has been coherently undone. For $\varphi_2 \approx 135°$, a coherent state with amplitude $2|\alpha|$ is generated by the two pulses.

The gauge measurement of the preceding section had its focus on the generation of well-defined displacement amplitudes $|\alpha|$. The displacement is, however, fully characterized by amplitude *and* phase, $\alpha = |\alpha|\, e^{i\varphi}$. Hence, this section concentrates on the investigation of generating displacements with different phases φ. These phases become detectable when two or more displacements are concatenated. For that reason, the following experiment

was carried out: A first displacement with fixed α_1 (i.e. fixed pulse parameters) acting on a near-ground state cooled ion generates the coherent state $|\alpha_1\rangle$. A second displacement pulse with the same amplitude and duration results in a total displacement $D(\alpha_2)D(\alpha_1) = e^{i\theta}\ D(\alpha_1+\alpha_2)$ with $|\alpha_1| = |\alpha_2| =: |\alpha|$ and $\theta = \mathrm{Im}(\alpha_2\alpha_1^*)$. For technical reasons, there is always a short, constant time gap Δt in between the two pulses. According to Eq. (9.12), this merely adds a constant phase factor $e^{i\omega_z\Delta t}$, which can be absorbed into the phase of the first pulse. The final state $|\alpha_\mathrm{f}\rangle$ is then given by

$$|\alpha_\mathrm{f}\rangle = e^{i\theta}\,|\alpha_1+\alpha_2\rangle = e^{i\theta}\,|e^{i\varphi_1}|\alpha_1| + e^{i\varphi_2}|\alpha_2|\rangle\,, \tag{6.29}$$

where φ_1 and φ_2 are the phases of the first and second displacement, respectively. After Eq. (6.29), the squared amplitude of $|\alpha_\mathrm{f}\rangle$ reads

$$|\alpha_\mathrm{f}|^2 = |\alpha|^2\cdot|1+e^{i\,(\varphi_2-\varphi_1)}|^2 = 4\,|\alpha|^2\ \cos^2\left(\frac{1}{2}\,(\varphi_2-\varphi_1)\right). \tag{6.30}$$

This means, that the final state's amplitude shows fringes when the relative phase between the two displacements, $\varphi_2-\varphi_1$, is scanned. This is because the overall action of the concatenated displacements critically depends on this phase difference. Figure 6.11(a) illustrates the measurement principle in phase space. While the first displacement is constant, the action of the second one can undo the first one, or both can work in phase, i.e. their action is equivalent to a single displacement with double amplitude.

In the experiment, both displacements were created by a voltage amplitude of $U = 10\,\mathrm{mV}$. The pulses had a duration of 30 periods at $\omega_z = 2\pi\times 1.43\,\mathrm{MHz}$. The time gap in between the pulses was $\approx 1.02\,\mu\mathrm{s}$. The phase of the second pulse with respect to the first one φ_2 was scanned, and for each value of φ_2, a motional state analysis yielded the corresponding phonon distribution, see Fig. 6.10.

The results for $|\alpha_f|^2$ obtained from these distributions can be seen in Fig. 6.11(b); the theoretically predicted behavior is obviously reproduced. The input state was not exactly ground state, but a thermal state with $\overline{n}\approx 0.55$. Therefore, the contrast of the oscillations is not maximal, but has an offset to the zero bottom line. A fit to the oscillation yields an offset of $\overline{n} = |\alpha_f|^2 = 0.58$, which is in very good agreement with the analysis of the input state.

The minimum of the oscillation corresponds to the situation, where the second displacement completely undoes the first displacement, leaving the ion in its starting state again. The "pendulum" that had been displaced from its resting position and oscillated for some periods has been decelerated by a force of the same amplitude, but shifted in phase by π.

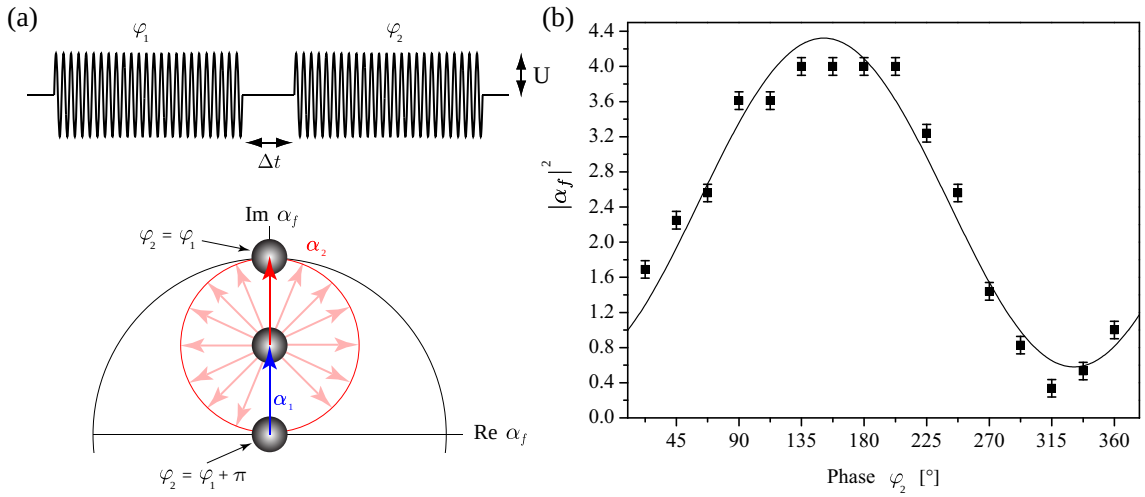

Figure 6.11: (a) Illustration of the double excitation by two displacement pulses. The initial state experiences a fixed displacement (blue arrow) and a second one with varying phase φ_2 (red arrows). The final coherent amplitude $|\alpha_f|$ depends on φ_2, as is depicted in phase space. (b) Results obtained by motional state analysis. For a certain phase, the energy imparted by the first displacement is completely extracted again by the second one, resulting in a minimum $|\alpha_f|^2$; whereas for in-phase excitation, a displacement of $2|\alpha|$ results in a maximum $|\alpha_f|^2$. The solid line is a fit to the data. It is in accordance with the input state and the experimental parameters (see text).

The maximal displacement occurs when both displacements act in phase, i.e. into the same "direction" in phase space (see Fig. 6.11(a)). The total displacement amplitude then is $2|\alpha|$. For the parameters chosen, we expect a maximal squared displacement amplitude of $(2|\alpha|)^2 \approx 1.8^2 = 3.2$. Again, this is – together with the observed thermal state offset – in good agreement with the measured value.

Altogether, it can be concluded that we achieved to realize the displacement operator $D(\alpha)$, where both amplitude and phase are under control. In particular, phase coherent series of excitations can be performed. Another important result is the very good revival of the initial state for $\varphi_2 = \varphi_1$; if this would not be the case, it would mean that the motional state was subject to rapid decoherence processes on the timescales of the displacement pulses, which could be caused by the electronics utilized to realize the displacement, for example. This is obviously not the case.

6.4 Complete Quantum State Analysis

When no a priori assumptions about the motional state can be made, then it is inevitable to measure a complete representation of the quantum state ρ. This can be, for example, the density matrix in a certain basis, or the Wigner function representation $W_\rho(\alpha)$ of the state[6]. A method based on the coherent Rabi flopping described in section 6.3 allows for both. Indeed, the Wigner function case is more descriptive and will be used to explain the procedure first.

$W_\rho(\alpha)$ is a quasi-probability distribution, describing the state ρ. It takes on real values, whereas negative values indicate non-classical states. A full review of the Wigner function shall not be given here, the reader may refer to the literature (see Ref. [Sch01a], for example). α is a complex number representing a point in phase space, cf. section 9.4.2 (again, we restrict ourselves to a one-dimensional movement of the ion in the trap). Both $W_\rho(\alpha)$ and ρ contain all information about the quantum state, so they are equivalent in that respect.

6.4.1 Wigner Function Measurement Scheme

The most convenient definition of the Wigner function for our purposes is

$$W_\rho(\alpha) := \frac{2}{\pi}\ \mathrm{Tr}\left\{D^\dagger(\alpha)\,\rho\,D(\alpha)\ e^{i\pi a^\dagger a}\right\}. \tag{6.31}$$

Herein, $D(\alpha)$ is an operator describing the displacement of a quantum state in phase space by α. $a^\dagger, a$ are the creation and annihilation operators of the harmonic oscillator, respectively. When a state ρ is displaced by $-\alpha$, the density operator ρ' of the resulting state is

$$\rho' := D(-\alpha)\,\rho\,D^\dagger(-\alpha). \tag{6.32}$$

Then, we can use the identity $D^\dagger(\alpha) = D(-\alpha)$ and rewrite Eq. (6.31) as

$$W_\rho(\alpha) = \frac{2}{\pi}\ \mathrm{Tr}\left\{\rho'\ e^{i\pi a^\dagger a}\right\}, \tag{6.33}$$

which means, that the value of the Wigner function at position α is – up to a constant normalization factor – equal to the expectation value of the phonon number parity operator $e^{i\pi a^\dagger a}$ applied to ρ'. The property of this operator can be most easily understood by looking at its action on the energy eigenstates, $e^{i\pi a^\dagger a}\,|n\rangle = (-1)^n\,|n\rangle$: it adds a phase shift of π to the odd number state amplitudes.

[6] The index indicating the state represented by W_ρ is omitted, when ambiguities are impossible.

In order to measure $W_\rho(\alpha)$, some interaction could be constructed to produce exactly this phase shift between neighboring phonon states, which can be achieved by harnessing the n-dependence of the Rabi frequencies of the atomic transitions in the harmonic potential. Such a scheme to directly measure $W_\rho(\alpha)$ was proposed, for example, in [Lut97].

We follow a slightly different approach first applied in [Lei96], based on the earlier mentioned possibility to obtain the phonon number distribution $P(n)$ for the motional state of the ion (chapter 6.3). In the energy eigenbasis, we can rewrite Eq. (6.33) as

$$W_\rho(\alpha) = \frac{2}{\pi} \sum_{n=0}^{\infty} (\quad 1)^n \; P'(n), \tag{6.34}$$

where $P'(n) := \langle n| \, \rho' \, |n\rangle$ is the phonon number distribution of the displaced state. This sum can be numerically performed for each α, once the probabilities $P'(n)$ are known[7].

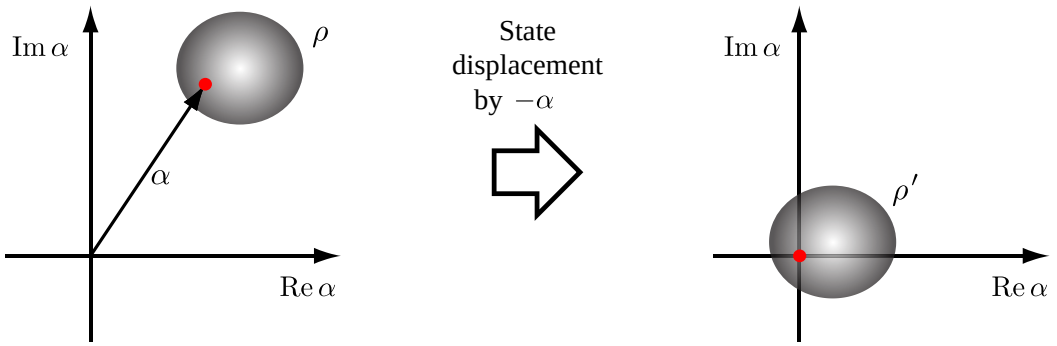

Figure 6.12: The applied scheme to measure the Wigner function $W_\rho(\alpha)$ of a state ρ (left) can be imagined like repeatedly measuring the quantity $W_{\rho'}(0)$ of a *shifted* state $\rho' = D(\quad\alpha)\rho D^\dagger(\quad\alpha)$. The shaded areas represent the Wigner functions of the respective states in phase space.

A very intuitive picture (see Fig. 6.12) of the measurement principle derived from Eq. (6.34) can be obtained by looking at what actually happens to the state during the measurement. Instead of measuring the value of W_ρ at different positions α in phase space, we permanently measure the Wigner function of a by $\quad\alpha$ *shifted* state ρ' at the origin ($\alpha = 0$).

This directly follows from $D(0) = D^\dagger(0) = 1$ and Eq. (6.34), as

$$\begin{aligned} W_{\rho'}(0) &:= \frac{2}{\pi} \; \mathrm{Tr} \left\{ D^\dagger(0) \, \rho' \, D(0) \; e^{i\pi a^\dagger a} \right\} = \frac{2}{\pi} \; \mathrm{Tr} \left\{ \rho' \; e^{i\pi a^\dagger a} \right\} \\ &= \frac{2}{\pi} \sum_{n=0}^{\infty} (\quad 1)^n \; P'(n) = W_\rho(\alpha). \end{aligned} \tag{6.35}$$

[7] In all practical cases, only states up to some phonon number n_{max} can be taken into account, which is justified since the distributions under consideration quickly go to zero for higher n. The sum in Eq. (6.34) is then finite.

In loose terms, instead of moving the "measuring apparatus" by α (and thus scanning phase space), it remains at the origin and it is the state that is moved to the apparatus by $-\alpha$.

6.4.2 Implementation and Results

The phonon distributions $P'(n)$ occuring in Eq. (6.34) can be obtained from coherent sideband dynamics exactly the way it has been described in the previous chapter. The crucial difference is, however, the application of a well-defined displacement field after the generation of the state and before the excitation pulse giving rise to the coherent sideband dynamics. This displacement field is generated by an ac voltage with frequency ω_z, applied to distant electrodes (see chapter 5.4).

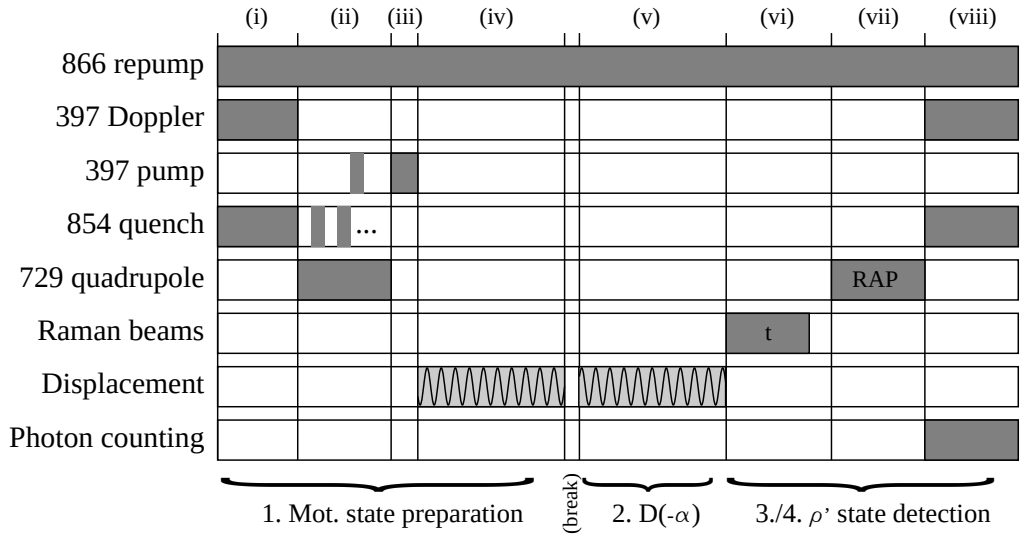

Figure 6.13: Schematic timing for measuring the Wigner function of a motional state ρ. After Doppler (i) and sideband cooling (ii), the internal state is prepared in $|\uparrow\rangle\langle\uparrow|$ by optical pumping (iii). A subsequent displacement pulse completes the preparation of ρ. Then, the analysis displacement pulse $D(-\alpha)$ results in ρ' (v), which is analyzed in the following steps by the Rabi flopping analysis method: coherent excitation on the bsb spin qubit transition with variable duration t (vi), shelving (vii) and qubit state discrimination (viii), cf. Fig. 6.7.

The recipe for measuring the Wigner function can be structured as follows:

0. Choose a set of points α_i, $i = 1, \ldots, M$ in phase space sufficient to characterize the state ρ. For each of these α_i, do the following:

1. Prepare $|\uparrow\rangle\langle\uparrow| \otimes \rho$, where ρ is the unknown motional state of the ion.

2. Displace the state by $-\alpha_i$. This results in ρ'.

3. Apply an excitation pulse of duration t on the first bsb transition.

4. Detect the qubit state ($|\uparrow\rangle$ or $|\downarrow\rangle$).

Steps 1-4 are repeated many times for different pulse durations t to obtain the excitation probabilities $P_\downarrow(t)$. From these, the phonon number distribution $P'(n)$, corresponding to α_i, can be obtained in the well-known manner. Equation (6.34) then directly yields $W_\rho(\alpha_i)$.

As only a finite number M of points can be investigated in a real measurement, the Wigner function will be known only on a very limited subset of phase space. Nevertheless, already a relatively small number of points can be sufficient when the phonon number distributions concentrate around low excitations [Lei96].

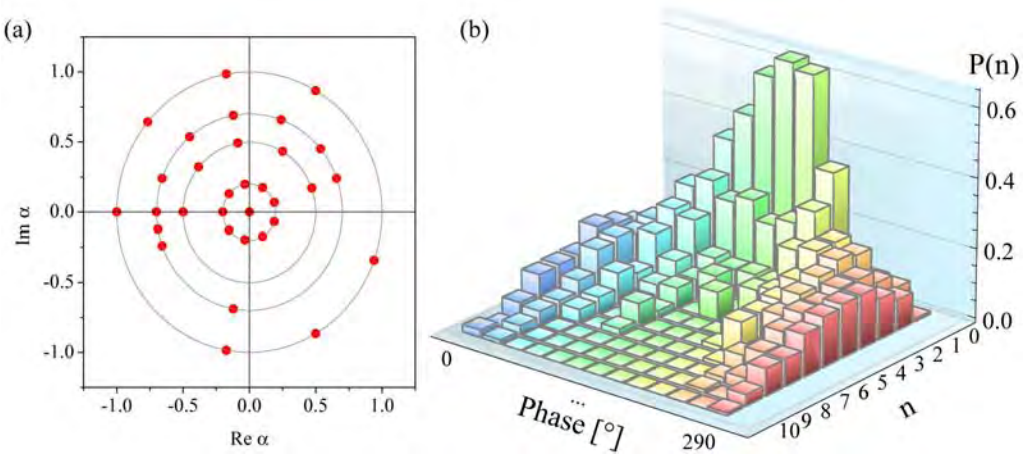

Figure 6.14: (a) Red dots indicate those points α_i, $i = 1, \ldots 32$ in phase space, where the Wigner function $W(\alpha_i)$ was measured experimentally. The circles correspond to voltage amplitudes of $20, 50, 70$ and $100\,\mathrm{mV}$, respectively. (b) Exemplary phonon distributions of the displaced state ρ'. They correspond to a fixed displacement amplitude ($20\,\mathrm{mV}$) with varying phase.

The scheme was tested by application to a coherent state $|\beta\rangle$. This state can be reproduced with high accuracy and its generation is not strongly influenced by common drift errors (laser frequency and magnetic field). The preparation of the state $\rho = |\beta\rangle\langle\beta|$ (step 1 in the list above) therefore consists of sideband cooling of the ion close to the ground state, optical pumping into the internal state $|\uparrow\rangle$ and the application of an ac displacement pulse. Both phase and amplitude of this displacement pulse were fixed all the time. The following second displacement pulse, which implements step 2, shifts the state in phase space by $-\alpha_i$. Its phase $\varphi = -\alpha_i/|\alpha_i|$ is defined relative to the phase of the first displacement pulse.

After that, coherent sideband dynamics giving $P'(n)$ are generated by excitation with the R1/R2 Raman beams. The whole sequence is illustrated in Fig. 6.13. The state was sampled at 32 different positions α_i, whereas the density of the points in phase space was adjusted during the measurement such that the interesting, non-zero regions were sampled more accurately, see Fig. 6.14(a).

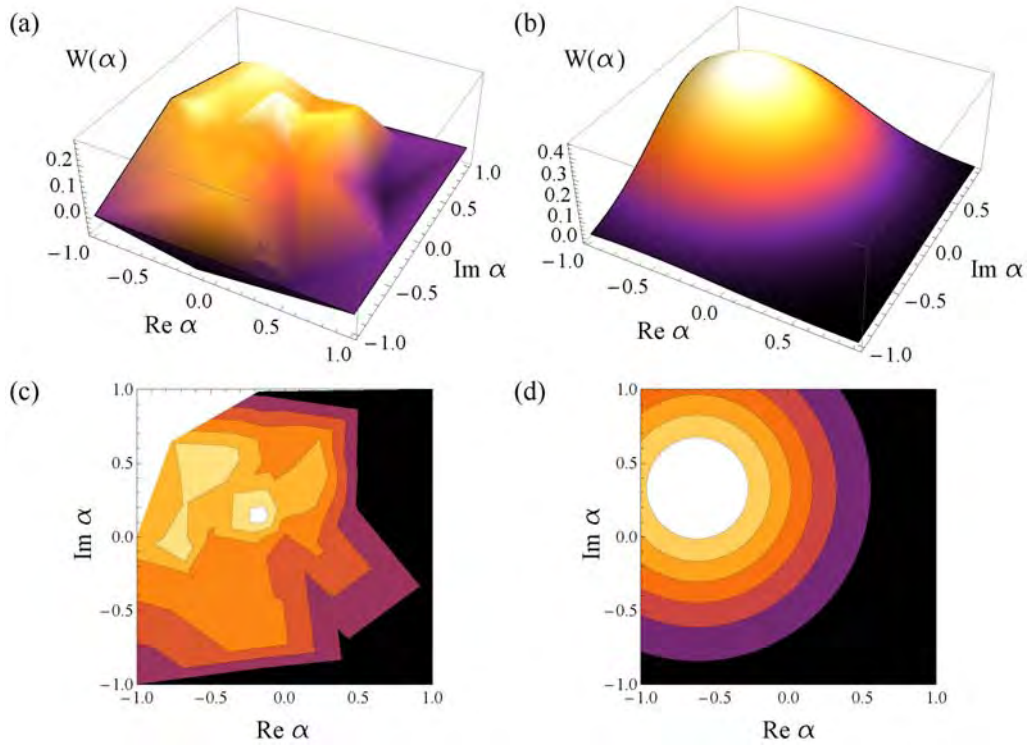

Figure 6.15: Wigner function representation $W(\alpha)$ of a coherent state $|\beta\rangle = |\beta|\, e^{i\xi}$. (a) shows measured data, obtained from 32 phonon distributions like those depicted in Fig. 6.14(b). The surface was linearly interpolated between the data points. For comparison, (b) shows $W(\alpha)$ derived from theory for a state with $|\beta| = 0.7$ and $\xi = 2.65$.
(c) and (d) are contour plots of the experimentally and theoretically obtained graphs, respectively.

In Fig. 6.14(b), typical distributions $P'(n)$, occurring during the measurement of the Wigner function, can be seen. Again, one recognizes a periodic variation in coherent state amplitude, similar to that discussed in chapter 6.3.2. The reason for this is the particular choice of ρ as a coherent state. For an arbitrary input state, the measurement displacement $D(-\alpha)$ does, of course, not result in a coherent state again.

From all 32 phonon distributions, the Wigner function is calculated after Eq. (6.35). Figure. 6.15 shows both measured data $W(\alpha)$, and the Gaussian expected from theory. The theoretically expected shape is reproduced well, even though the finite number of data points entails a fairly rough surface graph. The contour plots, however, prove a fairly

good accordance between measurement and theory.

6.4.3 The Density Matrix

Both the Wigner function representation $W(\alpha)$ and the density matrix ρ are a complete description of the quantum state. The former chapter demonstrated the reconstruction of $W(\alpha)$ from phonon number distributions $P'(n)$ of the unknown state, displaced by $-\alpha$. In the following, we shortly describe how the density matrix of the state in the energy eigenbasis can be obtained from the same data. To this end, we follow an ansatz described in Ref. [Lei96] and note that $P'(n) = \langle n|\rho'|n\rangle$; together with Eq. (6.32) and $|n\rangle = (a^\dagger)^n |0\rangle / \sqrt{n!}$ follows

$$\begin{aligned} P'(n) &= \frac{1}{n!} \langle 0| a^n D^\dagger(\alpha) \rho D(\alpha) (a^\dagger)^n |0\rangle = \frac{1}{n!} \langle \alpha| (a-\alpha)^n \rho (a^\dagger - \alpha^*)^n |\alpha\rangle \\ &= \frac{e^{-|\alpha|^2}}{n!} \sum_{l,m=0}^{\infty} \sum_{s,t=0}^{n} \frac{\sqrt{l!\,m!}}{(l-n+s)!(m-n+t)!} \binom{n}{s} \binom{n}{t} \times \\ &\quad \times \; (-1)^{s+t} \, (\alpha^*)^{l-n+s+t} \, \alpha^{m-n+s+t} \, \rho_{lm}. \end{aligned} \tag{6.36}$$

Taken for different values α_i, $i = 1, \ldots, M$, this is a matrix equation for the density matrix elements, which is in general overcomplete, but can be solved by standard fitting techniques.

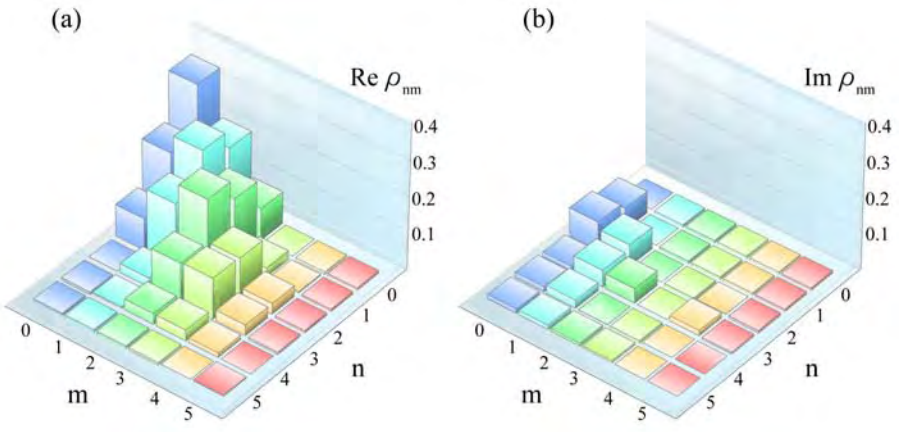

Figure 6.16: Density matrix of the measured coherent state in the energy eigenbasis. (a) Real part and (b) imaginary part of ρ_{nm}.

Figure 6.16 depicts real and imaginary parts of the derived density matrix $\rho_{nm} = \langle n|\rho|m\rangle$, calculated from the phonon distributions shown in Fig. 6.14(b). Here, the absolute value of the state's (arbitrary) phase was chosen to be minimal, resulting in imaginary parts close to zero. As expected from the Wigner function results, the matrix matches a coherent state

density matrix; the fidelity (see Eq. (1.7)) between the measured state and a coherent state with $|\alpha| = 0.94$ is $\mathcal{F} = 0.82$. This is in very good accordance with the expected value, as $|\beta\rangle$ was created by a displacement by a voltage amplitude of 100 mV, which should result in $|\beta| = 0.9$. Small discrepancies could be caused by axial frequency drifts during the long measurement time of several hours in total. Such effects can be excluded by regular monitoring measurements of the axial frequency, and by displacement gauge measurements like the one presented in chapter 6.3.1.

Altogether, we managed to demonstrate the feasibility to retrieve the complete quantum state information by means of coherent ion-light interaction, which has been first demonstrated in Ref. [Lei96]. Both the Wigner function and the density matrix representation could be retrieved. Apart from very high phonon populations, this method is not limited to any subset of input states but is applicable to arbitrary mixed states and hence seems predestined for quantum thermodynamic applications necessitating the full quantum state information. Another method has been proposed [Lut97], promising shorter measurement times on the one hand, but posing high demands on the coherence and stability properties of the system, on the other hand, so that the demonstrated technique seems more robust and suitable for our needs.

6.5 The Phonon Filter

This chapter introduces a procedure to measure the motional state of the ion, that differs from all other techniques in one crucial point: it does not average over an ensemble of many sequently prepared states, but non-destructively projects the quantum state of a single ion onto the energy basis. That is, the ion can be found in a *known* energy eigenstate after the measurement, so subsequent operations with the same system can be performed. Secondly, the non-destructiveness of the measurement can be exploited to increase the fidelity of the measurement, since the measurement can be repeated several times.

6.5.1 Nondestructive Detection Principle

The scheme relies on coupling the external motion of the ion to the internal qubit system, which can be discriminated with excellent efficiency (see chapter 3.2.1). This advantage of high detection efficiency must be bought dearly by the fact that the qubit can always only give a binary yes/no answer to the measurement question. The question we ask the system will be "is the ion in state $|m_{\text{test}}\rangle$ or not?", for an arbitrary phonon number $m_{\text{test}} \geq 0$.

The answer of the measurement scheme will be "yes" with probability $|c_{m_{\text{test}}}|^2$, when the unknown, motional state of the ion[8] is written as $|\varphi\rangle = \sum_n c_n |n\rangle$.

To understand the working principle of the measurement, we consider the level scheme of the optical qubit. At the beginning, the ion is assumed to be prepared in the electronic ground state $S_{1/2}$, and it is in a Fock state of motion,

$$|\Psi^{(0)}\rangle = |S_{1/2}, n\rangle\,. \tag{6.37}$$

After making a choice for m_{test} (where, at the moment, we assume $m_{\text{test}} \geq 2$), a red sideband pulse on the $S_{1/2} \rightarrow D_{5/2}$ transition is applied (step (i) in Fig. 6.17). Remember that the rsb Rabi frequencies $\Omega_{n,n\ -1}$ generated by this pulse are different for different n.

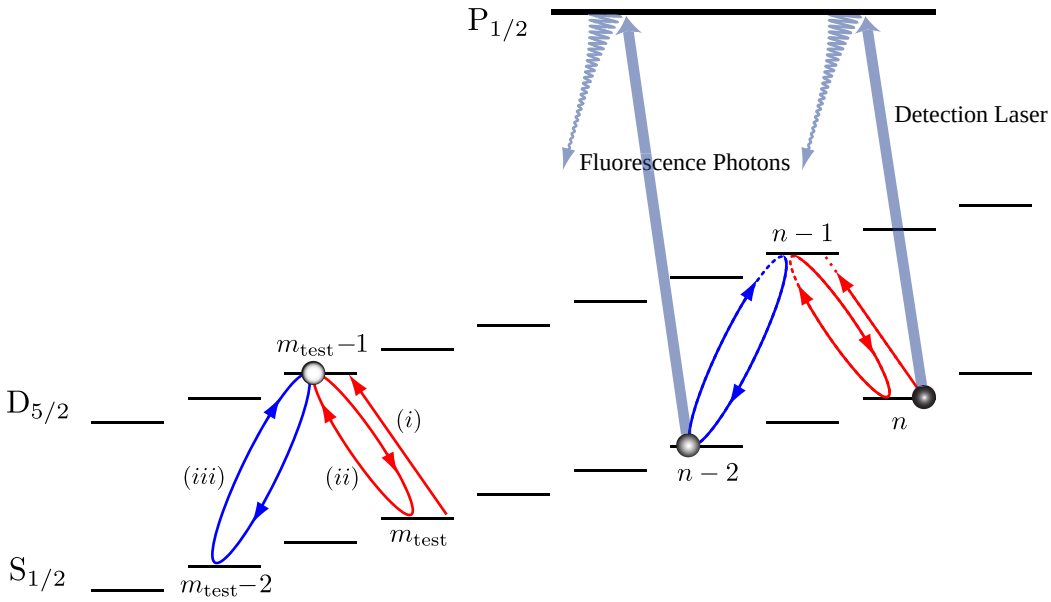

Figure 6.17: Levels and transitions involved in the filtering scheme. The optical qubit is excited on the $S_{1/2} \leftrightarrow D_{5/2}$ qubit transition and read out on the $S_{1/2} \leftrightarrow P_{1/2}$ transition after each excitation pulse. The durations of the exciting laser pulses are designed such that they leave an ion, that has initially been in $|S_{1/2}, m_{\text{test}}\rangle$, in the "dark" $|D_{5/2}\rangle$-state (full π and 2π-rotations, respectively; situation on the left). For an ion starting out from another motional state $|S_{1/2}, n \neq m_{\text{test}}\rangle$ (situation on the right), however, the population transfer of each pulse is imperfect, so that the successive detection step yields detectable fluorescence with nonzero probability. Shown are the first rsb π-pulse (i), and the successive rsb (ii) and bsb (iii) 2π-pulses. Thereafter, the scheme can be repeated with pulses (ii) and (iii) many times to increase the discrimination efficiency.

The first important step of the scheme is choosing the length t of the exciting laser pulse exactly such, that only $|m_{\text{test}}\rangle$ experiences an exact π-pulse, $t = \pi/\Omega_{m_{\text{test}},m_{\text{test}}\ -1}$. If the

[8] The assumption of a pure state of motion is justified, since only a single particle is considered here.

ion was in the state $|m_{\text{test}}\rangle$, then all population will be transferred from $S_{1/2}$ into $D_{5/2}$. For any other state $|n \neq m_{\text{test}}\rangle$, however, the pulse area is not exactly π, and the resulting state $|\Psi^{(0)}\rangle'$ is a superposition between $S_{1/2}$ and $D_{5/2}$,

$$|\Psi^{(0)}\rangle' = \begin{cases} |D_{5/2}, n-1\rangle & \text{for } n = m_{\text{test}} \\ a_S\,|S_{1/2}, n\rangle + a_D\,|D_{5/2}, n-1\rangle & \text{for } n \neq m_{\text{test}} \end{cases} \tag{6.38}$$

where, due to normalization, $|a_D|^2 + |a_S|^2 = 1$ and $a_S \neq 0$. In other words, the population transfer into $D_{5/2}$ is only complete for $n = m_{\text{test}}$.

This implies, that a subsequent qubit detection step, i.e. illumination on the $S_{1/2} \leftrightarrow P_{1/2}$ transition, will never yield resonance fluorescence for $n = m_{\text{test}}$ ("dark" ion, since the ion resides in the dark $D_{5/2}$ state), but does result in fluorescence detection with probability $|a_S|^2$ ("bright" ion) for $n \neq m_{\text{test}}$. Therefore, an initial state $|n \neq m_{\text{test}}\rangle$ can be detected to be the wrong phonon state with a probability of $|a_S|^2 > 0$ (Unfortunately, this "wrong" state $|n\rangle$ remains dark, too, with probability $1 - |a_S|^2$).

Let's recapitulate the two possible situations that may occur after the fluorescence detection:

1. The ion is bright. In this case, the initial state of the ion cannot have been $|m_{\text{test}}\rangle$ since this one is dark with unit probability. The answer to our question can therefore be answered with "no". The motional state of the ion is destroyed due to Doppler heating of the detection laser on the $S_{1/2} \leftrightarrow P_{1/2}$ transition, which is of minor interest since the question is already answered.

2. The ion remains dark. In this case, it is not possible to tell with certainty, whether the initial state was $|m_{\text{test}}\rangle$ or not, since also $|n\rangle$ is projected onto $|D_{5/2}\rangle$ with probability $|a_D|^2$. In contrast to the first case, however, the motional state has not been corrupted now, and the measurement scheme can be continued.

After the first "dark" detection, the state of the ion is

$$|\Psi^{(1)}\rangle = |D_{5/2}, n-1\rangle\,, \tag{6.39}$$

which is valid for all n including m_{test}. As the dark ion's motional state was not destroyed by the unsuccessful fluorescence detection, we can now go on and repeatedly apply 2π-rotations, interleaved by detection trials. The pulse durations are, again, timed such that only $|D_{5/2}, m_{\text{test}} - 1\rangle$ experiences an exact pulse area of 2π and all of its population returns back into the dark $D_{5/2}$ manifold, see steps (ii) and (iii) in Fig. 6.17. These states

being reproduced by 2π-rotations resemble the so-called "trapping states", which have been investigated in cavity-QED [Wei99].

6.5.2 Determination of the Filter Transmission

As illustrated in Fig. 6.17, qubit rotations on both the red and the blue sideband are considered for the filter scheme. The reasons for this are explained in the following. Additionally, it will become clear, why carrier excitations are not utilized.

The task of each rotation is to accomplish a complete population transfer for m_{test} and simultaneously make it as incomplete as possible for all other states. Take, for example, the first π-rotation on the red sideband (pulse (i)). The population in the state $\mathrm{D}_{5/2}$ after this pulse of duration $t = \pi/\Omega_{m_{\text{test}},m_{\text{test}}-1}$ equals

$$P_D^{(i)} = \sin^2\left(\frac{\Omega_{n,n-1}}{\Omega_{m_{\text{test}},m_{\text{test}}-1}}\frac{\pi}{2}\right) \tag{6.40}$$

for an initial phonon number of n. The smaller the right hand side of Eq. (6.40), the better is the state $|n\rangle$ distinguished from m_{test}. Similar expressions hold for the red and blue 2π-sideband pulses,

$$\begin{aligned} P_D^{(ii)} &= \cos^2\left(\frac{\Omega_{n,n-1}}{\Omega_{m_{\text{test}},m_{\text{test}}-1}}\pi\right) \quad \text{and} \\ P_D^{(iii)} &= \cos^2\left(\frac{\Omega_{n-2,n-1}}{\Omega_{m_{\text{test}}-2,m_{\text{test}}-1}}\pi\right), \end{aligned} \tag{6.41}$$

respectively.

Multiple Transmissions

These expressions show that the scheme works best, if the coupling constants of the used transitions vary strongly with n. Hence it is crucial to choose the respective type of transition, for which this effect is maximal. As we already derived in chapter 3.1, the dependence of $\Omega_{n,n+m}$ on n is maximal for the red sideband and minimal for the carrier transition. That's the reason for the preferred usage of the first red sideband.

There is, however, a good reason not to use the rsb exclusively, and this is due to the periodicity of the expressions (6.40) and (6.41). While the scheme including rsb pulses only would work in the closest vicinity of m_{test}, it fails, for instance, for a state $|n\rangle$, whose rsb coupling constant $\Omega_{n,n-1}$ is equal to twice the one for $|m_{\text{test}}\rangle$. Then, of course, the state would be subject to a 4π rotation, when $|m_{\text{test}}\rangle$ is rotated by 2π. Both cases result in a complete state transfer.

From the expressions in Eq. (3.20), we can see that $\Omega_{n,n-1} \propto \sqrt{n}$ for small n, so that the described unwanted scenario already takes place for $m_{\text{test}} = 1$ and $n = 4$, for example. These phonon numbers are certainly among those of greatest interest. As, however, these "bad" pairs of phonon number states differ for the red and the blue sideband, the alternating use of both efficiently avoids the problem: those states n passing through the "rsb filter" are suppressed by the "bsb filter" and vice versa. By this trick, the scheme becomes applicable for all values of n we are interested in ($n \lesssim 10$).

Special Cases

The above filter scheme is subject to the constraint $m_{\text{test}} \geq 2$, because the ladder states $|\mathrm{S}_{1/2}, m_{\text{test}}\rangle$, $|\mathrm{D}_{5/2}, m_{\text{test}} - 1\rangle$ and $|\mathrm{S}_{1/2}, m_{\text{test}} - 2\rangle$ are involved. For $m_{\text{test}} < 2$, the working principle of the filter is the same, but the pulses have to be slightly adapted. For $m_{\text{test}} = 0$, a pulse sequence similar to that proposed for stochastic cooling [Esc95, App98] is applied. A carrier π-pulse brings the ion from $|\mathrm{S}_{1/2}, 0\rangle$ into $|\mathrm{D}_{5/2}, 0\rangle$. Successive blue sideband π-pulses do not affect this state, but very effectively de-excite other phonon states back into $\mathrm{S}_{1/2}$, where they are subject to resonance fluorescence detection on the dipole transition. This pulse sequence is very efficient since the bsb pulses have zero coupling for $n = m_{\text{test}} = 0$, but a near optimal duration for all adjacent states.

For $m_{\text{test}} = 1$, an almost equal sequence can be applied like for $m_{\text{test}} = 0$, only the initial carrier pulse has to be replaced by a red sideband π-pulse. This pulse transfers populations from $|\mathrm{S}_{1/2}, 1\rangle$ into $\rightarrow |\mathrm{D}_{5/2}, 0\rangle$, then the procedure continues with bsb π-pulses as for $m_{\text{test}} = 0$.

Filter Transmission of the Alternating Scheme

The overall probability P_D to wrongly identify an initial state $|n \neq m_{\text{test}}\rangle$ as $|m_{\text{test}}\rangle$, i.e. the probability for this state to remain dark after N cycles, is the product of the $\mathrm{D}_{5/2}$-populations resulting from the single rotations (remember that after each dark detection step, the ion is completely projected into $\mathrm{D}_{5/2}$). In the proposed scheme consisting of an initial pulse+detection, followed by N_{r} red and N_{b} blue sideband pulse+detection cycles, this probability is given by

$$P_D = P_D^{(i)} \cdot (P_D^{(ii)})^{N_{\mathrm{r}}} \cdot (P_D^{(iii)})^{N_{\mathrm{b}}}, \tag{6.42}$$

where $N_{\mathrm{r}} = N_{\mathrm{b}} = (N-1)/2$ for odd N and $N_{\mathrm{r}} = N_{\mathrm{b}} + 1 = (N-2)/2 + 1$ for even N, respectively. Therefore, P_D, which can in some respect be interpreted as the filter

transmission, decreases exponentially with the number $N = 1 + N_\mathrm{r} + N_\mathrm{b}$ of detection trials.

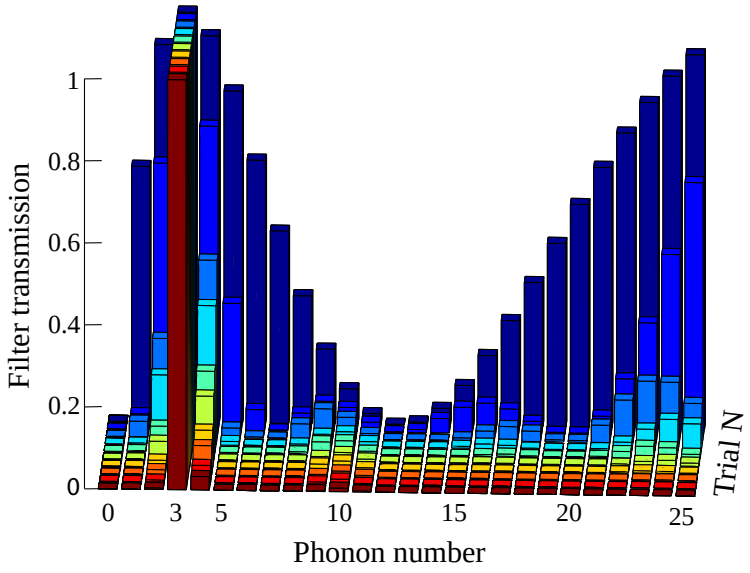

Figure 6.18: Probability for detection of zero fluorescence, called filter transmission, after $N = 0, 1, \ldots 10$ pulse and detection cycles. With increasing number of trials (back to front) the Fock state to be tested for, here $m_\mathrm{test} = 3$, survives the detection step and remains dark, whereas all other Fock states have an exponentially decreasing probability for zero fluorescence detection.

Figure 6.18 shows the probability for an input state $|n\rangle$ to remain dark after N iterations, i.e. after N excitation pulses and detection trials. The filter pulses were testing for $m_\mathrm{test} = 3$ in this case. The effect of the scheme as a Fock state filter becomes vivid in this figure. While only $|m_\mathrm{test}\rangle$ remains dark all the time and survives the procedure, all other states are suppressed. After $N = 10$ trials, there is no unwanted transmission higher than 5% for the wide range of input states shown in the figure.

6.5.3 Coherence and Time Consumption

The detection intervals destroy the qubit coherence. Therefore, the phase stability requirements put on the laser are moderate: it has to be maintained over a time period of a typical 2π-rotation, only, which is on the order of microseconds. In particular, successive pulses don't need to have a fixed phase relation. This makes the scheme much less demanding than typical gate operations relying on atom-light interaction.

The duration of the whole scheme is dominated by the detection time, which is of the order of a millisecond. This is enough time to separate bright from dark states (see chapter 3.2.1

and Fig. 3.4 therein). Compared with this, the sideband pulses can be neglected. Thus, one can assess about N milliseconds for a whole filter process. Regarding $N = 10$ and the $D_{5/2}$-lifetime of over one second, the error probability due to decay of the metastable qubit level is less than 1%.

Recently, a novel detection technique was demonstrated that achieves a significant reduction of the fluorescence detection time, while the discrimination error can be kept very low [Mye08]. The technique uses time-resolved photon counting and achieves discrimination errors far below 1%, with detection times being shorter than 100 μs. Therewith, the whole scheme could be sped up by almost one order of magnitude.

Chapter 7

Interaction with the Environment

A cold ion confined in a Paul trap is well isolated from its environment. Nevertheless, since we are dealing with highly sensitive quantum systems, the residual interaction is still the main source of disturbance [Zur03]. In accordance with the considerations leading to the qtd requirements (V) and (VI) in chapter 1.2, it is helpful to distinguish between the ion's internal and external degrees of freedom here, too. As could be seen in previous chapters, the coherent character of the utilized ion-light interactions is a crucial prerequisite for most of the techniques presented. Uncontrollable, noisy interaction with the environment leads to decoherence of the internal states and can completely spoil the observation of quantum effects.

The ion motion is directly affected by fluctuating electric fields coupling to the ion's charge. These interactions mostly imply an uncontrolled heating of the system. After all, the ion – effectively at the zero point of temperature – finds itself surrounded by trapping and housing material at room temperature (luckily enough, the ion is an oscillator which only accepts energy at sharply defined frequencies). It is obvious, that such unwanted heating constitutes a direct disturbance of the qtd system in the sense of requirement (I). On the other hand, this type of energy exchange can be utilized for preparation or equilibration of the system, for example. In the following, both internal decoherence processes and the motional state evolution during heating are investigated experimentally, and ways to overcome the related problems are presented.

7.1 Internal State Coherence

In order to observe pure internal decoherence effects, it was tried to exclude all other disturbances as far as possible. This mainly refers to dephasing effects due to motional excitation. Hence, the internal coherence time of the spin qubit was measured by the R1/CC Raman beam combination, which produces a light field not coupling to the external degrees of freedom.

In this context, sources of decoherence are mainly fluctuations in laser intensity and phase, respectively, and magnetic field fluctuations giving rise to a fluctuating level separation. Accordingly, the laser intensity was actively stabilized by direct observation with a fast photodiode with sub-percent accuracy. The Raman field phase, which is determined by the phase difference of the two Raman beams (see Table 3.1), is subject to fluctuations, if the optical path length of the two Raman beams differs; the two beams, derived from one laser source, effectively form an interferometer, where the ion sees the interference pattern of the intersecting beams. Consequently, the approaches to making the system more stable are the same as for interferometric setups: both the path length difference and the enclosed area was kept at a minimum. Additionally, mechanical shielding prevents air convection.

Magnetic field fluctuations occur on different time scales. Slow variations are predominantly caused by the laboratory's power supply at 50 Hz. This can be effectively suppressed by triggering each experiment at a certain phase of the sinusoidal power supply line. Faster fluctuations are hard to compensate for, and mostly shielding is the only remedy one can rely on. Spin-echo techniques are, however, a means to tackle the problem actively. A descriptive picture of this technique is that unwanted, magnetic interactions occurring during a certain time τ can be exactly undone by effectively time-reverting the interaction after $\tau/2$. Thus, all unwanted dynamics having happened in the first half are exactly reverted in the second half, and at the end, the system returns into its initial state again.

The time reversal is accomplished by a so-called "spin-echo" pulse. Its action can be most easily seen in the performed experiment, see Fig. 7.1(a). Starting from state $|\uparrow\rangle$, the qubit is driven into the superposition $(|\uparrow\rangle + |\downarrow\rangle)/\sqrt{2}$ by a $\frac{\pi}{2}$-pulse (*Ramsey pulse*) of the Raman beams. In the following waiting time of duration $\tau/2$, this superposition evolves into $(|\uparrow\rangle + e^{i\varphi}|\downarrow\rangle)/\sqrt{2}$, where the acquired phase φ depends on the momentary value of the magnetic field. Now, the spin-echo pulse swaps the qubit amplitudes, which is equivalent to producing $(|\uparrow\rangle + e^{-i\varphi}|\downarrow\rangle)/\sqrt{2}$. Thus, if the magnetic field has not significantly changed since the beginning, the time evolution again produces a phase of φ, and the initial

superposition $(|\uparrow\rangle+|\downarrow\rangle)/\sqrt{2}$ is restored at time τ. The final $\frac{\pi}{2}$-Ramsey pulse then transfers the state into $|\downarrow\rangle$, as if nothing had happened in between the two Ramsey pulses. Indeed, this is only true, if the second $\frac{\pi}{2}$-pulse is in-phase with the first one. If they are phase shifted by π, the second pulse brings the system back into $|\uparrow\rangle$, again. After the second Ramsey pulse, the qubit state is read out.

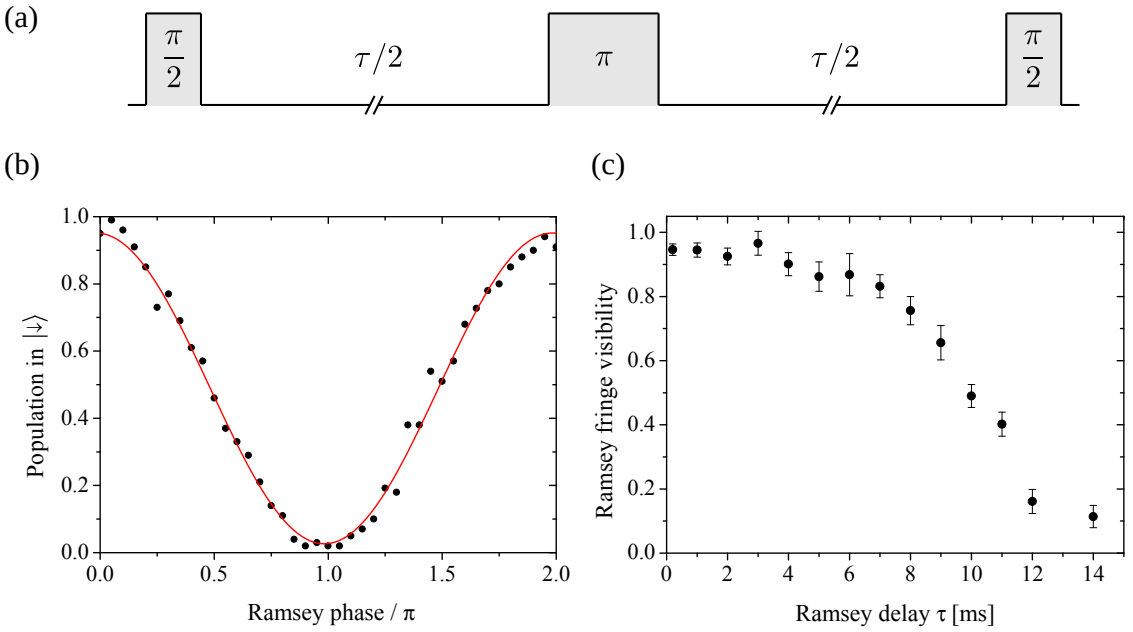

Figure 7.1: (a) Schematic of the Raman pulse sequence. The two Ramsey $\frac{\pi}{2}$-pulses are separated by a waiting time τ. After half of this time, a spin-echo pulse with pulse area π effectively time-reverses the state evolution. (b) Sinusoidal Ramsey fringes show the population transfer efficiency of the second $\frac{\pi}{2}$-pulse as a function of the relative phase of the $\frac{\pi}{2}$-pulses. The contrast of this signal is a measure for the coherence of the system maintained during waiting time τ. (c) Fringe contrast as a function of waiting time. The longer the time in between the pulses becomes, the more irreversible effects add up and destroy the internal system coherence.

As for state populations, one observes a sinusoidal dependence of the $|\uparrow\rangle$-population on the relative Ramsey pulse phase. Complete transfer into $|\downarrow\rangle$ is only accomplished for zero phase difference, and if the state was not corrupted during waiting time τ (including the spin-echo pulse[1]). Hence, the contrast of the population oscillations are a very good measure for the coherence properties of the system on timescale τ. Figure 7.1(b) shows the well-known Ramsey fringes in state population as a function of the Ramsey pulse phase. The visibility of the oscillation, obtained with $\tau = 1\,\text{ms}$ waiting time, amounts to 95(2) %. With increasing τ, the various decoherence effects add up and result in a lower contrast.

[1] The duration of the spin-echo pulse is of the order of some microseconds and can be neglected compared to τ.

This can be seen in Fig. 7.2(c), where the contrast is shown for different waiting times up to 14 ms. Even after 8 ms, the contrast of the operation is still as high as 76(4) %. This is sufficiently long compared to those times, during which the coherence of the interaction has to be maintained (typically < 1 ms).

Coming from the field of quantum information, a couple of approaches were proposed and realized to get around decoherence issues. The utilization of robust clock states [Aol07b] and decoherence-free subspaces [Lid98, Kie01, Häf05b, Aol07a, Mon09] are certainly among the most promising ones. Nevertheless, already such a seemingly simple technique like the presented one can increase the coherence time by almost an order of magnitude. Additionally, the spin-echo pulse sequence offers the advantage, that it can be easily incorporated into a given experimental schedule.

7.2 Heating Rates

As aforementioned, coupling to the environment causes motional heating. The reason for this are fluctuating electric fields that mainly originate from the trap surfaces. While the exact mechanisms are not clarified and still subject to current investigations, it is supposed that the main contribution to the heating stems from either fluctuating patch potentials or electric noise on the electrodes. The common observation of heating rates larger than those expected from Johnson noise is referred to as "anomalous heating" [Des06]; it is thermally driven and can be suppressed by cooling the trap apparatus. The effects and contributions have been studied theoretically [Lam97, Dub09] and experimentally [Tur00, Des06] and seem to differ in their respective scaling with the electrode-ion distance. It has been demonstrated in Ref. [Lab08], that cooling the trap material down to cryogenic temperatures (6 K) reduces the heating rate by seven orders of magnitude. Thus, this is the most effective way to overcome heating problems in ion traps at the moment.

Motional heating rates can be obtained by temperature measurements after different waiting times, during which the ion is neither cooled nor moved, but exclusively affected by the heating interaction. We applied the following scheme:

(i) Preparation of the ion close to the ground state by resolved sideband cooling.

(ii) Waiting for time T_h; no laser interaction during this period.

(iii) Application of motional state analysis (see section 6.3); this yields the phonon distribution $P(n)$ for each T_h. This way, not only the mean phonon number (temperature)

of the ion is obtained, but also the motional state evolution caused by the heating is revealed.

Figure. 7.2(a) depicts the time evolution of the three lowest phonon states during the heating process. The solid lines illustrate the expected evolution of a thermal state, whose mean phonon number grows linearly in time, $\dot{\overline{n}} := \mathrm{d}\overline{n}/\mathrm{d}t = 0.3$ phonons per millisecond. The mean phonon numbers $\overline{n}(T_\mathrm{h})$ deduced from the distributions are shown in Fig. 7.2(b), confirming the assumption of a constant heating rate.

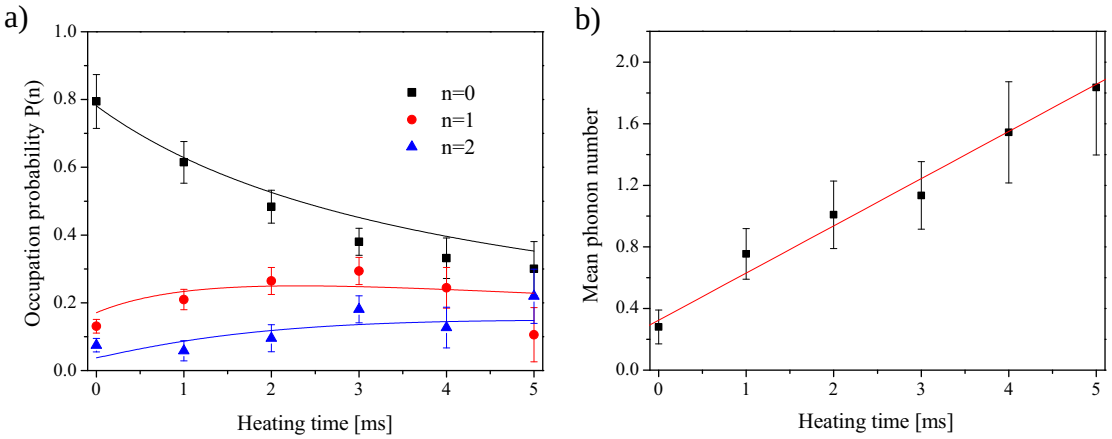

Figure 7.2: Heating rate measurement. An initially cold ion ($\overline{n} \approx 0.3$) is allowed to heat up for a time T_h. Then, its phonon distribution is detected. (a) shows the time development of $P(n)$ for $n = 0, \ldots, 3$ during 5 ms. The solid lines indicate the expected evolution of a thermal state with constant $\dot{\overline{n}}$. (b) Mean phonon numbers deduced from the measured distributions as a function of T_h. The red line is a linear fit with $\dot{\overline{n}} = 0.3(1)\,\mathrm{ms}^{-1}$.

The obtained heating rate is in accordance with values expected for a trap with the given ion-electrode distance of $\approx 250\,\mu$m. It does not pose a problem for most applications discussed above: Potential transformations lasting on the order of the inverse trap frequency and a subsequent motional state analysis (e.g. determining the Wigner function) can be performed in $\approx 300\,\mu$s or faster, so that the motional state is altered by heating by less than 0.1 phonon on average. However, for more advanced schemes like the phonon filter, where several detection intervals ($\sim$ ms) are necessary to end up with the desired accuracy, the gain of a couple of phonons by heating alone can completely corrupt the state under investigation. Therefore, it would be desirable to have a lower heating rate to be on the safe side when performing more complex experiments. A cryogenic setup seems to be the most promising approach, since the advantages of the microstructured trap should not be sacrificed to these circumstances.

7.3 Reservoir Engineering

We have become acquainted with two basic techniques rendering the ion in a thermal state of motion: Laser cooling on the one hand, and coupling to a reservoir (the ion's surroundings), on the other hand. The authors of Ref. [Poy96] introduced a theoretical interpretation of a special class of light-atom interactions, that in some sense bridges the two approaches. They showed, that the light fields can be interpreted as a special kind of reservoirs for the ion. The light applied for resolved-sideband cooling, for example, can be interpreted as a zero-temperature reservoir, which couples to the ion and makes it equilibrate to (almost) ground state. Both the type of interaction, its strength, and its temporal properties completely lie in the hands of the experimenter. Engineered reservoirs have been exploited experimentally to investigate the decoherence of quantum superpositions [Mya00].

The master equation describing the time evolution of the reduced density operator (with respect to the reservoir) ρ for the system in the interaction picture is given by [Poy96]

$$\dot{\rho} = \gamma \left(2 f \rho f^\dagger - f^\dagger f \rho - \rho f^\dagger f\right), \tag{7.1}$$

where the operator f models the system-environment interaction and γ is a parameter depending on the Rabi frequency, the Lamb-Dicke parameter and the upper state lifetime. While the described ground-state cooling relies on first red sideband transitions, which means that the coupling operator f is linear in the annihilation operator of the motional mode, $f = a$, tuning the laser to higher motional sidebands results in nonlinear couplings; for instance, when $\delta = -2\omega_z$, a photon absorption plus the following spontaneous decay annihilates two phonons and $f = a^2$.

By simultaneous application of multiple light fields, tuned to different motional sidebands, a variety of interactions can be realized, even those which may not have a "real" reservoir counterpart. Interestingly, the ion's final motional state of such engineered interactions can be highly non-classical, like entangled pure states [MF96]. This possibility to generate switchable, tailored reservoirs for the ion paves the way for experiments going far beyond classical notions of system-bath coupling. Additionally, allows for implementing a requirement often implied in standard textbooks, and strictly fulfilled by only very few implementations: Switching between open and closed systems, at arbitrary points in time.

Chapter 8

Conclusion and Outlook

Performing thermodynamic experiments in both the non-equilibrium and the quantum regime is a demanding task. At the beginning of this work, we have investigated the problem from an abstract point of view, and raised the question what requirements have to be fulfilled by the system itself, on the one hand, and the experimenter's possibilities, on the other hand. This lead us to the formulation of the six terms in chapter 1. The following chapters showed, that *each* of these requirements can be met by the trapped-ion system, where the motion of the ion is the respective degree of freedom under investigation.

A central tool within this approach is the coherent interaction between light and matter, which allows for an efficient manipulation of both the internal *and* the external degrees of freedom of the ion. The latter can happen on the single quantum level and thus in fact constitutes the experimental interface into the quantum regime. In addition to this concept, the trapped-ion approach profits from other developments and techniques on the field of quantum information such as different cooling techniques, the segmented trap idea, or the unrivaled detection efficiency and so forth. Moreover, it could be seen that by resorting to techniques stemming from two different qubit implementations, specific case-to-case requirements in terms of experimental effort, coherence times, pulse fidelity, detection efficiency and so on, can be optimally met. As for coherent ion-light interaction, all techniques necessary for the implementation of thermodynamic tasks were demonstrated.

It has been shown, that the motional state of a trapped ion constitutes a physical system best suited for quantum thermodynamic experiments. The system's state can be prepared into a well-defined initial thermal state. Thereby, the mean energy of the system can range from ground state ($\overline{n} < 10^{-3}$) to almost arbitrarily high excitations, where the range from $\overline{n} = 0$ to $\overline{n} = O(1)$ is very accurately adjustable. This is a regime of utmost

interest, since here, both finite temperature and quantum effects emerge. We discussed and experimentally demonstrated different preparation techniques, and measured the time-resolved state development during such a process. The preparation of non-thermal states, is possible, too.

The parametric transformation of the system Hamiltonian can take on diverse forms. We discussed and a couple of possible realizations under theoretical and practical aspects, and implemented a series of transformations within this work. The linear, segmented Paul trap design plays a prominent role when it comes to the realization of time-dependent electric potentials. Numerical and practical methods for the generation of arbitrary, time-dependent trapping potential were shown. The fidelity, desired potentials can be experimentally realized with, is remarkable, and paves the way for various applications in both the field of quantum thermodynamics and quantum information. Further transformations, like the coherent displacement process, were studied, extensively tested, and utilized for pursuing more sophisticated applications. The variety of realizable processes with highest accuracy pointed out to be one of the most substantial arguments for the trapped-ion system.

Equally powerful is the set of detection methods at hand. A set of fast, reliable methods for the measurement of the system's temperature has been demonstrated, covering both the ultra-cold ($\overline{n} < 1$), the intermediate ($\overline{n} = O(1)$) and the high temperature ($\overline{n} \gg 1$) region. As we are dealing with non-equilibrium processes, it is essential not to restrict oneself to thermal distributions. A very versatile tool has been presented enabling us to measure the phonon number distribution of arbitrary states. It also builds the basis for more complicated schemes. Among these applications is the measurement of the Wigner function and the full density matrix of the mixed quantum state, respectively; Both has been demonstrated experimentally. These are very powerful methods, since they allow for a complete description of the quantum state. Additionally, new, powerful and techniques have been developed in order to account for the specific needs of quantum thermodynamic experiments. A non-destructive procedure, allowing for the projective measurement of energy eigenstates has been discussed for the observation of fluctuation events in a non-equilibrium process. Again, we asses that the single-ion approach excels in terms of detection and measurement possibilities compared to other systems. In particular, the option to measure single processes rather than performing averaging ensemble measurements is a fascinating feature.

We presented methods to suppress decoherence in the system. Decoherence effects can be efficiently prevented by a careful choice of the internal dynamics involved, which is

closely connected to laser and magnetic field stability issues. For this, two different qubit systems, comprising an optical quadrupole and a Raman transition, respectively, have been implemented. Each of these qubit implementations poses different stability demands. By the aid of these systems, it could be demonstrated by various results, that decoherence is not a limiting factor for the presented experiments.

Finally, we have seen that one of the most prominent features of trapped ions compared to larger systems is their isolation from the environment. Reasons for this are the ultra-high vacuum environment, the high spectral insensitivity towards radiation, and the relative insensitivity towards motional energy transfer into a nearly perfect harmonic oscillator. The residual coupling is dominated by heating due to fluctuating electric fields, which is – roughly speaking – worse, the smaller the trap is. This showed to be a severe problem for the implementation of very complicated, time consuming operations like the phonon filter in our micro-trap, and hindered us from implementing experiments based on the filter technique apart from basic steps. Although, all other requirements for the filter, such as laser-driven state rotations and efficient fluorescence detection, for example, have been demonstrated. Together with the presented abilities to prepare, transform and detect the motional state of the ion, the confidence is well-founded, that a cryogenic setup [Lab08] will facilitate a series of further experiments exploring the quantum thermodynamic regime, like a test of the quantum Jarzynski equality [Hub08b]; a cryogenic Paul trap ($\sim 4\,\mathrm{K}$) is currently prepared and set up in our group.

Considering all presented theoretical and experimental findings, we draw the conclusion that the trapped-ion system is outstandingly well-suited for the implementation of quantum thermodynamic experiments. *All* properties postulated at the beginning of this work have been shown to be realizable and all requirements have been fulfilled. Concerning most points, not only a single, but a whole spectrum of possible solutions could be presented and demonstrated experimentally. It bears repeating that under most aspects, the system seems in deed predestined for our purposes; this is due to its intrinsic properties one the one hand, and the set of powerful, yet accurate tools the coherent ion-light interaction provides, on the other hand.

Close, fruitful connections to other fields have been unveiled: The transport transformation is of utmost interest in scalable quantum computation, and has been demonstrated to be applicable for the realization of a one-atom field probe [Hub10], just to give two of the numerous examples. The field calculation techniques presented here have facilitated the development of even more complex and miniaturized Paul and Penning trap designs [Hel10]. In future, thermodynamic considerations may help, for instance, to en-

gineer robust quantum gates, and bichromatic laser fields used for high-fidelity quantum gates [Ben08b] resemble engineered laser baths. A study of the decoherence processes in a Paul trap caused by exposing the system to more than one source of noise has been proposed in Ref. [Bee10]. Here, an effective temperature can be used to characterize the nonequilibrium environment.

The single ion system is very basic and extendable in many respects. Employing multiple ions allows for the simulation of the interaction between multiple systems and a controlled environment [Paz08, Cor09]. Anharmonic potentials can be used to study analytically unsolvable problems, and light forces can be used to implement state-dependent, time-varying potentials.

Altogether, the prospects on possible applications and new research perspectives opened by quantum thermodynamical experiments are manifold and promising. Apart from those treated above, experiments in the nearest future could comprise non-equilibrium processes by temperature changes [Wil08], the verification of recently found (in)equalities of fundamental thermodynamic quantities [Jar97, Kaw07], or quantum engines [Rez06, Qua07, Qua09]. For the first time, it could be comprehensively demonstrated how such experiments can be realized.

Chapter 9

Appendix

9.1 Segmented Linear Paul Traps

Two different linear Paul traps were used for the experiments presented in this thesis. This section presents all trap specific features that might be necessary for the understanding of the conducted experiments. All construction details can be found in references [Sch08, Deu07]. Most of the experiments were carried out in a micro-fabricated chip trap (denoted *micro-trap*), which is described in the following section 9.1.1.

The transport experiments presented in sections 5.2.2 and 6.2.2 were performed in a trap manufactured in printed circuit board (pcb) technology, therefore it is referred to as *pcb-trap*. Section 9.1.2 presents layout and construction details for this Paul trap.

9.1.1 The Micro-Trap

The *micro-trap* is a linear Paul trap with a three-dimensional electrode structure. Its layout is schematically depicted in Fig. 9.1 and shows the four plane electrode wafers kept at a certain distance. Two of them carry the structures for the dc electrodes responsible for axial confinement, the other two are connected to the radio frequency ac drive and provide radial confinement. The ion is trapped along a line in the middle of the central slit. The wafers itself consist of gold coated Aluminium-oxide (alumina, Al_2O_3) into which the electrode structures were cut by femtosecond laser pulses.

This trap was especially designed for scalable quantum information experiments and excels in its versatility to generate – static or time-dependent – external potentials for trapped

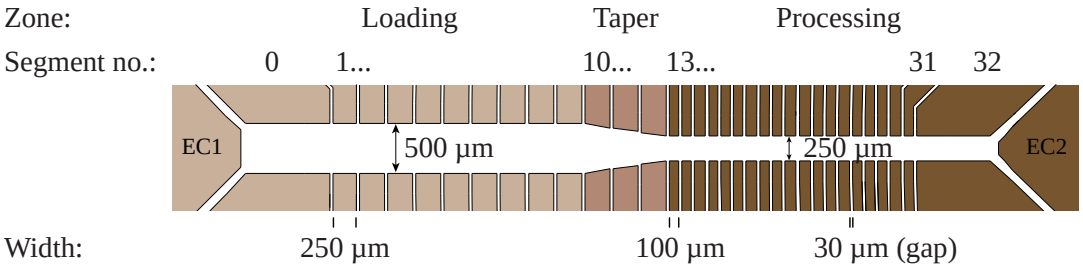

Figure 9.1: Schematic of the micro-trap layout (front view). It consists of a wider loading zone (to the left) and a narrower processing zone (to the right); these zones are connected by an intermediate region where the electrode-electrode distance is tapered from left to right. Each of the electrodes is individually addressable. EC1 and EC2 are end cap electrodes.

ions. This is mainly due to the high number of individually addressable electrodes: it provides 33 pairs of single electrode segments plus one pair of end cap electrodes (EC1 and EC2) on each end of the linear trap structure, making a whole of 70 independent electrodes.

The trap can be logically divided into three parts that differ in ion-electrode distance and electrode width. The first one called *trapping zone* offers the largest ion-trap distance and segment width. The design parameters of this region were chosen in order to facilitate the loading process by moderate trap frequencies. The calcium oven is aligned such that only this part of the trap is reached by neutral atoms. This prevents the other trap regions from being contaminated by the calcium beam. Patches of partially charged or chargeable material covering the electrodes are highly suspected to influence the trapping potentials and to increase heating rates.

In a second, intermediate *taper* zone the ion-electrode distance is linearly reduced from 250 μm down to 125 μm. The segment width is kept constant at 250 μm. This tapered structure offers interesting possibilities to investigate systematically the influence of the environment on the ion, as the distance between ion and electrodes can be varied in a very controlled manner by moving the ion further into the taper.

The taper zone ends into the so-called *processing zone*. Both segment width and slit height are reduced resulting in higher possible trap frequencies. This zone was designed to be the place where quantum information tasks like quantum gates can be performed best. The higher trap frequencies can be exploited to speed up quantum logic operations. Besides, due to the high segmentation of this zone (19 segment pairs), multiple individual, independent trapping potentials can be generated, each confining a small (processable) number of ions.

Both loading and processing zone have an additional pair of wide electrodes (0 and 32 in Fig. 9.1) that can be used as a sort of end cap electrodes of the trap. The true end caps (EC1 and EC2) completing the trap structure are not used most of the time, but can be useful to generate a field along the axial direction.

9.1.2 The PCB-Trap

The pcb-trap was mainly used to perform transport experiments with single cold ions. It is described in [Hub08a] or in more detail in the thesis of Dr. Th. Deuschle [Deu07]. The *pcb-trap* is a segmented linear Paul trap consisting of four printed circuit boards[1] (pcb) arranged in an x-shaped geometry, i.e. the boards are arranged in 90° angles such that dc and rf boards alternate, see Fig. 9.2. The two dc boards provide 2×15 independent electrodes and thus allow for designing the axial potential in a wide parameter range, a property we utilize for instance by generating time-dependent transport potentials.

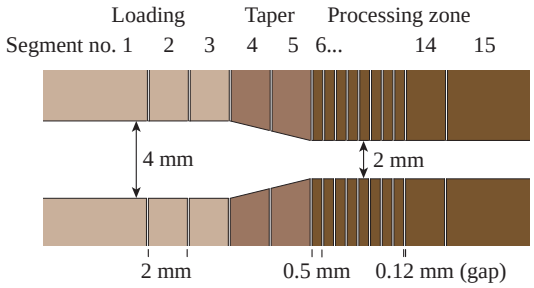

Figure 9.2: Schematic of the pcb-trap layout (front view). It consists of a wider loading zone (to the left) and a narrower processing zone (to the right); these zones are connected by an intermediate region where the electrode-electrode distance is tapered from left to right. Each of the electrodes is individually addressable. EC1 and EC2 are end cap electrodes.

The two rf electrodes (one on each board) are always kept at the same, alternating ac voltage, typically 400 V peak to peak amplitude resulting in 750 kHz radial trap frequency.

As the micro-trap described in the previous section, the trap can be divided into three parts that differ in the central slit's height or the ion-electrode distance, respectively. Note that the latter is a factor of eight larger than it is in the micro-trap; accordingly, the electrode segment widths are scaled up, too (2 mm and 0.5 mm, respectively). This results in lower trap frequencies for the same voltages applied.

The design objectives for the three trap zones were the same as for the micro-trap and are described in the previous section. The region with the highest trapping volume eases

[1] Material: P97 by Isola, pcb manufacturer micro pcb AG.

loading of new ions into the trap and helps to avoid contamination of the processing zone by the calcium oven. The processing zone is where all experiments presented in this thesis were performed.

9.2 FPGA-Based Fast Voltage Supply

To realize a fast voltage supply for the 64 independent electrodes of the micro-trap, the voltages are generated by a set of 16 digital to analog converters[2] (dac) in parallel, each of which is able to generate four independent voltages. This design offers the advantage to be scalable to even much higher electrode numbers. Each of the four outputs of one dac can be serially programmed to generate a voltage in the range from $-10\,\mathrm{V}$ to $+10\,\mathrm{V}$, where the amplitude resolution is 16 bit. All 16×4 voltages can be triggered and updated synchronously by additional control lines.

Thus, 16 parallel data lines, each addressing one dac, and each containing serial protocol data for its four outputs, have to be transmitted in parallel in order to perform synchronous, time-dependent voltage changes on all electrodes. For high update rates and large electrode numbers, the data rate can be significantly large. For instance, over $30\,\mathrm{MB/s}$ of digital data has to be transfered for 64 channels, 16 bit per channel and an update rate of $250\,\mathrm{kHz}$.

To this end, the protocol data is precomputed by the experimental control software. To realize a fast data transfer to the dac, the data is streamed to and buffered by a field-programmable gate array[3] (FPGA), which offers $\geq$ 64-bit bandwidth, and realizes the fast data transfer to the dac board via ethernet during the experiment. With this setup, it was possible to generate voltage sequences with update intervals down to $4\,\mu\mathrm{s}$ for all 64 channels.

9.3 Realization of a Single Photon Time Stamp

The utilized digital counter used for photon counting[4] has an internal 24-Bit register and two digital input ports, SRC and GATE. For standard use, the TTL-signals generated from the photomultiplier tube (PMT) for each detected photon are fed into SRC and increment

[2] DAC8814; Quad, Serial Input 16-Bit Multiplying Digital-to-Analog Converter by Texas Instruments. Maximum clock frequency 50 MHz.

[3] Xilinx Virtex-5 FX30T-1 on Xilinx Virtex-5 FXT Evaluation Board.

[4] National Instruments NI PCI-6733 High-Speed Analog Output with two digital 24-Bit counters.

the register by one for each photon. In regular time intervals (detection time), a rising edge on the GATE port writes the momentary register value into another memory area. Thus, the accumulated number of photon events from the beginning of the measurements until the rising GATE edge is read out and can be further processed by software (for instance, counter overflow is intercepted and corrected).

This standard technique yields the number of photons detected during those time intervals delimited by the GATE signals. The following trick makes it possible to obtain the arrival time of each photon with minimal memory consumption: The SRC port of the counter is fed with a TTL signal, whose edges are separated by a fixed interval ΔT, i.e. the value of the register always exactly contains the time in units of ΔT since the beginning of the measurement. The PMT-signals, however, are now fed into the GATE port. When a photon is detected by the PMT, a rising edge triggers the readout of the register, which exactly yields the time of the photon detection in units of ΔT. The result is a list of detection times, each corresponding to one detected photon.

The great advantage over a direct sampling of the detection interval is the minimal amount of data generated. The data rate does not depend on the time resolution but only on the number of photon events. For the longest implemented counting intervals of approximately 200 ms and a time resolution of 100 ns, sampling the whole interval would produce 7.6 MB of data (32-Bit) for each interval. For a mean photon count rate of 10 kHz, only 2000 photons are detected during this interval, giving a by three orders of magnitude reduced data rate of less than 8 kB. The SRC signal, which actually plays the role of the "clock" in the measurement, can be easily generated by standard function generators, so that sampling rates up to the GHz-range can be easily accomplished.

9.4 Quantum State Phonon Distributions

Explicit expressions and convenient formulas for the most common phonon distributions $P(n)$ are summarized in this section. Hereby, $P(n) = \rho_{nn} = \langle n|\rho|n\rangle$, where ρ is the density operator of the motional state. For a pure state $|\varphi\rangle$, this simplifies to $|\langle n|\varphi\rangle|^2$. All distributions are normalized, $\sum_{n=0}^{\infty} P(n) = 1$.

9.4.1 Thermal States

We begin with the most common state, the so-called *thermal* state. It is fully characterized by its temperature T. We define the inverse temperature $\beta := 1/(k_{\mathrm{B}}T)$, where k_{B} is

the Boltzmann's constant and T the temperature. With H being the Hamiltonian of the system, the eigenstates $|n\rangle$ and eigenenergies E_n of the system are given by $H|n\rangle = E_n|n\rangle$. The density matrix of a thermal state is given by the Boltzmann distribution,

$$\rho = \frac{1}{Z}\exp(-\beta H), \tag{9.1}$$

where

$$Z = \mathrm{Tr}\{\exp(-\beta H)\} \tag{9.2}$$

is the partition function of the canonical ensemble. From Eq. (9.1), we see that the density matrix of a thermal state has no (offdiagonal) coherences; its elements are $\rho_{nm} := \langle n|\rho|m\rangle = \delta_{nm}P_{\mathrm{th}}(n)$, with δ_{nm} being the Kronecker delta. The phonon number distribution follows from Eq. (9.1) as

$$P_{\mathrm{th}}(n) = \langle n|\rho|n\rangle = \frac{1}{Z}\, e^{-\beta E_n}. \tag{9.3}$$

For a harmonic oscillator with frequency ω_z, the eigenenergies are $E_n = \hbar\omega_z(n+\frac{1}{2})$, and

$$Z = \sum_{n=0}^{\infty} e^{-\beta E_n} = \frac{e^{\beta\hbar\omega_z/2}}{e^{\beta\hbar\omega_z}-1}. \tag{9.4}$$

For low temperatures $\beta\hbar\omega_z = O(1)$, it is convenient to use the mean phonon number $\overline{n} := \sum_{n=0}^{\infty} nP(n)$ instead of β to characterize the distribution. For a thermal state with inverse temperature β, the following equations help converting between these quantities:

$$\begin{aligned} \overline{n}(\beta) &= 1/(e^{\beta\hbar\omega_z}-1) \\ \beta(\overline{n}) &= \ln\left(1+\frac{1}{\overline{n}}\right)/(\hbar\omega_z) \\ P_{\mathrm{th}}(n) &= \frac{\overline{n}^n}{(\overline{n}+1)^{n+1}} \\ Z &= \sqrt{\overline{n}(\overline{n}+1)} \end{aligned} \tag{9.5}$$

Figure 9.3 depicts distributions for thermal states corresponding to different $\overline{n}$. A trapped $^{40}Ca^{+}$-ion with $\omega_z = 2\pi \times 1.4\,\mathrm{MHz}$ cooled down to a mean phonon number of $\overline{n} = 1$ has a temperature of $T \approx 100\,\mu\mathrm{K}$. It is noticeable that in such cases, $\beta\hbar\omega_z = (\hbar\omega_z)/(k_{\mathrm{B}}T) \approx 0.7$, so the thermal energy is on the same order of magnitude like the separation of the quantum levels, so the emergence of quantum effects is obvious in this low temperature regime.

9.4.2 Coherent States

In a classical picture, a particle confined in a harmonic potential has the lowest energy when resting at the potential minimum; this condition's quantum counterpart of the lowest

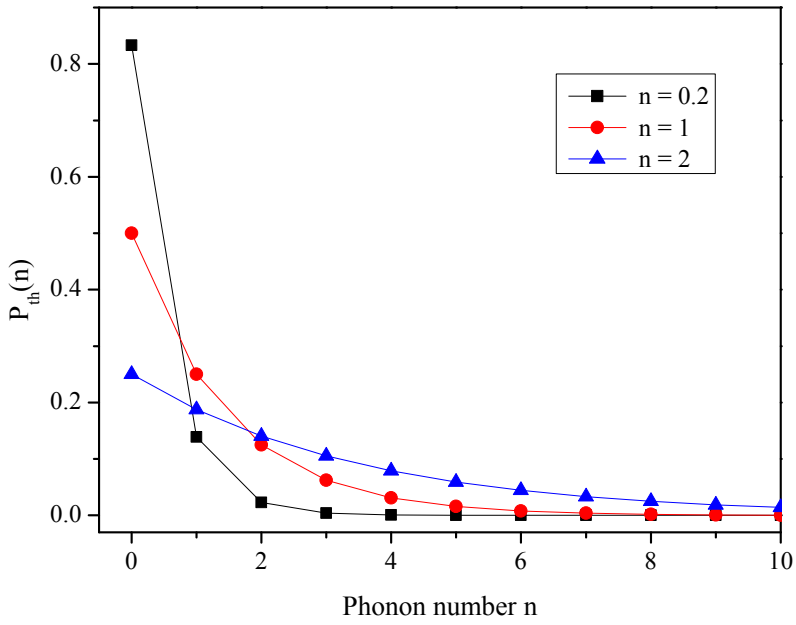

Figure 9.3: Phonon number distributions of different thermal states. These mixed states are completely defined by their inverse temperature $\beta = (k_\mathrm{B}T)^{-1}$. In the case of a harmonic oscillator with frequency ω_z, the mean number $\overline{n}$ of vibrational quanta (*phonons* of energy $\hbar\omega_z$), is more pictorial to characterize the state. Conversion formulas are given in Eq. (9.5). One can clearly see how the population more and more aggregates in the motional ground state $n = 0$ for temperatures approaching $\overline{n} = 0$ or $T = 0$, respectively. All these thermal distributions are exponential according to Eq. (9.3).

possible excitation energy is the ground state $|0\rangle$. If the classical particle is displaced from the potential minimum, it will undergo oscillations around the potential minimum. Its motion can be described by a trajectory in phase space (spanned by position and momentum), where each point of time corresponds to one point in phase space.

In the quantum case, due to the Heisenberg uncertainty principle, the state of the particle can not be described by a single point with definite position and momentum. Instead, the quantum counterpart is a so-called coherent state. Its position and momentum expectation values follow the classical phase space trajectory, and its phase space representation (e.g. the Wigner function) is centered around this classical trajectory point.

Consequently, we define the coherent state $|\alpha\rangle$ as a displaced ground state of motion,

$$|\alpha\rangle = D(\alpha)\,|0\rangle\,. \tag{9.6}$$

The displacement operator $D(\alpha) = \exp(\alpha a^\dagger - \alpha^* a)$ displaces the state in phase space by

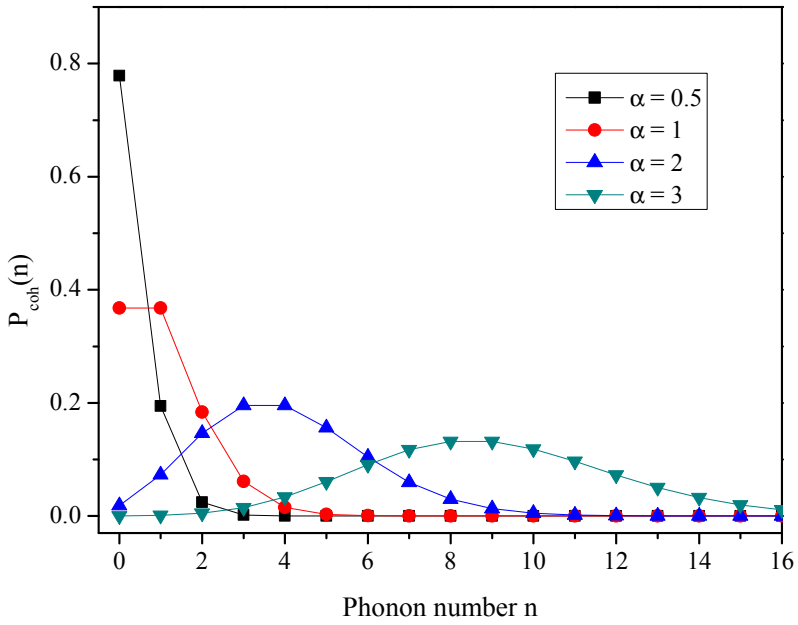

Figure 9.4: Phonon number distributions of different coherent states. These distributions are Poissonian according to Eq. (9.11). A coherent state is characterized by the complex parameter α, being a measure for its excitation. Accordingly, its mean phonon number is given by $\overline{n} = |\alpha|^2$. The complex phase of the state is not reflected in the phonon number distribution. For higher $\overline{n}$, the distribution is almost Gaussian while for $\overline{n} \to 0$, it becomes close to exponential.

α. The quantity α is a complex representation of a point in phase space,

$$\alpha = \sqrt{\frac{m\omega_z}{2\hbar}}\, x + i\sqrt{\frac{1}{2m\hbar\omega_z}}\, p, \tag{9.7}$$

where x and p are the position and momentum of the ion, respectively[5]. Figure 9.5 illustrates the effect of $D(\alpha)$. While the modulus $|\alpha|$ of the displacement parameter is a measure for the strength of the displacement "force" and hence the particle's excitation ($\overline{n} = |\alpha|^2$), its phase models the phase of the driving force. The displacement operator is unitary and its inverse is equal to a displacement with negative magnitude,

$$D^{-1}(\alpha) = D^{\dagger}(\alpha) = D(-\alpha). \tag{9.8}$$

Two subsequent displacements with magnitudes α_1 and α_2 are equal to one displacement with magnitude $\alpha_1 + \alpha_2$ and a phase shift depending on both magnitudes,

$$D(\alpha_2)D(\alpha_1) = e^{i\,\mathrm{Im}(\alpha_2\alpha_1^*)}\; D(\alpha_1 + \alpha_2). \tag{9.9}$$

[5] This can be most easily seen from α being the eigenvalue of $\hat{a}$ corresponding to the eigenstate $|\alpha\rangle$. The harmonic oscillator annihilation operator $\hat{a}$ can be written as $\sqrt{\frac{m\omega_z}{2\hbar}}\hat{x} + i\sqrt{\frac{1}{2m\hbar\omega_z}}\hat{p}$.

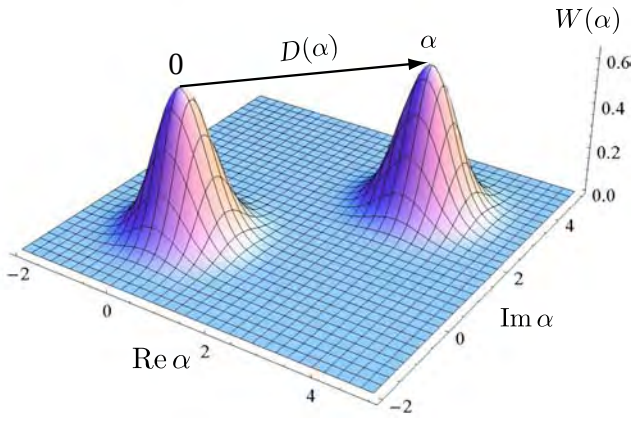

Figure 9.5: Illustration of the effect of the displacement operator $D(\alpha)$ on the ground state of motion $|0\rangle$ by the Wigner function in complex phase space. The ground state is a Gaussian state and therefore its phase space representation $W(\alpha)$ is a Gaussian around the origin $\alpha = 0$. The displacement operator shifts the state by $\alpha = 3(1+i)$ without distorting the distribution's shape.

In the number state basis, a coherent state reads

$$|\alpha\rangle = e^{-|\alpha|^2/2} \sum_{n=0}^{\infty} \frac{\alpha^n}{\sqrt{n!}} |n\rangle \,, \tag{9.10}$$

from which the phonon distribution

$$P_{\mathrm{coh}}(n) = |\, \langle n|\alpha\rangle \,|^2 = e^{-|\alpha|^2} \frac{|\alpha|^{2n}}{n!} \tag{9.11}$$

can be directly obtained. This is a Poissonian distribution with mean value $\overline{n} = |\alpha|^2$. For stronger displacements, the phonon distribution can hence be approximated by a Gaussian function. In the limit $\overline{n} \to 0$, the coherent and thermal state distributions become more and more indistinguishable, after all the ground state of motion $|n = 0\rangle$ is both a coherent ($|\alpha = 0\rangle$) and a thermal state (at $T = 0$). This can be comprehended by the coherent state distributions shown in Fig. 9.4.

The free time evolution of the coherent state $|\alpha\rangle$ in a harmonic oscillator of frequency ω_z can be described by a time-dependent displacement parameter as

$$\alpha(t) = e^{-i\omega_z t}\, \alpha(0). \tag{9.12}$$

This means, that the phase space distribution depicted in Fig. 9.5 simply rotates around the origin (at frequency ω_z), without changing its principal shape or spread.

Explicit expressions for phonon number distributions of displaced arbitrary Fock states can be found in Ref. [Cah69]. With that, one can, for example, derive displaced thermal state distributions.

9.4.3 Squeezed Vacuum States

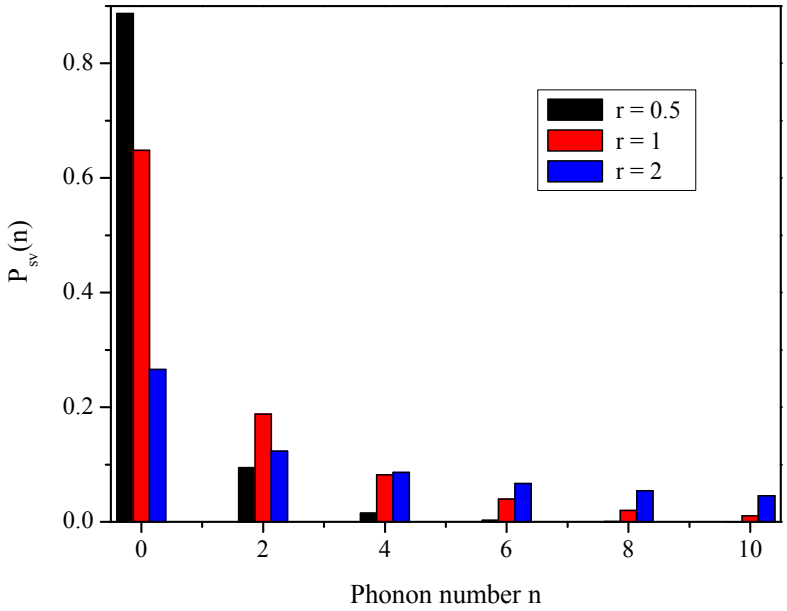

Figure 9.6: Phonon number distributions of squeezed vacuum states. The parameter r defines the squeezing amplitude. Note, that only even number states result from application of $\hat{S}(z)$ to the ground state, since the squeezing operator is quadratic in $\hat{a}$ and $\hat{a}^\dagger$, respectively.

A squeezed vacuum state results from application of the unitary squeezing operator

$$\hat{S}(z) = \exp\left\{\frac{1}{2}\left(z\hat{a}^\dagger - z^*\hat{a}^2\right)\right\} \tag{9.13}$$

to the vacuum (ground) state $|0\rangle$. Here, the squeezing parameter $z := r \cdot e^{i\theta}$ defines the amplitude r and the angle or phase (θ) of the squeezing. As the creation and annihilation operators appear only quadratically in Eq. (9.13), only even number states are populated in the squeezed vacuum state. The corresponding number state distribution has the form [Dod94]

$$P_{\mathrm{sv}}(n) = \begin{cases} \frac{1}{\cosh r}\left(\frac{\tanh r}{2}\right)^n \frac{n!}{[(n/2)!]^2}, & \text{for even } n \\ 0, & \text{for odd } n \end{cases} \tag{9.14}$$

$P_{\mathrm{sv}}(n)$ is depicted in Fig. 9.6 for different values of r. Its mean phonon number is given by $\overline{n} = \sinh^2 r$. The application of the squeezing operator is, of course, not restricted to the vacuum state. The function $P(n)$ for an arbitrary mixed input state is very complicated in general. Phonon number distributions for arbitrary squeezed coherent and Fock states can be found, for example, in Ref. [Dod94].

9.5 Magnetic Level Splitting

For a weak magnetic field, the fine structure levels (spin $S = 1/2$, orbital angular momentum J and total angular momentum J) of $^{40}Ca^{+}$split into $2J + 1$ sublevels due to the Zeeman effect. These levels are labeled by their magnetic quantum number $m = -J, -J + 1, ..., +J$. Given a magnetic field strength B, the magnetic field-dependent energy of a certain level $\lambda := (S, L, J, m)$ reads

$$E_\lambda(B) = E_\lambda(0) + \Delta E_\lambda = E_\lambda(0) + \mu_\mathrm{B} B \cdot m\, g_\lambda \tag{9.15}$$

where $\mu_\mathrm{B} = h \times 1.400\,\mathrm{MHz/Gauss}$ is the Bohr magneton, h the Planck constant and g_λ is the Landé-factor of the fine structure level. It depends only on L and J ($S = 1/2$ for all transitions here) and can be calculated from

$$g_{(L,J)} = 1 + \frac{J(J+1) - L(L+1) + S(S+1)}{2J(J+1)}, \tag{9.16}$$

where the g-factor of the spin was approximated with 2. The following table shows $g_{(L,J)}$ for all relevant levels:

Level	$S_{1/2}$	$P_{1/2}$	$P_{3/2}$	$D_{3/2}$	$D_{5/2}$
S,L,J	$\frac{1}{2}$,0,$\frac{1}{2}$	$\frac{1}{2}$,1,$\frac{1}{2}$	$\frac{1}{2}$,1,$\frac{3}{2}$	$\frac{1}{2}$,2,$\frac{3}{2}$	$\frac{1}{2}$,2,$\frac{5}{2}$
$g_{(L,J)}$	2	2/3	4/3	4/5	6/5

Table 9.1: Quantum numbers and Landé-factors of all relevant levels in $^{40}Ca^{+}$.

Therewith, the transition energy between two Zeeman levels λ_1 and λ_2 is given by

$$E_{\lambda_2}(B) - E_{\lambda_1}(B) = \Delta E_{12}(0) + \mu_\mathrm{B} B \cdot (m_2\, g_{\lambda_2} - m_1\, g_{\lambda_1}), \tag{9.17}$$

where $\Delta E_{12}(0)$ is the transition energy at zero magnetic field. In special, the $S_{1/2}$-Zeeman splitting of the spin qubit is obtained (here in terms of frequency) with $g_{\lambda_1} = g_{\lambda_2} = 2$ as

$$\Delta_\mathrm{Z} := \frac{1}{\hbar}\left(E_{(0,\frac{1}{2},+\frac{1}{2})} - E_{(0,\frac{1}{2},-\frac{1}{2})}\right) = \frac{2}{\hbar}\,\mu_\mathrm{B}\; B \approx 2\pi \times 2.799\,\mathrm{MHz} \times B/\mathrm{Gauss}. \tag{9.18}$$

Note that neither are there magnetic field insensitive levels nor is it possible to find a pair of sublevels in $S_{1/2}$ and $D_{5/2}$, respectively, so that the differential energy shift cancels.

This would be advantageous to avoid loss of phase coherence by magnetic field fluctuations. The odd isotope $^{43}Ca^{+}$, that has – in contrast to $^{40}Ca^{+}$– a non-zero nuclear spin $I = 7/2$ and thus a hyperfine structure, exhibits magnetic field insensitive levels with $m_F = 0$, so that in first order of B magnetic field insensitive transitions are possible [Kir09].

9.6 Scientific Publications

The following scientific papers (in chronological order) were published in the course of the thesis:

- *Transport of ions in a segmented linear Paul trap in printed-circuit-board technology*
  G. Huber, T. Deuschle, W. Schnitzler, R. Reichle, K. Singer and F. Schmidt-Kaler
  New Journal of Physics **10**, 013004 (2008)

- *Employing trapped cold ions to verify the quantum Jarzynski equality*
  G. Huber, F. Schmidt-Kaler, S. Deffner and E. Lutz
  Physical Review Letters **101**, 070403 (2008)

- *Coherent Manipulation of a $^{40}Ca^{+}$ Spin Qubit in a Micro Ion Trap*
  U. G. Poschinger, G. Huber, F. Ziesel, M. Deiß, M. Hettrich, S. A. Schulz, K. Singer, G. Poulsen, M. Drewsen, R. J. Hendricks and F. Schmidt-Kaler
  Journal of Physics B: Atomic, Molecular and Optical Physics **42**, 154013 (2009)

- *A trapped-ion local field probe*
  G. Huber, F. Ziesel, U. Poschinger, K. Singer and F. Schmidt-Kaler
  Accepted for publication in Applied Physics B: Lasers and Optics (2010), in print
  DOI 10.1007/s00340-010-4148-x

Transport of ions in a segmented linear Paul trap in printed-circuit-board technology

G. Huber, T. Deuschle, W. Schnitzler, R. Reichle, K. Singer and F. Schmidt-Kaler

Published 14 January 2008 in the scientific journal:

New Journal of Physics

(Volume: 10 / Page: 013004 / Year: 2008)

New Journal of Physics
The open-access journal for physics

Transport of ions in a segmented linear Paul trap in printed-circuit-board technology

G Huber[1], T Deuschle, W Schnitzler, R Reichle, K Singer and F Schmidt-Kaler

Institut für Quanteninformationsverarbeitung, Universität Ulm, Albert-Einstein-Allee 11, D-89069 Ulm, Germany
E-mail: gerhard.huber@uni-ulm.de

New Journal of Physics **10** (2008) 013004 (15pp)
Received 5 October 2007
Published 14 January 2008
Online at http://www.njp.org/
doi:10.1088/1367-2630/10/1/013004

Abstract. We describe the construction and operation of a segmented linear Paul trap, fabricated in printed-circuit-board technology with an electrode segment width of 500 μm. We prove the applicability of this technology to reliable ion trapping and report the observation of Doppler-cooled ion crystals of $^{40}Ca^{+}$ with this kind of trap. Measured trap frequencies agree with numerical simulations at the level of a few percent from which we infer a high fabrication accuracy of the segmented trap. To demonstrate its usefulness and versatility for trapped ion experiments we study the fast transport of a single ion. Our experimental results show a success rate of 99.0(1)% for a transport distance of 2×2 mm in a round-trip time of $T = 20\,\mu$s, which corresponds to 4 axial oscillations only. We theoretically and experimentally investigate the excitation of oscillations caused by fast ion transports with error-function voltage ramps: for a slightly slower transport (a round-trip shuttle within $T = 30\,\mu$s) we observe non-adiabatic motional excitation of 0.89(15) meV.

[1] Author to whom any correspondence should be addressed.

Contents

1. Introduction

Three-dimensional (3D) linear Paul traps are currently used for ion-based quantum computing [1]–[4] and high-precision spectroscopy [5]–[7]. An axial segmentation of the dc electrodes in these traps enables the combination of individual traps to a whole array of micro-traps. Structure sizes down to the range of a few tens of micrometres [8, 9] are nowadays in use and mainly limited by fabrication technology. However, most of these fabrication methods require advanced and non-standard techniques of micro-fabrication as is known from micro-electro-mechanical system (MEMS) processing or advanced laser machining. Long turn-around times and high costs are complicating the progress in ion trap development. In this paper, we present a segmented 3D ion trap which is fabricated in UHV-compatible printed-circuit-board (PCB) technology. While with this technology, spatial dimensions of electrodes are typically limited to more than 100 μm, the production of sub-millimetre sized segments is simplified by the commonly used etching process. The advantages of PCB-traps are therefore a fast and reliable fabrication and consequently a quick turn-around time, combined with low fabrication costs. The feasibility of the PCB-technique for trapping ion clouds in a surface-electrode trap has already been shown in [10]. In future, we anticipate enormous impact of the PCB-technology by including standard multi-layer techniques in the trap design. On a longer timescale on-board electronics may be directly included in the layout of the PCB-boards, e.g. digital-to-analog (DA) converters may generate axial trap control voltages or digital radio frequency (RF)-synthesizers could be used for dynamical ion confinement.

In this paper, we first describe the fabrication of our PCB-trap and the overall experimental set-up in section 2. The following section 3 is dedicated to a comparison of measured trap frequencies with numerical simulations for a characterization of radial and axial trapping. Special attention is paid in section 4 to the compensation of electrical charging effects of the

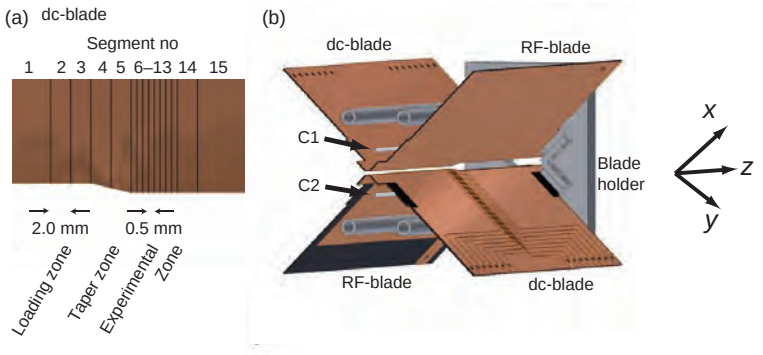

Figure 1. Electrode design. (a) Close-up view of the blade design: the dc-blade segment width is 2 mm in the loading and taper zone, and 0.5 mm in the experimental zone. The trap consists of a 4 mm wide loading zone, a tapered intermediate zone, and a 2 mm wide experimental zone. (b) Sketch of the assembled X-trap consisting of four blades, drawn with missing front blade holder for sake of clarity. Compensation electrodes C1 and C2 are parallel to the trap axis.

trap electrodes since PCB-technology requires insulating grooves between the electrodes that may limit the performance of the trap. We adjust the compensation voltages to cancel the effect of stray charges and investigate the stability of these compensation voltages over a period of months. Our measurements show that PCB-traps are easy to handle, similar to standard linear traps comprising solely metallic electrodes. In section 5, the segmentation of the dc-electrodes is exploited to demonstrate the transport of a single ion, or a small crystal of ions, along twice the distance of 2 mm in a round-trip shuttle over three axial trap segments. Special attention is given to fast transports within total transport times of $T = 20$–$100\,\mu$s, corresponding to only 4–20 times the oscillation period of the ion in the potential. We checked the consistency of the measured data with a simple transport model.

2. Experimental set-up

2.1. Design, fabrication and operation of PCB-traps

The trap consists of four blades, two of them are connected to a RF supply and the two remaining, segmented blades are supplied with static (dc) voltages, see figure 1. The dc- and RF-blades are assembled normal to each other (the cross-section is X-shaped). In a loading zone, the two opposing blades are at a distance of 4 mm. A tapered zone is included in order to flatten the potential during a transport between the wider loading and the narrower experimental zone. In the latter zone, the distance between the blades is reduced to 2 mm. The material of the blades is a standard polyimide material coated by $\sim 18\,\mu$m of copper on all sides of the substrate. Etched insulation grooves of $120\,\mu$m in the copper define dc-electrodes. The RF-drive frequency near $\Omega/2\pi = 11.81$ MHz is amplified and its amplitude is further increased

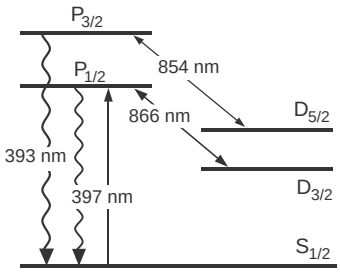

Figure 2. Energy levels and relevant optical transitions of $^{40}Ca^{+}$.

by a helical resonator before it is applied to the RF blades. At typical operating conditions, we measure a peak-to-peak voltage of about $V = 400\ V_{pp}$ by using a home-built capacitive divider with a small input capacitance to avoid artificial distortion of the signal by the measurement. The dc-control voltages from a computer card are connected to the trap segments via low-pass RC-filters with corner frequency at 1 MHz. The trap is housed in a stainless steel vacuum chamber with enhanced optical access held by an ion getter and a titanium sublimation pump at a pressure of 3×10^{-10} mbar. This value was reached without bakeout, indicating the UHV-compatibility of the PCB-materials[2].

2.2. Laser excitation and fluorescence detection

The relevant energy levels of $^{40}Ca^{+}$ ions are shown in figure 2. All transitions can be either driven directly by grating stabilized diode lasers, or by frequency doubled diode lasers[3]. The lasers are locked according to the Pound–Drever–Hall scheme to Zerodur Fabry–Perot cavities for long-term frequency stability. Each laser can quickly be switched on and off by acousto–optical modulators. Optical cooling and detection of resonance fluorescence is achieved by simultaneous application of laser light at 397 and 866 nm. Radiation near 854 nm depopulates the $D_{5/2}$ metastable state (1.2 s lifetime).

Two laser sources at 423 ($\leqslant$5 mW) and 375 nm ($\leqslant$1 mW) are used for photoionization loading of ions [11, 12]. The high loading efficiency allows for a significant reduction of the Ca flux from the resistively heated oven and minimizes the contamination of the trap electrodes. By avoiding the use of electron impact ionization the occurrence of stray charges is greatly suppressed.

In this experiment, laser beams near 397, 866 and 854 nm are superimposed and focused into the trap along two directions: one of these directions (D1) is aligned vertically under 5° with respect to the top–bottom axis and the other beam (D2) enters horizontally and intersects the trap axis under an angle of 45°. A high-NA lens is placed 60 mm from the trap center behind an inverted viewport to monitor the fluorescence of trapped ions at an angle perpendicular to the trap axis direction. The fluorescence light near 397 nm is imaged on to the chip of an EMCCD camera[4] in order to achieve a photon detection efficiency of about 40%.

[2] Material P97 by Isola, PCB manufacturer (http://www.micro-pcb.ch).
[3] Toptica DL100, DL-SHG110 and TA100.
[4] Electron multiplying CCD camera, Andor iXon DV860-BI.

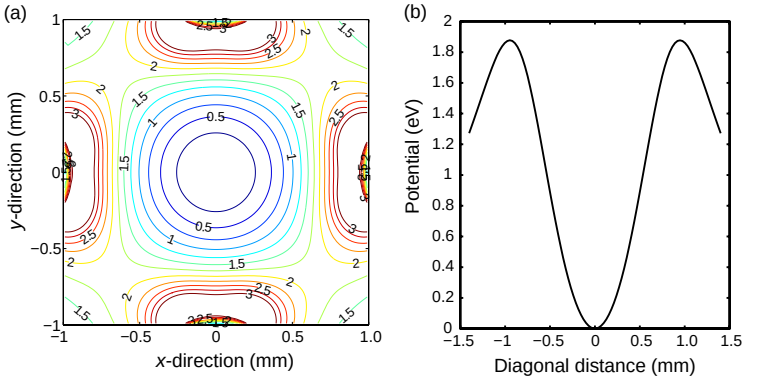

Figure 3. (a) Simulation of the pseudo-potential in the $(x–y)$-plane in the experimental zone for $V = 408\,V_{\mathrm{pp}}$. (b) Cross-section through the potential shown in (a) along the $x = y$-direction yielding a radial trap frequency of $\omega_{\mathrm{rad}}/2\pi = 663\,\mathrm{kHz}$ and a trapping depth of approx. 1.9 eV.

3. Numerical simulations

3.1. Radial confinement

The complex layout of the multi-segmented trap requires elaborate numerical techniques to simulate the electrical potentials accurately in order to avoid artificial effects. Instead of using widespread commercial FEM routines that mesh the whole volume between the electrodes, boundary-element methods (BEM) are more suited but also more complex in their implementation. The effort in such methods is reduced for large-space computations since they only need to mesh surfaces of nearby electrodes and multipole approximations are done to include far distant segments in order to speed up computations. We have written a framework for the solution of multipole-accelerated Laplace problems[5]. This method is not limited in the number of meshed areas and thus allows for accurate calculations with a fine mesh. In the simulations presented here, we typically subdivide the surfaces of the trap electrodes into approx. 29 000 plane areas to determine the charge distributions and the free-space potential within the trap volume numerically. Figure 3(a) shows the calculated pseudo-potential in the $(x–y)$-plane of the experimental zone for a RF of $\Omega/2\pi = 11.81\,\mathrm{MHz}$ and a RF peak-to-peak voltage $V = 408\,V_{\mathrm{pp}}$. By symmetry the diagonal directions along $x = \pm y$ contain the nearest local maximum and thus determine the relevant trap depth of approx. 1.9 eV for the applied experimental parameters. A cross-section through the pseudo-potential along this direction is shown in figure 3(b) at the same axial position as in figure 3(a). From these simulations, we are able to extract a radial trap frequency of $\omega_{\mathrm{rad}}/2\pi = 663\,\mathrm{kHz}$ in the absence of applied dc potentials.

[5] The solver was developed by the MIT Computational Prototyping Group (http://www.rle.mit.edu/cpg).

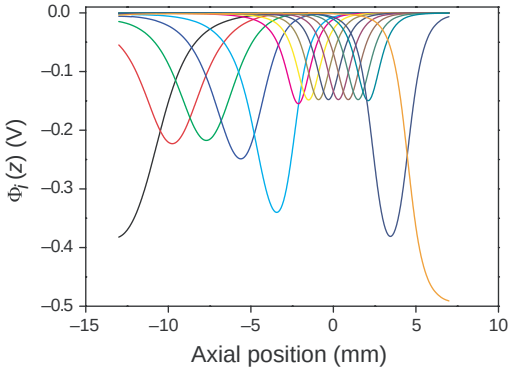

Figure 4. Individual axial electrode pair potentials $\phi_i(z)$. For detailed description see text in section 3.2. Narrow electrodes show a lower maximum potential due to the smaller amount of surface charges. An arbitrary axial potential is formed by superposing individual contributions.

3.2. Axial confinement

For axial confinement opposing dc electrodes are set to the same voltage U_i, $i = 1, \ldots, 15$ labeling the electrode number as depicted in figure 1. These voltages are supplied by DA converters covering a voltage range of ± 10 V with a maximum update rate of 1 MHz. Figure 4 illustrates the potentials $\phi_i(z)$ obtained when only U_i is set to -1 V and all other voltages are set to zero. For arbitrary voltage configurations, the axial potential $\phi(z) = \sum_i U_i \phi_i(z)$ is a linear superposition of the single electrode potentials. Tailored axial potentials for the generation of single or multiple axial wells with given secular frequency, depth and position of the potential minimum are obtained by solving the linear equation given above for the voltages U_i. Time-dependent voltages are used to move the potential minimum guiding the trapped ion along the trap axis.

4. Cold ion crystals

4.1. Observation of linear crystals and measurement of trap frequencies

The trap is operated in the loading configuration with dc voltages of $U_{\text{load}} = \{\ldots, U_7, \ldots, U_{13}, \ldots\}_{t=0} = \{\ldots, 6\,\text{V}, \ldots, 8\,\text{V}, \ldots\}$ while non-specified segment voltages are held at ground potential. From simulations we estimate that the axial trap frequency is $\omega_z/2\pi = 199$ kHz at the potential minimum close to the center of electrode 10. Linear strings and single ions crystallize under continuous Doppler cooling with beams D1 and D2, consisting of superimposed beams at 397 (0.3 mW with 60 μm beam waist), 866 and 854 nm (both 3 mW with 100 μm beam waist), cf figure 5.

Applying a sinusoidal waveform with 1 mV amplitude to electrode segment 10 allows for a parametrical excitation near resonance. Observation of the ion excitation through decreasing fluorescence on the EMCCD image signifies a resonance condition. This way,

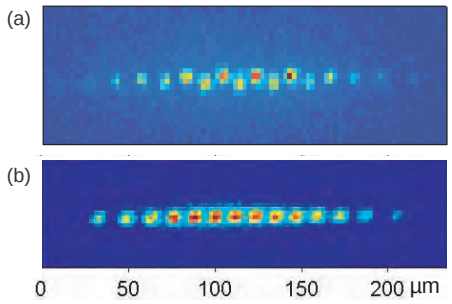

Figure 5. (a) Fluorescence of an ion crystal with 14 ions in a zig-zag configuration as observed with the EMCCD camera. Exposure time was set to 100 ms (optical magnification is 10.4). (b) Linear crystal with 14 ions and a slightly more relaxed axial trap frequency than in (a). This induces a phase transition into a purely linear configuration of ion positions.

we experimentally find a radial frequency of $\omega_{\mathrm{rad}}/2\pi = 700(2)$ kHz and an axial frequency of $\omega_z/2\pi = 191(2)$ kHz. We attribute the 5% deviations to residual electric fields arising mainly from charging of the etched insulation groove cuts as well as to the limited accuracy of the RF-voltage amplitude measurement. Stable trapping at a q-value of about 0.16 is achieved. Measuring the mutual distances in a linear two- or three-ion crystal easily allows for calibrating the optical magnification of the imaging optics to be 10.4, with a CCD-pixel size of 24 μm. For determining the resonant frequency of the cycling transition used for Doppler cooling the fluorescence is detected on a photomultiplier tube (PMT) while scanning the laser frequency at 397 and/or 866 nm. This yields an asymmetric line profile of about 30–50 MHz FWHM, exhibiting the features of a dark resonance with a maximum count rate of 20 kHz. For all following measurements we keep the detuning of the 397 nm laser at $\Gamma/2$ (half of the linewidth) fixed and adjust the frequency of the 866 nm laser to obtain a maximum fluorescence rate.

4.2. Compensation of micromotion

Ions in small traps are likely to be affected by stray charges that shift the ions out of the RF null since those charges can often not be neglected in most ion traps. Therefore, the dynamics of ions in general exhibits a driven micromotion oscillation at a frequency of $\Omega/2\pi$ leading to a broadening of the Doppler cooling transition and higher motional excitation [13]. A second disadvantage of micromotion is a reduced photon scattering rate at the ideal laser detuning of $\Gamma/2$. To correct for potentials induced by stray charges and maybe geometric imperfections we can apply compensation voltages to the electrodes labeled C1 and C2, as sketched in figure 1(b).

For detecting the micromotion we trigger a counter with a photon event measured by the PMT in the experimental zone and stop the counter by a TTL phase locked to half the trap drive frequency $\Omega/2\pi$. If the ion undergoes driven motion, the fluorescence rate is modulated as a cause of a modulated Doppler line shape, see figure 6(a). Here, we detect the ion motion

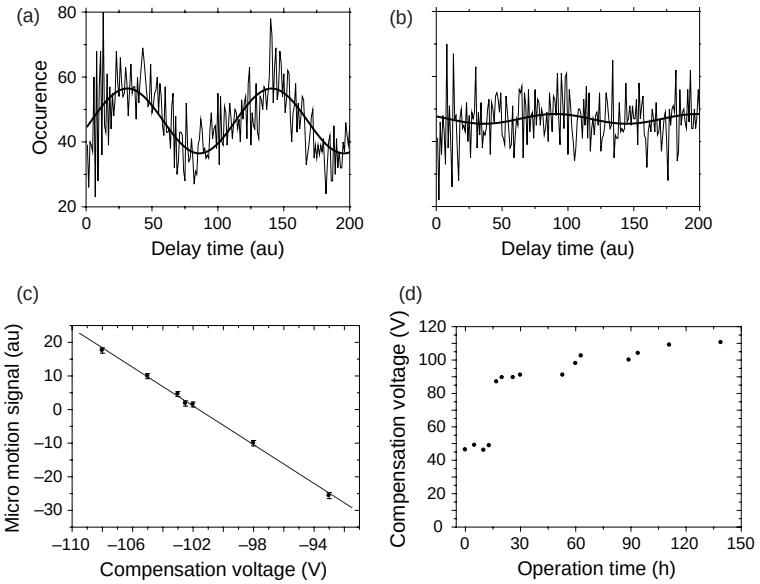

Figure 6. Histogram of photon count events for different values of micromotion compensation voltages: (a) Trace far from compensation with $U_{C1} = 98\,V$ fitted to a sine function. (b) Near to optimum compensation with $U_{C1} = 102.5\,\mathrm{V}$. (c) The amplitude of a sinusoidal fit for different compensation voltages shows a linear dependence between the amplitude and applied compensation. Negative amplitudes correspond to a 180° phase flip; this happens when the ion passes the RF null. A linear fit reveals the optimal value at $U_{C1} = 101.6\,\mathrm{V}$. With this data an optimal compensation is determined within an uncertainty of less than 0.3 V. The overall data collection time is less than 5 min. (d) Optimum compensation voltage plotted versus the operation time of the oven. We attribute the long-term drift of this voltage to an increasing calcium contamination on the trap electrodes in the experimental zone.

in the direction of the laser beam. If a flat histogram is measured the ion does not possess a correlated motion with the RF driving voltage. Then, it resides close to the RF null where the modulation vanishes, cf figure 6(b). From taking a series of histograms for different values of the compensation voltage a linear relation between observed modulation and applied compensation is obtained. The optimal compensation voltage can then be read from the abscissa for zero correlation amplitude, figure 6(c).

Our long-term observation of the optimum compensation voltage indicates a weak increase over three months. Since we did not bakeout the vacuum chamber, storage times of ions are several minutes so that we needed to reload ions from time to time. During all experimental sessions, we kept the temperature of the oven fixed so that the flux of neutral Ca atoms was

sustained. This is not necessary in a better vacuum environment. An oven current of 7 A leads to a flux such that we reach a high loading rate of 0.1–0.4 ions per second. Thus, by operating the oven continuously we could accumulate a long operation time of over 150 h. The 20% step in figure 6(d) was caused by a power failure.

By comparing our measurements to the long-term recording of [14] for a 2 mm linear trap [15] with stainless steel electrodes we find similar drifts in compensation voltages. Thus, it seems that PCB-traps can be corrected equally well for micromotion so that the larger insulation grooves do not harm the performance.

In all of the experiments presented here the beam of neutral calcium is directed into the narrow experimental zone where micromotion is compensated as described above. In future, however, we plan to use the loading zone where a higher loading rate through the larger involved phase space during trapping is expected. Then, ions can be shuttled into the cleaner experimental zone 8 mm apart. Calcium contamination will then be completely avoided and much lower compensation voltages and drifts are expected. The segmented PCB-trap operated this way may even show an improved micromotion compensation stability as compared to traditional linear and 3D traps having less insulation exposed to the ions.

5. Transport of single ions and ion crystals

As recently suggested [16], ions in a future quantum computer based on a segmented linear Paul trap might be even shuttled through stationary laser beams to enable gate interactions. In a different approach, one might shuttle ions between the quantum logic operations [17]. This would alleviate more complex algorithms and reduce the enormous technological requirements extensively. According to theoretical investigations [18], transport could occupy up to 95% of operation time in realistic algorithms. Given the limited coherence time for qubits, shuttling times need therefore to be minimized. Our work as described below may be seen in the context of the theoretical and experimental works found in [19]–[21]. With our multi-segmented Paul trap, we have made first investigations of these speed limits in order to enter the non-adiabatic regime and studied the corresponding energy transfer. Preferred transport ramps are theoretically well understood [22]. The current challenge arises from experimental issues, i.e. how accurate potentials can be supplied, how drifts in potentials can be avoided and whether sophisticated shuttling protocols can be used [23]. First transport studies have been made some years ago by the Boulder group using an extremely sparse electrode array [24]. Non-adiabatic transports of cold neutral atom clouds in a dipole trap have been demonstrated in [25] and show very similar qualitative behavior, even though on a completely different timescale (axial frequency of approx. $2\pi \times 8$ Hz).

The PCB-trap described here contains 15 pairs of dc-segments. Using a suitable time sequence of control voltages $U_i(t), i = 1, \ldots, 15$, the axial potential can be shaped time-dependently in a way to transport ions along the trap axis. In the following, we present the results of various transport functions for a distance of $2d = 4$ mm.

For these measurements, we follow a six-step sequence:

1) Initially, we confine an ion in an axial trapping potential in the loading configuration U_{load}, figure 7(a). The single ion is laser cooled by radiation near 397 and 866 nm. Compensation voltages have previously been optimized for this trap configuration such that the width of the excitation resonance near 397 nm is minimal. Then, the laser beams are switched off.

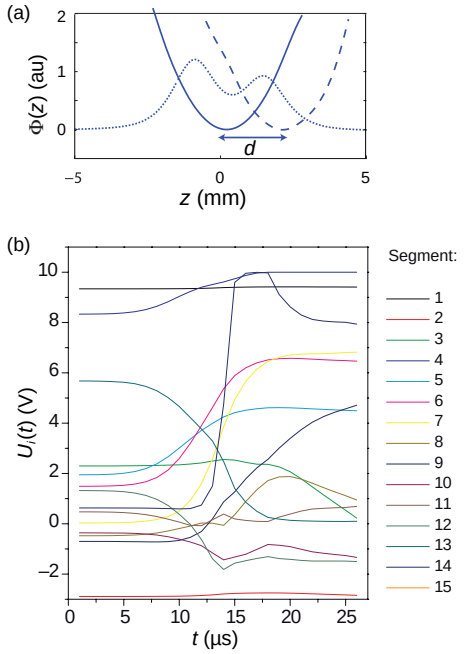

Figure 7. (a) Axial potentials for loading and observing ions (dotted line) U_{load}, at the beginning (solid line) of the transport with $U_{\text{trans}}(t=0) = \{-8.77, 9.34, -2.89, 2.30, 8.33, 1.95, 1.49, 0.03, -0.48, -0.70, -0.36, 0.47, 1.32, 5.68, 0.63\}$V and at its turning point (dashed line). (b) Trap control voltages U_1 to U_{15} for transporting the ion by an error function ramp. Discontinuities in the curves result from the time discretization in steps of 1 μs.

2) Before starting the transport, U_{load} is linearly changed into the initial transport potential $U_{\text{trans}}(t=0)$ in 10 steps each taking 1 μs. Note that the transport potential should be adapted in shape and depth, and is not necessarily identical to the optimum potential for laser excitation, for fluorescence observation, and for quantum logic gate operations. In our case, the axial trap frequency for $U_{\text{trans}}(t=0)$ is adjusted for $\omega_z/2\pi = 200$ kHz, and the minimum positions of U_{load} and U_{trans} both coincide with the center of segment 10. The voltages for the transport potential are chosen according to the regularization of [22].
3) By changing the control voltages such that the potential minimum of U_{trans} moves according to an error function, the ion is accelerated and moved to a turning point 2 mm away, centered roughly above segment 13.
4) The ion is accelerated back to the starting point again using the same time-inverted waveforms. By our calculations, we aim to determine the control voltages such that the ion always remains within a harmonic potential well of constant frequency ω_z throughout the whole transport procedure.

5) Finally, the transport potential U_{trans} is ramped back linearly in 10 μs into the initial potential U_{load}.
6) The laser radiation is switched on again to investigate either the success probability of the transport or the motional excitation of the ion.

The sequence is repeated about 10^3–10^5 times, then the parameters of the transport ramp in step (3) and (4) are changed and the scheme is repeated.

Ideally, we would create an axial potential that closely approximates $\phi(z,t) = m\omega_z^2(z - z_0(t))^2/2q$ with an explicit time-dependent position of the potential minimum $z_0(t)$. However, all presented simulations and motional excitation energies were deduced from the numerical axial potentials instead. Moving the potential minimum from its starting point $z_0(0) = 0$ to the turning point $z_0(T/2) = 2$ mm and back again to $z_0(T) = 0$ leads to a drag on the trapped ion. For sake of convenience, we express the total time for a round-trip T in units of the trap period $\tau \equiv T\omega_z/2\pi$. The dimensionless parameter τ then denotes the number of oscillations the ion undergoes in the harmonic well during the transport time. The functional form of the time-dependent position of the potential minimum $z_0(t)$ is crucial for the transport success and the motional excitation. We have chosen a truncated error-function according to

$$f_\sigma(t) = \frac{d}{2}\left(1 + \frac{\mathrm{Erf}\left[(4t/T - 1)\,\sigma\right]}{\mathrm{Erf}[\sigma]}\right), \qquad z_0(t) = \begin{cases} f_\sigma(t), & 0 \leqslant t \leqslant T/2, \\ d - f_\sigma(T - t), & T/2 < t \leqslant T, \end{cases} \tag{1}$$

as input to find the waveforms of all contributing electrode pairs, figure 7(b).

Small first and second derivatives at the corner points assure that the ion experiences only smoothly varying accelerations at these times. The parameter σ determines the maximum slope of the function. The smoother the shuttling begins the higher average and maximum velocities are needed for a fast transport. A high maximum velocity $\dot{z}_0$ results in far excursions of the ion from the potential minimum so that it may experience higher derivatives not fulfilling the harmonic potential approximation anymore. A compromise can be found between slowly varying corner point conditions and ion excitation due to fast, non-adiabatic potential movements. Experimentally, we found the lowest energy accumulated for $\sigma = 2.3$. In our experiment, the update time of the supply hardware for the electrode voltages is limited to 1 μs. To account for this effect in our simulations we also discretize $z_0(t)$ in time steps. These discontinuities are evident in figure 7(b) already indicating that a higher sampling rate of the DA channels would be desirable. Furthermore, for short shuttles the amplitude discretization through the DA converters makes an exact reproduction of $z_0(t)$ impossible. This gives rise to discrete dragging forces transferring motional excess energy to the ion. We verified by numerical simulations that even for the fastest transports with durations of only $T \approx 10$–12 μs, deviations from the non-discretized time evolution were negligible. Since in our case, the typical involved motional energies are much larger than $\hbar\omega$, a simple classical and one-dimensional model of the ion transport is justified with the equation of motion

$$\ddot{z}(t) = -\frac{q}{m}\frac{\mathrm{d}\phi(z,t)}{\mathrm{dz}} = -\omega^2(z - z_0(t))^2. \tag{2}$$

We solve this equation numerically for functions $z_0(t)$ with varying σ. The resulting phase space trajectories $\{z(t), \dot{z}(t)\}$ are plotted in figure 8 for $T = 20$ μs ($\tau = 4$) and $T = 16$ μs ($\tau = 3.2$). In the first case, the phase space trajectory starts and ends close to {0,0}, i.e. both the potential and the kinetic energy are modest after the transport. In the second case, the particle reaches

IOP Institute of Physics DEUTSCHE PHYSIKALISCHE GESELLSCHAFT

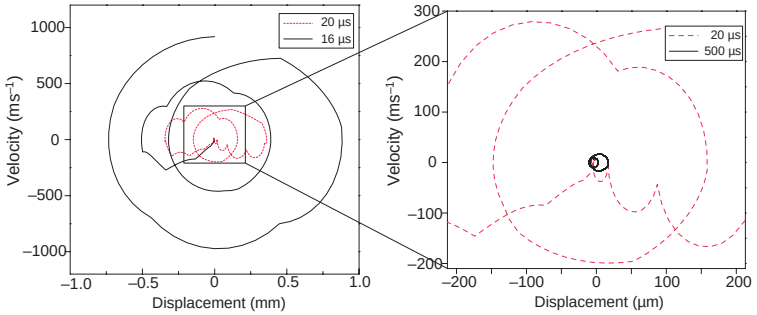

Figure 8. Phase space trajectories of an ion for two different transport durations. The closed loop (dotted line, $\tau = 4$) indicates a transport with low final motional energy. For $\tau = 3.2$ (dashed line) the ion does not reach zero velocity at $t = T$ and a final energy of 171 meV. Discontinuities in the trajectories result from the time discretization in steps of 1 μs.

its starting point $z_0(T) = z(0)$ again, but resides with a high oscillating velocity $\dot{z}(T)$ but small displacement.

5.1. Transport probabilities

This section addresses the question of how fast the transport of an ion in the manner described above can eventually be performed before it gets lost. In the following, we discuss transports in the adiabatic regime $\tau \gg 1$ and far off this regime. For the measurements, an experimental sequence with transport duration τ is interleaved by Doppler cooling cycles of 1 s duration to ensure to start always from the same initial energy close to the Doppler limit. After n_i successful transports with $i = 1, \ldots, N$, the ion may finally be lost. After 100–1000 repetitions, we bin the data into a histogram of n_i approximating the success probability $P_\tau(n)$ that allows for deduction of the fraction of ions having performed at least n successful transports. $P_\tau(n)$ is fitted to an exponential decay introducing the single transport success probability $\tilde{p}_\tau$, $P_\tau(n) = (\tilde{p}_\tau)^n$. The probability for n successful transports equals $(\tilde{p}_\tau)^n$ as the processes are independent with a sufficiently long Doppler cooling period. To account for other sources of ion loss, e.g. from background gas collisions, a loss rate without transport in sequence steps (3) and (4) was subtracted. These losses can be modeled by introducing a second decay channel in $P_\tau(n)$ to finally yield net transport probabilities p_τ.

Figure 9 depicts values p_τ for different transport durations τ performed with a transport function $z_0(t)$ according to equation (1) with $\sigma = 2$. In the adiabatic regime, we obtain a success probability of 99.8% for $\tau = 100$. The ion stays deep within the potential well guaranteeing low losses. This is in good agreement with theoretical predictions. The very high success probability stays almost constant within the adiabatic regime down to $\tau = 4$ ($p_4 = 99.0\%$). According to our model, the ion experiences a relative displacement of over 300 μm gaining a potential energy of more than 30 meV. Even faster transports lead to higher transport losses resulting in probabilities around 85%. When the energy of the ion exceeds about 30% of the depth of the potential, we observe a strongly increased loss probability.

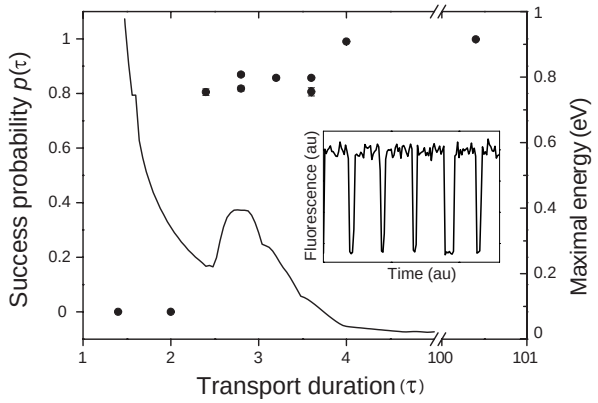

Figure 9. Transport success probability as a function of transport time (dots), y-scale on left. Slow transports with large τ show a success probability close to unity. In the intermediate range $2.5 \leqslant \tau \leqslant 4$, the probability reduces to approx. 85%. From the model we deduce the ion's maximum energy during the transport (solid), y-scale on right side. Inset: fluorescence level as observed by the CCD camera showing the dark periods during the transport while the bright periods indicate a successful transport.

5.2. Coherent excitation during transport

If the ions are to be laser-cooled after a fast shuttle, it is important to keep the excitation of vibrational degrees of freedom minimal. Therefore, we quantitatively investigate the ion's kinetic energy after the transport for ramps in the non-adiabatic regime with $4 < \tau \leqslant 20$. We generalize a method which was recently employed [26, 27] to measure motional heating rates in a micro-ion trap.

After a transport, in step (6) of the experimental sequence, the oscillating ion is Doppler-cooled by laser light, and scatters an increasing amount of photons as it cools down. We observe the scattered photons by a PMT as a function of time. The scattering rate in our model depends on the laser power quantified by a saturation parameter s, the laser detuning Δ, and the motional energy of the ion. In contrary to [26] we do not average over a thermal state. For large excitations, the oscillation amplitude exceeds the waist of the cooling laser resulting in a low scattering rate. A uniform laser intensity is therefore not appropriate for describing our experiments. We take this effect into account by including a Gaussian beam waist of $w_0 = 60\,\mu$m in our simulations. The efficiency of the laser cooling sets in with a sharp rise of PMT counts shortly after t_{recover}. Only then, the scattering rate reaches its steady state value at the Doppler-cooling limit, see figure 10(a). Adapting the theoretical treatment for a thermal motional state in [26] to the case of a coherent motional oscillation [27] and including a spatial laser beam profile, the recovery time of fluorescence is quantitatively identified with the energy after the transport. The results are shown in figure 10(b) and compared to the theoretical simulations of our simple classical model. As expected, the motional excitation

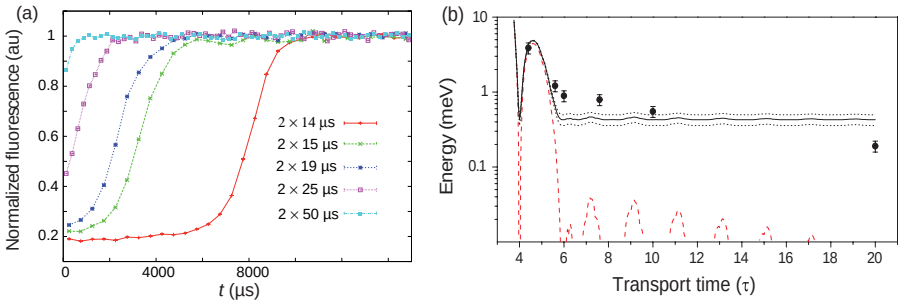

Figure 10. (a) Fluorescence rate after the transport and during application of Doppler cooling. Fast transport results in large excitation and a late recovery of the fluorescence level from vibrational excitation. (b) Measured excitation energy after an error function transport with $\tau = 4$–20. Error bars of the data points account for the uncertainty of the excitation energy from the photon scattering rate, taking into account uncertainties in the laser beam waist 60(10) μm, laser saturation uncertainty of 15%, and laser detuning uncertainty of 30 MHz. The overall uncertainty results in 15% errors for the excitation energy. The theoretical prediction of the simple model (dashed line) for solely the error function transport does not agree with the data. However, we found a motional excitation of 0.427(73) meV due to the morphing steps of the potential before and after the transport by replacing steps (3) and (4) in the measurement cycle by a waiting time of equal length. The solid line shows this modified prediction together with its standard deviation (dotted).

increases for short transport times τ. For slow transports, i.e. $\tau \gg 1$, the excitation does not drop below a certain threshold. We found that this excess excitation is due to the morphing steps (2) and (5) and might be caused by a non-ideal matching of the respective potential minima. Even a few micrometres difference leads to a large kick during the linear morphing ramp. We measured this effect independently by replacing steps (3) and (4) by equal waiting times without voltage ramps. Corrected for this excess heating, the model agrees well with the measured data.

The motional heating rate omitting any transport or morphing steps has been measured independently for our trap by replacing steps (2)–(4) by waiting times of 500 and 2000 ms. We deduce an energy gain of 3(1) meV s^{-1}. During our transport cycles this increase in energy only amounts to about 1.5 μeV. This minor energy gain does not affect our measurement results and conclusions on the transport-induced excitation.

6. Conclusion and outlook

Employing a novel segmented linear Paul trap, we demonstrated stable trapping of single ions and cold ion crystals. For the first time we have shown fast, non-adiabatic transports over 2×2 mm travels within a few microseconds by error function ramps. The main achievement

is the characterization of the ion's motional excitation. The method is based on the measured modification of the ion's scattering rate during Doppler cooling. In the future, however, sideband cooling and spectroscopic sideband analysis will be applied yielding a much more sensitive tool to investigate motional energy transfers. This will lead to a largely improved determination of ion excess motion. Then subtle changes of the parameters and the application of optimal control theory for the voltage ramps may be applied to yield lower motional excitation. Furthermore, we will establish a dedicated loading zone and optimize the transport of single ions and linear crystals through the tapered zone.

For micro-structured segmented ion traps with axial trap frequencies of several megahartz, the application of the demonstrated techniques will lead to transport times of a few microseconds only. This way, future quantum algorithms may no longer be limited by the ion transport but only by the time required for logic gate operations.

Acknowledgments

We acknowledge financial support by the Landesstiftung Baden-Württemberg, the Deutsche Forschungsgemeinschaft within the SFB-TR21, the European Commission and the European Union under the contract no. MRTN-CT-2006-035369 (EMALI).

References

[1] Wineland D J *et al* 2005 *Proc. 17th Int. Conf. on Laser Spectroscopy* (Singapore: World Scientific) p 393
[2] Becher C *et al* 2005 *Proc. 17th Int. Conf. on Laser Spectroscopy* (Singapore: World Scientific) p 381
[3] Barrett M D *et al* 2004 *Nature* **429** 737
[4] Riebe M *et al* 2004 *Nature* **429** 734
[5] Schmidt P O *et al* 2005 *Science* **309** 749
[6] Rosenband T *et al* 2007 *Phys. Rev. Lett.* **98** 220801
[7] Roos C F *et al* 2006 *Nature* **443** 316
[8] Stick D *et al* 2006 *Nat. Phys.* **2** 36
[9] Seidelin S *et al* 2006 *Phys. Rev. Lett.* **96** 253003
[10] Brown K R *et al* 2007 *Phys. Rev.* A **75** 015401
[11] Gulde S *et al* 2001 *Appl. Phys.* B **73** 861
[12] Kjaergaard N *et al* 2000 *Appl. Phys.* B **71** 207
[13] Berkeland D J *et al* 1998 *J. Appl. Phys.* **83** 5025
[14] Rotter D 2003 *Diploma Thesis* Universität Innsbruck
[15] Schmidt-Kaler F *et al* 2003 *Appl. Phys.* B **77** 789
[16] Leibfried D, Knill E, Ospelkaus C and Wineland D J 2007 *Phys. Rev.* A **76** 032324
[17] Kielpinski D, Monroe C and Wineland D J 2002 *Nature* **417** 709
[18] Chuang I 2006 private communication
[19] Home J P *et al* 2006 *Quantum Inf. Comput.* **6** 289
[20] Hucul D *et al* 2007 *Preprint* quant-ph/0702175v2
[21] Hensinger W K *et al* 2006 *Appl. Phys. Lett.* **88** 034101
[22] Reichle R *et al* 2006 *Fortschr. Phys.* **54** 666
[23] Schulz S, Poschinger U, Singer K and Schmidt-Kaler F 2006 *Fortschr. Phys.* **54** 648
[24] Rowe M A *et al* 2002 *Quantum Inf. Comput.* **2** 257
[25] Couvert A *et al* 2007 *Preprint* 0708.4197v1
[26] Wesenberg J H *et al* 2007 *Preprint* 0707.1314
[27] Reichle R *et al* in preparation

Employing Trapped Cold Ions to Verify the Quantum Jarzynski Equality

G. Huber, F. Schmidt-Kaler, S. Deffner, E. Lutz

Published 15 August 2008 in the scientific journal:

Physical Review Letters

(Volume: 101 / Page: 070403 / Year: 2008)

PRL **101,** 070403 (2008) PHYSICAL REVIEW LETTERS week ending 15 AUGUST 2008

Employing Trapped Cold Ions to Verify the Quantum Jarzynski Equality

Gerhard Huber and Ferdinand Schmidt-Kaler
Institut für Quanten-Informationsverarbeitung, Universität Ulm, Albert-Einstein-Allee 11, D-89069 Ulm, Germany

Sebastian Deffner and Eric Lutz
Department of Physics, University of Augsburg, D-86135 Augsburg, Germany
(Received 11 April 2008; revised manuscript received 28 May 2008; published 14 August 2008)

We propose a scheme to investigate the nonequilibrium work distribution of a quantum particle under well controlled transformations of the external potential, exploiting the versatility of a single ion in a segmented linear Paul trap. We describe in detail how the motional quantum state of a single ion can be prepared, manipulated, and finally readout to fully determine the free energy difference in both harmonic and anharmonic potentials. Uniquely to our system, we show how an ion may be immersed in an engineered laser-field reservoir. Trapped ions therefore represent an ideal tool for investigating the Jarzynski equality in open and closed quantum systems.

DOI: 10.1103/PhysRevLett.101.070403 PACS numbers: 05.30.−d, 05.70.Ln, 37.10.−x

Nonequilibrium phenomena at the nanoscale are dominated by fluctuations and by quantum effects. The interplay of nonequilibrium thermodynamics and quantum theory is hence of fundamental interest. Only a decade ago Jarzynski published a major discovery in *classical* nonequilibrium physics [1], relating the free energy difference ΔF after a given transformation to the probability distribution of the total work W done on the system:

$$\Delta F = -kT \ln\langle e^{-W/kT}\rangle, \tag{1}$$

where $\langle e^{-W/kT}\rangle = \int dW e^{-W/kT} P(W)$ is the average exponentiated work and k denotes the Boltzmann constant. This remarkable equality highlights the role of work fluctuations and provides a generic way of computing the free energy difference for any transformations, quasistatic or not, once the work distribution $P(W)$ is known. Most importantly, the Jarzynski relation allows us to determine ΔF even in the case of arbitrarily fast transformations, when irreversible thermodynamics is not applicable. Prior to the discovery of Eq. (1), the determination of the free energy difference in such far from equilibrium conditions was not believed to be possible [2]. Recently, the classical Jarzynski equality and its generalization by Crooks [3] have been successfully tested in single-molecule stretching experiments [4,5]. Later, the work distribution was recovered from repeated measurements of the mechanical work done on a colloidal particle [6].

The situation is much different at the *quantum* level. So far only studied theoretically, the Jarzynski equation holds in its classical form for closed quantum systems [7], while quantum corrections appear in the case of open systems due to the coupling to an external reservoir [8]. Further difficulties arise when considering the quantum-mechanical nature of work [9] and the question of how to measure it experimentally. It is evident that the classical definition of work as force times displacement cannot simply be taken over unmodified. It has recently been established that work is actually not an observable in the usual sense, as it is not given by an expectation value of some Hermitian work operator, but rather by a time-ordered correlation function [10]. On the other hand, the problem of how to determine quantum work still remains unsolved, explaining the absence of an experimental verification of the Jarzynski equality in the quantum domain.

We show in this Letter how to experimentally measure nonequilibrium work using a single ion in a segmented linear Paul trap. A unique property of ion traps is the possibility to study the quantum Jarzynski equality, as well as the quantum Crooks relation [11], for systems that are either isolated or coupled to tailored quantum environments using reservoir engineering [12,13]. Single ions trapped in radio frequency Paul traps are quantum nanosystems with remarkable properties. They can be laser cooled to very low temperatures, reaching to the motional ground state in the potential. Arbitrary quantum states can be prepared, manipulated, and measured with high fidelity [14,15]. Using the so-called electron shelving method, the quantum state is revealed with close to unity detection efficiency. The use of a segmented trap further allows for engineering a vast variety of time-dependent trapping potentials and hence the implementation of different model Hamiltonians. In the following, we generalize the detection methods for the motional state [16,17] in order to realize an efficient filter for vibrational number states. We show that trapped ions are not only good candidates for quantum computing, but may also allow us to experimentally approach the emergent field of quantum thermodynamics.

Quantum Jarzynski equality.—We begin by considering an isolated quantum system whose time-dependent Hamiltonian is varied from an initial value $H(0)$ to a final value $H(\tau)$. We denote by ϕ_n^t and E_n^t the respective eigenfunctions and eigenvalues of the Hamiltonian $H(t)$ at any given time t. We further assume that the system is initially thermalized at temperature T. The free energy difference ΔF between final and initial state is then given by the

PRL **101,** 070403 (2008) PHYSICAL REVIEW LETTERS week ending 15 AUGUST 2008

Jarzynski equality, Eq. (1). The probability distribution of the random work W is given by [10]

$$P(W) = \sum_{m,n} \delta[W - (E_m^\tau - E_n^0)] P_{m,n}^\tau P_n^0, \quad (2)$$

where $P_n^0 = (1/Z_0)\exp(-E_n^0/kT)$ is the initial (thermal) occupation probability and $P_{m,n}^\tau$ are the transition probabilities between initial and final states n and m,

$$P_{m,n}^\tau = \left| \int dx_0 \int dx \phi_m^{\tau *}(x) U(x, x_0; \tau) \phi_n^0(x_0) \right|^2. \quad (3)$$

Here $U(x, x_0; \tau)$ is the propagator of the quantum system. The physical meaning of Eq. (2) is clear: the total work done during a given transformation of the Hamiltonian is obtained from the energy difference between final and initial eigenstates, $E_m^\tau - E_n^0$, averaged over all possible initial and final states. Equation (2) shows in addition that the randomness of the work stems from the initial thermal distribution P_n^0, and from the quantum nature of transitions between states, as described by $P_{m,n}^\tau$. The origin of work fluctuations is therefore of both thermodynamical and quantum-mechanical nature. The free energy difference can be evaluated for an arbitrary transformation of the Hamiltonian with the help of the Jarzynski relation, once the work probability density $P(W)$ has been determined. We next describe a method to realize a quantum nonequilibrium situation for a single ion in a linear Paul trap and how to measure its corresponding work distribution.

Harmonic ion trap.—Linear Paul traps are characterized by a strong dynamical confinement in the radial direction (yz plane) and electrostatically bound in the axial direction (x axis). With a radial confinement much stronger than the axial, we will restrict ourselves to the axial external degree of freedom. Near the center of the axial potential, the confinement is harmonic and the axial frequency ω can be varied in time by changing the control voltages [18]. The quantum state of motion along the axial direction can be described by the Hamiltonian

$$H(t) = \frac{p^2}{2M} + \frac{M}{2}\omega^2(t)x^2, \quad (4)$$

where M is the mass of the ion. For this simple potential, the nonequilibrium work distribution (2) can be studied analytically [19]. Besides the external, motional degree of freedom, the ion provides an internal, electronic level scheme. In our case, we consider a Λ system comprising the ground state $S_{1/2}$ and two excited states $P_{1/2}$ and $D_{5/2}$. The $P_{1/2}$ state rapidly decays into the $S_{1/2}$, thus providing a high spontaneous photon scatter rate used for fluorescence detection. Laser-induced transitions from the ground to the metastable $D_{5/2}$ state are induced on the narrow quadrupole transition [linewidth $\Gamma_D \ll \omega(t)$], if the spectral bandwidth of the $S_{1/2} - D_{5/2}$ exciting light field is small compared to the sideband structure. Coherent laser pulses on this narrow band optical transition allow us to exploit and to store the motional quantum state information in the internal quantum states.

The experimental *measurement protocol* of the work distribution consists of four consecutive steps.

(I) The ion is first prepared in a thermal state with mean phonon number, $\bar{n} = [\exp(\hbar\omega_0/kT) - 1]^{-1}$, in the electronic ground state S level by laser cooling and optical pumping. We prepare this state deterministically by resolved-sideband laser cooling [20] into the vibrational ground state $|n = 0\rangle$ and subsequently allowing the ion to heat up for a certain time without laser cooling. As the heating rate of the ion within the trap can be precisely measured, this procedure is favorable for very low values of $\bar{n}$. An alternative method, suited for higher values of $\bar{n}$, is Doppler cooling on the $S_{1/2}$ to $P_{1/2}$ transition. Varying the detuning of the cooling laser from the atomic resonance results in different thermal states with mean phonon numbers down to the Doppler limit.

(II) In the second step, we measure the initial phonon number n using the filtering scheme described in detail below. In this way, we determine the initial energy eigenstate E_n^0 (from spectroscopy measurements).

(III) In the third step, we transform the trap potential from an initial value $\omega(0)$ to a final value $\omega(\tau)$. This changing potential will in general modify the ion's motional state into a nonequilibrium state, while its internal state remains unaffected. For simplicity, we consider a linear variation of the axial potential $\omega^2(t)$ from $\omega^2(0)$ to $\omega^2(\tau)$. Figures 1 and 2 show a numerical evaluation, based on the results of Ref. [19], of the transition probabilities (3) and the work distribution (2) for realistic experimental parameters and different transformation times τ.

(IV) In the last step, we measure the new phonon number m using the filtering scheme and determine the final energy eigenstate E_m^τ. The distribution of the nonequilibrium work, $W = E_m^\tau - E_n^0$, Eq. (2), is then reconstructed by

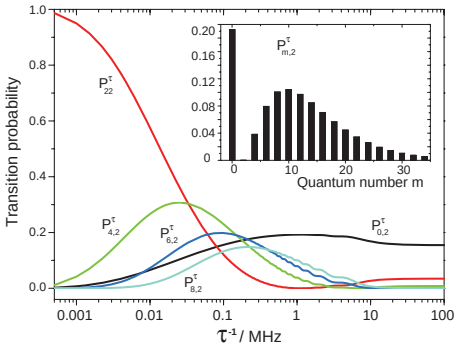

FIG. 1 (color). Transition probabilities $P_{m,n}^\tau$ for quantum numbers $n = 2$, $m = 0$–8 as a function of the inverse switching time τ^{-1} for a linear transformation of $\omega^2(t)$ with $\omega(0) = 0.1$ MHz and $\omega(\tau) = 3.0$ MHz. The inset shows the transition probabilities $P_{m,2}^\tau$ for a transformation time of $\tau = 1$ μs.

PRL **101,** 070403 (2008) PHYSICAL REVIEW LETTERS week ending 15 AUGUST 2008

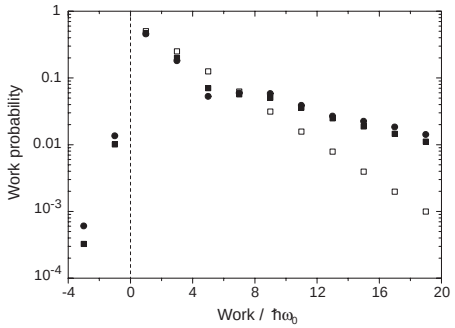

FIG. 2. Work probability distribution, Eq. (2), for a linear change of the harmonic potential $\omega^2(t)$ with $\omega(0) = 1$ MHz and $\omega(\tau) = 3$ MHz, for $\bar{n} = 1$. Shown are the adiabatic case $\tau \to \infty$ (□) and two fast transformations with $\tau = 0.1$ μs (■) and $\tau = 0.05$ μs (●). For the latter, deviations from the adiabatic case are clearly visible. Even negative work processes arise: the probability contribution at $W = -\hbar\omega_0$ mainly stems from the transition $n = 2 \to m = 0$, which occurs with probability $P^{\tau}_{2,0} = 10\%$ (for $\tau = 0.05$ μs). This contribution can be readily tested by the number state filter.

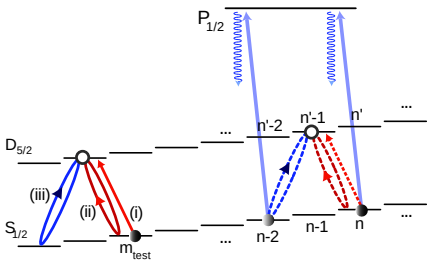

FIG. 3 (color online). Levels and transitions involved in the filtering scheme. Shown are transitions driven by the initial π pulse (i) and the successive 2π red sideband (ii) and 2π blue sideband pulses (iii), respectively. For $|m_{\text{test}}\rangle$, these pulses induce perfect π and 2π transitions between the metastable $D_{5/2}$ and the ground state level $S_{1/2}$ (left side). No fluorescence is observed when the ion is exposed to resonant light on the S to P transition. For any other $|n\rangle$, the transfer will be imperfect (dashed lines, right side) and there will be population in the S. Thus, the excitation to the P level is successful and we observe the emission of fluorescence photons.

repeating the measurement sequence. By evaluating Eq. (1) for adiabatic and nonadiabatic processes, we can verify the Jarzynski equality.

Filtering scheme.—A sequence of laser pulses on the narrow S to D transition is applied to the ion, coherently processing its internal and external degrees of freedom [21]. We tailor this pulse sequence such that the ion will end in the metastable $D_{5/2}$ state with certainty if the vibrational quantum state was $|m_{\text{test}}\rangle$. Subsequently, the ion is illuminated with light resonant to the $S_{1/2}$ to $P_{1/2}$ transition. If we observe no fluorescence, the ion is measured in the D state. However, for vibrational states different from $|m_{\text{test}}\rangle$, the laser pulse sequence leads to a superposition state, $\alpha|S\rangle + \beta|D\rangle$, such that there remains a nonvanishing probability $|\beta|^2$ of projecting the superposition into $|D\rangle$, and thus observing no fluorescence. We therefore repeat the procedure a few times such that a high quality of the filtering procedure is ensured. Considering the evolution of the quantum state itself, the influence of the above sequence reminds one of the operating principle of a filter: its projective ''transmission'' is unity for a certain input state $|m_{\text{test}}\rangle$ and zero otherwise. We adapt the laser pulse sequence timing to reach all relevant eigenstates $|n\rangle$ and $|m\rangle$ with the filter.

The crucial requirement for a well-suited filter procedure is to ensure the nonzero fluorescence outcome for all states but $|m_{\text{test}}\rangle$. It is sufficient to design the number state filter to have high suppression factors in a vicinity of $|m_{\text{test}}\rangle$, since $P^{\tau}_{m,n}$ is rapidly vanishing for high values of $|m - n|$. Varying the duration of the pulses, we use the following procedure; see Fig. 3. Starting from state $|S, m_{\text{test}}\rangle$, we apply a π pulse on the first red sideband leaving the ion in $|D, m_{\text{test}} - 1\rangle$. As the Rabi frequency $\Omega_{n,n'}$ between vibrational states n and n' depends on both initial n and final n', the laser pulse does not completely transfer other vibrational states to the D state. When we expose the ion to resonant light on the S to P transition, zero fluorescence is observed if the ion was in $|m_{\text{test}}\rangle$, but for other vibrational states there is a certain probability to observe fluorescence. To sharpen the discrimination, we apply 2π pulses on the red and blue sideband, respectively, interleaved by a fluorescence detection trial after each pulse. Again, the 2π pulses and detections leave the ion in the dark state $|D, m_{\text{test}} - 1\rangle$, but yield a nonzero fluorescence signal for all other states. This resembles so-called trapping states which have been investigated in cavity QED experiments [22]. This probability for zero fluorescence detection decreases exponentially with the number N of pulse or detection runs, as shown in Fig. 4, for a wide range of states $m_{\text{test}} \geq 3$. After $N = 10$ runs, all probabilities but for $|m_{\text{test}}\rangle$ drop below 5%. As no coherence is remaining after each detection interval, the scheme has modest requirements on the phase stability. The driving laser needs preserving phase only for one single 2π pulse, but not during the entire filter sequence. The two lowest vibrational states are treated even simpler: For $m_{\text{test}} = 0$, a π pulse on the carrier transition brings the ion into $|D, 0\rangle$. Successive red sideband π pulses do not affect this state, but fluorescence is observed with nonzero probability for all other states. This scheme has been proposed for stochastic cooling [16,17]. For $m_{\text{test}} = 1$, the carrier pulse is simply replaced by a red sideband π pulse $|S, 1\rangle \to |D, 0\rangle$. Then the procedure continues as for $m_{\text{test}} = 0$. The length of the pulses is specific for each choice of m_{test}; varying the pulse allows us to access measurements over a wide range of vibrational levels.

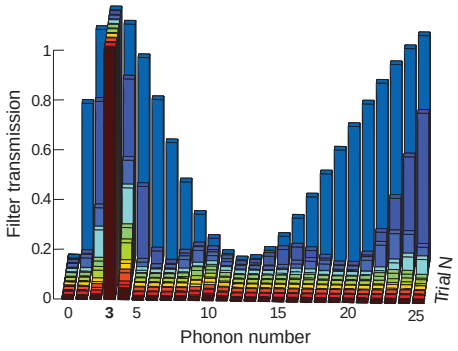

FIG. 4 (color). Probability for detection of zero fluorescence, called filter transmission, after $N = 1, 2, \ldots, 10$ pulse or detection trial cycles. With increasing number of trials (from back to front) the Fock state to be tested for, here $m_{\text{test}} = 3$, always remains dark under excitation with resonant light on the $S_{1/2}$ to $P_{1/2}$ transition. All other states show an exponential decrease of zero fluorescence detection probability.

To estimate the time taken by one experimental cycle from preparation to detection, we assume a few 10 μs for sideband pulses and a few hundred μs fluorescence detection time; one cycle with multiple filtering iterations will then take less than 10 ms, short compared to the lifetime of the D state (1.2 s for $^{40}Ca^{+}$). To also assure that unwanted dissipative effects do not introduce errors, the trap's heating rate needs to be smaller than 1 phonon within the cycle time. Traps with much lower rates have been reported. The statistical error of the values $P^{\tau}_{m,n}$ is further reduced by repeating the measurement sequence.

Designing the bath properties and the potential shape.— As discussed before, single trapped ions are highly isolated from external reservoirs. However, it has been shown theoretically [12], and also in first experiments [13], that it is possible to introduce a coupling between the ion and an artificially laser-induced bath. The variation of laser frequencies and intensities allows one to engineer the coupling and select the master equation describing the motion of the ion. Here, the interaction is mediated by sideband transitions between the $S_{1/2}$ and $D_{5/2}$ level; see Fig. 3. For example, a zero-temperature reservoir can be implemented by a light field tuned to the (cooling) red sideband transition. A large variety of other tailored reservoirs, such as squeezed baths, can be generated as well. Within the framework of this proposal, it is therefore possible to investigate nonequilibrium transformations of open systems with tailored couplings between system and reservoir. In particular, the distribution of the heat exchanged with a reservoir can be determined using the same measurement protocol by keeping the trap frequency constant, that is, performing no work.

Exploiting the flexibility provided by a segmented trap design, it is moreover feasible to investigate anharmonic trapping potentials. Especially in the situation of a nonadiabatic transport along the segments of the trap [18], the ion is shifted out of the harmonic center of the electric potential and experiences nonharmonic potential contributions [20]. For future work, one might include forces by laser light on the ion, which depend on its internal electronic state, investigating the influence of quantum thermodynamics on qubit gate operations [23].

In conclusion, we have shown how the quantum Jarzynski equality can be experimentally investigated using a single ion in the time-varying electrical potential of a Paul trap, for both open and closed quantum systems. Our proposal is based on the state of the art in many laboratories working with single trapped ions and uses realistic parameters. Experiments with such a device would allow us to shine more light on the amazing interplay of quantum mechanics and thermodynamics.

This work was supported by the German Science Foundation within the SFB/TRR-21 and the Emmy Noether Program (Contract LU1382/1-1), by the European commission within MICROTRAP (Contract 517675) and EMALI (Contract MRTN-CT-2006-035369), and the cluster of excellence Nanosystems Initiative Munich (NIM). We thank W. Schleich for discussion.

[1] C. Jarzynski, Phys. Rev. Lett. **78**, 2690 (1997).
[2] C. Bustamante, J. Liphardt, and F. Ritort, Phys. Today **58**, No. 7, 43 (2005).
[3] G. E. Crooks, Phys. Rev. E **60**, 2721 (1999).
[4] J. Liphard *et al.*, Science **296**, 1832 (2002).
[5] D. Collin *et al.*, Nature (London) **437**, 231 (2005).
[6] V. Blickle *et al.*, Phys. Rev. Lett. **96**, 070603 (2006).
[7] S. Mukamel, Phys. Rev. Lett. **90**, 170604 (2003).
[8] V. Chernyak and S. Mukamel, Phys. Rev. Lett. **93**, 048302 (2004).
[9] A. E. Allahverdyan and Th. M. Nieuwenhuizen, Phys. Rev. E **71**, 066102 (2005).
[10] P. Talkner, E. Lutz, and P. Hänggi, Phys. Rev. E **75**, 050102(R) (2007).
[11] P. Talkner and P. Hänggi, J. Phys. A **40**, F569 (2007).
[12] J. F. Poyatos, J. I. Cirac, and P. Zoller, Phys. Rev. Lett. **77**, 4728 (1996).
[13] C. J. Myatt *et al.*, Nature (London) **403**, 269 (2000).
[14] H. Häffner *et al.*, Nature (London) **438**, 643 (2005).
[15] D. Leibfried *et al.*, Nature (London) **438**, 639 (2005).
[16] J. Eschner, B. Appasamy, and P. E. Toschek, Phys. Rev. Lett. **74**, 2435 (1995).
[17] B. Appasamy, Y. Stalgies, and P. E. Toschek, Phys. Rev. Lett. **80**, 2805 (1998).
[18] G. Huber *et al.*, New J. Phys. **10**, 013004 (2008).
[19] S. Deffner and E. Lutz, Phys. Rev. E **77**, 021128 (2008).
[20] S. Schulz, U. Poschinger, F. Ziesel, and F. Schmidt-Kaler, New J. Phys. **10**, 045007 (2008).
[21] A. Ben-Kish *et al.*, Phys. Rev. Lett. **90**, 037902 (2003).
[22] M. Weidinger *et al.*, Phys. Rev. Lett. **82**, 3795 (1999).
[23] M. J. Henrich, F. Rempp, and G. Mahler, Eur. Phys. J. Special Topics **151**, 157 (2007).

Coherent Manipulation of a $^{40}Ca^{+}$ Spin Qubit in a Micro Ion Trap

U. G. Poschinger, G. Huber, F. Ziesel, M. Deiß, M. Hettrich, S. A. Schulz, K. Singer, G. Poulsen, M. Drewsen, R. J. Hendricks and F. Schmidt-Kaler

Published 15 July 2009 in the scientific journal:
Journal of Physics B: Atomic, Molecular and Optical Physics
(Volume: 42 / Page: 154013 / Year: 2009)

IOP Publishing Journal of Physics B: Atomic, Molecular and Optical Physics

J. Phys. B: At. Mol. Opt. Phys. **42** (2009) 154013 (9pp) doi:10.1088/0953-4075/42/15/154013

Coherent manipulation of a $^{40}Ca^{+}$ spin qubit in a micro ion trap

U G Poschinger[1], G Huber[1], F Ziesel[1], M Deiß[1], M Hettrich[1], S A Schulz[1], K Singer[1], G Poulsen[2], M Drewsen[2], R J Hendricks[3] and F Schmidt-Kaler[1]

[1] Institut für Quanteninformationsverarbeitung, Universität Ulm, Albert-Einstein-Allee 11, 89069 Ulm, Germany
[2] QUANTOP—Danish National Research Foundation Center for Quantum Optics, Department of Physics and Astronomy, Aarhus University, Denmark
[3] Centre for Cold Matter, Blackett Laboratory, Imperial College London, Prince Consort Road, London SW7 2AZ, UK

E-mail: ulrich.poschinger@uni-ulm.de

Received 10 February 2009, in final form 9 April 2009
Published 15 July 2009
Online at stacks.iop.org/JPhysB/42/154013

Abstract
We demonstrate the implementation of a spin qubit with a single $^{40}Ca^{+}$ ion in a micro ion trap. The qubit is encoded in the Zeeman ground state levels $m_J = +1/2$ and $m_J = -1/2$ of the $S_{1/2}$ state of the ion. We show sideband cooling close to the vibrational ground state and demonstrate the initialization and readout of the qubit levels with 99.5% efficiency. We employ a Raman transition close to the $S_{1/2}$–$P_{1/2}$ resonance for coherent manipulation of the qubit. We observe single qubit rotations with 96% fidelity and gate times below 5 μs. Rabi oscillations on the blue motional sideband are used to extract the phonon number distribution. The dynamics of this distribution is analysed to deduce the trap-induced heating rate of 0.3(1) phonons ms^{-1}.

(Some figures in this article are in colour only in the electronic version)

1. Introduction

Our research is aimed at the realization of scalable quantum simulation and information processing [1, 2]. Quantum computing with cold ions [3–6] has currently reached an experimental limit of scalability with up to eight ions if a conventional macroscopic trap is used [7]. This purely technical limitation is believed to be lifted using a segmented linear micro Paul trap, where only small groups of ions are to be kept in the quantum processing unit, and multiple trap sites are used for the storage of large-scale entanglement [8]. Several different options for encoding a qubit with a trapped ion are possible and have been realized in various groups. One might either employ superpositions of a long-lived electronic metastable state and the ground state, or alternatively use coherent superpositions of hyperfine or Zeeman ground states. In this paper, we focus on $^{40}Ca^{+}$ ions in a micro trap and qubits which are encoded in Zeeman sublevels of the $S_{1/2}$ ground state. We will discuss in detail how these qubits are initialized, coherently manipulated and how finally the quantum information is read out with high fidelity. With the ion cooled close to its vibrational ground state, we are well set for two-qubit quantum logic gate operations in a multi-segmented linear micro trap, a scalable approach to ion quantum processing.

The paper is organized as follows. First, we give a brief overview on the experimental apparatus used including the micro trap and the various laser sources. In section 3, we discuss the advantages of our choice of Zeeman ground state superpositions for the qubit encoding. Two basic steps for qubit utilization, namely state preparation and readout, are demonstrated in section 4. Finally, we explain in detail how Raman transitions for the spin qubit manipulations are characterized (section 5) and present results for sideband cooling and coherent qubit dynamics (section 5.3). We show how phonon number distributions can be extracted from the analysis of Rabi oscillations on the blue sideband of the Raman transition and investigate the dynamics of the phonon

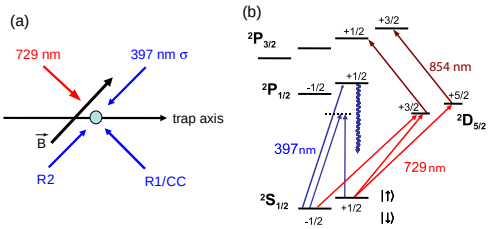

Figure 1. (a) Geometric arrangement of the lasers driving Raman (R1, R2 and CC), dipole (397 nm) and quadrupole transitions (729 nm), relative to the trap axis and magnetic field direction $\vec{B}$. (b) Level scheme of a $^{40}Ca^+$ ion and all relevant transitions. A magnetic field of about 6.8 G splits each fine structure level into several Zeeman components, indicated by fractional numbers.

distribution in the micro trap. The outlook sketches the future perspectives of our experiment for multi-qubit quantum logic.

2. Experimental apparatus

2.1. A segmented micro ion trap

We use a segmented linear micro ion trap. It is a sandwich structure of three alumina wafers, of which the top and bottom ones are gold coated and the middle one acts as a spacer. The trap structure is created by laser cutting with μm-scale resolution. Each trap layer consists of a RF electrode providing ponderomotive confinement in the radial plane and a set of dc electrodes for confinement in the axial direction. The RF electrodes extend along the whole length of the trap and have notches at the positions of the gaps between neighbouring dc segments in order to suppress axial bumps in the RF field. They are supplied by up to 300 V_{pp} at 24.8 MHz. The dc electrodes are supplied with voltages in a $\pm$10 V range by a computer-controlled battery-powered supply which is designed to provide fast and accurate voltage waveforms to the electrodes at low noise and output impedance. The ionic motion exhibits one vibrational mode along the trap axis which is to be used as the 'bus' mode for entangling operations. Under typical trapping conditions, when a voltage of -6 V is applied to one pair of dc segments and all other dc electrodes are grounded, an axial frequency of $\omega_{ax}/2\pi = 1.35$ MHz is measured. The radial confinement leads to two nondegenerate radial modes with typical frequencies of $\omega_{rad}^{x,y}/2\pi = \{2.0, 3.5\}$ MHz. For further details we refer to the description in [9, 10].

2.2. Laser sources and ion detection

A single ion is loaded by the photoionization of a weak neutral calcium beam by resonant two-photon photoionization [11]. Doppler cooling is achieved by means of a grating-stabilized diode laser at 397 nm, slightly red detuned with respect to the $S_{1/2}$ to $P_{1/2}$ dipole transition; see figure 1(a). As the cooling cycle is not closed, a grating-stabilized diode laser at 866 nm is used for repumping from the metastable $D_{3/2}$ state. The light from both sources is switched by means of acousto-optical modulators (AOM). For Doppler cooling, we irradiate 100 μW and 500 μW near 397 nm and 866 nm, respectively. The waist size of both beams is about 30 μm at the ion's location. When necessary, population in the $D_{5/2}$ state (1.2 s lifetime) can be pumped to the $P_{3/2}$ by a grating stabilized laser diode near 854 nm, followed by a fast decay to the $S_{1/2}$ ground state, which is referred to as quenching. Since the long lifetime of the $D_{5/2}$ state is important for qubit measurement, no quench light must be present during readout. To ensure sufficient extinction of the quench laser, a light of about 10 μW in a beam waist of about 50 μm is switched by a double-pass AOM. All diode lasers are locked to Pound–Drever–Hall (PDH) error signals from stable Fabry–Perot cavities which are tuned by a piezo-driven mirror.

In order to drive the $S_{1/2}$ to $D_{5/2}$ quadrupole transition, we use an amplified diode laser system. This laser source near 729 nm is PDH locked to an ultra-low expansion cavity in a UHV vessel. We estimate the laser linewidth to be better than 5 kHz as determined from Ramsey contrast measurements on the quadrupole transition, where coherence decay times of up to 200 μs were observed. The laser light near 729 nm is switched and modulated by a double-pass AOM controlled by a versatile function generator[4] (VFG), a DDS/FPGA based RF source [12]. This allows for generation of laser pulses with almost arbitrary frequency, phase and amplitude profiles. The resulting laser beam has a power of up to 140 mW and is focussed down to roughly 10 μm, allowing Rabi frequencies up to 1.5 MHz on the $S_{1/2}, m_J = +1/2$ to $D_{5/2}, m_J = +5/2$ transition. The polarization is chosen to be at an angle of 45° to the quantizing magnetic field, whereas the propagation direction is orthogonal to it. This way, all allowed transitions between the Zeeman sublevels of the $S_{1/2}$ and $D_{5/2}$ states become accessible [4] (figure 1). The beam enters at an angle of 45° with respect to the trap axis, allowing for momentum transfer to the axial and the radial modes. We calculate the coupling to ion motion (Lamb–Dicke factors) of $\eta_{ax} = 0.06$ and $\eta_{rad}^{x,y} = \{0.034, 0.026\}$.

Raman transitions between the spin levels $m_J = +1/2$ and $-1/2$ of the $S_{1/2}$ ground state are driven by two laser beams close to the strong $S_{1/2}$ to $P_{1/2}$ dipole transition. The beams are derived from a frequency doubled amplified laser diode system delivering up to 120 mW of power at 397 nm. The laser is divided into three different beams which are termed R1, R2 and CC. The Raman transitions are then driven either by the pair R1/R2 or the pair R1/CC; see figure 1(b). All Raman beams are switched and modulated by single-pass AOMs. The AOMs for R2 and CC are supplied by the same VFG source as the AOM for the 729 nm laser. The AOM for R1 is supplied by an RF synthesizer, which also serves as a phase reference for the VFG; therefore, the necessary phase stability between R1/CC and R1/R2 is guaranteed. The limit of accuracy for the relative frequency between the VFG and synthesizer was measured to be 10 mHz, which has no adverse effect, because the timescale on which a single measurement cycle is carried out is much shorter (up to 20 ms).

[4] *VFG 150*, Toptica Photonics.

The 397 nm fluorescence light emitted by the ion during Doppler cooling is detected by an electron multiplier CCD camera and a photomultiplier tube. With typical fluorescence rates of 50 counts in 3 ms from a single ion with a background of about 5 counts from scattered light, we can discriminate the state with a statistical error in the sub-per mil range [4].

All laser sources are controlled by a versatile computer control program and continuously monitored by a wavemeter with 5 MHz accuracy. A typical experimental sequence consists of four steps: (a) the ion is Doppler cooled for 3 ms, (b) then it is cooled close to the ground state of the axial vibrational mode by resolved sideband cooling (section 5.3). (c) The qubit is then initialized (section 4.1), and (d) coherent manipulations are performed on the Raman transition (section 5.1). Finally, (e) the population in the $m_J = +1/2$ qubit level is shelved (section 4.2) to the $D_{5/2}$ level, and (f) the state is read out by counting 397 nm laser induced fluorescence for 3 ms. After quenching the state by light near 854 nm, the cycle (a)–(f) is repeated, typically 100 times, giving the average transfer probability on the qubit transition.

3. Qubit realizations with Ca^+ ions and arguments for a ground state spin qubit

The level scheme of Ca^+ ions allows for at least three options to encode qubit information in a long-lived superposition of two electronic quantum states. The *optical qubit* is encoded in a superposition of the ground state $|0\rangle \equiv S_{1/2}$ and the metastable state $|1\rangle \equiv D_{5/2}$. Coherent manipulations are driven directly on this quadrupole transition by laser pulses near 729 nm; an approach has been realized with great success by the Innsbruck group [13, 14]. Disadvantages to this approach are limitations to the coherence due to phase stability of the laser source at 729 nm and ambient magnetic field fluctuations, as well as the relatively small Lamb–Dicke factor which leads to a rather weak momentum kick of the laser excitation on the ion's vibrational motion, affecting the two-qubit gate speed. The optical qubit is read out efficiently and simply by state-dependent fluorescence, as the ground state scatters photons while the $D_{5/2}$ remains dark.

Another option is to use $^{43}Ca^+$ with nuclear spin $I = 7/2$ and to encode the qubit in *hyperfine ground state levels* $|F = 4, m_F = 0\rangle$ and $|F = 3, m_F = 0\rangle$. Coherent manipulations are achieved by employing a Raman transition, which means that an ultra-stable laser source is no longer required. It is straightforward to achieve excellent relative phase stability if the two Raman beams are derived from a single laser source. However, a large frequency gap of about 3.4 GHz must be bridged with high-bandwidth AOMs. Hyperfine clock states, insensitive to the linear Zeeman effect, can be used as computational basis states [15], which greatly increases the qubit phase coherence. The qubit readout is based on state-dependent fluorescence.

For the measurements presented here we have chosen the option to encode the *qubit in spin sublevels* $|\downarrow\rangle$ and $|\uparrow\rangle$ of the ion's electronic ground state $S_{1/2}\, m_J = \pm 1/2$ of $^{40}Ca^+$ with $I = 0$, Zeeman split by an applied magnetic field. Quite similar work has been performed with great success by the Oxford group [16, 17]. However, in this work the scheme for state preparation, readout and cooling is entirely different from our approach. Furthermore, the experiments were carried out in a conventional Paul trap and do not suffer from the enhanced heating rates in a microtrap.

Coherent manipulations of the spin qubit are achieved by employing a Raman transition, and the requirement of an ultra-stable laser source can then be dropped as in the case of hyperfine qubits, but a much smaller frequency splitting of about 20 MHz allows the use of simple and efficient AOMs. The high Lamb–Dicke factor of UV–Raman transitions ensures fast two-qubit gate operations. As compared to ion species with a hyperfine structure we work with a much simpler level structure reducing the experimental complications. Qubit readout, however, is more complicated since both the $|\downarrow\rangle$ and $|\uparrow\rangle$ states can scatter photons near 397 nm. In order to discriminate between the two-qubit states, the population in $|\uparrow\rangle$ must first be completely transferred to the metastable $D_{5/2}$ state. A future possibility of avoiding qubit dephasing due to its magnetic field sensitivity for the $^{40}Ca^+$ spins will be using two physical qubits (ions), in a decoherence-free subspace of Bell states to encode one logical qubit [18, 19], in the spirit of designer atoms [20].

4. Qubit preparation and readout

According to the DiVincenzo criteria [21], the initialization of qubits to a well-defined state and the readout of the full quantum state of the qubits are essential criteria for the realization of quantum information experiments. In our experiment, both steps are realized by using a narrow optical quadrupole transition at 729 nm, and both are optimized to achieve high fidelities even under the presence of experimental imperfections and noise.

4.1. State preparation via optical pumping

The common technique for preparing an initial quantum state via optical pumping employs a circularly polarized laser beam resonant with the $S_{1/2}$ to $P_{1/2}$ dipole transition at 397 nm. In this case, both birefringence by the vacuum windows and a small offset angle between the propagation direction $\vec{k}_{397}$ and the quantizing magnetic field results in spurious polarization components. The improper polarization components deteriorate the initialization fidelity. Furthermore, as the target state is not completely dark anymore, this leads to a continuous photon scattering of Doppler cooling light, which counteracts the ground state sideband cooling (section 5.3). Therefore, we use the high spectral selectivity of the narrow quadrupole transition for optical pumping [20]. If the ion is to be initialized in the $|\uparrow\rangle$ level, the population from $|\downarrow\rangle$ is transferred to the $D_{5/2}, m_J = +3/2$ level by a pulse at 729 nm and transferred back to the ground state by the quench laser via the $P_{3/2}$ state. This cycle is repeated until the desired initialization is reached with high fidelity.

We compare two different schemes for this pumping: either we use a pulsed scheme or we switch on both light

J. Phys. B: At. Mol. Opt. Phys. **42** (2009) 154013 U G Poschinger *et al*

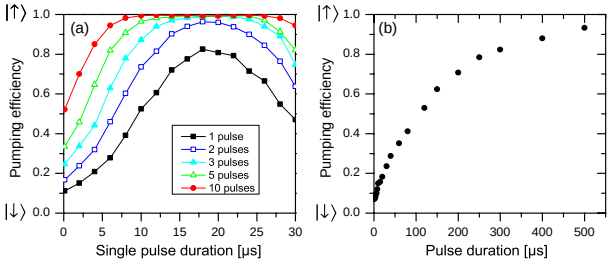

Figure 2. Single ion population is pumped by the application of circularly polarized light at 397 nm to the $|\downarrow\rangle$ state. From this state we use optical pumping by laser light at 729 nm and 854 nm to pump to the $|\uparrow\rangle$ via the $D_{5/2}, m_J = +3/2$ level. (a) Pumping efficiency of the pulsed scheme versus the 729 nm pump time of the individual pulses. The curves for various pulse numbers show how performance and robustness increase for more pulses. Note that the total duration of the pump process increases with the number of pulses. (b) The cw scheme is found less efficient.

fields continuously (figure 2). In the pulsed scheme, after an approximate π pulse on the quadrupole transition the quench beam at 854 nm is briefly switched on. We find that a quench pulse of just 2 μs is sufficient for complete quenching of the $D_{5/2}$ state.

A 729 nm π-pulse length of about 10 μs determines the amount of off-resonant excitation and thus the fidelity of the scheme: the target transition $|\downarrow\rangle$ to $D_{5/2}, m_J = +3/2$ is separated from the parasitic transition $|\uparrow\rangle$ to $D_{5/2}, m_J = +5/2$ by ∼8 MHz for a magnetic field of 6.7 G. The frequency component of the Fourier transform of the effective square pulses (without any pulse shaping) already results in an expected pumping fidelity better than 99.6%, in agreement with the value for the combined pumping and readout fidelity (see below) in the experiment of 99.6%; figure 2(a). The cw scheme suffers from the fact that the presence of the quench beam hinders the coherent buildup of population in the $D_{5/2}$ state[5].

4.2. Spin readout

A simple readout of the spin state by fluorescence observation is impossible because the Zeeman splitting of the spin levels $|\uparrow\rangle$ and $|\downarrow\rangle$ is smaller than the natural linewidth $\Gamma/2\pi \approx$ 22 MHz of the corresponding 397 nm dipole transition. A scheme circumventing this by means of electromagnetically induced transparency has been proposed and experimentally realized [22], reaching a fidelity of 86%.

Our scheme reaches 99.6% fidelity and additionally shows a high robustness against imperfect laser settings or noise in the control parameters, still with a remarkably modest experimental effort. In a first step we apply a rapid adiabatic passage pulse (RAP) [12] where the amplitude is adiabatically switched on and off, and the frequency is chirped across

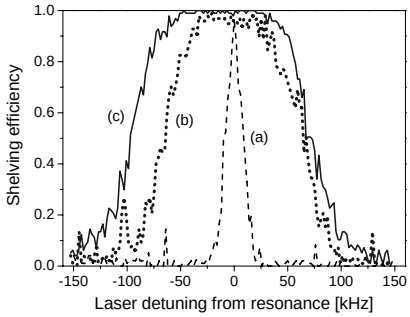

Figure 3. Transfer efficiency of the spin qubit $|\uparrow\rangle$ for various schemes versus central detuning of the readout pulse. (a) Dashed: the narrow peak is the result for a Gaussian pulse with a resonant pulse area of π. (b) Dotted: the much broader peak corresponding to a single RAP pulse shows that the robustness against frequency errors has greatly improved. (c) Solid: the curve for the double RAP shows that both performance and robustness have increased with respect to the single RAP.

resonance[6]. Even for an ion after Doppler cooling, a single RAP pulse on the $|\uparrow\rangle$ to $D_{5/2}, m_J = +5/2$ transition yields a fidelity of 95%; the leftover population in the $|\uparrow\rangle$ state is then transferred by a second RAP to the $D_{5/2}, m_J = +3/2$ state, and we reach a 99.6% readout fidelity with a high resilience against a drift of 729 nm laser frequency; see figure 3.

5. Raman transitions between the spin qubit levels

5.1. Raman spectroscopy and characterization of the transition

In our experiment, we use Raman beams derived from one laser source (see section 2). The laser is detuned from the

[5] The quench laser couples the metastable state to the rapidly decaying $P_{3/2}$ state. Upon decay from this state, a photon is emitted which can be, in principle, detected, indicating that the system has ended up in the ground state. This represents an effective continuous measurement, disturbing the coherent evolution of the $S_{1/2}$–$D_{5/2}$ superposition.

[6] As stability against Rabi frequency errors is the main issue for readout robustification, we have also employed the SCROFOLOUS technique [23, 24] which is robustified by using a series of three π pulses with different phases. Although the technique was found to yield the same performance and an enhanced robustness against pulse area errors, the low resilience against the laser frequency drift strongly limited the practical use.

$S_{1/2} \rightarrow P_{1/2}$ resonance frequency by Δ, referred to as the Raman detuning. It is up to several tens of GHz and can be chosen to be both positive (blue detuning) or negative (red detuning). As Δ is very large compared to the Zeeman splittings within the $S_{1/2}$ and $P_{1/2}$ manifolds, which is on the order of 10–20 MHz, it can be considered constant for the different transitions between the Zeeman levels. The $P_{1/2}$ state can be adiabatically eliminated from the dynamics, giving an effective two-level system. The Raman Rabi frequency now reads $\frac{\Omega_1\Omega_2}{2\Delta}$, where Ω_i are the resonant single-dipole Rabi frequencies associated with the individual beams.

A great advantage of the utilization of Raman transitions for quantum logic is the better control over the Lamb–Dicke factor. The difference *k*-vector of the beams strongly depends on the chosen geometry; see figure 1(a). In our setup, two different beam geometries are employed. In the first of these, a pair of Raman beams, R1 and CC, propagates parallel to each other and orthogonal to the magnetic field. The difference *k*-vector of the two beams is effectively zero, so the Lamb–Dicke factor is extremely small and electronic excitation is insensitive to the ion's motion. One of the beams (referred to as 'R1') is π-polarized, driving the $\Delta m_J = 0$ transition. The other beam (referred to as 'CC', cocarrier) is polarized orthogonal to the magnetic field. Therefore it yields two circular components, one of which contributes to the coherent dynamics of the effective two-level system if the Raman resonance condition is fulfilled, i.e. if the relative detuning of the beams matches the Zeeman splitting between the qubit levels. The alternative geometry consists of R1 and a beam propagating along the magnetic field direction (referred to as 'R2') such that the *k*-vector of the beat pattern is aligned along the trap axis. With no component of the *k*-vector in the radial plane of the trap, this Raman light field interacts only with the axial vibrational mode, and avoids any phonon-induced dephasing from the radial modes commonly called spectator modes. This fact is of tremendous importance for our microtrap with prospects to many ions, as we can drop the requirement of ground state cooling of all vibrational modes which would be experimentally undesirable.

From the beam geometry and the axial vibrational frequency, we deduce a Lamb–Dicke factor of $\eta = 0.21$, which is much larger than for the optical transition.

A Raman spectrum is shown in figure 4, clearly displaying the axial sidebands of motion for a single ion after Doppler cooling with $\bar{n} \sim 15$ quanta and an axial trap frequency of 1.35 MHz.

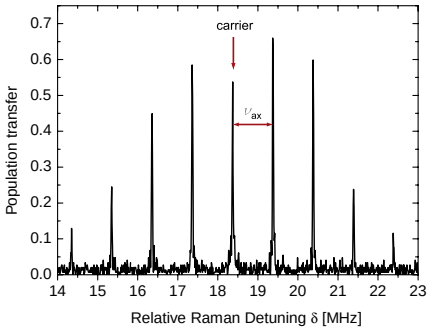

Figure 4. Raman spectrum obtained as R1 is fixed in frequency, and R2 is scanned over the sideband resonances. The excitation geometry leads to a difference *k*-vector along the trap axis, such that only axial, but no radial modes show up.

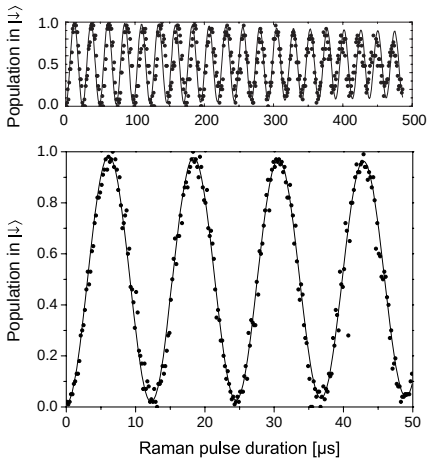

Figure 5. Rabi oscillations on the Raman transition driven by the R1/CC pair. No phonon-induced dephasing occurs because the Lamb–Dicke factor is virtually zero, which allows for driving many single-qubit rotations with high fidelity. The upper curve shows the long coherence time, while the lower curve displays the first four Rabi oscillations with high resolution. The two scans were taken with different Rabi frequencies.

5.2. Raman Rabi oscillations on the carrier transition

Rabi oscillations driven by the R1/CC beams pair are shown in figure 5. Here, with $\eta = 0$, no phonon-induced dephasing can occur. For the experiment, we follow the sequence in section 2 without ground state cooling in step (b) and apply in step (c) both beams R1 and CC simultaneously for an interaction time *t*. The experiment is repeated 100 times, and the average excitation probability is plotted.

Showing no influence of the phonon number distribution, this technique provides an excellent opportunity for studying other sources of decoherence. These are ambient magnetic field fluctuations, fluctuations of the relative phases of the beams due to air currents or mechanical vibrations and laser intensity fluctuations and spontaneous photon scattering. The latter two mechanisms scale with the total effective pulse area imparted to the ion on each of the dipole transitions pertaining to the Raman transition. Because of this, a Ramsey contrast measurement on a spin superposition created by R1/CC with fixed pulse areas and variable delay between the Ramsey pulses allows us to study the limits imposed by magnetic field noise and interferometric stability. Such a measurement has given a contrast of 90% after a delay time of 1.5 ms.

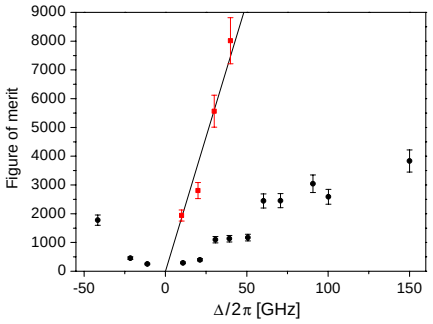

Figure 6. Rabi frequency divided by geometric mean of the scattering rates versus Raman detuning for the R1/CC pair (red squares) and the R1/R2 pair (black dots). The solid line through the R1/CC data is the theoretical value of $\sqrt{18}\Gamma^{-1}|\Delta|$.

As π-times of down to 2 μs are routinely achieved, this separation of time scales appears sufficient for quantum logic experiments. We find in our setup that an air shield and the high passive mechanical interferometer stability of the optical setup are sufficient to avoid technically induced dephasing. The fundamental physical coherence limit of qubits is given by spontaneous photon scattering [25, 26].

During operations with the Raman beams, the small amount of population off-resonantly excited to the $P_{1/2}$ state decays with a rate corresponding to the inverse lifetime of this state, which results in random repopulation of the qubit levels. This off-resonant excitation reads for each beam i as $p_{P_{1/2}} = \Omega_i^2/2\Delta^2$, decreasing with the ratio of Rabi frequency and Raman detuning. Similar to far-detuned optical dipole traps [27], the photon scattering rate can be reduced if a large Δ is chosen at a high laser intensity. We investigated the photon scattering experimentally: for a given Raman detuning and fixed beam powers, the Rabi frequency is measured from Rabi oscillations as in figure 5 along with the scattering rates caused by each of the Raman beams individually. For this, the ion is initialized in $|\uparrow\rangle$, and one of the Raman beams is blocked. We apply the remaining Raman beam with a pulse of variable length. Finally, from the population in $|\downarrow\rangle$ we infer the scattering rate of beam i.

For the analysis, we normalize the measured Rabi frequency by the geometric mean of both scattering rates, such that in the resulting quantity, the individual Raman beam dipole coupling strengths Ω_i are cancelled.

A value of $\sqrt{18}\Gamma^{-1}|\Delta|$ is expected when the Clebsch–Gordan coefficients for the transitions are taken into account. The result is shown in figure 6, where the vertical axis can be interpreted as the number of Rabi cycles that could be driven on average before a single spontaneous scattering event occurs, in the absence of any other decoherence sources. The results for the R1/CC pair match very well the theoretical expectation. The fact that the values for the R1/CC pair match the theoretical expectation was initially not taken for granted because of the type of laser source used: a tapered amplifier generates a background of amplified spontaneous emission whose width in the range of a few nm is given by the gain profile of the semiconductor laser medium. Through sum frequency generation, it is, in principle, possible that photons at frequencies $\omega_0 + n\omega_{FSR}$ are generated in the doubling stage, where ω_0 is the laser mode frequency, and ω_{FSR} is the free spectral range of the doubling stage. If such a frequency matches the direct optical $S_{1/2}$ to $P_{1/2}$ transition, resonant photon scattering would occur.

The same experiment, but with the R1/R2 pair of Raman beams, yields lower values for the Raman Rabi frequency. As in this geometry the excitation is sensitive to the motional degree of freedom along the trap axis, we attribute the lower value to the decrease of the Raman Rabi frequency with increasing phonon number and axial micromotion components[7] at a trap drive frequency of 24.8 MHz.

Another characterization of the Raman interaction is done by the determination of the ac-Stark shifts, given by $\Delta_S = \Omega_i^2/4\Delta$ for one beam i. The absolute ac-Stark shift might be different for the two-qubit levels $|\uparrow\rangle$ and $|\downarrow\rangle$, leading to a differential shift. Under these circumstances, the quantum phase of qubit superpositions, or of multi-ion entangled states, evolves not only according to the desired gate operations, but shows an additional intensity-dependent rapid phase evolution. If this is the case, intensity fluctuations of the Raman lasers lead to qubit phase fluctuations, which represents an additional strong decoherence source.

The absolute ac-Stark shifts for all beams and qubit states is measured with the following procedure: first, the qubit is prepared either in the $|\uparrow\rangle$ or the $|\downarrow\rangle$ level by optical pumping with circularly polarized 397 nm laser light. Then, a superposition on the quadrupole transition is created by means of a $\pi/2$ pulse with the 729 nm laser, either with the $D_{5/2}, m_J = +5/2$ level for the $|\uparrow\rangle$ state or $D_{5/2}, m_J = +3/2$ level for the $|\downarrow\rangle$ state. A second $\pi/2$ pulse after a delay time of 50 μs concludes the Ramsey sequence. During this delay, a phase shift pulse from one of the Raman beams is irradiated on the ion, leading to a Ramsey fringe signal as the duration of the shift pulse is scanned. The absolute shift is then calculated from the fringe period t_R according to $\Delta_S = 2\pi/t_R$. For the R1 beam the $|\uparrow\rangle$ level is shifted by $2\pi \cdot 0.32(2)$ MHz, and the $|\downarrow\rangle$ level is shifted by $2\pi \cdot 0.33(2)$ MHz. Within the experimental errors, the differential shift from R1 vanishes. In contrast, we measured shifts from the R2 beam with $2\pi \cdot 0.17(2)$ MHz for the $|\uparrow\rangle$ level and $2\pi \cdot 0.29(2)$ MHz for the $|\downarrow\rangle$ level, resulting in a differential shift of about $2\pi \cdot 120$ kHz. Compensation of the differential shift is possible by proper adjustment of the polarization of the corresponding beam.

5.3. Resolved sideband cooling and blue sideband Rabi oscillations

Cooling close to the ground state of at least one vibrational mode is an essential prerequisite for two-ion gates, as even gate schemes for 'hot' ions require operation in the Lamb–Dicke

[7] The presence of axial micromotion was confirmed by checking for RF echoes in the Raman spectrum of the R1/R2 pair, i.e. Raman resonances at relative detunings of $\omega_{Zeeman} + n\omega_{RF}$. Note that the effect of micromotion on the Raman Rabi frequency has even been used to allow the fine tuning of Rabi frequencies in quantum gate experiments with Be^+ ions [28].

regime, $\eta\sqrt{n} \ll 1$ [29]. For cooling close to the ground state one has to resort to a narrow transition with resolved motional sidebands [30], such that transitions to states with one less phonon (red sideband, RSB) can be driven preferentially and the $n = 0$ state acts as a dark state in which the population is finally trapped. In our system, we have two options to spectroscopically resolve sidebands, either the R1/R2 Raman transition or the quadrupole transition.

As the cooling always competes with the heating rate from trap-induced electric field noise, a high cooling rate is essential for a good cooling result. *A priori*, the Raman transition seems to be better suited for cooling because of the higher ratio of RSB to carrier Rabi frequency, which is essentially given by η on the decisive 'bottleneck' step from $n = 1$ to $n = 0$. This is because, ideally, the cooling rate is limited by off-resonant excitation of the carrier transition with subsequent spontaneous decay which can lead to the creation of one phonon. However, the problem arises in the dissipative step of cooling where the ion is repumped to the initial state to restart the RSB excitation. In the case of the Raman cooling scheme, the repumping is accomplished by the circular 397 nm beam which suffers from the spurious polarization error discussed in section 4.1. Therefore, the dark state $n = 0$ is not completely dark anymore, leading to a competing Doppler re-heating process which limits the attainable temperature.

In contrast, the sideband cooling on the $|\uparrow\rangle$ to $D_{5/2}$, $m_J = +5/2$ quadrupole transition does not suffer from this because the repumping is achieved by the quench laser near 854 nm, which does not interact with the ion anymore once one photon is spontaneously scattered. The cooling cycle is almost closed, because the decay from the $P_{3/2}$ state during the quench leads preferentially to the $|\uparrow\rangle$ level due to the selection rules. Only unlikely decay events into one of the D-states can lead to population of the $|\downarrow\rangle$ level. We utilize a pulsed sideband cooling scheme, since as for the qubit initialization, the power and frequency of the quench laser are no longer critical parameters then. The cooling pulse time is set such that an excitation maximum is reached on the RSB. This time typically ranges between 10 μs and 20 μs, and increases as lower phonon numbers are reached because the RSB Rabi frequency scales as $\eta_{ax}\sqrt{n}$ with the phonon number n. After the RSB pulse, a quench pulse of typically 2 μs completes the cooling cycle. After ten cooling cycles, about 10% of the population is accumulated in the wrong ground state spin level, such that a 397 nm repump pulse has to be employed. After eight such sequences, we employ a second cooling stage where the RSB pulse duration is increased, and the 729 nm optical pumping procedure is used instead of the circular 397 nm pulses. The longer time for repumping has no adverse effect on the cooling rate because it is used only every ten cycles.

5.4. Determination of the phonon number distribution

We confirm the sideband cooling result by employing either the quadrupole transition or the R1/R2 Raman transition. The optimization of the cooling is performed by minimizing the peak excitation of the RSB of the quadrupole transition, which is essentially given by the probability of not finding the ion in the ground state. For more accurate determination of the phonon number distribution we employ Rabi oscillations on the R1/R2 blue side band (BSB), with the advantage that no contributions from the radial vibrational modes can influence the result, and on the other hand the larger Lamb–Dicke factor of the Raman transition leads to a better separation of the Rabi frequencies for the various $n \rightarrow n + 1$ transitions. Excitation data are acquired until the oscillation contrast of the excitation signal has decreased beyond the projection noise limit for long pulse widths; see figure 7. The recorded traces

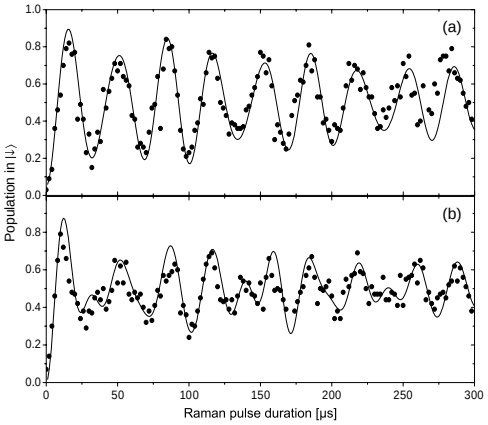

Figure 7. Coherent dynamics on the R1/R2 BSB after sideband cooling. The graphs show the population in the $|\downarrow\rangle$ level versus pulse duration of a square Raman excitation pulse (a) directly after sideband cooling, and (b) after a delay of 3 ms. The data were obtained with a Raman detuning of $\Delta \approx 40$ GHz. The solid lines are reconstructed from the extracted phonon distribution data with the inclusion of a coherence decay time of 280 μs. We extract a mean phonon number of 0.24 for the data set without waiting time.

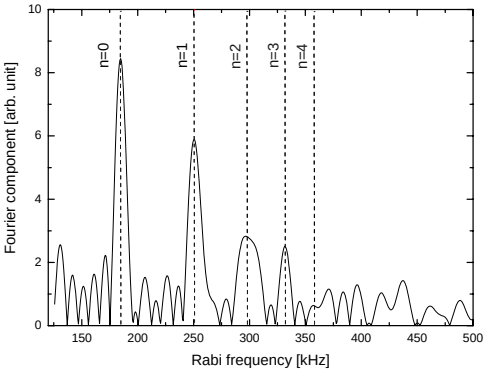

Figure 8. (a) Cosine transform of a R1/R2 pulse width scan on the BSB after a 3 ms delay between cooling and probing. The dashed lines indicate the different flopping frequencies given by the matrix element for the given transition.

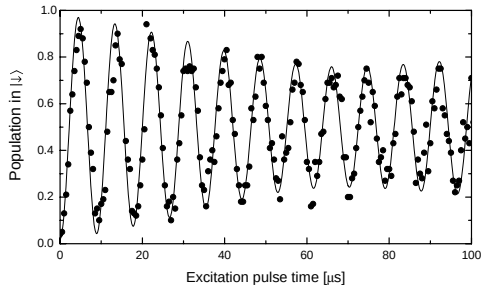

Figure 9. Coherent dynamics on the R1/R2 carrier transition after sideband cooling. The graph shows the population in the $|\downarrow\rangle$ state versus pulse duration of a square Raman excitation pulse directly after sideband cooling. The mean phonon number of 0.24 is used for fitting the data.

are analysed by a cosine transform to obtain the frequency components for the different contributing transitions, in full analogy to experiments on the cavity QED realization of the Jaynes–Cummings model [31]. Due to the finite data acquisition time, the peaks in the cosine transform pertaining to a given transition frequency are accompanied by aliases at other frequencies which lead to systematic errors when the phonon number occupation probability is inferred directly from the peak heights. A deconvolution procedure was used to remove this effect. The correctness of the method is proven by the fact that the method yields the correct input phonon number distribution when Monte Carlo generated data with realistic parameters are used. The resulting accuracy is then limited by the readout projection noise of the pulse width scan data.

A resulting spectrum is shown in figure 8. Upon proper normalization, the peak heights directly correspond to the occupation probabilities for the different phonon numbers. These data can then be used to reconstruct the coherent dynamics, allowing for the empirical inclusion of a coherence decay time [32]. This is done according to

$$P_{|\downarrow\rangle}(t) = \sum_n \frac{P_n}{2}(A\cos(\Omega_{n,n+1}t)\,\mathrm{e}^{-\gamma t} + 1), \qquad (1)$$

where $P_{|\downarrow\rangle}(t)$ is the probability for finding the ion in $|\downarrow\rangle$, P_n is the phonon number distribution, $\Omega_{n,n+1}$ is the Rabi frequency pertaining to the specific BSB transition, A is the readout contrast and γ is the coherence decay rate. The coherence time $1/\gamma$ is found to be 280(20) μs. The enhanced decoherence stems from spontaneous photon scattering [33]. The phonon distribution is reconstructed for various waiting times after sideband cooling in order to reveal the trap-induced heating dynamics. The time-dependent phonon number distribution is shown in figure 10, along with the resulting mean phonon number. This directly gives the lowest attainable mean phonon number of 0.24 and the heating rate to be 0.3(1) phonons ms^{-1}. This is about one order of magnitude better than earlier findings of 2.13 phonons ms^{-1} [10], which is attributed to an improved trap voltage supply.

The corresponding Rabi oscillations on the carrier of the R1/R2 Raman transition are shown in figure 9. Taking the phonon number after sideband cooling from the BSB Rabi oscillations, we find excellent agreement with the measurements made on the carrier transition.

6. Outlook

In the future, the full control of a single spin qubit demonstrated here will be extended to two-ion crystals. Then, a two-qubit quantum gate utilizing spin-dependent light forces will be used for the deterministic generation of Bell states. Taking advantage of the multi-segmented micro ion trap we intend to split the entangled two-ion crystal and investigate the separation of entangled states over distances of a few mm. As the lifetime of entangled Bell states in the decoherence-free basis states is long [19], measured to be a few seconds in

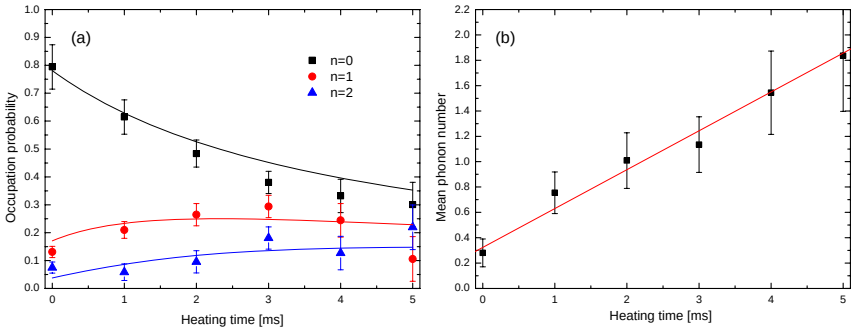

Figure 10. (a) Occupation probabilities P_n for the lowest vibrational levels $n \leqslant 2$, extracted from frequency spectra of the BSB pulse width scans (see figure 8) after different waiting times. For comparison, the solid lines show the occupation probabilities given by a thermal distribution $p(n) = \bar{n}^n/(\bar{n}+1)^{n+1}$, where $\bar{n}(t)$ is given by a linear fit through the mean phonon numbers calculated from the data. (b) Mean occupation number $\bar{n}$ calculated from P_n at different times after cooling. The linear fit indicates a constant heating rate of $\dot{n} = (0.3 \pm 0.1)$ ms^{-1}.

experiments using the Zeeman sublevels of $^{40}Ca^{+}$, we expect to be able to generate many of these Bell states within their coherence time. Protocols such as entanglement purification [34], entanglement swapping [35] and the generation of cluster states [36] will then be possible.

Acknowledgments

We acknowledge financial support by the German science foundation DFG within the SFB/TRR-21 and by the European commission within MICROTRAP (contract no 517675) and EMALI (contract no MRTN-CT-2006-035369).

References

[1] Nielsen M and Chuang I L 2000 *Quantum Computation and Quantum Information* (Cambridge: Cambridge University Press)
[2] European and the US quantum information roadmaps are found at http://qist.ect.it and at http://qist.lanl.gov
[3] Roos C, Zeiger Th, Rohde H, Nägerl H C, Eschner J, Leibfried D, Schmidt-Kaler F and Blatt R 1999 Quantum state engineering on an optical transition and decoherence in a Paul trap *Phys. Rev. Lett.* **83** 4713
[4] Roos C 2000 Controlling the quantum state of trapped ions *PhD thesis* Leopold–Franzens-Universität Innsbruck
[5] Schmidt-Kaler F *et al* 2003 How to realize a universal quantum gate with trapped ions *Appl. Phys.* B **77** 789
[6] Seidelin S *et al* 2006 A microfabricated surface-electrode ion trap for scalable quantum information processing *Phys. Rev. Lett.* **96** 253003
[7] Häffner H *et al* 2005 Scalable multiparticle entanglement of trapped ions *Nature* **438** 643
[8] Kielpinski D, Monroe C R and Wineland D J 2002 Architecture for a large-scale ion-trap quantum computer *Nature* **417** 709
[9] Schulz S, Poschinger U, Singer K and Schmidt-Kaler F 2006 Optimization of segmented linear Paul traps and transport of stored particles *Fortschr. Phys.* **54** 648
[10] Schulz S, Poschinger U, Ziesel F and Schmidt-Kaler F 2008 Sideband cooling and coherent dynamics in a microchip multi-segmented ion trap *New J. Phys.* **10** 045007
[11] Gulde S, Rotter D, Barton P, Schmidt-Kaler F, Blatt R and Hogervorst W 2001 Simple and efficient photoionization loading of ions for precision ion-trapping experiments *Appl. Phys.* B **73** 861
[12] Wunderlich C, Hannemann Th, Körber T K, Häffner H, Roos Ch, Hänsel W, Blatt R and Schmidt-Kaler F 2007 Robust state preparation of a single trapped ion by adiabatic passage *J. Mod. Opt.* **54** 1541
[13] Monz T, Kim K, Hänsel W, Riebe M, Villar A S, Schindler P, Chwalla M, Hennrich M and Blatt R 2009 Realization of the quantum toffoli gate with trapped ions *Phys. Rev. Lett.* **102** 040501
[14] Kirchmair G, Benhelm J, Zähringer F, Gerritsma R, Roos C F and Blatt R 2009 Deterministic entanglement of ions in thermal states of motion *New. J. Phys.* **11** 023002
[15] Benhelm J, Kirchmair G, Roos C F and Blatt R 2008 Experimental quantum information processing with $^{43}Ca^{+}$ ions *Phys. Rev.* A **77** 062306
[16] Home J P, McDonnell M J, Lucas D M, Imreh G, Keitch B C, Szwer D J, Thomas N R, Webster S C, Stacey D N and Steane A M 2006 Deterministic entanglement and tomography of ionspin qubits *New. J. Phys.* **8** 188
[17] Home J 2006 Entanglement of two trapped-ion spin qubits *PhD thesis* Oxford University
[18] Kielpinski D, Meyer V, Rowe M A, Sackett C A, Itano W M, Monroe C and Wineland D J 2001 A decoherence-free quantum memory using trapped ions *Science* **291** 1013
[19] Häffner H *et al* 2005 Robust entanglement *Appl. Phys.* B **81** 151
[20] Roos C F, Chwalla M, Kim K, Riebe M and Blatt R 2006 'Designer atoms' for quantum metrology *Nature* **443** 316
[21] DiVicenzo D P 2000 The physical implementation of quantum computation *Fortschr. Phys.* **48** 711–83
[22] McDonnell M J, Stacey J-P, Webster S C, Home J P, Ramos A, Lucas D M, Stacey D N and Steane A M 2004 High-efficiency detection of a single quantum of angular momentum by suppression of optical pumping *Phys. Rev. Lett.* **93** 153601
[23] Cummins H K, Llewellyn G and Jones J A 2003 Tackling systematic errors in quantum logic gates with composite rotations *Phys. Rev.* A **67** 042308
[24] Timoney N, Elman V, Glaser S, Weiss C, Johanning M, Neuhauser W and Wunderlich C 2008 Error-resistant single-qubit gates with trapped ions *Phys. Rev.* A **77** 052334
[25] Ozeri R *et al* 2005 Hyperfine coherence in the presence of spontaneous photon scattering *Phys. Rev. Lett.* **95** 030403
[26] Ozeri R *et al* 2007 Errors in trapped-ion quantum gates due to spontaneous photon scattering *Phys. Rev.* A **75** 042329
[27] Grimm R, Weidemüller M and Ovchinnikov Y B 2000 Optical dipole traps for neutral atoms *Adv. At. Mol. Opt. Phys.* **42** 95
[28] Turchette Q A, Wood C S, King B E, Myatt C J, Leibfried D, Itano W M, Monroe C and Wineland D J 1998 Deterministic entanglement of two trapped ions *Phys. Rev. Lett.* **81** 3631
[29] Leibfried D *et al* 2002 Experimental demonstration of a robust, high-fidelity geometric two ion-qubit phase gate *Nature* **422** 412
[30] Marzoli I, Cirac J I, Blatt R and Zoller P 1994 Laser cooling of trapped three-level ions: designing two-level systems for sideband cooling *Phys. Rev.* A **49** 2771
[31] Brune M, Schmidt-Kaler F, Maali A, Dreyer J, Hagley E, Raimond J M and Haroche S 1996 Quantum Rabi oscillation: a direct test of field quantization in a cavity *Phys. Rev. Lett.* **76** 1800
[32] Meekhof D M, King B E, Monroe C, Itano W M and Wineland D J 1996 Generation of nonclassical motional states of a trapped atom *Phys. Rev. Lett.* **77** 2346
[33] Di Fidio C and Vogel W 2000 Damped Rabi oscillations of a cold trapped ion *Phys. Rev.* A **62** 031802
[34] Pan J-W, Gasparoni S, Ursin R, Weihs G and Zeilinger A 2003 Experimental entanglement purification of arbitrary unknown states *Nature* **423** 417
[35] Riebe M, Monz T, Kim K, Villar A S, Schindler P, Chwalla M, Hennrich M and Blatt R 2008 Deterministic entanglement swapping with an ion-trap quantum computer *Nat. Phys.* **4** 839
[36] Briegel H J and Raussendorf R 2001 Persistent entanglement in arrays of interacting particles *Phys. Rev. Lett.* **86** 910

A trapped-ion local field probe

Gerhard Huber, Frank Ziesel, Ulrich Poschinger, Kilian Singer and Ferdinand Schmidt-Kaler

Published online 17 July 2010, in print for the scientific journal:
Applied Physics B: Lasers and Optics
(DOI 10.1007/s00340-010-4148-x / Year: 2010)

Appl Phys B
DOI 10.1007/s00340-010-4148-x

Applied Physics B
Lasers and Optics

A trapped-ion local field probe

G. Huber · F. Ziesel · U. Poschinger · K. Singer · F. Schmidt-Kaler

Received: 18 March 2010 / Revised version: 22 June 2010

Abstract We introduce a measurement scheme that utilizes a single ion as a local field probe. The ion is confined in a segmented Paul trap and shuttled around to reach different probing sites. By the use of a single atom probe, it becomes possible characterizing fields with spatial resolution of a few nm within an extensive region of millimeters. We demonstrate the scheme by accurately investigating the electric fields providing the confinement for the ion. For this we present all theoretical and practical methods necessary to generate these potentials. We find sub-percent agreement between measured and calculated electric field values.

1 Introduction

The concept to realize and investigate quantum processes with single ions in Paul traps was subject to an impressive development over the last years. As for quantum information with single to a few ions, there has hardly been an experimental challenge that could withstand this development; consider, for instance, high fidelity quantum gates [1], multi-qubit entanglement [2, 3], and error correction [4]. There has been a recent development in ion trap technology that was primarily initiated by the necessity—and possibility—to scale up the established techniques to process larger numbers of ions. This idea how to scale up an ion trap computer is to create multiple trap potentials, each keeping only a small, processable number of ions [5]. Time dependent potentials can then be used to shuttle the ions between different sections. To generate such spatially separated potentials, the respective trap electrodes are segmented along the transport direction and supplied individually with time dependent voltages. There have also been proposals to incorporate the shuttling process into the quantum gate time by letting the ion cross laser beams or magnetic field arrangements [6]. Another application of the shuttling ability is the exact positioning of the ion in the mode volume of an optical cavity to perform cavity quantum electrodynamic experiments. Recently, multi-trap configurations with locally controlled, individual trap frequencies were proposed to generate cluster states in linear ion traps to perform one-way quantum computations [7].

This paper presents the implementation of a method using a single trapped ion to investigate local electric fields. The method profits from the accuracy of spectroscopic frequency measurements and relies on the ability to shuttle the ion in order to reach different probing sites. We can demonstrate that the new technique is suitable to characterize local trapping potentials in segmented traps over extensive lengths and even under conditions where imaging of the ion is limited. First, we describe the experimental system and the way the electric trapping and shuttling potentials are generated. After that, the measurement scheme using the ion as a local field probe is presented. Then, the quantitative experimental results are discussed and compared to numerical simulations of the trapping fields.

2 Experimental field generation

We confine a single, laser cooled $^{40}Ca^{+}$-ion in a linear Paul trap. The radial confinement is generated by a harmonic radio-frequency pseudo potential resulting from a

G. Huber (✉) · F. Ziesel · U. Poschinger · K. Singer · F. Schmidt-Kaler
Institut für Quanteninformationsverarbeitung, Universität Ulm, Albert-Einstein-Allee 11, 89069 Ulm, Germany
e-mail: gerhard.huber@uni-ulm.de

Published online: 17 July 2010

25 MHz drive with an amplitude of about 350 V_{pp}. The distance between the ion and the radio-frequency electrodes is ∼250 µm. This results in radial trap frequencies around 3.5 MHz. For the axial confinement, 32 pairs of electrodes are available. Each of these 64 segments can be individually biased to a voltage V_i, $|V_i| \leq 10$ V. In the trap region the experiments were performed in, the segments are 250 µm wide and separated by 30 µm gaps (details can be found in [8]). The voltage data are preprocessed by a computer and transmitted to a home-built electronics device. This device houses an array of 16 serial input digital-to-analog converters (dac, 50 MHz maximum clock frequency), each of which supplying four individual voltage lines, so that a data bus conveying 16 bit in parallel suffices to obtain the desired 64 outputs. The amplitude resolution of the converters is 16 bit with a measured noise level well below the least significant bit. The serial input design of the converters keeps the amount of data being transmitted in parallel at a minimum. This makes the design extendable to a large number of channels.

In this work, we restrict ourselves to the investigation of harmonic potentials. This is rectified by the fact that a resting, laser cooled ion only experiences the very minimum of the potential. Such potentials are generated by applying control voltages to the trap segments. Thereby, each specific voltage configuration results in an axial trap with a given trap frequency; the position of the potential minimum—this is where the ion resides—can be changed to shuttle the ion between different locations on the trap axis. Doing so, two requirements have to be met by the time dependent voltages: (i) The amplitudes must range within the limits given by the dac electronics, ±10 V in our case. (ii) Each segment's voltage is to change as continuously as possible to avoid unfeasibly high frequencies. All these requirements are fulfilled by the field simulation and voltage calculation techniques presented in Appendices A and B, respectively. For the experiments presented here, it is advantageous to perform slow, adiabatic potential changes, and thus to avoid excess oscillations of the ion. For that reason, the update rate of the digital-to-voltage converters was chosen as ∼3.3 ms, and a parallel port connection between computer and dac device was used. In an alternative operation modus of the trap supply device, the data transmission and updated rate is significantly sped up by using a field programmable gate array. Then we reach 4 µs even when updating all 64 channels simultaneously. For the application presented here, it is sufficient to use a Doppler cooled probe ion. The probe's spatial extent can then be estimated from the ion temperature and the consequential extent of the motional wave function to be ∼60 nm. This value could be reduced to ∼5 nm by sub-Doppler cooling and a tighter confinement of the ion.

3 The local field probe measurement scheme

To test both the numerical methods and the developed electronic devices for accuracy, we employ a single ion as a probe for the electrostatic potential. We exploit the fact that it is possible to exactly measure the trap frequency of the confining axial potential by spectroscopic means. Consider, for example, a voltage configuration $\{V_i\}^{(z_p)}$ to be tested for; this configuration is meant to result in a trap at position z_p with frequency $\omega(z_p)$. Then we can use time dependent potentials to shuttle the ion from a loading position to z_p [9], whereby the final voltage configuration must be $\{V_i\}^{(z_p)}$. The spectroscopically obtained trap frequency at z_p can then be compared to the theoretically expected one, $\omega_{\text{sim}}(z_p)$.

The trap frequency is determined by measuring the difference frequency of the carrier and the first motional red sideband (rsb) excitation of the ion in a resolved sideband regime. For that, we excite the quadrupole transition $(4S_{1/2}, m_J = +1/2) \leftrightarrow (3D_{5/2}, m_J = +5/2)$ at 729 nm. As the carrier resonance frequency does not depend on the trap frequency,[1] it is sufficient to measure the rsb frequency at different locations z_p.

The measurement scheme is illustrated in Fig. 1. It consists of the following steps:

(i) An initial voltage configuration is chosen to trap and cool the ion at the starting position z_0. All lasers necessary for cooling, repumping, state preparation and detection are aligned to interact with the ion here. Additionally, z_0 is the position where fluorescence emitted by the ion can be detected by a photomultiplier tube and a camera.

(ii) The ion is shuttled to the probing position z_p. This is accomplished by applying voltage configurations resulting in a series of harmonic potentials whose minimum positions lead the ion from z_0 to z_p. For simplicity, these potentials were chosen such that their harmonic frequencies were almost constant and close to $\omega(z_p)$.

(iii) Applying a spectroscopy pulse at the probing position z_p. Now, the voltages are exactly $\{V_i\}^{(z_p)}$. Resting at z_p, the ion is exposed to a spectroscopy pulse of fixed duration (100 µs). The pulse is detuned from the (carrier) resonance by Δf. This excites the ion with a probability P into the upper state $|D_{5/2}\rangle$.

(iv) Shuttle the ion back to z_0, inverting step (ii).

(v) Having arrived back at the starting position, the state of the ion is read out by illuminating it on the cooling transition. Whenever we detect a fluorescence level above a certain threshold, the ion is found in the ground state

[1] Nevertheless, the carrier frequency was monitored to exclude drifts in laser frequency or Zeeman splitting.

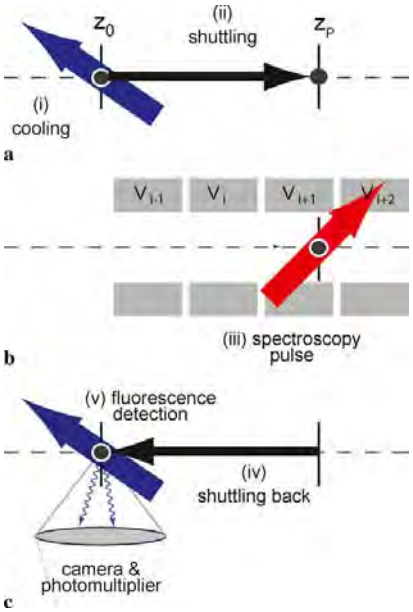

Fig. 1 Illustration of the measurement procedure: (*i*) cooling and preparation of the ion at the starting position z_0 and (*ii*) transport of the ion to the probing position z_p. A spectroscopy pulse with a certain detuning excites the ion there (*iii*). After shuttling the ion back (*iv*), the quantum state of the ion is read out (*v*). After many repetitions for different detunings an excitation spectrum of the ion at z_p is obtained, from which the trap frequency $\omega(z_p)$ can be deduced

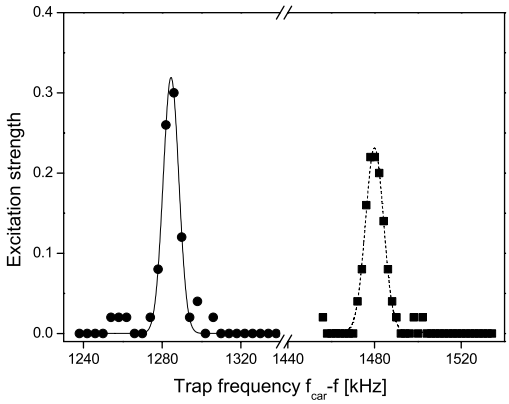

Fig. 2 Resonances of the first red sideband excitation on the $S_{1/2} \rightarrow D_{5/2}$ transition. The two peaks are measured at different trap positions along the trap axis. The resonance frequencies are given with respect to the carrier resonance f_{car}, so that the trap frequency at the respective trap position can be read off. The full width at half maximum of the peaks is 8 kHz and determines the measurement accuracy. The different peak heights stem from slightly different field intensities experienced by the ion

$|S_{1/2}\rangle$, while a low fluorescence level indicates that the ion has been excited to the state $|D_{5/2}\rangle$.

The excitation probability for a specific detuning, $P(\Delta f)$, at the remote position z_p is obtained by averaging over many repetitions of steps (i) to (v). By varying Δf, a spectrum of the quadrupole excitation at the remote position is obtained without moving any lasers or imaging optics but the spectroscopy laser used in step (iii). This is a significant advantage because that way even such trap positions can be investigated that cannot be directly observed by the imaging devices or reached by all lasers.

The frequency difference between the red sideband and the carrier transition yields the trap frequency. Figure 2 shows two rsb resonance peaks obtained at different positions within the trap volume.

It is noticeable that each iteration cycle (i–v) including two ion transports results—due to the binary nature of the projective readout—in exactly one bit information about the spectrum. Therefore, thousands of transports, each relying on the calculated potentials, are performed for the determination of one frequency $\omega(z_p)$. The transport, however, can be performed so fast (∼100 µs) that its contribution to the overall experiment duration is secondary; this duration is still dominated by cooling and detection times (∼ms). In future experiments, one might increase the frequency resolution of sideband spectroscopy to better than a few parts in 10^4 relative accuracy [10].

4 Implementation and results

To implement the measurement scheme, we first calculated voltage sets $\{V_i\}^{(z)}$, where z covers the whole extent of the trap in steps of 5 µm (For arbitrary positions, the voltages can be interpolated). Each set results in a certain, wanted frequency $\omega_{\text{sim}}(z)$. That means that for each arbitrary position z in the trap, a set of voltages can be found, resulting in a potential with its minimum at z and with trap frequency $\omega_{\text{sim}}(z)$. Then, in order to shuttle the ion, we simply subsequently apply the voltage configurations for $z = z_0, \ldots, z_p$.

The calculated voltages are tested with high axial resolution, i.e., in small steps of z_p, in two faraway regions of the trap. Doing this, both small local deviations should be detectable and the stability over the whole trap structure can be tested for. To see a variation in $\omega(z_p)$ when increasing z_p, it is of advantage that small variations of the trap frequency around its mean value occur. This is a reliable way to ensure that the ion, in fact, probes the remote position.

Figure 3 shows the expected, simulated trap frequencies and the measured ones. The data are in excellent agreement with the predicted frequencies. On both ends of the investi-

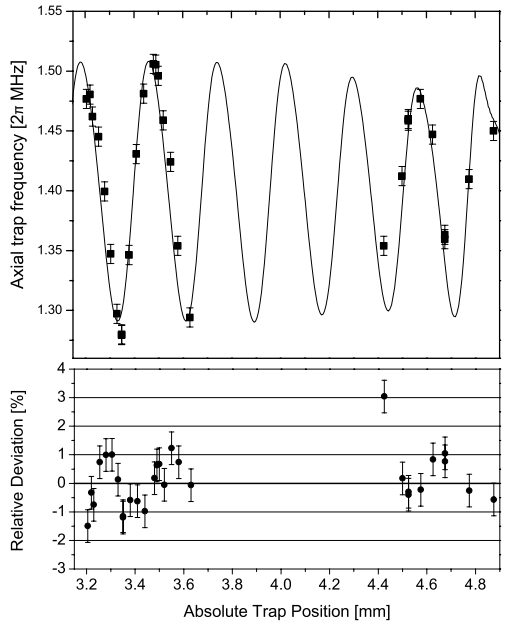

Fig. 3 (**a**) Harmonic trap frequency as a function of the position along the trap axis. The electrode voltages were calculated and applied such that the trap frequency shows a small oscillatory variation around a mean value of about 1.4 MHz to see the ion proceed along the axis. The *solid line* shows the frequency of the wanted harmonic potential. The data points are the spectroscopically measured, real trap frequencies. The error bars show the uncertainty due to the finite resonance linewidth. (**b**) Relative deviation of the measured from the simulated frequency $|\omega(z) - \omega_{\mathrm{sim}}(z)|/\omega_{\mathrm{sim}}(z)$

gated trap structure, the predicted course of $\omega_{\mathrm{sim}}(z)$ is confirmed within the spectroscopic accuracy of 0.6%. The mean deviation of all measured data points is only 0.73%. Note that the solid line shown in Fig. 3 is based solely on geometric data from a technical drawing of the trap; there is no free parameter that was used to match the simulations with the measurement.

5 Discussion and outlook

The high accordance between the simulated and the real trap frequencies, as can be observed in the presented experiments, indicates the reliability of at least four independent contributions: First, the numerical field simulation is accurate. This simulation is independent from a specific set of voltages, but relies on a model of the three dimensional trap design.

Second, the physical realization of this geometry is very good, i.e., the manufacturing and assembling process of the micro-trap is so precise that it is not limiting the field accuracy. This aspect is coming more an more into the experimental focus, since the miniaturization of the trap layouts still proceeds. For example, a possible axial misalignment Δx of the two dc electrode wings with respect to each other would mainly result in an axial shift of the oscillations depicted in Fig. 3(a) by approximately $\Delta x/2$. Additionally, the amplitude of these oscillations decreases with increasing Δx. Indeed, the residuals (Fig. 3(b)) show a small oscillatory behavior. This oscillation signal is shifted by at most $\sim$15 µm with respect to the trap frequency oscillation. Such an effect could stem from a small misalignment of the two trap layers (see [8]) or from a small offset of the theoretical and the real, axial zero point of position. We attribute the observed shift to an offset error since, in this case, the amplitude of the oscillation is not decreased, as it is the case in the measured data.[2] This shift is systematic and could be corrected for. Third, the calculation of the voltages leading to the wanted potentials is highly reliable. This is also qualitatively confirmed by the successful shuttling process itself. From our measurements, we find that the generation of the voltages and their supply to the trap electrodes is indeed highly accurate. We also conclude that trapping fields from the applied voltages are not significantly perturbed by background fields from stray charges.

As the generation of trapping fields in the multi-segment trap was found to be accurate over the whole considered volume, it is possible to tailor potentials for special purposes. For quantum computing tasks, a harmonic potential of constant frequency is mostly required. Simulations show that it is possible to obtain fixed frequency potentials with a relative frequency deviation on the order of 10^{-4}. The fast transport of quantum information in harmonic wells also requires a high degree of control over the trap voltages [11]. The application of optimal control methods can help optimizing tailored time dependent potentials. Alternatively, one can feed-back information, gained from the measurement presented here, into the generation process to refine the results iteratively [12].

However, the scope of possible applications of the described techniques is much wider than quantum computing tasks: Ions in time dependent potentials were proposed to be used as a testbed for quantum thermodynamic processes [13] or for quantum simulation [14, 15]. The presented method is just a first proof of principle of using single atoms as ultra-sensitive probes. The measurement principle is not restricted to the investigation of the electric trapping fields. Using a transition in the ion level scheme with high differential magnetic moment, we can also employ our method to investigate local magnetic fields with the ion. The

[2] The misalignment error can also be verified to be smaller than $\sim$10 µm from microscope pictures of the trap.

method might be seen as an alternative to cold atom sensors for microscopic magnetic-field imaging [16] or to investigate local current variations in a metal film [17]. Then, a single atom field probe might be used as well for probing magnetic micro-structures with a relative accuracy better than 10^{-3}. While the electric stray fields from surface contamination might be equally well investigated with an ion as with neutral atoms [18], smallest forces can be detected with ions [19] or atoms [20]. Also, a study of decoherence and heating effects and their dependence on the ion-electrode separation or ion location is in reach.

Acknowledgement We thank S. Schulz for his contributions at an earlier stage of the experiment. Financial support from the DFG within the SFB/TRR-21, the German–Israel Science Foundation and by the European Commission within MICROTRAP, EMALI and SCALA is acknowledged.

Appendix A: Field calculations

To create a specific electric potential $\phi(z)$ on the trap axis, it is necessary to find the right set of voltages $\{V_i\}$ being applied to the trap electrodes labeled by $i = 1, \ldots, N$. The potential generated by such a set of voltages is the linear superposition of the N individual electrodes, whereby the contribution of each electrode i is weighted by the applied voltage V_i. After subdividing the axial position into a grid of M points z_j, $j = 1, \ldots, M$, we can write the overall potential at any z_j by

$$\phi(z_j) = \phi_j = \sum_{i=1}^{N} A_{ij} \cdot V_i.$$

Here we introduced the electrode potential matrix A_{ij}. It describes the influence of the ith electrode to the overall potential at x_j. Each row i of A can be seen as a position-dependent function, describing the potential generated by electrode i (in units of V_i), when all other electrodes are set to zero voltage. This quantity A is independent from the specific voltage and is solely given by the trap geometry, i.e., the shape and size of the electrode and its distance from z_j, for instance.

Therewith, the potential generation can be logically divided into two parts: The matrix A can be calculated independently from voltage constraints and independent from the desired potential. Second, for each desired potential $\boldsymbol{\phi}$, a set of voltages $\mathbf{v}$ has to be found by inverting the matrix equation above. Tackling the first problem, one recognizes that modern segmented trap geometries can be realized in such a geometric complexity that conventional simulation techniques like the finite element method (FEM) fail. Instead, we obtained the potentials by solving the boundary element problem of the segmented trap design. Details can be found in [21–24].

Appendix B: Calculation of the voltages

In the following, we address the problem of how to obtain a set of voltages $\{V_i\}$ that generates a given potential $\boldsymbol{\phi}$ when applied to the respective electrodes. The problem is formally solved by matrix inversion as $A^{-1}\boldsymbol{\phi}$. Several circumstances make this straightforward ansatz unfeasible: First, there is often no exact solution to the problem because $\boldsymbol{\phi}$ is not an exactly realizable potential (note that, in general, $M \gg N$ is possible). In this case, an approximate solution has to be found. Additionally, as a specific electrode does not effectively contribute to the potential at a faraway point, this electrode's voltage is ill-determined. These cases have to be treated adequately by the algorithm. We solved the inversion problem with a singular-value decomposition of the matrix A to identify its critical, singular values. The real $N \times M$ matrix A is decomposed into the product

$$A = USW^T, \tag{1}$$

of the unitary matrices U ($N \times N$) and W ($M \times M$) and the diagonal $N \times M$ matrix S with non-negative entries $s_k, k = 1, \ldots, \min(M, N)$. This decomposition is part of many standard numerical libraries and can be performed for any input matrix A. The inverse can then be written as

$$A^{-1} = WS^{-1}U^T. \tag{2}$$

This step is numerically trivial because the unitary matrices are simply transposed and the entries of S^{-1} are given by $1/s_k$. At this point, the advantage of the decomposition becomes obvious since small values of s_k indicate an (almost) singular, critical value. One way to overcome these singular values would be to cut off their diverging inverse values. Instead, the Tikhonov regularization [25] method implies a more steady behavior as it makes the displacement $1/s_k \to s_k/(s_k^2 + \alpha^2)$. The latter expression behaves like the original $1/s_k$ for large values $s_k \gg \alpha$, has its maximum at $s_k = \alpha$ and tends to zero for small, critical values $s_k \ll \alpha$. From this we can see that the choice of the optimization parameter α is a compromise between exactness and boundedness of the results. For $\alpha = 0$, the exact solution (if existent) is obtained, whereas large values of α guarantee small inverse values and thus bounded voltage results. Therefore, we label the regularized quantities with index α. The approximate solution $\mathbf{v}_\alpha = (V_1, \ldots, V_N)$ is

$$\mathbf{v}_\alpha = WS_\alpha^{-1}U^T\boldsymbol{\phi}, \tag{3}$$

with S_α^{-1} being the regularized matrix with entries $s_k/(s_k^2 + \alpha^2)$.

Before the problem of finding an optimal α is addressed, another constraint regarding time dependent voltages, i.e., series of voltage configurations, has to be accounted for.

While moving the ion by one step, i.e., from a position z_p to z'_p, the control voltage should vary as less as possible. This is achieved by extending (3) to

$$\mathbf{v}'_\alpha = \mathbf{v}_\alpha + W D_\alpha W^T \mathbf{v}, \tag{4}$$

where $\mathbf{v}$ represents any previous voltage set, providing trapping at z_p. The second term in (4) contains a diagonal matrix D with entries $d_k = \alpha^2/(s_k^2 + \alpha^2)$. d_k tends to zero for $s_k \gg \alpha$, so that uncritical voltages are affected only little by the second term. For all critical voltages indicated by a value $s_k \ll \alpha$, however, the first term in (4) vanishes due to the regularization replacement and what remains is the contribution from $\vec{v_0}$ since then $d_k \approx 1$. Here, the choice of α determines how strong the algorithm tries to generate similar voltages in a (time) series of voltage sets.

The algorithm described above minimizes $\|A\mathbf{v}'_\alpha - \vec{\phi}\|^2 + \alpha\|\mathbf{v}'_\alpha - \mathbf{v}\|^2$ with respect to the Euclidian norm. That is, the potential $\boldsymbol{\phi}$ is reproduced as well as possible under the constraint that solutions similar to the previous one are preferred. What remains is to find the proper value of α. Hereby, one has to make a tradeoff between the boundedness of the voltages and their continuity. Under practical circumstances requiring $|V_i| \leq V_{\max}$ for some maximal voltage $V_{\max}$, α can be iteratively increased to fulfill this constraint, on the one hand, and to obtain as continuous voltage sets as possible, on the other hand.

References

1. J. Benhelm, G. Kirchmair, C.F. Roos, R. Blatt, Nat. Phys. **4**, 463 (2008)
2. H. Häffner, W. Hänsel, C.F. Roos, J. Benhelm, D. Chek-al-kar, M. Chwalla, T. Körber, U.D. Rapol, M. Riebe, P.O. Schmidt, C. Becher, O. Gühne, W. Dür, R. Blatt, Nature **438**, 643 (2005)
3. D. Leibfried, E. Knill, S. Seidelin, J. Britton, R.B. Blakestad, J. Chiaverini, D.B. Hume, W.M. Itano, J.D. Jost, C. Langer, R. Ozeri, R. Reichle, D.J. Wineland, Nature **438**, 639 (2005)
4. J. Chiaverini, D. Leibfried, T. Schaetz, M.D. Barrett, R.B. Blakestad, J. Britton, W.M. Itano, J.D. Jost, E. Knill, C. Langer, R. Ozeri, D.J. Wineland, Nature **432**, 602 (2004)
5. D. Kielpinski, C. Monroe, D.J. Wineland, Nature **417**, 709 (2002)
6. D. Leibfried, E. Knill, C. Ospelkaus, D.J. Wineland, Phys. Rev. A **76**, 032324 (2007)
7. H. Wunderlich, C. Wunderlich, K. Singer, F. Schmidt-Kaler, Phys. Rev. A **79**, 052324 (2009)
8. S. Schulz, U. Poschinger, F. Ziesel, F. Schmidt-Kaler, New J. Phys. **10**, 045007 (2008)
9. G. Huber, T. Deuschle, W. Schnitzler, R. Reichle, K. Singer, F. Schmidt-Kaler, New J. Phys. **10**, 013004 (2008)
10. M. Drewsen, A. Mortensen, R. Martinussen, P. Staanum, J.L. Sørensen, Phys. Rev. Lett. **93**, 243201 (2004)
11. M. Murphy, L. Jiang, N. Khaneja, T. Calarco, Phys. Rev. A **79**, 020301(R) (2009)
12. J. Eble, S. Ulm, P. Zahariev, F. Schmidt-Kaler, K. Singer, J. Opt. Soc. Am. **27**(6), A99 (2010)
13. G. Huber, F. Schmidt-Kaler, S. Deffner, E. Lutz, Phys. Rev. Lett. **101**, 070403 (2008)
14. R. Schützhold, M. Uhlmann, L. Petersen, H. Schmitz, A. Friedenauer, T. Schätz, Phys. Rev. Lett. **99**, 201301 (2007)
15. M. Johanning, A. F Varón, C. Wunderlich, J. Phys. B, At. Mol. Opt. Phys. **42**, 154009 (2009)
16. S. Wildermuth, S. Hofferberth, I. Lesanovsky, E. Haller, L. Mauritz Andersson, S. Groth, I. Bar-Joseph, P. Krüger, J. Schmiedmayer, Nature **435**, 440 (2005)
17. S. Aigner, L. Della Pietra, Y. Japha, O. Entin-Wohlman, T. David, R. Salem, R. Folman, J. Schmiedmayer, Science **319**, 1226 (2008)
18. J.M. Obrecht, R.J. Wild, E.A. Cornell, Phys. Rev. A **75**, 062903 (2007)
19. M.J. Biercuk, H. Uys, J.W. Britton, A.P. VanDevender, J.J. Bollinger, arXiv:1004.0780
20. D.M. Harber, J.M. Obrecht, J.M. McGuirk, E.A. Cornell, Phys. Rev. A **72**, 033610 (2005)
21. L. Greengard, V. Rokhlin, in *Vortex Methods*, vol. 121 (Springer, Berlin, 1988)
22. K. Nabors, F.T. Korsmeyer, F.T. Leighton, J. White, SIAM J. Sci. Comput. **15**, 713 (1994)
23. K. Singer, U. Poschinger, M. Murphy, P. Ivanov, F. Ziesel, T. Calarco, F. Schmidt-Kaler, arXiv:0912.0196
24. C. Pozrikidis, *A Practical Guide to Boundary Element Methods with the Software Library BEMLIB* (Chapman and Hall/CRC, Boca Raton, 2002)
25. A.N. Tikhonov, V.A. Arsenin, *Solution of Ill-posed Problems* (Winston, Washington, 1977)

Bibliography

[All05] A. E. Allahverdyan and T. M. Nieuwenhuizen, *Fluctuations of work from quantum subensembles: The case against quantum work-fluctuation theorems*, Phys. Rev. E **71**, 066102 (2005).

[And84] B. Andresen, P. Salamon, and R. S. Berry, *Thermodynamics in finite time*, Physics Today **37** (1984).

[Aol07a] L. Aolita, L. Davidovich, K. Kim, and H. Häffner, *Universal quantum computation in decoherence-free subspaces with hot trapped ions*, Phys. Rev. A **75**, 052337 (2007).

[Aol07b] L. Aolita, K. Kim, J. Benhelm, C. F. Roos, and H. Häffner, *High-fidelity ion-trap quantum computing with hyperfine clock states*, Phys. Rev. A **76**, 040303 (2007).

[App98] B. Appasamy, Y. Stalgies, and P. E. Toschek, *Measurement-Induced Vibrational Dynamics of a Trapped Ion*, Phys. Rev. Lett. **80**, 2805 (1998).

[Bar00] P. A. Barton, C. J. S. Donald, D. M. Lucas, D. A. Stevens, A. M. Steane, and D. N. Stacey, *Measurement of the lifetime of the* $3d^2D_{5/2}$ *state in* $^{40}Ca^+$, Phys. Rev. A **62**, 032503 (2000).

[Bee10] J. Beer and E. Lutz, *Decoherence in a general nonequilibrium environment*, arXiv:1004.3921v1 (2010).

[Ben82] C. H. Bennett, *The Thermodynamcs of Computation – a Review*, International Journal of Theoretical Physics **21**, 905 (1982).

[Ben03] A. Ben-Kish, B. DeMarco, V. Meyer, M. Rowe, J. Britton, W. M. Itano, B. M. Jelenković, C. Langer, D. Leibfried, T. Rosenband, and D. J. Wineland, *Experimental Demonstration of a Technique to Generate Arbitrary Quantum Superposition States of a Harmonically Bound Spin*-1/2 *Particle*, Phys. Rev. Lett. **90**, 037902 (2003).

[Ben08a] J. Benhelm, G. Kirchmair, C. F. Roos, and R. Blatt, *Experimental quantum-information processing with $^{43}Ca^{+}$ ions*, Phys. Rev. A **77**, 062306 (2008).

[Ben08b] J. Benhelm, G. Kirchmair, C. F. Roos, and R. Blatt, *Towards fault-tolerant quantum computing with trapped ions*, Nature Physics **4**, 463 (2008).

[Ber98] D. J. Berkeland, J. D. Miller, J. C. Bergquist, W. M. Itano, and D. J. Wineland, *Laser-Cooled Mercury Ion Frequency Standard*, Phys. Rev. Lett. **80**, 2089 (1998).

[Bla08] R. Blatt and D. Wineland, *Entangled states of trapped atomic ions*, Nature **453**, 1008 (2008).

[Bla09] R. B. Blakestad, C. Ospelkaus, A. P. VanDevender, J. M. Amini, J. Britton, D. Leibfried, and D. J. Wineland, *High-Fidelity Transport of Trapped-Ion Qubits through an X-Junction Trap Array*, Phys. Rev. Lett. **102**, 153002 (2009).

[Bli06] V. Blickle, T. Speck, L. Helden, U. Seifert, and C. Bechinger, *Thermodynamics of a Colloidal Particle in a Time-Dependent Nonharmonic Potential*, Phys. Rev. Lett. **96**, 070603 (2006).

[Bow99] P. Bowe, L. Hornekær, C. Brodersen, M. Drewsen, J. S. Hangst, and J. P. Schiffer, *Sympathetic Crystallization of Trapped Ions*, Phys. Rev. Lett. **82**, 2071 (1999).

[Bra08] F. G. S. L. Brandão and M. B. Plenio, *Entanglement theory and the second law of thermodynamics*, Nature Physics **4**, 873 (2008).

[Bru96a] M. Brune, E. Hagley, J. Dreyer, X. Maître, A. Maali, C. Wunderlich, J. M. Raimond, and S. Haroche, *Observing the Progressive Decoherence of the "Meter" in a Quantum Measurement*, Phys. Rev. Lett. **77**, 4887 (1996).

[Bru96b] M. Brune, F. Schmidt-Kaler, A. Maali, J. Dreyer, E. Hagley, J. M. Raimond, and S. Haroche, *Quantum Rabi Oscillation: A Direct Test of Field Quantization in a Cavity*, Phys. Rev. Lett. **76**, 1800 (1996).

[Bud02] A. A. Budini, R. L. de Matos Filho, and N. Zagury, *Localization and dispersivelike decoherence in vibronic states of a trapped ion*, Phys. Rev. A **65**, 041402 (2002).

[Bus05] C. Bustamante, J. Liphardt, and F. Ritort, *The Nonequilibrium Thermodynamics of Small Systems*, Physics Today **58**, 43 (2005).

[Cah69] K. E. Cahill and R. J. Glauber, *Ordered Expansions in Boson Amplitude Operators*, Phys. Rev. **177**, 1857 (1969).

[Car88] J. Carrier, L. Greengard, and V. Rokhlin, *A fast adaptive multipole algorithm for particle simulations*, SIAM J. Sci. Stat. Comput. **9**, 669 (1988).

[Car99] J. Carrier, L. Greengard, and V. Rokhlin, *A fast adaptive multipole algorithm in three dimensions*, J. Comput. Phys. **155**, 468 (1999).

[Che04] V. Chernyak and S. Mukamel, *Effect of Quantum Collapse on the Distribution of Work in Driven Single Molecules*, Phys. Rev. Lett. **93**, 048302 (2004).

[Cir95] J. I. Cirac and P. Zoller, *Quantum Computations with Cold Trapped Ions*, Phys. Rev. Lett. **74**, 4091 (1995).

[Col05] D. Collin, F. Ritort, C. Jarzynski, S. B. Smith, I. T. Jr, and C. Bustamante, *Verification of the Crooks fluctuation theorem and recovery of RNA folding free energies*, Nature **437**, 231 (2005).

[Cor09] C. Cormick and J. P. Paz, *Observing different phases for the dynamics of entanglement in an ion trap*, arXiv:0912.1602v1 (2009).

[Cou08] A. Couvert, T. Kawalec, G. Reinaudi, and D. Guéry-Odelin, *Optimal transport of ultracold atoms in the non-adiabatic regime*, EPL **83**, 13001 (2008).

[Cro99] G. E. Crooks, *Entropy production fluctuation theorem and the nonequilibrium work relation for free energy differences*, Phys. Rev. E **60**, 2721 (1999).

[Cum65] F. W. Cummings, *Stimulated Emission of Radiation in a Single Mode*, Phys. Rev. **140**, A1051 (1965).

[Def08] S. Deffner and E. Lutz, *Nonequilibrium work distribution of a quantum harmonic oscillator*, Phys. Rev. E **77**, 021128 (2008).

[Def10a] S. Deffner, O. Abah, and E. Lutz, *Quantum work statistics of linear and nonlinear parametric oscillators*, arXiv:1001.3055 (2010).

[Def10b] S. Deffner and E. Lutz, *Generalized Clausius inequality for nonequilibrium quantum processes*, arXiv:1005.4495v1 (2010).

[Des06] L. Deslauriers, S. Olmschenk, D. Stick, W. K. Hensinger, J. Sterk, and C. Monroe, *Scaling and Suppression of Anomalous Heating in Ion Traps*, Phys. Rev. Lett. **97**, 103007 (2006).

[Deu07] T. W. Deuschle, *Kalte Ionenkristalle in einer segmentierten Paul-Falle*, Dissertation, Universität Ulm (2007).

[Die89] F. Diedrich, J. C. Bergquist, W. M. Itano, and D. J. Wineland, *Laser Cooling to the Zero-Point Energy of Motion*, Phys. Rev. Lett. **62**, 403 (1989).

[Die98] M. Diederich, H. Häffner, N. Hermanspahn, M. Immel, H. Kluge, R. Ley, R. Mann, W. Quint, S. Stahl, and G. Werth, *Observing a single hydrogen-like ion in a Penning trap at T=4 K*, Hyperfine Interactions **115**, 185 (1998).

[Die08] S. Diehl, A. Micheli, A. Kantian, B. Kraus, H. P. Büchler, and P. Zoller, *Quantum states and phases in driven open quantum systems with cold atoms*, Nature Physics **4**, 878 (2008).

[DiV95] D. P. DiVincenzo, *Quantum Computation*, Science **270**, 255 (1995).

[DiV00] D. P. DiVincenzo, *The Physical Implementation of Quantum Computation*, Fortschr. Phys. **48**, 771 (2000).

[Dod94] V. V. Dodonov, O. V. Man'ko, and V. I. Man'ko, *Photon distribution for one-mode mixed light with a generic Gaussian Wigner function*, Phys. Rev. A **49**, 2993 (1994).

[DR04] W. De Roeck and C. Maes, *Quantum version of free-energy–irreversible-work relations*, Phys. Rev. E **69**, 026115 (2004).

[Dub09] R. Dubessy, T. Coudreau, and L. Guidoni, *Electric field noise above surfaces: A model for heating-rate scaling law in ion traps*, Phys. Rev. A **80**, 031402 (2009).

[Eke96] A. Ekert and R. Jozsa, *Quantum computation and Shor's factoring algorithm*, Rev. Mod. Phys. **68**, 733 (1996).

[Eps07] R. J. Epstein, S. Seidelin, D. Leibfried, J. H. Wesenberg, J. J. Bollinger, J. M. Amini, R. B. Blakestad, J. Britton, J. P. Home, W. M. Itano, J. D. Jost, E. Knill, C. Langer, R. Ozeri, N. Shiga, and D. J. Wineland, *Simplified motional heating rate measurements of trapped ions*, Phys. Rev. A **76**, 033411 (2007).

[Esc95] J. Eschner, B. Appasamy, and P. E. Toschek, *Stochastic Cooling of a Trapped Ion by Null Detection of Its Fluorescence*, Phys. Rev. Lett. **74**, 2435 (1995).

[Esc03] J. Eschner, G. Morigi, F. Schmidt-Kaler, and R. Blatt, *Laser cooling of trapped ions*, J. Opt. Soc. Am. B **20**, 1003 (2003).

[Esp09] M. Esposito, U. Harbola, and S. Mukamel, *Nonequilibrium fluctuations, fluctuation theorems, and counting statistics in quantum systems*, Rev. Mod. Phys. **81**, 1665 (2009).

[Eva93] D. J. Evans, E. G. D. Cohen, and G. P. Morriss, *Probability of second law violations in shearing steady states*, Phys. Rev. Lett. **71**, 2401 (1993).

[Eva94] D. J. Evans and D. J. Searles, *Equilibrium microstates which generate second law violating steady states*, Phys. Rev. E **50**, 1645 (1994).

[Eva02] D. J. Evans and D. J. Searles, *The Fluctuation Theorem*, Advances in Physics **51**, 1529 (2002).

[Fey82] R. P. Feynman, *Simulating Physics with Computers*, International Journal of Theoretical Physics **21** (1982).

[Gal95] G. Gallavotti and E. G. D. Cohen, *Dynamical Ensembles in Nonequilibrium Statistical Mechanics*, Phys. Rev. Lett. **74**, 2694 (1995).

[Gal09] F. Galve and E. Lutz, *Nonequilibrium thermodynamic analysis of squeezing*, Phys. Rev. A **79**, 055804 (2009).

[Gre88] L. Greengard and V. Rokhlin, *The rapid evaluation of potential fields in three dimensions*, in: C. Anderson and C. Greengard (Eds.), *Vortex Methods*, 121, Springer,Berlin, 1988.

[Gre97] L. Greengard and V. Rokhlin, *A new version of the fast multipole method for the Laplace equation in three dimensions*, Acta Numerica **6**, 229 (1997).

[Gum05] N. A. Gumerov and R. Duraiswami, *Comparison of the efficiency of translation operators used in the fast multipole method for the 3D Laplace equation*, University of Maryland, Department of Computer Science Technical Report CS-TR-4701 (2005).

[Har07] N. C. Harris, Y. Song, and C.-H. Kiang, *Experimental Free Energy Surface Reconstruction from Single-Molecule Force Spectroscopy using Jarzynski's Equality*, Phys. Rev. Lett. **99**, 068101 (2007).

[Hel10] M. Hellwig, A. Bautista-Salvador, K. Singer, G. Werth, and F. Schmidt-Kaler, *Fabrication of a planar micro Penning trap and numerical investigations of versatile ion positioning protocols*, New Journal of Physics **12**, 065019 (2010).

[Hen06] W. K. Hensinger, S. Olmschenk, D. Stick, D. Hucul, M. Yeo, M. Acton, L. Deslauriers, and C. Monroe, *T-junction ion trap array for two-dimensional ion shuttling, storage, and manipulation*, Appl. Phys. Lett **88**, 034101 (2006).

[Hen07] M. J. Henrich, F. Rempp, and G. Mahler, *Quantum thermodynamic Otto machines: A spin-system approach*, Eur. Phys. J. Special Topics **151**, 157 (2007).

[Häf05a] H. Häffner, W. Hänsel, C. F. Roos, J. Benhelm, D. C. al kar, M. Chwalla, T. Körber, U. D. Rapol, M. Riebe, P. O. S. andC. Becher, O. Gühne, W. Dür, and R. Blatt, *Scalable multiparticle entanglement of trapped ions*, Nature **438**, 643 (2005).

[Häf05b] H. Häffner, F. Schmidt-Kaler, W. Hänsel, C. Roos, T. Körber, M. Chwalla, M. Riebe, J. Benhelm, U. Rapol, C. Becher, and R. Blatt, *Robust entanglement*, Appl. Phys. B: Lasers and Optics **81**, 151 (2005).

[Hil09] S. Hilt and E. Lutz, *System-bath entanglement in quantum thermodynamics*, Phys. Rev. A **79**, 010101 (2009).

[Hom09] J. P. Home, D. Hanneke, J. D. Jost, J. M. Amini, D. Leibfried, and D. J. Wineland, *Complete Methods Set for Scalable Ion Trap Quantum Information Processing*, Science **325**, 1227 (2009).

[Hub08a] G. Huber, T. Deuschle, W. Schnitzler, R. Reichle, K. Singer, and F. Schmidt-Kaler, *Transport of ions in a segmented linear Paul trap in printed-circuit-board technology*, New Journal of Physics **10**, 013004 (2008).

[Hub08b] G. Huber, F. Schmidt-Kaler, S. Deffner, and E. Lutz, *Employing Trapped Cold Ions to Verify the Quantum Jarzynski Equality*, Phys. Rev. Lett. **101**, 070403 (2008).

[Hub10] G. Huber, F. Ziesel, U. Poschinger, K. Singer, and F. Schmidt-Kaler, *A trapped-ion local field probe*, Appl. Phys. B: Lasers and Optics (2010).

[Huc07] D. Hucul, M. Yeo, W. Hensinger, J. Rabchuk, S. Olmschenk, and C. Monroe, *On the Transport of Atomic Ions in Linear and Multidimensional Ion Trap Arrays*, arXiv:quant-ph/0702175v3 (2007).

[Hus53] K. Husimi, *Miscellanea in Elementary Quantum Mechanics, II*, Progress of Theoretical Physics **9**, 381 (1953).

[Ita95] W. M. Itano, J. C. Bergquist, J. J. Bollinger, and D. J. Wineland, *Cooling methods in ion traps*, Phys. Scr. **T59**, 106 (1995).

[Jan92] J. Janszky and P. Adam, *Strong squeezing by repeated frequency jumps*, Phys. Rev. A **46**, 6091 (1992).

[Jar97] C. Jarzynski, *Nonequilibrium Equality for Free Energy Differences*, Phys. Rev. Lett. **78**, 2690 (1997).

[Jar08] C. Jarzynski, *Nonequilibrium work relations: foundations and applications*, Eur. Phys. J. B **64**, 331 (2008).

[Jay63] E. Jaynes and F. Cummings, *Comparison of quantum and semiclassical radiation theories with application to the beam maser*, Proceedings of the IEEE **51**, 89 (1963).

[Joh09] M. Johanning, A. Varón, and C. Wunderlich, *Quantum Simulations with Cold Trapped Ions*, Journal of Physics B: At. Mol. Opt. Phys. **42**, 154009 (2009).

[Jos09] J. D. Jost, J. P. Home, J. M. Amini, D. Hanneke, R. Ozeri, C. Langer, J. J. Bollinger, D. Leibfried, and D. J. Wineland, *Entangled mechanical oscillators*, Nature **459**, 683 (2009).

[Kaw07] R. Kawai, J. M. R. Parrondo, and C. V. den Broeck, *Dissipation: The Phase-Space Perspective*, Phys. Rev. Lett. **98**, 080602 (2007).

[Kie01] D. Kielpinski, V. Meyer, M. A. Rowe, C. A. Sackett, W. M. Itano, C. Monroe, and D. J. Wineland, *A Decoherence-Free Quantum Memory Using Trapped Ions*, Science **291**, 1013 (2001).

[Kie02] D. Kielpinski, C. Monroe, and D. J. Wineland, *Architecture for a large-scale ion-trap quantum computer*, Nature **417**, 709 (2002).

[Kir09] G. Kirchmair, J. Benhelm, F. Zähringer, R. Gerritsma, C. F. Roos, and R. Blatt, *High-fidelity entanglement of* $^{43}Ca^{+}$ *hyperfine clock states*, Physical. Rev. A **79**, 020304(R) (2009).

[Lab08] J. Labaziewicz, Y. Ge, P. Antohi, D. Leibrandt, K. R. Brown, and I. L. Chuang, *Suppression of Heating Rates in Cryogenic Surface-Electrode Ion Traps*, Phys. Rev. Lett. **100**, 013001 (2008).

[Lam97] S. K. Lamoreaux, *Thermalization of trapped ions: A quantum perturbation approach*, Phys. Rev. A **56**, 4970 (1997).

[Lei96] D. Leibfried, D. M. Meekhof, B. E. King, C. Monroe, W. M. Itano, and D. J. Wineland, *Experimental Determination of the Motional Quantum State of a Trapped Atom*, Phys. Rev. Lett. **77**, 4281 (1996).

[Lei03] D. Leibfried, R. Blatt, C. Monroe, and D. Wineland, *Quantum dynamics of single trapped ions*, Rev. Mod. Phys. **75**, 281 (2003).

[Lei05] D. Leibfried, E. Knill, S. Seidelin, J. Britton, R. B. Blakestad, J. Chiaverini, D. B. Hume, W. M. Itano, J. D. Jost, C. Langer, R. Ozeri, R. Reichle, and D. J. Wineland, *Creation of a six-atom "Schrödinger cat" state*, Nature **438**, 639 (2005).

[Lia95] S.-S. Liaw, *Ab initio calculation of the lifetimes of 4p and 3d levels of* $Ca+$, Phys. Rev. A **51**, R1723 (1995).

[Lid98] D. A. Lidar, I. L. Chuang, and K. B. Whaley, *Decoherence-Free Subspaces for Quantum Computation*, Phys. Rev. Lett. **81**, 2594 (1998).

[Lip02] J. Liphardt, S. Dumont, S. B. Smith, J. Tinoco, Ignacio, and C. Bustamante, *Equilibrium Information from Nonequilibrium Measurements in an Experimental Test of Jarzynski's Equality*, Science **296**, 1832 (2002).

[Llo96] S. Lloyd, *Universal Quantum Simulators*, Science **273**, 1073 (1996).

[Lut97] L. G. Lutterbach and L. Davidovich, *Method for Direct Measurement of the Wigner Function in Cavity QED and Ion Traps*, Phys. Rev. Lett. **78**, 2547 (1997).

[Mai06] R. Maiwald, *Abbildungs- und Steuerungssystem für ein Experiment mit einzelnen Ionen*, Diplomarbeit, Universität Ulm (2006).

[Mar94] I. Marzoli, J. I. Cirac, R. Blatt, and P. Zoller, *Laser cooling of trapped three-level ions: Designing two-level systems for sideband cooling*, Phys. Rev. A **49**, 2771 (1994).

[Mee96] D. M. Meekhof, C. Monroe, B. E. King, W. M. Itano, and D. J. Wineland, *Generation of Nonclassical Motional States of a Trapped Atom*, Phys. Rev. Lett. **76**, 1796 (1996).

[MF96] R. L. de Matos Filho and W. Vogel, *Even and Odd Coherent States of the Motion of a Trapped Ion*, Phys. Rev. Lett. **76**, 608 (1996).

[Mon95] C. Monroe, D. M. Meekhof, B. E. King, S. R. Jefferts, W. M. Itano, D. J. Wineland, and P. Gould, *Resolved-Sideband Raman Cooling of a Bound Atom to the 3D Zero-Point Energy*, Phys. Rev. Lett. **75**, 4011 (1995).

[Mon96] C. Monroe, D. M. Meekhof, B. E. King, and D. J. Wineland, *A "Schrödinger Cat" Superposition State of an Atom*, Science **272**, 1131 (1996).

[Mon09] T. Monz, K. Kim, A. S. Villar, P. Schindler, M. Chwalla, M. Riebe, C. F. Roos, H. Häffner, W. Hänsel, M. Hennrich, and R. Blatt, *Realization of Universal Ion-Trap Quantum Computation with Decoherence-Free Qubits*, Phys. Rev. Lett. **103**, 200503 (2009).

[Mor00] G. Morigi, J. Eschner, and C. H. Keitel, *Ground State Laser Cooling Using Electromagnetically Induced Transparency*, Phys. Rev. Lett. **85**, 4458 (2000).

[Muk03] S. Mukamel, *Quantum Extension of the Jarzynski Relation: Analogy with Stochastic Dephasing*, Phys. Rev. Lett. **90**, 170604 (2003).

[Mur09] M. Murphy, L. Jiang, N. Khaneja, and T. Calarco, *High-fidelity fast quantum transport with imperfect controls*, Phys. Rev. A **79**, 020301 (2009).

[Mya00] C. J. Myatt, B. E. King, Q. A. Turchette, C. A. Sackett, D. Kielpinski, W. M. Itano, C. Monroe, and D. J. Wineland, *Decoherence of quantum superpositions through coupling to engineered reservoirs*, Nature **403**, 169 (2000).

[Mye08] A. H. Myerson, D. J. Szwer, S. C. Webster, D. T. C. Allcock, M. J. Curtis, G. Imreh, J. A. Sherman, D. N. Stacey, A. M. Steane, and D. M. Lucas, *High-Fidelity Readout of Trapped-Ion Qubits*, Phys. Rev. Lett. **100**, 200502 (2008).

[Nab94] K. Nabors, F. T. Korsmeyer, F. T. Leighton, and J. White, *Preconditioned, adaptive, miltipole-accelerated iterative methods for three-dimensional first-kind integral equations of potential theory*, SIAM J. Sci. Comput. **15**, 713 (1994).

[Nag86] W. Nagourney, J. Sandberg, and H. Dehmelt, *Shelved optical electron amplifier: Observation of quantum jumps*, Phys. Rev. Lett. **56**, 2797 (1986).

[Neu78] W. Neuhauser, M. Hohenstatt, P. Toschek, and H. Dehmelt, *Optical-Sideband Cooling of Visible Atom Cloud Confined in Parabolic Well*, Phys. Rev. Lett. **41**, 233 (1978).

[Nie00] M. A. Nielsen and I. L. Chuang, *Quantum Computation and Quantum Information*, Cambridge Univ. Press, Cambridge, UK, 2000.

[NIS10] *NIST Atomic Spectra Database*, National Institute of Standards and Technology, http://www.nist.gov/physlab/data/asd.cfm (2010).

[Our06] A. Ourjoumtsev, R. Tualle-Brouri, J. Laurat, and P. Grangier, *Generating Optical Schrödinger Kittens for Quantum Information Processing*, Science **312**, 83 (2006).

[Paz08] J. P. Paz and A. J. Roncaglia, *Dynamics of the Entanglement between Two Oscillators in the Same Environment*, Phys. Rev. Lett. **100**, 220401 (2008).

[Pos09] U. G. Poschinger, G. Huber, F. Ziesel, M. Deiß, M. Hettrich, S. A. Schulz, K. Singer, G. Poulsen, M. Drewsen, R. J. Hendricks, and F. Schmidt-Kaler, *Coherent manipulation of a $^{40}Ca^{+}$ spin qubit in a micro ion trap*, Journal of Physics B: Atomic, Molecular and Optical Physics **42**, 154013 (2009).

[Pow02] H. F. Powell, D. M. Segal, and R. C. Thompson, *Axialization of Laser Cooled Magnesium Ions in a Penning Trap*, Phys. Rev. Lett. **89**, 093003 (2002).

[Poy96] J. F. Poyatos, J. I. Cirac, and P. Zoller, *Quantum Reservoir Engineering with Laser Cooled Trapped Ions*, Phys. Rev. Lett. **77**, 4728 (1996).

[Poz02] C. Pozrikidis, *A Practical Guide to Boundary Element Methods with the software library BEMLIB*, Chapman & Hall/CRC, Boca Raton, FL, USA, 2002.

[Qua07] H. T. Quan, Y.-x. Liu, C. P. Sun, and F. Nori, *Quantum thermodynamic cycles and quantum heat engines*, Phys. Rev. E **76**, 031105 (2007).

[Qua09] H. T. Quan, *Quantum thermodynamic cycles and quantum heat engines. II.*, Phys. Rev. E **79**, 041129 (2009).

[Rei06] R. Reichle, D. Leibfried, R. B. Blakestad, J. Britton, J. D. Jost, E.Knill, C. Langer, R. Ozeri, S. Seidelin, and D. J. Wineland, *Transport dynamics of single ions in segmented microstructured Paul trap arrays*, Fortschr. Phys. **54**, 666 (2006).

[Rez06] Y. Rezek and R. Kosloff, *Irreversible performance of a quantum harmonic heat engine*, New Journal of Physics **8**, 83 (2006).

[Rit03] F. Ritort, *Work fluctuations, transient violations of the second law and free-energy recovery methods: Perspectives in Theory and Experiments*, arXiv:cond-mat/0401311v1 (2003).

[Roo99] C. Roos, T. Zeiger, H. Rohde, H. C. Nägerl, J. Eschner, D. Leibfried, F. Schmidt-Kaler, and R. Blatt, *Quantum State Engineering on an Optical Transition and Decoherence in a Paul Trap*, Phys. Rev. Lett. **83**, 4713 (1999).

[Roo00] C. Roos, *Controlling the quantum state of trapped ions*, Dissertation, Leopold-Franzens-Universität Innsbruck (2000).

[Roo06] C. F. Roos, M. Chwalla, K. Kim, M. Riebe, and R. Blatt, *"Designer atoms" for quantum metrology*, Nature **443**, 316 (2006).

[Sch01a] W. P. Schleich, *Quantum Optics in Phase Space*, Wiley-VCH, 2001.

[Sch01b] F. Schmidt-Kaler, J. Eschner, G. Morigi, C. F. Roos, D. Leibfried, A. Mundt, and R. Blatt, *Laser cooling with electromagnetically induced transparency: Application to trapped samples of ions or neutral atoms*, Appl. Phys. B: Lasers and Optics **73**, 807 (2001).

[Sch03] F. Schmidt-Kaler, H. Häffner, S. Gulde, M. Riebe, G. Lancaster, T. Deuschle, C. Becher, W. Hänsel, J. Eschner, C. Roos, and R. Blatt, *How to realize a universal quantum gate with trapped ions*, Appl. Phys. B: Lasers and Optics **77**, 789 (2003).

[Sch06] S. Schulz, U. Poschinger, K. Singer, and F. Schmidt-Kaler, *Optimization of segmented linear Paul traps and transport of stored particles*, Fortschr. Phys. **54**, 648 (2006).

[Sch07] R. Schützhold, M. Uhlmann, L. Petersen, H. Schmitz, A. Friedenauer, and T. Schätz, *Analogue of Cosmological Particle Creation in an Ion Trap*, Phys. Rev. Lett. **99**, 201301 (2007).

[Sch08] S. Schulz, U. Poschinger, F. Ziesel, and F. Schmidt-Kaler, *Sideband cooling and coherent dynamics in a microchip multi-segmented ion trap*, N. J. Phys. **10** (2008).

[She07] L. Shen and Y. J. Liu, *An adaptive fast multipole boundary element method for three-dimensional potential problems*, Acta Numerica **39**, 681 (2007).

[Sin10] K. Singer, U. Poschinger, M. Murphy, P. Ivanov, F. Ziesel, T. Calarco, and F. Schmidt-Kaler, *Colloquium: Experiments with atomic quantum bits - essential numerical tools*, arXiv:0912.0196v2 (2010).

[Ste86] S. Stenholm, *The semiclassical theory of laser cooling*, Rev. Mod. Phys. **58**, 699 (1986).

[Ste97] A. Steane, *The ion trap quantum information processor*, Appl. Phys. B: Lasers and Optics **64**, 623 (1997).

[Tal07a] P. Talkner and P. Hänggi, *The Tasaki-Crooks quantum fluctuation theorem*, Journal of Physics A: Mathematical and Theoretical **40**, F569 (2007).

[Tal07b] P. Talkner, E. Lutz, and P. Hänggi, *Fluctuation theorems: Work is not an observable*, Phys. Rev. E **75**, 050102 (2007).

[Tal08] P. Talkner, P. S. Burada, and P. Hänggi, *Statistics of work performed on a forced quantum oscillator*, Phys. Rev. E **78**, 011115 (2008).

[Tas00] H. Tasaki, *Jarzynski Relations for Quantum Systems and Some Applications*, arXiv:cond-mat/0009244v2 (2000).

[Tho09] R. C. Thompson, S. Donnellan, D. R. Crick, and D. M. Segal, *Applications of laser cooled ions in a Penning trap*, J. Phys. B **42**, 154003 (2009).

[Tik77] A. N. Tikhonov and V. A. Arsenin, *Solution of Ill-posed Problems*, Winston and Sons, Washington, USA, 1977.

[Tur00] Q. A. Turchette, D. Kielpinski, B. E. King, D. Leibfried, D. M. Meekhof, C. J. Myatt, M. A. Rowe, C. A. Sackett, C. S. Wood, W. M. Itano, C. Monroe, and D. J. Wineland, *Heating of trapped ions from the quantum ground state*, Phys. Rev. A **61**, 063418 (2000).

[Ume62] H. Umegaki, *Conditional expectation in an operator algebra. IV. Entropy and information*, Kodai Math. Sem. Rep. **14**, 59 (1962).

[Wan02] G. M. Wang, E. M. Sevick, E. Mittag, D. J. Searles, and D. J. Evans, *Experimental Demonstration of Violations of the Second Law of Thermodynamics for Small Systems and Short Time Scales*, Phys. Rev. Lett. **89**, 050601 (2002).

[Wei99] M. Weidinger, B. T. H. Varcoe, R. Heerlein, and H. Walther, *Trapping States in the Micromaser*, Phys. Rev. Lett. **82**, 3795 (1999).

[Wes07] J. H. Wesenberg, R. J. Epstein, D. Leibfried, R. B. Blakestad, J. Britton, J. P. Home, W. M. Itano, J. D. Jost, E. Knill, C. Langer, R. Ozeri, S. Seidelin, and D. J. Wineland, *Fluorescence during Doppler cooling of a single trapped atom*, Phys. Rev. A **76**, 053416 (2007).

[Wil08] S. R. Williams, D. J. Searles, and D. J. Evans, *Nonequilibrium Free-Energy Relations for Thermal Changes*, Phys. Rev. Lett. **100**, 250601 (2008).

[Win79] D. J. Wineland and W. M. Itano, *Laser cooling of atoms*, Phys. Rev. A **20**, 1521 (1979).

[Win98] D. J. Wineland, C. Monroe, W. M. Itano, D. Leibfried, B. E. King, and D. M. Meekhof, *Experimental Issues in Coherent Quantum-State Manipulation of Trapped Atomic Ions*, J. Res. Natl. Inst. Stand. Technol. **103**, 259 (1998).

[Wun07] C. Wunderlich, T. Hannemann, T. Körber, H. Häffner, C. Roos, W. Hänsel, R. Blatt, and F. Schmidt-Kaler, *Robust state preparation of a single trapped ion by adiabatic passage*, J. Mod. Opt. **54**, 1541 (2007).

[Wun09] H. Wunderlich, C. Wunderlich, K. Singer, and F. Schmidt-Kaler, *Two-dimensional cluster-state preparation with linear ion traps*, Phys. Rev. A **79**, 052324 (2009).

[Zur03] W. H. Zurek, *Decoherence, einselection, and the quantum origins of the classical*, Rev. Mod. Phys. **75**, 715 (2003).

Danksagung

Zum Gelingen dieser Arbeit hat im Laufe der Jahre eine ganze Reihe von Personen beigetragen, denen ich allen meinen herzlichen Dank aussprechen will. Im Besonderen danke ich Prof. Ferdinand Schmidt-Kaler, der meine Arbeit nicht nur betreut hat, sondern mich stets mit Rat und Tat unterstützt hat. Sein Weitblick, Vertrauen und nicht zuletzt seine ansteckende Begeisterung für die Physik waren entscheidende Triebfedern für das Gelingen dieser Arbeit. Ausgesprochen dankbar bin ich auch Eric Lutz und Sebastian Deffner von der Universität Augsburg, die einen ganz wesentlichen Beitrag von Seiten der Theorie geleistet haben, und die nie müde wurden, meine Experimentalphysiker-Fragen zu beantworten.

Kilian Singer war während der gesamten Zeit nicht nur ein kompetenter Ansprechpartner für alle physikalischen und technischen Fragen, sondern auch ein wertvolles Mitglied der Gruppe und ein unvergesslicher Büropartner. Ich danke weiterhin Thomas Deuschle, Rainer Reichle und Wolfgang Schnitzler für die angenehme und erfolgreiche Zusammenarbeit an der X-Falle, nie werde ich die ersten Ionen vergessen!

Die Ergebnisse an der Mikrofalle wären nicht möglich gewesen ohne meine Kollegen Ulrich Poschinger, Frank Ziesel, Markus Deiß, Max Hettrich, Andreas Walther, Manfred Bürzele, Michaela Petrich und Stephan Schulz, welcher die Falle entwickelt hat. Die vielen im Labor verbrachten Tage und Nächte wären ohne Euch kaum möglich und sicher nicht so erfolgreich gewesen.

Mein größter Dank gilt jedoch meinen Eltern, die mir nicht nur das Studium und die Promotion ermöglicht haben, sondern auch stets den Rückhalt und das Vertrauen entgegen gebracht haben, die es mir ermöglicht haben, meinen eigenen Weg zu gehen. Ebenso danke ich meinem Bruder und meiner Freundin für die persönliche und moralische Unterstützung während der ganzen Zeit, und dass Sie mich nie die wirklich wichtigen Dinge im Leben vergessen ließen.

Hiermit erkläre ich, dass ich die vorliegende Arbeit selbständig angefertigt und keine anderen als die angegebenen Quellen und Hilfsmittel benutzt habe, sowie die wörtlich oder inhaltlich übernommenen Stellen als solche kenntlich gemacht habe und die Satzung der Universität Ulm zur Sicherung guter wissenschaftlicher Praxis beachtet habe.

Ulm, den 28. Juli 2010 Gerhard Thomas Huber